Celia Hughes, B.A.I.

An in silico framework for the design and optimisation of bioinspired, 3D-printed, fibre-reinforced polymer heart valve leaflets

Trinity College Dublin, March 2025

A thesis submitted to the University of Dublin in partial fulfilment of the requirements for the degree of

Doctor in Philosophy

Supervisor: Prof. Caitríona Lally

Internal examiner: Prof. Bruce Murphy

External examiner: Prof. Petra Mela

Declaration

I declare that this thesis has not been submitted as an exercise for a degree at this or any other university and it is entirely my own work.

I agree to deposit this thesis in the University's open access institutional repository or allow the library to do so on my behalf, subject to Irish Copyright Legislation and Trinity College Library conditions of use and acknowledgement.

I consent to the examiner retaining a copy of the thesis beyond the examining period, should they so wish (EU GDPR May 2018).

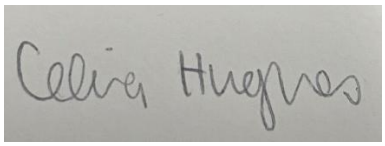

Celia Hughes

March 2025

Summary

Current valve replacement devices used to treat aortic stenosis carry significant drawbacks such as the need for patients to adopt lifelong anticoagulant therapy or the possibility of premature failure. There is significant potential for bioinspired polymer-based prosthetic valves to outperform the current commercial devices, improving patient outcomes and delivering a cheaper, more easily manufacturable device. The aim of this thesis was to create a methodology to design, optimise, and assess possible polymer valve materials and structures to enable effective and efficient development of future devices.

To deliver on this aim, benchmarks for a bioinspired structure and desired material properties were established based on mechanical testing and imaging of native aortic valve leaflets. The collagen fibre structures in the leaflets were characterised by their orientation and level of crimp, and the material and mechanical response of the whole leaflet and its layers were established. Melt electrowriting (MEW) was identified as an ideal additive manufacturing technique to create a bioinspired fibre structure, and thus a finite element model of a MEW fibre-reinforced silicone leaflet with bioinspired fibre orientations was developed. This leaflet model was expanded to simulate a trileaflet valve, modelling the leaflet opening and closing through the cardiac cycle. Using this model to predict the material response and valve performance, design of experiments (DOE) was employed to investigate the impact of various structural components within this fibre-reinforced leaflet. Through this, the most effective MEW and silicone combination was identified. To optimise the leaflet performance and material outcomes, a fibre reorientation algorithm was applied to identify an ideal fibre reinforcement structure for this particular leaflet shape. Ultimately, this formed a fibre-reinforced leaflet design framework to enabling effective development of bioinspired polymer leaflets.

The best MEW and silicone combination and fibre reinforcement structure was identified and manufactured. By performing mechanical testing on these materials, the material response under different loading cases was compared to those predicted by the finite element models, and have informed future model validation methods. Additionally, leaflets were created and suturability was assessed to determine the feasibility of implementing these leaflets into current manufacturing workflows. The insights from this have informed future fibre reinforcement structures for these leaflets. Overall, this work has developed a methodology to develop, assess, and optimise future bioinspired, fibre-reinforced polymer leaflets, and shown the feasibility of manufacturing and implementation of these materials.

Acknowledgements

Firstly, I would like to thank my supervisor, Professor Caitríona Lally, for enabling me to pursue a PhD and for her endless support and guidance throughout my time in her lab. Tríona's enthusiasm, dedication, and knowledge has been integral throughout the duration of this work as well as in my own professional development, and working in her group has been an overwhelmingly wonderful experience. I would also like to thank Research Ireland (formerly Irish Research Council) and Boston Scientific for funding this work, and my industry mentors, Evelyn Campbell and David O'Reilly, for their support. Thank you to Professor Bruce Murphy and Professor Petra Mela for taking the time to read this thesis.

Much of this work was made possible thanks to collaborators. A massive thank you to Brenton Cavanagh in RCSI for training me on and letting me use their microscope for SHG, as well as Kenny from Rosderra Meats for supplying the tissue used for mechanical testing. All work in parsons is improved with help from the incredible staff here, thank you for your support (and chats): Gordon O'Brien, Brendan Caffrey, Rob Dunbar, Alex Kearns, Peter O'Reilly, and Owen Hughes.

Thank you to the entire Lally Lab, current and former members, whom I have had the privilege to work with over the years. I have had such great support and learned an incredible amount from everyone. The office chats, tea breaks, jokes, walks, and trips to Kennedy's have made my time in office 2.14 an absolute joy. You all made this experience as great as it could be and I could never thank you enough.

I feel incredibly lucky to have had such a strong support network of friends and family. Notably, I would like to thank Brooke Tornifoglio who has been an invaluable friend, mentor, and colleague, and from whom I have learned so much. Thank you to everyone who has supported me and listened to my ceaseless voice messages throughout the years, especially: Imogen, Malcolm, Marta, Phil, Dave, Grace, Senan, Hannah, Mick, Fran, Anne, Percy, and my mom, Celia. You all have kept me sane, fed, and, most importantly, laughing, and I couldn't be more appreciative. Finally, a huge thank you to Sam whose love, support, and cooking has kept me going; I simply cannot put my gratitude or love into words.

I'd like to dedicate this to my grandmother, Mary Munro.

List of publications, conference proceedings, and awards

First author publications

Hughes, C., Whelan, A., O'Reilly, D., Campbell, E., Lally, C., 2025. Aortic valve leaflet assessment to inform novel bioinspired material: understanding the impact of collagen fibres on the tissue's mechanical behaviour. JMBBM. 132. DOI:10.1016/j.jmbbm.2024.106881

Co-author publications

Tornifoglio, B., Hughes, C., Digeronimo, F., Guendouz, Y., Johnston, R. D., Lally, C. 2025. Imaging the microstructure of the arterial wall – ex vivo to in vivo potential. Acta Biomaterialia. https://doi.org/10.1016/j.actbio.2025.05.022. [In press]

Conference proceedings

Hughes, C., Johnston, R. D., Campbell, E., Lally, C., (2025) "An in-silico framework for design and optimisation of 3D-printed bioinspired polymer heart valve leaflets" in European Solid Mechanics Conference (ESMC). Lyon, France.

Guerin, L., Hughes C., Burke, R., Campbell E., Growney E., Lally C., (2025) "Simultaneous Structural Damage and Calcification Dramatically Reduces Porcine Pericardium Durability" in European Solid Mechanics Conference (ESMC). Lyon, France.

Gupta, P., Hughes, C., Vahab, A., Campbell, E., Lally, C., (2025) "Manufacturing Bioinspired Polymeric Heart Valve Leaflet Material" in 30th Congress of the European Society of Biomechanics (ESB), Zürich, Switzerland.

Hughes, C., Johnston, R. D., Campbell, E., Lally, C., (2025) "Establishment of an in-silico framework for designing 3D-printed bioinspired polymer heart valve leaflets" in Bioengineering in Ireland (BINI). Athlone, Ireland.

Gupta, P., Hughes, C., Vahab, A., Lally, C., (2025) 'Manufacturing Bioinspired Polymeric Heart Valve Leaflet Material' in Bioengineering in Ireland (BINI). Athlone, Ireland.

Guerin, L., Hughes C., Campbell E., Burke, R., Growney E., Lally C., (2025) "Synergistic Effect of Calcification and Structural Damage Dramatically Reduces Lifetime of Porcine Pericardium used in Bioprosthetic Heart Valve Leaflets" in Bioengineering in Ireland (BINI). Athlone, Ireland.

Hughes, C., Johnston, R.D., Campbell, E., Lally, C., (2024) 'Bioinspired fibre-reinforced polymer heart valve leaflets.' in 29th Congress of European Society of Biomechanics (ESB). Edinburgh, Scotland.

Guerin, L, Hughes, C, Johnston, R., Growney, E, Campbell, E, Zhang, M, Lally, C (2024) 'Predicting Damage Accumulation of Porcine Pericardium Using Experimental and Machine Learning Approaches' The 29th Conference of the European Society of Biomechanics. Edinburgh, Scotland

Guerin, L, Hughes, C, Growney, E, Campbell, M, Lally, C (2024) 'Minimising Calcification and Structural Damage of Porcine Pericardium (PP) to Improve Bioprosthetic Valve Leaflet Durability' The 27th Sir Bernard Crossland Symposium. Belfast, Northern Ireland

Hughes, C., Johnston, R.D., Whelan, A., O'Reilly, D., Campbell, E., Lally, C., (2024) 'Creation of a Bioinspired Fibre-Reinforced Polymer Leaflet Valve for Transcatheter Aortic Valve Implantation (TAVI),' in Bioengineering in Ireland (BINI). Newcastle, Northern Ireland.

Guerin, L, Hughes, C, Growney, E, Campbell, E, Lally, C (2024) 'Determining the Dominant Factors Affecting the Flexural Damage Accumulation of Porcine Pericardial (PP) Leaflets to Improve TAVR Device Durability' Proceedings of the 29th Annual Conference of the Section of Bioengineering of the Royal Academy of Medicine in Ireland. Newcastle, Northern Ireland

Hughes, C., Johnston, R.D., Whelan, A., O'Reilly, D., Campbell, E., Lally, C., (2023) 'Informing a Bioinspired Fibre-Reinforced Polymer Leaflet Valve for Transcatheter Aortic Valve Implantation using Finite Element Modelling', in Inauguaral School of Engineering Research Symposium (SERS). Dublin, Ireland.

Hughes, C., Johnston, R.D., Whelan, A., O'Reilly, D., Campbell, E., Lally, C., (2023) 'Development of melt electrowriting based polymer heart valve leaflets informed through finite element modelling,' in Summer Biomechanics, Bioengineering and Biotransport Conference. Vail, Colorado, USA.

Guerin, L, Hughes, C, Growney, E, Campbell, E, Zhang, M, Lally, C (2023) 'Determining the Role Crimping Damage Plays in the Flexural Damage Accumulation of Porcine Pericardial

(PP) Leaflets to Improve TAVR Leaflet Durability' 26th Sir Bernard Crossland Symposium. Limerick, Ireland

Hughes, C., Johnston, R., Whelan, A., O'Reilly, D., Campbell, E., Lally, C., (2023) 'Using finite element modelling to inform fibre reinforcement in polymer heart valve leaflets,' in Proceedings of the 28th Bioengineering in Ireland. Enfield, Ireland.

Guerin, L, Hughes, C, O'Reilly, D, Campbell, E, Lally, C (2023) 'An Investigation into the Role of Crimping Damage on Subsequent Flexural Damage Accumulation in Porcine Pericardial Leaflets' Proceedings of the 28th Annual Conference of the Section of Bioengineering of the Royal Academy of Medicine in Ireland. Enfield, Ireland

Hughes, C., Whelan, A., Florea, L., O'Reilly, D., Campbell, E., Lally, C., (2022) 'Characterisation of the mechanical and structural properties of the native aortic valve leaflet and its layers,' at the 25th annual Sir Bernard Crossland Symposium. Galway, Ireland.

Hughes, C., Whelan, A., Florea, L., O'Reilly, D., Campbell, E., Lally, C., (2022) 'Investigation of Native Aortic Leaflet Structure and Mechanics,' in 11th European Solid Mechanics Conference. Galway, Ireland.

Hughes, C., Whelan, A., Florea, L., O'Reilly, D., Campbell, E., Lally, C., (2022) 'Characterisation of the Mechanical and Structural Properties of the Native Aortic Leaflet and its Layers,' in Proceedings of the 27th Bioengineering in Ireland. Galway, Ireland.

Hughes, C., Whelan, A., Florea, L., O'Reilly, D., Campbell, E., Lally, C., (2021) 'Investigating 3D Printed Polymer Resin for Biomimetic Polymer Aortic Valve Leaflets,' in 26th Congress of the European Society of Biomechanics. Virtual platform.

Awards

Trinity Centre for Biomedical Engineering Annual Research Day, 2024: Best Rapid Fire Presentation

Nominated for The Trinity Teaching Award for Postgraduate Students 2024.

School of Engineering Research Day, 2023: Best Presentation from 3rd or 4th year PhD

Sir Bernard Crossland Symposium, 2022: 2nd Place Best Poster

Contents

Declaration iii

Summary iv

Acknowledgements v

List of publications, conference proceedings, and awards vi

Chapter 1 Introduction 1

1.1 Research motivation 1

1.2 Objectives 2

1.3 Thesis structure 3

Chapter 2 Literature review 4

2.1 Native aortic valve 4

2.1.1 The heart 4

2.1.2 The aortic valve 5

2.1.3 Aortic valve leaflet imaging 8

2.1.4 Mechanical properties 9

2.2 Aortic stenosis: disease and treatment 15

2.2.1 Aortic stenosis 15

2.2.2 Mechanical heart valves 16

2.2.3 Bioprosthetic heart valves 17

2.2.4 Structural valve degeneration and bioprosthetic valve failure 20

2.2.5 Polymer heart valves 21

2.3 Finite element modelling in polymer valve development 32

2.4 Melt electrowriting (MEW) 34

2.5 Summary 37

Chapter 3 Aortic valve leaflet assessment to inform novel bioinspired materials 39

3.1 Introduction 39

3.2 Methods 40

3.2.1 Tissue dissection and freezing 40
3.2.2 Histology 40
3.2.3 Second harmonic generation (SHG) imaging 41
3.2.4 Uniaxial tensile testing 42
3.2.5 Statistics 44
3.3 Results 44
3.3.1 Histology 44
3.3.2 SHG imaging 45
3.3.3 Uniaxial tensile testing 47
3.4 Discussion 49
Chapter 4 Using design of experiments and finite element modelling to determine optimal bioinspired polymeric leaflet structural combinations 55
4.1 Introduction 55
4.2 Methods 56
4.2.1 Discrete fibre model 57
4.2.2 Trileaflet valve model 58
4.2.3 Fibre orientation verification 62
4.2.4 Design of experiments 62
4.2.5 Statistical analysis 63
4.3 Results 63
4.3.1 Fibre orientation analysis 63
4.3.2 Design of experiments 66
4.4 Discussion 72
Chapter 5 Optimisation of a fibre-reinforced polymer leaflet valves using a fibre reorientation algorithm 78
5.1 Introduction 78
5.2 Methods 79
5.2.1 Single leaflet model 79

5.2.2 Reorientation algorithm 80
5.2.3 Implementation in dynamic model 82
5.2.4 Asymmetric orifice model 82
5.3 Results 83
5.3.1 Fibre reorientation 83
5.3.2 Dynamic implementation 85
5.3.3 Asymmetric orifice model 87
5.4 Discussion 89
Chapter 6 Comparison of finite element predictions to benchtop testing of fibre-reinforced materials 93
6.1 Introduction 93
6.2 Methods 94
6.2.1 Sample manufacturing 94
6.2.2 Flexural bulge testing 96
6.2.3 Modelling 97
6.2.4 Mechanical testing 99
6.3 Results 99
6.3.1 Mesh embedding 99
6.3.2 Bulge testing 100
6.3.3 PDMS calibration 101
6.3.4 MEW-embedded calibration 102
6.3.5 Comparison to uniaxial data 104
6.3.6 Valve models 104
6.4 Discussion 106
Chapter 7 Manufacturing customised, fibre-reinforced polymer leaflets informed by finite element modelling 109
7.1 Introduction 109
7.2 MEW-embedded leaflets, Iteration 1 109

7.2.1 MEW printing and embedding 109
7.2.2 Leaflet manufacture 109
7.2.3 Insights 110
7.3 MEW embedded leaflets, Iteration 2 111
7.3.1 MEW fibre structure 111
7.3.2 Results 113
7.4 Discussion 113
Chapter 8 Final discussion 116
8.1 Future directions 121
Chapter 9 Concluding remarks 124
References 126
Appendix A1 152
Appendix A2 160
Appendix A3 161
Appendix A4 163

List of figures

Figure 1-1 Graphical summary of primary studies detailed throughout this thesis..... 3
Figure 2-1 Diagram of the human heart with arrows indicating direction of blood flow..... 4
Figure 2-2 Diagram of heart during diastole and systole phases..... 5
Figure 2-3 The aortic valve..... 6
Figure 2-4 Wigger's Diagram detailing the pressure and flow conditions around the aortic valve (ISO 5840-1). 6
Figure 2-5 (A) Diagram of the layers of the aortic valve leaflet (Li et al. 2019)and (B) an image of a histological slice through the leaflet detailing the three layers, adapted from (Schoen 2012)..... 7
Figure 2-6 An image of the aortic valve leaflet showing the alignment of collagen fibre bundles in the circumferential direction (Sauren 1981)..... 7
Figure 2-7 Schematic of fibre crimping and stretching within the aortic valve leaflet in systole and diastole: 1) Collagen fibres, 2) Elastin fibres, 3) Aortic root; adapted from (Coulter et al. 2019). 8
Figure 2-8 (a) Image taken using polarised light microscopy of porcine aortic valve leaflet and (b) artistic rendering of primary fibrous structure (Rock et al. 2014) 9
Figure 2-9 Image of plots from Vesely, 1997 showing the tension vs strain curves for whole aortic leaflet in circumferential and radial directions. 11
Figure 2-10 Schematic of rotating collagen fibres under differing loading conditions allowing for high degree of radial strain. Adapted from (Billiar and Sacks 2000)..... 13
Figure 2-11 Equibiaxial tension/stretch response of fibrosa (F), ventricularis (V), and intact (I) tissue in both circumferential and radial direction. 14
Figure 2-12 (A) Experimental setup and (B) plot of radius of curvature vs bending moment (Vesely and Boughner 1989) 14
Figure 2-13 Severe aortic stenosis showing calcium nodules on leaflets (Schoen and Edwards 2001)..... 15
Figure 2-14 Mechanical heart valves, (A) Starr-Edwards caged ball valve, (B) Kay-Shiley non-tilting disc valve, (C) Bjork-Shiley tilting disc valve, (D) St. Jude Medical bileaflet valve. Adapted from Gott et al., 2003..... 16
Figure 2-15 Flow dynamics in different valve designs (A) Starr-Edwards caged ball valve, (B) Bjork-Shiley tilting disc valve, and (C) St. Jude Medical bileaflet valve. Adapted from (Vyavahare & Tam, 2018). 17
Figure 2-16 BHVs for surgical use. Adapted from (Marco et al., 2017) 18

Figure 2-17 (A) Number of isolated SAVR, all SAVR, and TAVR surgeries over the last 10 years, arrows indicate points where TAVR overtook SAVR and (B) number of TAVR procedures over the last 10 years, red and number in white indicate failure. Adapted from (Carroll et al., 2020). 19
Figure 2-18 Most recent FDA approved or CE marked BHV from each company 20
Figure 2-19 (A) Prevalence of SVD 15-20 years after implantation by age at implantation (Rahimtoola, 2010), and (b) freedom from SVD up to 25 years by age group (Bourguignon, El Khoury, et al., 2015)..... 21
Figure 2-20 The TRISKELE valve detailing dimensions, components, and deployment. Adapted from Rahmani et al., 2016 26
Figure 2-21 Development of the PolyNova valve, from origin to current PolyV-2 iteration (Kovarovic et al. 2023) 27
Figure 2-22 The Endurance valve (Rotman et al. 2018) 28
Figure 2-23 (A) TAVR system and (B) valve developed by Strait Access Technolgies Bezuidenhout et al., 2017) 28
Figure 2-24 Tria valve developed by Foldax (Jenney et al. 2020) 29
Figure 2-25 (A) Finite element modelling of fibrous reinforcements with plot showing reduction in stress along commissural region, (b) 3D-printed valve construct, (c) leaflet coaptation in a pulse duplicator. Adapted from (Coulter et al. 2019)..... 30
Figure 2-26 Optimisation of PolyNova valve leaflet shape and thickness (Kovarovic et al., 2022) 32
Figure 2-27 Finite element modelling of mesh valve leaflets (A) without and (B) with NiTi fibre reinforcement in the radial direction. T1, T2, T3, and T4 correspond to times of interest across the cycle; legend refers to stress in MPa (Chen et al., 2023)..... 33
Figure 2-28 Fibre orientations in FE model of the PoliValve before and after reorientation algorithm applied to reduce leaflet stress (Serrani et al., 2016). 34
Figure 2-29 A diagram of a typical MEW system (Eichholz & Hoey, 2018) 34
Figure 2-30 (a) SEM images of two different MEW scaffolds, (b) SEM images of cell growth on scaffolds at iii. 1 and vi. 2 weeks, and (c) valve construct from i. side view, ii. Aortic view, and iii. Ventricular view. Adapted from (Saidy et al., 2019)..... 36
Figure 2-31 Images of bioinspired interfacing between MEW meshes with different structures (Vernon et al. 2022). Scale = 1 mm 37
Figure 3-1 Overview of methods used in this study. (A,B) Clearing porcine valve leaflets using 1:2 BABB and SHG imaging, (B) acquisition and analysis. (C) Separation of (i) whole

leaflets into (ii) fibrosa and (iii) ventricularis layers, and further into strips in the radial and circumferential directions. (D) Diagram of radial and circumferential directions on intact leaflet and (E) diagram of uniaxial tensile testing setup. 42
Figure 3-2 Representative histology images of sample slices in the circumferential and radial directions stained with PSR and AB for collagen (red) and GAG (blue) (A, B), and the slices from the same samples stained with Verhoeff's for elastin (black) (C, D). Samples are oriented with the fibrosa layer (*) at the top and ventricularis (†) at the bottom. 44
Figure 3-3 Representative SHG images from each leaflet type (left coronary, LC; right coronary, RC; and non-coronary, NC) at both the commissure and belly regions. Each column shows a single tile view of the collagen microstructure from the fibrosa layer down through the thickness to the ventricularis. Distance between individual tiles: 60-75 μm. Tile size: 425 x 425 μm. More sample images in supplementary..... 45
Figure 3-4 Overview of fibre crimp analysis measured using fibre straightness, with (A) representative SHG images for each location and layer. (B) All straightness measurements organised by layer and location, (C) for the belly region separated by layer and leaflet type, (D) for commissure region separated by layer and leaflet type, (E) for belly regions separated by layer and animal, (F) for commissure region separated by layers and animal. Scale: 100 μm; n refers to number of measurements from N=3 valves. 46
Figure 3-5 Fibre orientation analysis in fibrosa layer. Histograms of fibre orientations in (A) belly and (B) commissure regions, for both plots bin width: 5°. Fibre orientations separated by (C) leaflet region and valve, (D) leaflet region and type. n refers to number of measurements from N=3 valves. 47
Figure 3-6 Uniaxial tensile testing data overview. (A) Thickness measurements for all samples, significance tested using Kruskal-Wallis with Dunn's multiple comparisons test. (B) Average true stress and strain curves for all samples. (C) Initial stress modulus values, significance tested using Kruskal-Wallis with Dunn's multiple comparisons test; 3 outliers removed using ROUT (Q=1%). (D) Final stress modulus values, significance tested using Brown-Forsythe and Welch ANOVA tests with Dunnett's multiple comparisons. (E) Average tension and true strain curves for all samples. (F) Initial tension modulus values, significance tested using ordinary one-way ANOVA with Tukey's multiple comparisons; 2 outliers removed using ROUT (Q=1%). (G) Final tension modulus values, significance tested using ordinary one-way ANOVA with Tukey's multiple comparisons test. Normality tested for in all data using Shapiro-Wilk test; p*≤0.05, P**≤0.01, p***≤0.001, p****≤0.0001. 49

Figure 4-1 Uniaxial dogbone model with discrete fibre inclusions showing (A) fibres embedded in matrix with different material assignments, and (B) model boundary conditions. 58
Figure 4-2 Porcine pericardium leaflet from ACURATE neo2 aortic valve compared to (B) leaflet model including partitions and local fibre orientations, and (C) diagram of fibre orientations across leaflet. Orange and blue regions in (B) correspond to fibre orientations informed from imaging of native leaflets' commissures and belly regions. 59
Figure 4-3 Valve model setup steps before pressure application to simulate sutured leaflet. 60
Figure 4-4 (A) Pressure applied to aortic and ventricular surfaces across a step, and (B) diagram showing resultant aortic pressure alongside an example OA curve detailing the regions taken for average OA and average closed OA calculations. 60
Figure 4-5 diagram comparing image of valve from the top view extracted from Abaqus to the output from custom MATLAB script to determine valve opening area. 61
Figure 4-6 Strain and stress outputs from fibre orientation analysis showing (A) bioinspired orientation, (B) circumferential, (C) radial, (D) isotropic, and (E) matric only with no fibre reinforcement. 64
Figure 4-7 Stress and strain values extracted from models with differing fibre reinforcement structures at three different regions. (A) Average stress for each model in each region, (B) average strain for each model in each region, and volume percent of elements in different strain bands for (C) suture edge, (D) free edge, and (E) belly. 65
Figure 4-8 Opening area analysis for valve models with different fibre reinforcement structures. (A) Opening area for each model throughout the cycles, and (B) maximum and average opening area values for each configuration. 66
Figure 4-9 Results of all models run in DOE analysis, showing (A) stress-strain curves from uniaxial model, (B) opening areas throughout the circle, (C) detailed view of closed opening areas, and detailed view of valve models with (D) stiffest material response and (E) most compliant material response. Arrows indicate response of two valve examples. 67
Figure 4-10 Scatter plots for every factor and response with a statistically significant relationship with an indicative line of best fit. (A) Suture stress, (B) suture strain, (C) belly stress, (D) belly strain, (E) maximum opening area, (F) average opening area, and (G) time to open. 69

Figure 4-11 Heatmaps of all paired factors and responses with statistically significant relationships. (A) Suture edge stress, (B) belly stress, (C) maximum opening area, (D) time to maximum opening, (E) average closed area. 70
Figure 4-12 Stress and strain results of three most desirable (MD) combinations: 2 layers, 0.5 mm fibre spacing, 0.4 mm thickness (MD04); 2 layers, 0.5 mm fibre spacing, 0.3 mm thickness (MD03); and 5 layers, 0.5 mm fibre spacing, 0.2 mm thickness (MD02). Visualisations of stress and strain in leaflets for (A) MD04, (B) MD03, and (C) MD02, as well as results compared to DOE predictions for (D) stress in the suture edge and belly regions, and (E) strain in the suture edge and belly regions for all combinations. 71
Figure 4-13 Opening area results for the three most desirable combinations, showing (A) opening areas versus pressure for a cycle, (B) maximum and average opening area results versus predictions, (C) average closed areas versus predictions, and (D) time to maximum opening versus predictions. 72
Figure 5-1 Visualisation of leaflet suturing, pressurisation, reorientation, and flattening steps for single leaflet model. 80
Figure 5-2 Representation of fibres in reorientation algorithm showing A) visualisation of fibre splay and components, B) fibre orientations in reorientation method 1, and C) fibre orientations in reorientation method 2. 82
Figure 5-3 Deformation of frame to form asymmetric orifice, showing A) initial frame shape and arrow indicating location of displacement boundary condition, and B) the frame shape after displacement. 83
Figure 5-4 Results of reorientated leaflet models, showing (A) stress and strain in the pressurised isotropic leaflet before reorientation, and stress, strain, and fibre orientations in (B) M1 without dispersion, (C) M1 with dispersion, (D) M2 without dispersion, and (E) M2 with dispersion. 84
Figure 5-5 Results of average (A) stress and (B) strain in the isotropic leaflet and all reorientation methods 85
Figure 5-6 Comparison of dynamic valve models' strain, stress, and fibre orientations in the (A) original bioinspired structure, (B) M1 structure, and (C) M2 structure. 86
Figure 5-7 Results from dynamic valve models showing A) average strain in the leaflet, B) volume percent of elements within various strain bands, C) average stress in the leaflet, and D) volume percent of elements within various stress bands. 87
Figure 5-8 Results of asymmetric orifice model, showing the stress and strain in the leaflet A) before and B) after fibre reorientation, and C) the optimised fibre orientations. 88

Figure 6-1 Image of MEW printer highlighting (A) camera to monitor filament extrusion, (B) heated barrel containing polymer-filled syringe, (C) collector plate, (D) stepper motors to enable motion in the X- and Y-directions. 95
Figure 6-2 Flexural bulge loading rig. (A) Top view of rig showing locations of sample holders, orange circles indicate locations of test samples in this study. (B) Image of rig with DIC dual-camera setup highlighted. Example of sprayed PDMS sample (C) loaded and (D) unloaded. (A) and (B) adapted from Whelan et al., 2021. 97
Figure 6-3 Details of bulge model, (A) disc mesh and (B) boundary conditions showing pinned edge and pressure from below. 98
Figure 6-4 Sample embedding details showing representative (A) 10° and (B) 45° embedded samples. (C) Measured angle between fibre bundles with target angle indicated by the dotted line. (D) Measured fibre diameters, normality tested using Shapiro-Wilk normality test and significance tested with unpaired t test. (E) Average thickness for each tested sample with target indicated by dotted line, normality tested using Shapiro-Wilk normality test and significance tested with Brown-Forsythe and Welch ANOVA test with Dunnett's T3 multiple comparisons test. 100
Figure 6-5 Bulge testing results. (A) Displacement of all samples, significance tested using Brown-Forsythe and Welch ANOVA test. (B) Displacement of 45° samples for 100 and 150 mmHg pressure conditions, significance tested with a paired t test. Normality was tested for all data using Shapiro-Wilk normality test; $p^* \leq 0.05$. 101
Figure 6-6 Bulge modelling results of PDMS calibrations. (A) True stress-strain curves of each model compared to test data, and bulge displacements for (B) uniaxial calibration, (C) uniaxial + biaxial calibration, and (D) custom adjusted calibration. 102
Figure 6-7 True stress-strain curves for discrete fibre-embedded dogbone models of varying sizes. 103
Figure 6-8 Bulge results of MEW-embedded samples, showing samples calibrated with full stiffness PCL for (A) 45° and (B) 10° structures, and samples calibrated with reduced stiffness PCL for (C) 45° and (D) 10° structures. 103
Figure 6-9 Comparison of discrete fibre models to uniaxial testing data for PDMS embedded with (A) 45° fibres, 4 layers, and 1.5 mm spacing, and (B) 80° fibres, 10 layers, and 0.5 mm spacing. 104
Figure 6-10 Dynamic full valve models with different material calibrations for PDMS (A) uniaxial, (B) uniaxial + biaxial, (C) custom to bulge, and MEW-embedded with (D) full stiffness and (E) reduced stiffness PCL. 105

Figure 6-11 Moulding and suturing of MEW-embedded polymer leaflets. (A) Open mould showing the base, top, and assembled mould. (B) Embedded silicone cured and removed from mould, and leaflet cut from silicone sheet. (C) Leaflets sutured onto rubber sheet with detailed view of sutures and tears. 110
Figure 6-12 Visualisation of fibre orientations translation from FE to printing. (A) Reoriented fibre families in the FE model. (B) Programmed toolpath for fibre structure and edge reinforcement strip, orange dot indicates start and end point for each section. (C) Final printed leaflet fibre structure. 112

List of tables

Table 2-1 Tensile mechanical properties of aortic leaflets. *Note that modulus of elasticity is calculated differently based on study, see text for detail. **Values estimated from plots based on leaflet thickness of 1 mm, see text for detail. 10

Table 2-2 Flexural stiffness measurements of native aortic valve leaflet 15

Table 2-3 Dip coated polymer valves..... 23

Table 2-4 Injection and compression moulded polymer valves 24

Table 2-5 Film fabricated, 3D-printed, and mesh polymer valves 25

Table 2-6 Bioinspired TEHVs, manufactured to replicate structure of native heart valve leaflets 31

Table 2-7 Tensile mechanical properties of PCL manufactured by MEW 35

Table 4-1 Responses investigated using DOE, with objective for each and target, if applicable 62

Table 4-2 Embedded MEW structure combination runs as indicated by DOE 63

Table 4-3 Results of relationships between all input factors and the resulting response. Red numbers indicate a significant p-value less than 005, yellow numbers indicate a p-value less than 0.01. 68

Table 6-1 PDMS calibrations with their corresponding Ogden model parameters and maximum bulge height..... 102

Table 6-2 GOH model parameters for MEW-embedded materials. 104

Chapter 1 Introduction

1.1 Research motivation

Aortic stenosis (AS) is a prevalent disease, affecting 4% of people over the age of 70, and leads to a 50% chance of mortality within 2 years (Généreux et al. 2023; Otto et al. 1999). It is characterised by the stiffening and thickening of aortic valve leaflets through fibrosis and calcification, preventing the valve from adequately opening or closing (Vyas, Hutcheson, and Aikawa 2018). In recent years, the occurrence of AS has been increasing (Ambrosy et al. 2023). This disease is largely treatable through prosthetic valve implantation, either with a mechanical heart valve (MHV) or a bioprosthetic heart valve (BHV). MHVs are typically used in younger patients due to their durability and requirement of open heart surgery, but due to their non-physiological structure they cause thrombosis, requiring patients with these to adopt life-limiting anticoagulant therapy (Tadros and Shakib 2010). On the other hand, BHVs utilise porcine or bovine pericardium as their leaflet material to mimic the trileaflet structure of native valves. Additionally, a subset of these valves can be used with minimally invasive transcatheter aortic valve replacement (TAVR), enabling valve replacement in patents otherwise not suitable for surgery (Leon et al. 2010). However, BHV leaflets suffer from structural valve degeneration (SHV), which eventually leads to device failure. This can happen in as little as 15 years, and occurs earlier in younger patients (Bourguignon, El Khoury, et al. 2015).

Due to the challenges posed by current commercial devices, there is a push in the field to develop new devices with polymer-based leaflets. The benefit of using polymers is the availability of tuneable material properties and customised geometries that can be implemented in minimally invasive valves and outlast the current commercial devices. With freedom of design and materials, these can be utilised to manufacture a leaflet which mimics the native aortic valve leaflets. Additionally, the implementation of polymer-based valves have the potential to deliver a cheaper, more easily manufacturable device, saving companies and patients money (Bezuidenhout et al. 2017).

Native aortic valve leaflets have a complex trilayer structure to enable effective function and lifelong durability (Gross and Kugel 1931). The mechanical response of these tissue layers is dominated by collagen fibres which have a specialised alignment to bear the load imposed by blood flow. Polymer technology allows for the replication of the complex leaflet structure through the creation of bioinspired fibre structures that can be embedded within an elastomeric matrix.

While much about the structure and function of aortic leaflets is known, there are not yet clear benchmarks of fibre microstructure or mechanical response, of both the whole leaflet and its layers, to enable effective replication in novel devices (Hasan et al. 2014). A key need in the space is known mechanical response of the leaflet and its layers that can be compared to potential novel materials using accessible methods.

Additionally, while there have been steps towards creating bioinspired, fibre-reinforced polymer valve leaflets, there has not yet been a structured and informed approach to the design of these structures or the materials within them. To date, polymer valve development has largely been on an ad-hoc basis, with development focused around a single material, structure, or manufacturing process. This promotes a slow development process and limits the scope of design within the device.

1.2 Objectives

The overall aim of this thesis is to provide the information and methods necessary to design and develop novel, bioinspired, fibre-reinforced polymer leaflets for future transcatheter valve replacements that can outlast the current commercially available devices. Beginning by establishing design benchmarks based on native leaflet tissue, this work will develop a framework to enable effective design and assessment of potential polymer leaflet candidates. It will also explore the translation of these materials from in silico models to benchtop testing, realising the full scope of the polymer leaflet design process. Ultimately, these studies aim to deliver a flexible and adaptable approach to enable future polymer leaflet design. The key objectives are summarised below:

1. Identify mechanical and structural benchmarks based on native aortic valve leaflet tissue for the design and comparison to novel prosthetic leaflet materials.

2. Develop an in-silico framework for the design, assessment, and optimisation of fibre-reinforced polymer leaflets.

3. Use this framework to identify the most effective combination and structure of a pair of materials.

4. Manufacture the previously identified best material candidate and assess the validity of the in silico predictive tool, as well as assess availability of the material to be integrated into current manufacturing procedures.

1.3 Thesis structure

This thesis is comprised of 9 chapters detailing the studies performed in order to achieve the objectives identified in section 1.2. A brief overview of the chapters is as follows:

Chapter 1: Outline of the motivation and key research questions explored and addressed in this work.

Chapter 2: A literature review describing the cardiovascular system and the aortic valve and its leaflets, highlighting what is known and yet to be explored in this area. Next follows a discussion of aortic stenosis and current treatment options, including the drawbacks of current devices. A brief history of polymer valve development is then presented, highlighting recent devices on the path to commercialisation. Finally, melt electrowriting and finite element modelling are discussed as methods to manufacture and design future polymer heart valve devices.

Chapter 3: Characterisation of the native aortic leaflet's mechanical properties and collagen microstructure in order to inform future polymer valve development.

Chapter 4: Creation of a finite-element methodology to model a trileaflet, polymer valve and optimise the structural features of this using design of experiments.

Chapter 5: Outline of the design of a fibre-reinforced polymer leaflet valve by optimising the reinforcement structure using a fibre reorientation algorithm.

Chapter 6: Assessment of the ability of the finite element models to predict the mechanical response of fibre-reinforced polymer materials.

Chapter 7: Demonstration of the feasibility of valve leaflet manufacturing, exploring the customisability of structures based on outputs from the finite element models and lab-based insights.

Chapters 8 and 9: Final discussion of the individual studies in the context of the primary aim of the thesis, highlighting the conclusions gained from this work and areas of potential future development both within this field and in other areas of biomedical engineering.

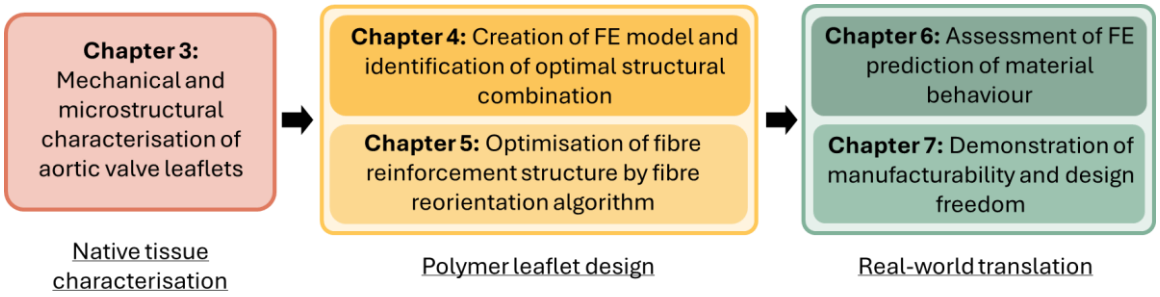

Figure 1-1 *Graphical summary of primary studies detailed throughout this thesis.*

Chapter 2 Literature review

2.1 Native aortic valve

2.1.1 The heart

As the central organ of the cardiovascular system, the heart acts as a pump to ensure constant blood flow through the body and its tissues, delivering nutrients and removing waste (Rogers 2011). Structured like a synchronised two-pump mechanism, it can be identified by its similar left and right sides, each composed of two chambers - an atrium and a ventricle - separated by the septum, see **Figure 2-1**. Deoxygenated blood moves through the right side of the heart, while oxygenated blood is pumped through the left side; the septum ensures that there is no mixing of the blood between these two sides (Rogers 2011; Sevre 2006; Whitaker 2018). Additionally, each chamber contains a valve through which the blood can only flow in one direction, creating a single-direction loop of blood flow throughout the heart.

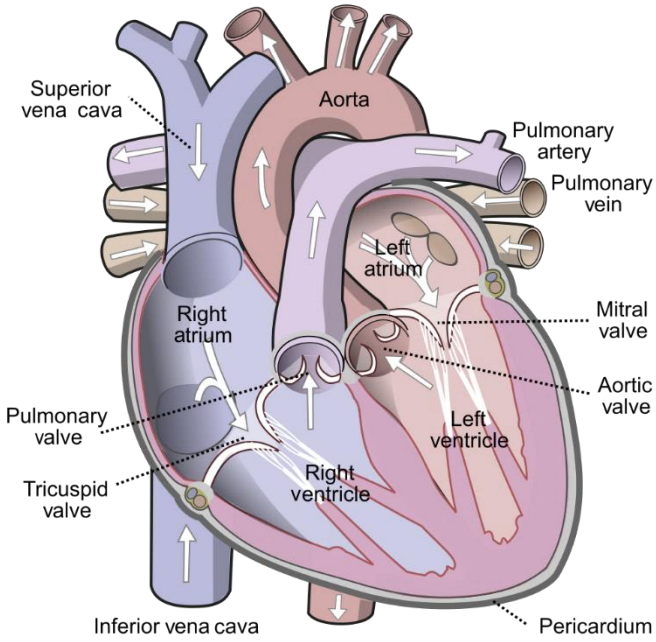

Figure 2-1 *Diagram of the human heart with arrows indicating direction of blood flow.*

Throughout the cardiac cycle the blood follows a defined path, see **Figure 2-1**. Starting from the superior and inferior vena cava, deoxygenated blood flows into the right atrium, through the tricuspid atrioventricular valve, and into the right ventricle. The ventricle then pumps the blood out through the pulmonary semilunar valve into the pulmonary arteries, bringing it to the lungs. There, the blood is removed of its carbon dioxide and replenished with oxygen, a process called oxygenation. After this, the blood travels back to the heart into the left atrium through the pulmonary veins, then down through the mitral atrioventricular valve into the left ventricle.

Finally, it is pumped out of the ventricle through the aortic semilunar valve into the aorta and subsequent arteries to deliver oxygen to the body's tissues (Sevre 2006). This cycle repeats thousands of times a day, about 40 million times a year, and over 3 billion times in an average lifetime (Schoen and Gotlieb 2016).

During this cycle, the heart manages the blood flow through two phases: diastole and systole, see ***Error! Not a valid bookmark self-reference.***. Diastole refers to the "relaxation" of the heart, with blood flowing at low pressure into the ventricles from the atria, passing through the atrioventricular valves. Conversely, during systole, the ventricular walls contract to push the blood at high pressures through the semilunar valves and out of the heart (Rogers 2011). Blood pressure is highest during systole, rising to around 120 mmHg before dropping to around 80 mmHg during diastole.

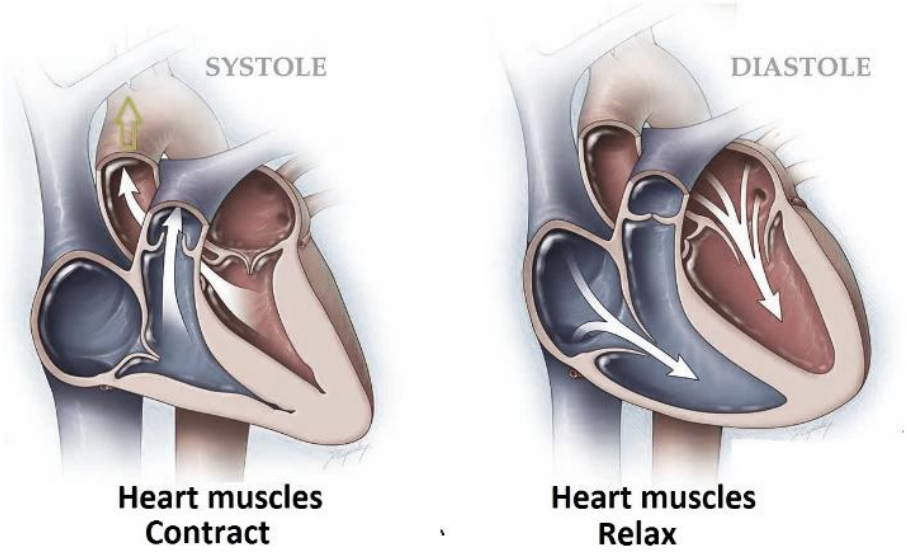

Figure 2-2 *Diagram of heart during diastole and systole phases*

2.1.2 The aortic valve

The aortic valve is characterised by its semilunar-shaped trileaflet structure. This allows unobstructed blood flow from the left ventricle to the aorta during systole, and prevents backflow of blood into the ventricle during diastole, see **Figure 2-3** (Rogers 2011). All the blood flowing into the arteries and tissues of the body exits the heart through this valve, giving it an important function and severe consequences if there is a malfunction. Standard pressure and flow conditions around the valve are shown in **Figure 2-4**.

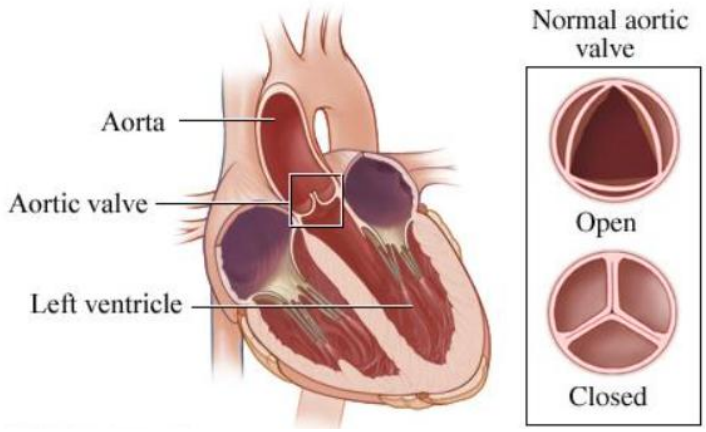

Figure 2-3 *The aortic valve*

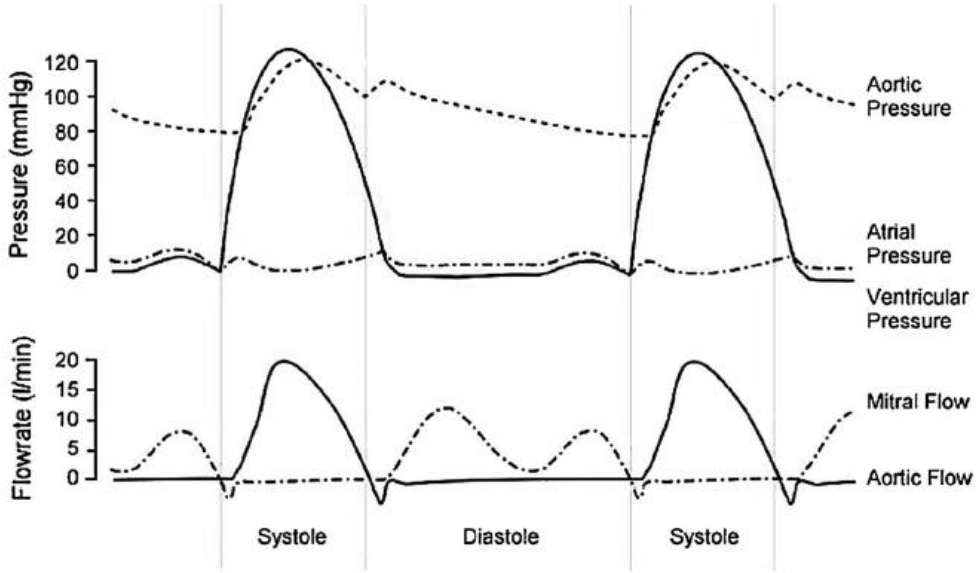

Figure 2-4 *Wigger's Diagram detailing the pressure and flow conditions around the aortic valve (ISO 5840-1).*

Throughout the cardiac cycle, the aortic leaflets undergo complex flexure, tension, and shearing modes of loading (Sacks, David Merryman, and Schmidt 2009). Due to this, the leaflets require a specialised and sturdy geometry to maintain function and last the average 3 billion cycles of opening and closure expected in a single lifetime. To accommodate the bending regimes and extended life required, the leaflets are composed of three distinct layers: the fibrosa, ventricularis, and spongiosa, see **Figure 2-5** (Gross and Kugel 1931).

On the aortic side of the leaflet is the fibrosa, a fibrous layer characterised by its large collagen fibre bundles and highly folded nature, see **Figure 2-6**. This layer serves as the primary load bearing structure of the leaflet, containing a high collagen content which is densely packed into fibres orientated primarily in the circumferential direction (Broom 1978; Missirlis and Armeniades 1977; Vesely and Noseworthy 1992). Opposite to this on the ventricular side is the smooth ventricularis layer. Containing a higher percentage of elastin than the fibrosa, elastin

aligned in the axial direction provides the elastic recoil for the leaflet to close (Vesely and Noseworthy 1992). In between these two layers is the spongiosa, a dense collection of glycosaminoglycans (GAGs) and proteoglycans allowing for slippage and shear between the fibrosa and ventricularis (Vesely and Noseworthy 1992).

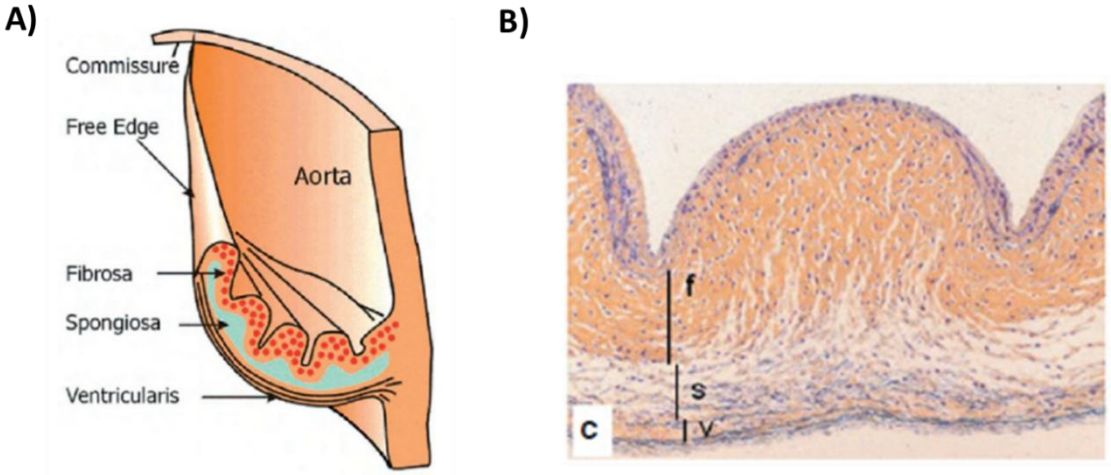

Figure 2-5 *(A) Diagram of the layers of the aortic valve leaflet* (Li et al. 2019) *and (B) an image of a histological slice through the leaflet detailing the three layers, adapted from* (Schoen 2012).

Figure 2-6 *An image of the aortic valve leaflet showing the alignment of collagen fibre bundles in the circumferential direction* (Sauren 1981)

While the heart is in its diastolic phase, the aortic valve leaflets are closed. Here, the collagen fibrils in the fibrosa are stretched and become aligned to close the valves and prevent blood backflow (Sacks et al. 2009; Schoen and Gotlieb 2016). Meanwhile, the elastin within the ventricularis is being stretched. When the ventricles contract during systole and blood pushes the leaflets open again, the elastin fibres contract to their resting state and collagen fibres become more crimped and less aligned, while the fibrosa regains its folds. This change in structure can be seen in, **Error! Reference source not found.**; the intricate structures and i nteractions within the leaflet allow for a durable and long-lasting valve designed specifically for the complex loading it endures.

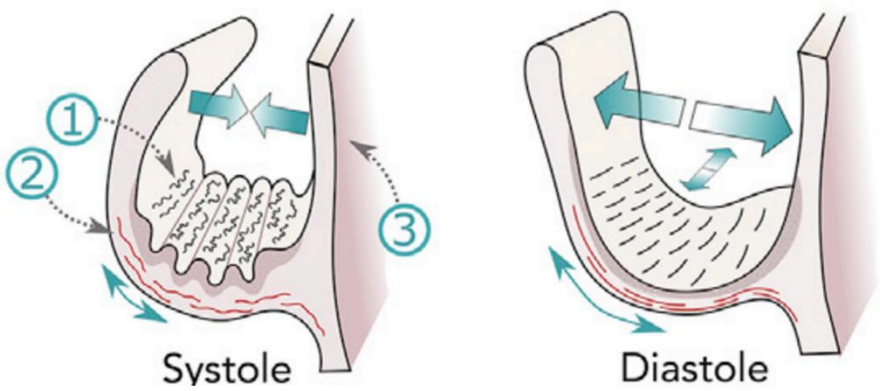

Figure 2-7 *Schematic of fibre crimping and stretching within the aortic valve leaflet in systole and diastole: 1) Collagen fibres, 2) Elastin fibres, 3) Aortic root; adapted from* (Coulter et al. 2019).

2.1.3 Aortic valve leaflet imaging

Histology has commonly been used to visualise the leaflet microstructure, notably by Sauren 1981 who obtained an image of the collagen fibre bundles throughout the fibrosa layers, see **Figure 2-6** (Sauren 1981). More recently, it has been used to visualise the different layers in leaflet tissue (Lee et al. 2015; Manji, Lee, and Cooper 2015; Martin and Sun 2012; Pierlot et al. 2015) or visual changes in microstructure after treatment (Sacks, Smith, and Hiester 1998). However, histology is time consuming, destructive, and only able to provide a discrete profile of tissue structure in one plane.

Small angle light scattering (SALS) is a non-destructive transmissive light based technique that can be used to characterise collagen fibre orientations and dispersion throughout the thickness of a tissue (Gaul, Nolan, and Lally 2017; Sacks et al. 1998; Whelan et al. 2019).

Sacks et al. used SALS to identify dominant fibre orientations and dispersion on glycerol-cleared aortic valve tissue to measure changes in fibre orientation with increasing fixation pressures (Sacks et al. 1998). SALS has since been used on valve leaflet tissue to measure microstructural changes (Joyce et al. 2009; Liao, Joyce, and Sacks 2008; Manji et al. 2015). However, it is only able to identify a singular, average fibre orientation throughout a sample depth which reduces its ability to identify the presence and orientation of more than one family of fibres. Additionally, to obtain information from a singular layer, the leaflet needs to be separated. This separation results in stretching of the fibrosa and contraction of the ventricularis which can give an inaccurate depiction of the fibre orientations in a whole, intact leaflet in vivo (Stella and Sacks 2007).

A detailed analysis of the aortic leaflets' mesostructure used white and polarised light microscopy techniques to characterise the dominant fibre bundles within the leaflet (see **Figure 2-8**) (Mega et al. 2016; Rock, Han, and Doehring 2014). Primary findings from this study detail the fibrous structure across the right, coronary, and non-coronary leaflets and characterise unique modes of fibre branching. Images developed give a good depiction of the collagen fibre bundles within the leaflets, indicating regions of high tensile strength.

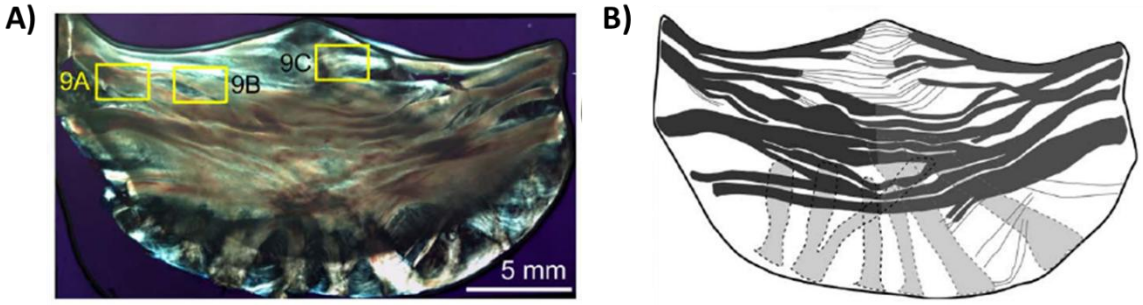

Figure 2-8 *(a) Image taken using polarised light microscopy of porcine aortic valve leaflet and (b) artistic rendering of primary fibrous structure* (Rock et al. 2014)

Second harmonic generation (SHG) microscopy is a non-destructive, two-photon imaging technique commonly used to obtain high resolution images of collagen microstructure throughout various thickness in tissues (Campagnola and Dong 2011; Chen et al. 2012). Hepfer et al. used SHG to visualise collagen structure in pulmonary leaflet tissue organisation after high-temperature treatment (Hepfer et al. 2018). Huston et al. investigated fibre density and alignment in sections of fibrosa and ventricularis layers from aortic leaflets' belly (Hutson et al. 2016). This imaging technique is limited by depth, and is generally unable to penetrate depths greater than 150 μm (Campion et al. 2021; Torun et al. 2023; Whelan, Williams, et al. 2021). To improve this, Schriefl et al. and Sadeghinia et al. used a benzyl alcohol and benzyl benzoate (BABB) solution on arterial tissue and mitral leaflets, respectively, to clear the tissue and achieve images at depths greater than 1 mm (Sadeghinia et al. 2022; Schriefl et al. 2013). BABB is a hydrophobic tissue clearing method that causes dilapidation to minimise light scattering within the tissue without altering collagen structure; consequently, it results in minor tissue shrinkage (Ueda et al. 2020).

2.1.4 Mechanical properties

2.1.4.1 Tensile properties

Over the last few decades, various groups have carried out studies investigating tensile mechanical properties of the aortic valve leaflets, an overview of which can be found in **Table 2-1**.

Table 2-1 *Tensile mechanical properties of aortic leaflets. *Note that modulus of elasticity is calculated differently based on study, see text for detail. **Values estimated from plots based on leaflet thickness of 1 mm, see text for detail.*

	Modulus of Elasticity* (MPa)		Ultimate Tensile Strength (MPa)		Ultimate Tensile Strain (%)	
	Radial	Circumferential	Radial	Circumferential	Radial	Circumferential
(Vesely and Noseworthy 1992)						
Porcine fibrosa (n=14R, 9C)	4.57 ± 2.34 kPa	13.02 ± 5.14 kPa	--	--	27.77 ± 13.53	19.40 ± 4.97
Porcine ventricularis (n=9R, 10C)	3.68 ± 0.55 kPa	7.41 ± 1.69 kPa	--	--	62.66 ± 16.10	21.79 ± 6.58
(Vesely 1997)						
Porcine leaflet (n=8R, 15C)	--	--	1-5 kPa**	>5 kPa**	40-70**	20-45**
Porcine Fibrosa (n=10R, 7C)	--	--	~0.7 kPa**	1.4-3.5 ± kPa**	20-60**	20-40**
Porcine ventricularis (n=10R, 8C)	--	--	0.6-1.5 kPa**	3.5 ± kPa**	50-150**	20-50**
(Mavrilas and Missirlis 1991)						
Human leaflet (n=13)	1.57 ± 0.18	14.55 ± 3.7	--	--	--	--
Porcine leaflet (n=7)	1.28 ± 0.34	7.78 ± 1.7	--	--	--	--
(Stradins et al. 2004)						
Human leaflet (n=11)	1.98 ± 0.15	15.34 ± 3.84	0.32 ± 0.04	1.74 ± 0.29	23.93 ± 3.94	18.35 ± 7.61
(Balguid et al. 2007)						
Human leaflet (n=36?)	2.0 ± 1.5	15.6 ± 6.4	0.42 ± 0.24	2.6 ± 1.2	29.8 ± 13.9	21.9 ± 10.6
(Kalejs et al. 2009)						
Porcine leaflet (n=8?)	5.33 ± 0.61	42.3 ± 4.96	0.55 ± 0.11	1.58 ± 0.26	8.57 ± 0.8	7.26 ± 0.69

Early studies carried out by Vesely (Vesely 1997; Vesely and Noseworthy 1992) evaluated the material properties of the fibrosa and ventricularis individually, see **Figure 2-9**. Looking the radial and circumferential directions, both layers of the leaflets were stiffer in the circumferential direction, with elastic moduli evaluated at around 13 kPa for the fibrosa and 7 kPa for the ventricularis, decreasing to 5 and 4 kPa respectively in the radial direction (Vesely and Noseworthy 1992). However, it is difficult to compare results of this study to following research as mechanical properties are evaluated at a low stress of 300 kPa.

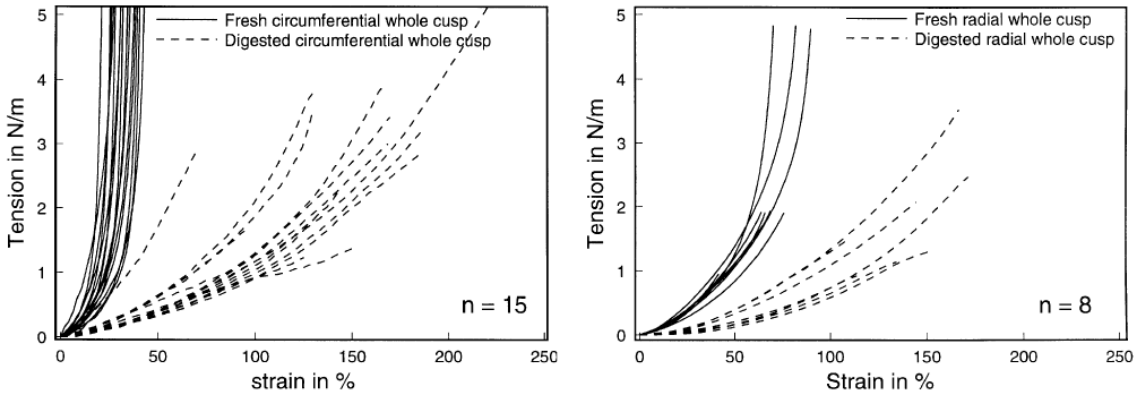

Figure 2-9 *Image of plots from Vesely, 1997 showing the tension vs strain curves for whole aortic leaflet in circumferential and radial directions.*

Following studies repeated similar test methods to obtain elastic modulus, ultimate tensile strength, and ultimate tensile strain of aortic valve leaflets on both human and porcine tissue (Balguid et al. 2007; Kalejs et al. 2009; Mavrilas and Missirlis 1991; Stradins et al. 2004). Mavrilas and Missirlis, 1991 looked at whole human and porcine leaflets, defining a particular strain region for each sample (L_o and L_{max}) to load samples into the post-transition region without inducing failure (Mavrilas and Missirlis 1991). For circumferentially aligned samples, this corresponded to up to 1-1.2 MPa and 11-19% strain, while for the radially aligned samples it was up to 0.15-0.2 MPa and 15-44% strain. For modulus calculation, the region for analysis was defined as 0.05-0.1 MPa for radial samples and 0.4-1 MPa for circumferential.

In a different approach, Stradins et al. and Kalejs et al. calculated the modulus value at 1 MPa; however, Kalejis used 0.1MPa for porcine samples in the radial direction (Kalejs et al. 2009; Stradins et al. 2004). Details on test method are not provided, and it is unclear how many samples were tested by Kalejs et al.; numbers are estimated to be 8 in each group since there is a total of 8 hearts harvested.

Balguid et al. carried out uniaxial tensile testing on human aortic valve leaflets. Again, sample numbers are not provided, but it is likely that 36 samples representing 9 hearts were tested in the circumferential and radial directions. Samples were tested at a strain rate of initial length per minute (l_o/min) until failure, and modulus values were calculated along the “linear part of the curve” (Balguid et al. 2007).

Mavrilas and Missirlis, 1991, Stradins et al. 2004, and Balguid et al. 2007 all have comparable values for modulus of elasticity of the tissue. Balguid et al. 2007 data contain higher error than the other studies, but are comparable to Stradins et al. 2004 values for strength and strain. Kalejis et al. presents tissue that shows a much stiffer response than the previous studies.

Overall, excluding Vesely’s studies due to test method differences, these studies suggest the elastic modulus for the aortic leaflet in the radial direction is between 1.5 and 5 MPa and

around 15 MPa in the circumferential direction. In terms of ultimate tensile strength, the leaflets are weaker in the radial direction, withstanding between 0.3 and 0.4 MPa stress, while they fail at around 2 MPa in the circumferential direction. Finally, the leaflets are more extensible in the radial direction, at about 20-30%, while this number is closer to 20% for the circumferential direction. This is a reasonable conclusion, that the leaflets are more extensible and weaker in the radial direction, as the primary alignment of collagen fibres within the fibrosa is along the circumferential direction of the leaflet.

It is important to remember, however, that these results were obtained at different portions of the stress-strain curves for each data set, and they may not be directly comparable. To add to this, differences in test method will also change results acquired, further supporting that the results should not be directly compared.

Additionally, this data describes the mechanical properties of the whole leaflets rather than of the individual layers. While this is valuable information, more depth is required to characterise the mechanical contribution of the fibrosa and spongiosa in order to develop a more wholistic understanding of the leaflets' uniaxial tensile properties and the structural features driving this.

2.1.4.2 Biaxial properties

The Sacks group has also carried out studies characterising the mechanical properties of native aortic tissue, however, rather than uniaxial tensile properties, they investigated biaxial properties (Billiar and Sacks 2000; Stella and Sacks 2007) (Billiar and Sacks 2000; Stella and Sacks 2007).

Billiar and Sacks, 2000 investigated the biaxial properties of square aortic leaflet specimens 10-16 mm in width to inform development of a computational model (Billiar and Sacks 2000). Since the tissue is anisotropic and will not bear the load uniformly through the thickness, and since it has a variable thickness, they used 2-dimensional membrane stress (T_{ij}, N/m, force over length) rather than 3-dimensional stress to define the load applied to the samples. Stress was applied to samples under a variation of regimes in the circumferential (T_{CC}) and radial (T_{RR}) directions (T_{CC}: T_{RR}): 10:60, 30:60, 45:60, 60:60, 60:45, 60:30, 60:2.5. Samples were prestressed at 0.5 N and preconditioned for 10-20 seconds at 0.05-0.15 N/ms^{-1}. During the loading phase, samples were loaded at a strain rate of 4-15% in the circumferential direction and 1-5% in the radial direction. Key results from this study verified that the tissue is more compliant in the direction perpendicular to the primary fibre alignment, which generally corresponds to the radial direction of the leaflet. The authors suggested that this compliance is due to fibre rotation within the tissue in response to strains, see **Figure 2-10**.

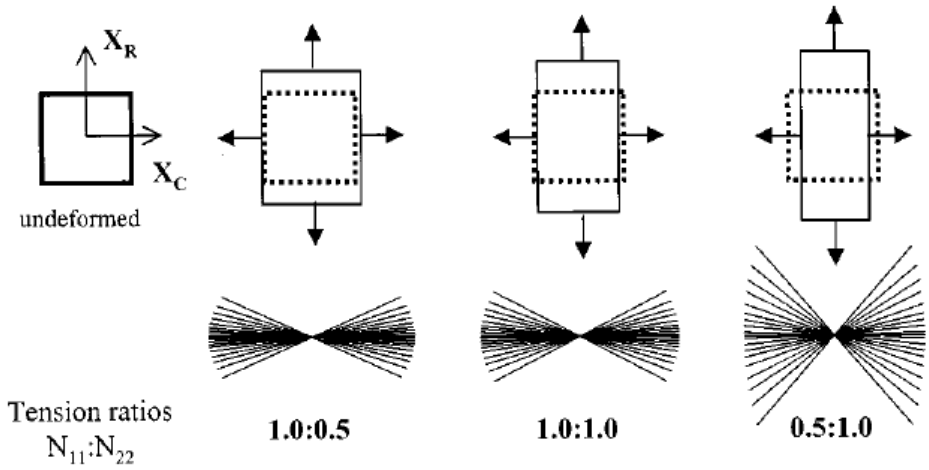

Figure 2-10 *Schematic of rotating collagen fibres under differing loading conditions allowing for high degree of radial strain. Adapted from* (Billiar and Sacks 2000)

A few years later, in 2007, Stella and Sacks carried out a similar study, but this time investigating the fibrosa and ventricularis layers (Stella and Sacks 2007). They cut 9 x 6 mm rectangular samples from whole leaflets, separated them into the fibrosa and ventricularis layers, and measured contraction/elongation of the tissue layers after separation. The authors applied a similar testing protocol as described previously to the leaflets, with near identical tension ratios, except reducing the tension for the ventricularis to 20 N/m from 60 N/m. Primary results showed significant changes in the dimensions of the layers once separated: the fibrosa elongated 28.2% radially and 4.8% circumferentially, while the ventricularis contracted 10.9% radially and 8.2% circumferentially, showing the high amount of residual strain within the whole leaflet. From their biaxial testing, they were able to show that the ventricularis dominates the leaflet's mechanical response in the radial direction at higher stress levels, while the fibrosa predominantly provides the properties at other times, see **Error! Reference s ource not found.**.

2.1.4.3 Flexural properties

In vivo, leaflets are constantly opening and closing through flexure rather than uniaxial or biaxial tension (Sacks et al. 2009). Due to this, evaluating flexural stiffness of the native leaflets may give a good indication of the mechanical properties required under these specific in vivo conditions (Vesely and Boughner 1989).

Vesely and Boughner performed the first study looking into this (Vesely and Boughner 1989), with the aim to characterise the bending mechanics of native leaflets in comparison to treated porcine leaflets used in bioprosthetic valves, focusing on identifying the difference in shearing stresses between the tissues. They developed a unique testing apparatus to bend the tissue, which involved clamping it at both ends, bending it around a mandrel by pulling on a silk string, and calculating the bending moment. Circumferentially orientated tissue specimens were bent fibrosa side up. Through plots, they showed that the bending moment varied based on radius of curvature: the moment increased to a curvature of just past 1 mm^{-1}, after which it declined rapidly, see **Figure 2-12**.

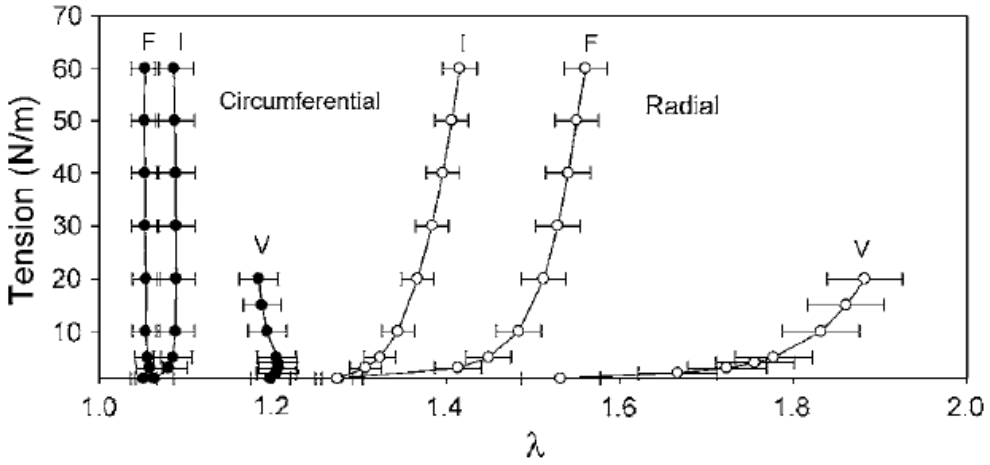

Figure 2-11 *Equibiaxial tension/stretch response of fibrosa (F), ventricularis (V), and intact (I) tissue in both circumferential and radial direction.*

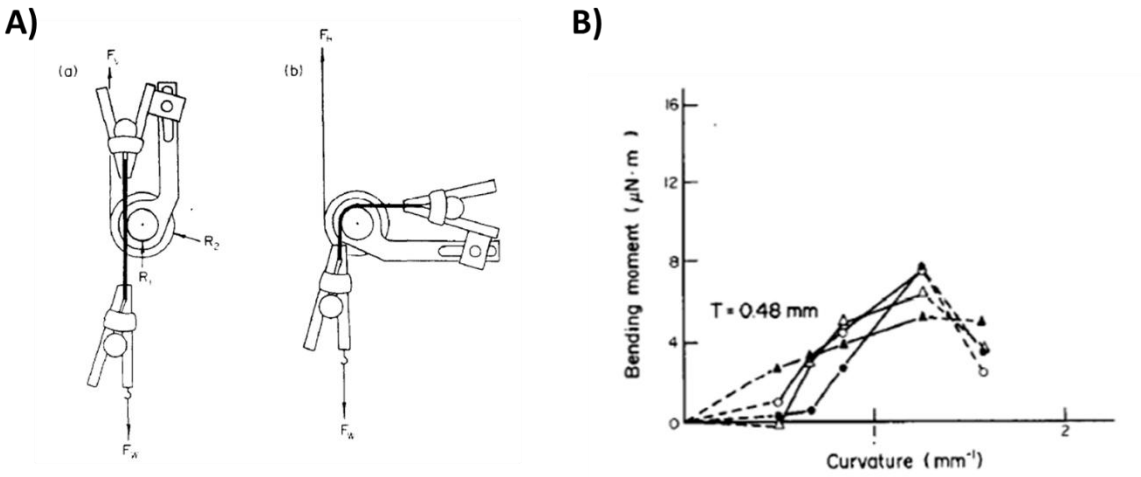

Figure 2-12 *(A) Experimental setup and (B) plot of radius of curvature vs bending moment* (Vesely and Boughner 1989)

Years later, a study from the Sacks group looked at similar mechanical characteristics, presented in **Table 2-2** (Merryman et al. 2006). Merryman et al. used a setup similar to a three-point bend test: samples were bent around a deflecting beam, and the deflection of this beam

was used to calculate the leaflet's bending stiffness. The study assessed the flexural stiffness of circumferentially aligned leaflet samples in two directions: "with curvature" putting the ventricularis in tension, and "against curvature" putting the fibrosa in tension.

Table 2-2 *Flexural stiffness measurements of native aortic valve leaflet*

	Flexural Stiffness (kPa)
(Merryman et al. 2006)	
Porcine Fibrosa (n=9)	703.05 ± 132.58
Porcine Ventricularis (n=9)	491.69 ± 135.17

2.2 Aortic stenosis: disease and treatment

2.2.1 Aortic stenosis

Aortic stenosis (AS) is a disease of the aortic valve that affects as many as 4% of people over the age of 70, and is had become more prevalent over the last 10 years (Ambrosy et al. 2023; Otto 2000; Otto et al. 1999).

Over the development of the disease, it initially presents as leaflet thickening, eventually worsening to a stiffening due to scarring and calcification which can cause severe changes to the leaflet behaviour, see **Figure 2-13** (Vyas et al. 2018). These changes lead to obstruction of the left ventricle outflow and valve regurgitation. Due to this, the mortality rate of aortic stenosis without treatment is 50% at 2 years post-diagnosis, increasing dramatically to 70-80% at 5 years (Généreux et al. 2023; Otto 2000; Virani et al. 2021).

Due to the high prevalence and severity of AS, it is necessary to replace the diseased valve. Current methods achieve this through either surgical aortic valve replacement (SAVR) or transcatheter aortic valve replacement/implantation (TAVR/I). Surgically implanted valves can either be mechanical or bioprosthetic, while transcatheter valves are solely bioprosthetic.

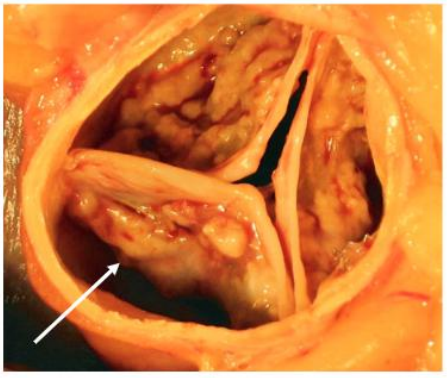

Figure 2-13 *Severe aortic stenosis showing calcium nodules on leaflets* (Schoen and Edwards 2001)

2.2.2 Mechanical heart valves

In 1952 a “caged ball” device designed by Dr. Charles Hufnagel was implanted into a patient’s thoracic aorta and became the first surgical valve implantation (Gott, Alejo, and Cameron 2003; MacIsaac et al. 2019). Later, in 1960, an updated version of this device was implanted in the mitral position, becoming the first mechanical heart valve (MHV), and kickstarting a new gold standard for treatment for stenosed valves which would develop into what is now multi-billion dollar industry (Harken 1986; Starr and Edwards 1961; Wang 2015).

Now known as the Starr-Edwards valve, this device consisted of a rubber ball inside of a metal cage, allowing for blood to exit the left ventricle but not to return, see **Figure 2-14**A. It has since been implanted in hundreds of thousands of patients in both the aortic and mitral positions (Gott et al. 2003). However, due to its non-physiological structure, this valve experienced poor hemodynamic performance by introducing turbulent flow and experiencing paravalvular leakage, see **Figure 2-15**A (Chaikof 2009; Marco et al. 2017).

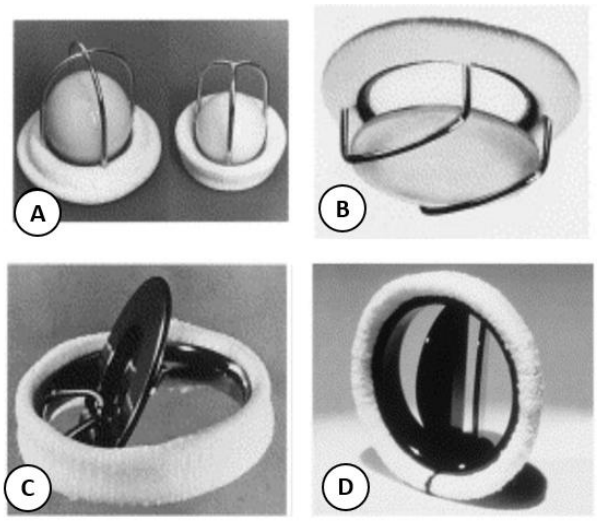

Figure 2-14 *Mechanical heart valves, (A) Starr-Edwards caged ball valve, (B) Kay-Shiley non-tilting disc valve, (C) Bjork-Shiley tilting disc valve, (D) St. Jude Medical bileaflet valve. Adapted from Gott et al., 2003*

The need for a valve with improved hemodynamic performance lead to the Kay-Shiley disc valve and then the Björk-Shiley tilting disc valve, which use a disc rather than a ball to regulate the blood flow, see **Figure 2-14**B, C and **Figure 2-15**B (Lindblom, Bjork, and Semb 1986; Lindblom, Rodriguez, and Bjork 1989). Although an improvement on the previous devices, this valve also proved to be problematic and underwent design adjustments to modify its shape and freedom of movement in order to mitigate problems with leaflet lockage and embolism.

Improving on the disc valve came the St. Jude bileaflet valve, which allows more favourable laminar flow through the three flow areas, see **Figure 2-14**D and **Figure 2-15**C (Nicoloff et al. 1981). Additionally, this valve has an improved profile and sewing ring which made for an easier procedure and greater orifice area (Czer et al. 1990).

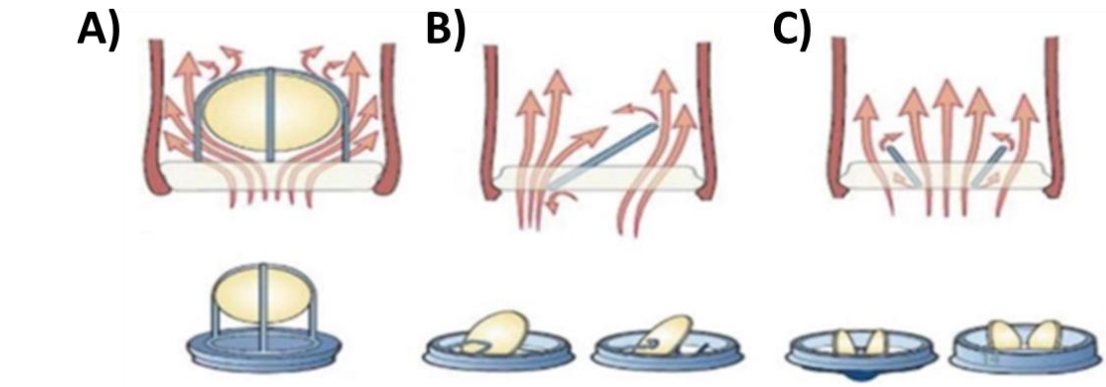

Figure 2-15 *Flow dynamics in different valve designs (A) Starr-Edwards caged ball valve, (B) Bjork-Shiley tilting disc valve, and (C) St. Jude Medical bileaflet valve. Adapted from (Vyavahare & Tam, 2018).*

More than 70 years since the first valve implantation, mechanical heart valves have been improved and optimised, producing more favourable results and decreasing mortality (Czer et al. 1990; Palatianos et al. 2007). However, these valves still carry a significant issue of blood coagulation, requiring patients to take vitamin K antagonist (VKA) drugs to limit risk of clotting. These drugs come with a heavy burden on the patient, from the requirement of regular check-ups and adjustments to tight restrictions on food intake (Palareti et al. 1997; Tadros and Shakib 2010). Additionally, some patients cannot take them as they come with risk of bleeding, allergy, or intolerance and have been found to impact pregnancy (D'Souza et al. 2019; Palareti et al. 1997).

2.2.3 Bioprosthetic heart valves

Around a similar time as advancements were being made in the mechanical heart valve space, developments in bioprosthetic heart valves (BHV) were beginning. In 1962 the first BHV, a cadaveric homograft, was implanted in the aortic position by Donald Ross (Ross 1962). This development led to the use of porcine xenograft tissue for valve replacement, which, with the added use of glutaraldehyde as a tissue fixing solution, created the enormous BHV market we have today. Many companies still have porcine xenograft valves, such as Carpentier Edwards' Porcine Mitral (Edwards Lifesciences, California, USA), Medtronic's Hancock (Medtronic, Minnesota, USA), and St Jude's Epic (St. Jude Medical, Minnesota, USA).

Further development in this area lead to the identification of bovine (and later porcine) pericardium as a suitable bioprosthetic material due to its thickness and flexibility, along with its wide availability (Ionescu 2014). This lead the way for more BHVs: Carpentier Edwards' Perimount Magna Ease and St. Jude's Trifecta.

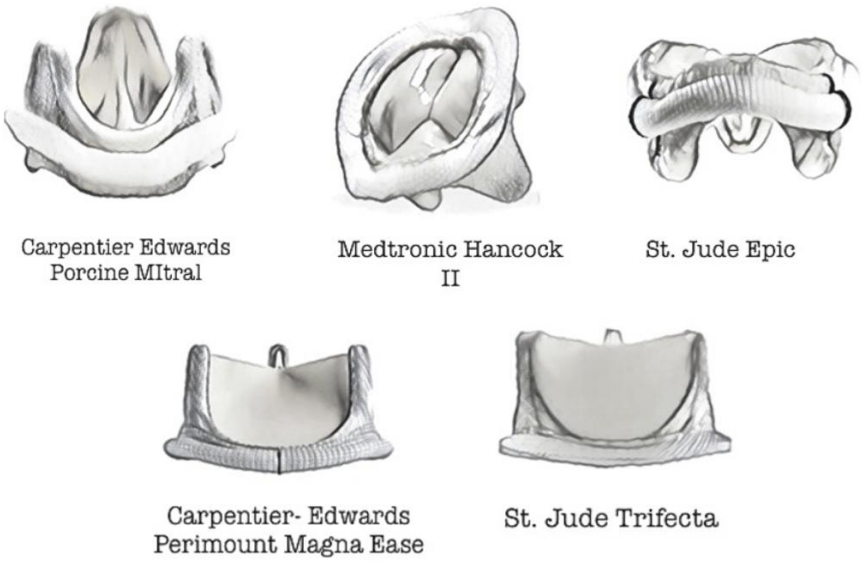

Figure 2-16 *BHVs for surgical use. Adapted from (Marco et al., 2017)*

All of these BHVs use some form of tissue sutured on to polymer ring which can be sutured into the aortic position. Implantation of these valves requires open heart surgery where a surgeon will open the patient's sternum and remove the diseased native leaflets. This procedure is highly invasive and excludes 30% of all patients due to high risk for surgery (Bouma et al. 1999; Leon et al. 2010).

To provide a safer procedure that can be used in those 30% of patients, in 2001, Cribier et al. implanted the first aortic valve through minimally-invasive transcatheter techniques, now called transcatheter aortic valve replacement (TAVR) (Cribier et al. 2002). This valve was made of three bovine pericardium leaflets sutured to a collapsible, balloon-expandable stent. Although the patient died 17 weeks post-procedure, the success of implantation and lack of valve-related complications lead to the next study on five more patients, outlining the success of this new, minimally-invasive procedure (Cribier et al. 2004).

Cribier's work kickstarted the TAVR industry with Medtronic's CoreValve and Edward's Sapien becoming the first devices to gain a CE mark in 2007 and FDA approval in 2014 and 2011 respectively for inoperable high-risk cases (Hale 2020; Lange et al. 2012). Since then, following successful clinical trials, these devices have been approved for use in intermediate and low-risk cases. Now, TAVR has been shown to be a competitor to traditional surgical methods, opening it up into a $5 billion market (Virtanen et al. 2019; Wang 2015).

Over the last decade, particularly with the availability of performing TAVR on intermediate- and low-risk patients, TAVR has been steadily climbing in popularity and has now overtaken SAVR as the most performed valve replacement mode in the US, see **Figure 2-17** (Carroll et al. 2020).

Studies are now reaching advanced endpoints and beginning to release data on long-term survival rates of TAVR and SAVR. A study published in 2024 presents data from the NOTION (Nordic Aortic Valve Intervention) trial, which has all-cause mortality rates for TAVR and SAVR 10 years post-implantation at 62.7% and 64%, respectively (Hørsted Thyregod et al. 2024). Of note, this trial includes an early generation CoreValve from Medtronic, as well as the surgical Trifecta valve (Abbott) which was discontinued in 2023. In contrast, the 10-year OBSERVANT trial, also using early generation devices, noted 63% all-cause mortality with SAVR compared to 81.5% mortality with TAVR (Biancari et al. 2024).

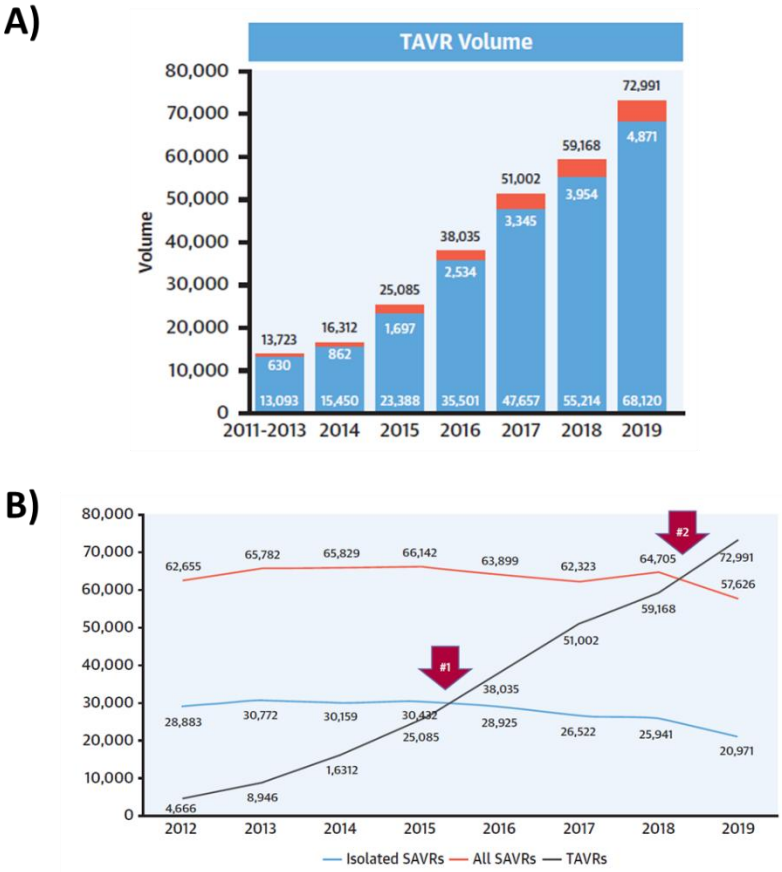

Figure 2-17 *(A) Number of isolated SAVR, all SAVR, and TAVR surgeries over the last 10 years, arrows indicate points where TAVR overtook SAVR and (B) number of TAVR procedures over the last 10 years, red and number in white indicate failure. Adapted from (Carroll et al., 2020).*

Looking newer iterations of devices, a Danish TAVR study had a higher 5-year survival rate for more recent treatments (2017-2021) at 61.5%, compared to groups treated between 2012 and 2016 (56.3%) and 2007 to 2011 (52.9%), showing improvement of devices and procedures as time goes on (Vanhaverbeke et al. 2022).

Since the emergence of TAVR in 2001 and initial approval of devices in 2007, many companies now have FDA approved or CE marked devices. The most recently approved device from each company can be seen in **Figure 2-18**. All of these valves are composed of either bovine or porcine pericardial tissue sutured onto a collapsible metal frame which is either crimped onto a balloon or into a capsule for delivery.

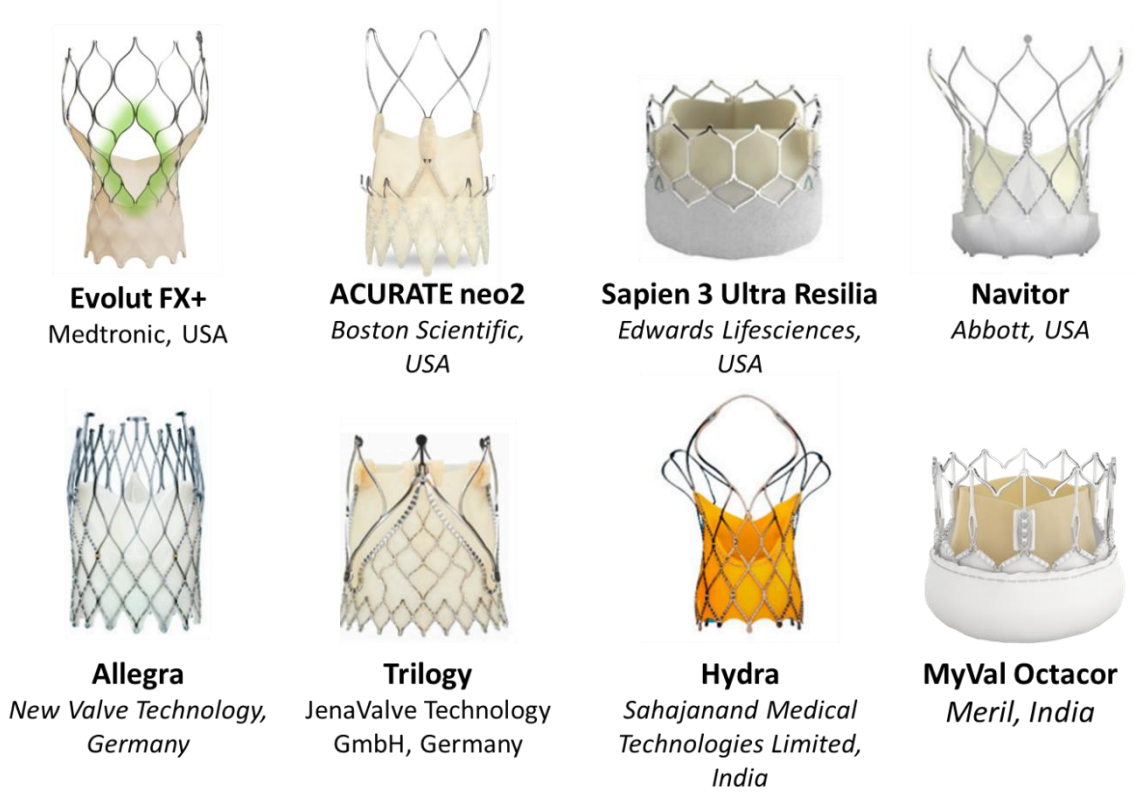

Figure 2-18 *Most recent FDA approved or CE marked BHV from each company*

2.2.4 Structural valve degeneration and bioprosthetic valve failure

Structural valve deterioration or degeneration is a phenomenon that occurs in implanted valves and is characterised by intrinsic permanent changes to the valve, which can include wear and tear, leaflet flail, fibrosis, calcification, and frame strut failure (Généreux et al. 2021). Eventually, these can lead to device dysfunction presenting as stenosis or regurgitation. This degeneration is known to be exacerbated by glutaraldehyde fixation, which increases tissue stiffness, promotes calcification, and impacts the tissue's permanent strain behaviour (Schoen and Levy 2020). Ultimately, BHV leaflets are greatly limited in their longevity, beginning to experience SVD after a few years, leading to failure within 15 to 20 years in 50% of cases (Bourguignon, Bouquiaux-Stablo, et al. 2015; Bourguignon, El Khoury, et al. 2015; Schoen and Levy 2020; Wang et al. 2017).

Due to their need to be crimped on or into a catheter for delivery, valves used with TAVR systems use glutaraldehyde-fixed porcine or bovine pericardium as this tissue is thinner than porcine xenograft leaflets. A key problem with this tissue, and with BHVs in general, is the prevalence of structural valve degeneration (SVD) which greatly reduces their longevity (Bourguignon, El Khoury, et al. 2015; Schoen and Levy 2020; Vyavahare and Tam 2018).

It is also known that SVD is accelerated in younger patients, with an occurrence of 63% at 20 years for patients under the age of 60 (Bourguignon, El Khoury, et al. 2015). As can be seen in **Figure 2-19**, the prevalence of SVD at 15-20 years following surgery dramatically decreases with an increase in age.

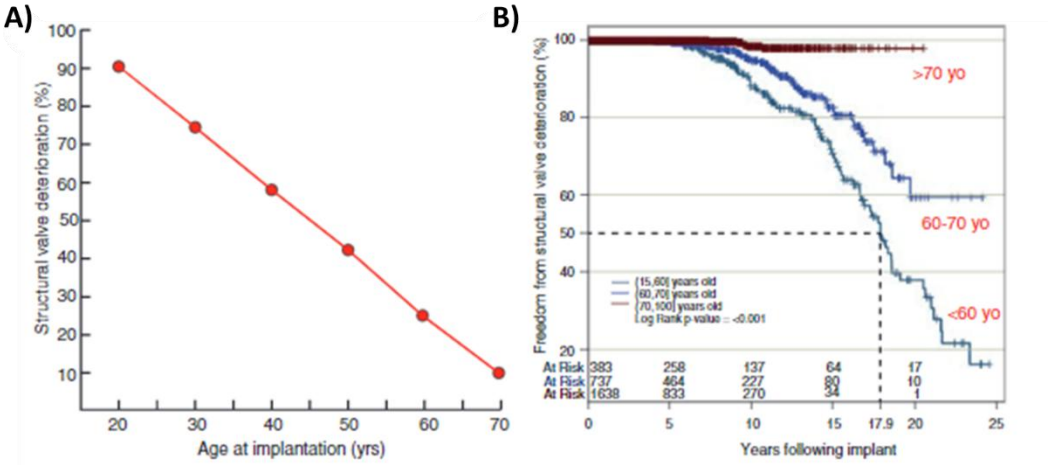

Figure 2-19 *(A) Prevalence of SVD 15-20 years after implantation by age at implantation (Rahimtoola, 2010), and (b) freedom from SVD up to 25 years by age group (Bourguignon, El Khoury, et al., 2015)*

While a device lasting 15 years is sufficient for older patients, this is not ideal for patients under the age of 65 as they will almost certainly require revision surgery in the future.

In an potential to improve outcomes for tissue valves, Edwards Lifesciences have released their newest TAVR valve featuring their dry storage RESILIA tissue. Through the use of free aldehyde capping, the company claims that this material can reduce the incidence of calcification. Recently, 7-year follow up data on patients with this tissue implanted in surgical valves has been released, showing freedom from SVD at 99.3%, and overall freedom from all-cause mortality at 85.4% (Beaver et al. 2024).

Current research has been looking into the microstructural cause of this early failure, and looking to improve the tissue lifetime by introducing methods of pre-screening for collagen alignment (Whelan et al. 2019). It is unlikely, however, that companies will invest the costly resources needed for a lengthy process, and uncertain if this would improve the tissue's lifetime to what is needed.

2.2.5 Polymer heart valves

Since the beginning of prosthetic heart valve development in the mid-20th century, synthetic valves with polymer leaflet material have been in development. Polymers offer the unique quality of possibly being able to combine the advantages of both BHVs (hemodynamic properties, ability to be used with minimally invasive techniques) and MHVs (superior durability). However, there are no polymer valves that are currently commercially available.

With the need for longer lasting transcatheter valves, popularity in this field has increased over the last few decades.

Roe developed the first polymer valve that was implanted in humans: a device made from silicone rubber (Roe, Owsley, and Boudoures 1958). An initial study involving 18 patients contained high rates of mortality, with only four patients surviving at 5 years. None of the deaths resulted from the mechanical performance of the valve, however, and an explanted valve at 5 years showed no apparent signs of damage (Roe 1969).

Many more valve implantations were seen throughout the 70s and 80s, predominantly in sheep and calves. Notable studies include: a segmented polyurethane valve (SPU) which saw survival of up to 960 days in sheep, calves, and goats, although very high calcification levels; polyurethane valves lasting up to 291 days in calves, although again failing from calcification; and a PTFE device implanted in sheep which also suffered from calcification as well as thrombus formation (Boretos and Pierce 1967; Hilbert et al. 1987; Imamura and Kaye 1977; Imamura, Kaye, and Davis 1977; Lo et al. 1988; Nistal et al. 1990; Wiseman et al. 1982).

Details of devices developed over the last seven decades are given in **Table 2-3**, **Table 2-4**, and **Table 2-5**. Organised by mode of manufacture, information on the valve's mechanical properties and performance are given if available. Valves that are currently in commercial development are named with bold lettering.

Table 2-3 *Dip coated polymer valves*

Material	Mechanical Properties	Performance		
		In vitro	*In vivo*	*Properties*
(Ghista 1976; Ghista and Reul 1977)				
Avcothane 51 Polyurethane	*Modulus:* 2.4MPa *Elongation*: 100%	>350m cycles	--	--
(Boretos and Pierce 1967; Hilbert et al. 1987; Wiseman et al. 1982)				
Segmented polyurethane (SPU)	*UTS*: 46 MPa *Elongation*: 750% *Stress at 100% elongation:* 5.9MPa *Shore A Hardness*: 75	--	Survival up to 960 days (calves, sheep, goats); high levels of calcification, few functioning at explant	--
(Li et al. 2019; Lo et al. 1988)				
Cardiomat 610 Mitrathane M2007 Pampul-3 Ameo PUR 1025/1	*UTS:* 28 MPa *Elongation:* 500% *Hardness (Shore A):* 80 *UTS:* 39.2 MPa *Elongation:* 775% *Hardness (Shore A):* 65 *UTS:* 49 MPa *Elongation:* 605% *Hardness (Shore A):* 75 *UTS:* 50.6 MPa *Elongation*: 649% *Hardness (Shore A):* 87	Up to 93m cycles	Survival up to 291 days in vivo (calf); all valves failed due to calcification, thrombosis, and perforation	--
(Jansen et al. 1991; Jansen and Reul 1992)				
Polyurethane	--	400-648m cycles	lasted >150 days in 5/7 calves	--
(Leat and Fisher 1994, 1995; Li et al. 2019)				
Eurothane 2003 (polyurethane)	*Modulus:* 6MPa	160+m cycles	--	--
(Bernacca et al. 1997; Bernacca, Straub, and Wheatley 2002; Mackay et al. 1996; Wheatley et al. 2000)				
Estane (Polyetherurethane)	*Modulus:* 16.2 MPa	544-800m cycles	lasted 6 months in sheep	--
(Daebritz, Fausten, Hermanns, Franke, et al. 2004; Daebritz, Fausten, Hermanns, Schroeder, et al. 2004; Sachweh and Daebritz 2006)				
ADIAMat PCU	--	600m cycles	lasted 6 months in sheep	--
(Attmann et al. 2006; Metzner et al. 2010)				
Polyurethane	--	--	8 of 9 valves lasted 4 weeks in sheep	--
(Kannan et al. 2005, 2007; Rahmani et al. 2012, 2016, 2017)				
POSS-PCU **TRISKELE Valve**	*Modulus:* 15.9-26.2 MPa *UTS*: 31.0-55.9 MPa *Elongation:* 762.7-852.4%	--	Successful implantation in a sheep; better performance than commercial device	*Comparable to SAPIEN XT and CoreValve for all sizes*
(Bezuidenhout et al. 2017; Scherman et al. 2019)				
Heparinized polyurethane **Life Polymer SAT valve**	--	>500 million cycles	Implanted 5 months in sheep	*Gradient:* 8.50±5.38 mmHg

Table 2-4 *Injection and compression moulded polymer valves*

Material	Mechanical Properties	Performance		
		In vitro	*In vivo*	*Properties*
(Roe 1969, 1989; Roe et al. 1958)				
Silastic silicone	*UTS*: 5 MPa *Elongation:* 250% *Hardness (Shore A):* 75	Up to 786m cycles	Implanted in 18 humans, 4 survivors 79-100 months; valves remained physically unchanged after 82 months, 1/4 died at 82	--
(Chetta and Lloyd 1980; Li et al. 2019)				
RTV-615 silicone rubber	--	Up to 280m cycles, experienced significant work hardening	--	--
(Wang et al. 2010)				
SIBS	--	Up to 280m cycles, experienced significant work hardening	Failure in 3/4 sheep due to calcification and material damage	--
(Claiborne, Sheriff, et al. 2013a; Claiborne, Xenos, et al. 2013; Kovarovic et al. 2020, 2023; Piatti et al. 2015; Rotman et al. 2019, 2020)				
xSIBS **PolyNova Valve**	*UTS:* 5 MPa	>900m cycles	--	*EOA:* 1.8±0.04 cm2 *Gradient:* 14.6±0.8 - 10.4±0.9 *Regurgitation:* 6.5±0.8% - 10.1±0.9%
(Brubert et al. 2016; De Gaetano et al. 2015; Serrani et al. 2016; Stasiak et al. 2010, 2014, 2015, 2020)				
SIS30 block copolymer; manufactured to introduce directionality within layers **PoliValve**	--	>1.2 billion cycles	--	EOA and regurgitation remain within ISO standards
(Masheane, Combrinck, and Masheane 2023; Masheane, Preez, and Combrinck 2024)				
Polyurethane	*Density*: 830 kg/m^3	--	--	--

Table 2-5 *Film fabricated, 3D-printed, and mesh polymer valves*

Material	Mechanical Properties	Performance		
		In vitro	*In vivo*	*Properties*
(Imamura and Kaye 1977; Imamura et al. 1977; Nistal et al. 1990)				
PTFE	*Tensile strength:* 414MPa	--	Implantation in 12 juvenile sheep; calcification present on every device, moderate thrombosis	--
(Cacciola, Peters, and Baaijens 2000)				
Rubber, fibre reinforced	*Modulus, leaflet:* 1.5MPa *Modulus, fibres:* 30GPa	--	--	Poor gradient and regurgitation performance
(Koh et al. 2005)				
ePTFE	--	--	Implanted in 47 humans, free from calcification or obstruction at 1.5 years	--
(Bui, Ishrat, et al. 2021; Bui, James, and Dasi 2021; Khair et al. 2025; Prawel et al. 2014; Simon-Walker et al. 2018)				
Hyaluronan-linear low-density polyethylene (HA-LLDPE) **Endurance Valve**	*Modulus*: 76-100MPa *Yield stress*: 8-10MPa *Elongation*: 476-787%	Good toxicity and thrombogenic performance	--	*Gradient:* 6.06-6.73 mmHg *EOA:* 1.77-1.91cm^2 *Regurgitation:* 15.2-16.7%
(Dandeniyage et al. 2017, 2019; Jenney et al. 2020; Kereiakes et al. 2021)				
Siloxane poly(urethane-urea) (SiPUU) **Tria valve**	*Modulus*: 8-20MPa *UTS*: 12-45MPa *Elongation*: 453-688%	Implanted in 15 patients: good EOA and gradient at 1 year (n=12)	Implantation in 8 sheep; good toxicity, biocompatibility, no thrombus at 14 days	--
(Coulter et al. 2019; Zeugin et al. 2024)				
3D-printed silicone	<u>Fibres:</u> *Shore hardness:* 73 A *Modulus:* 4.3MPa <u>Leaflet:</u> *Shore hardness:* 43 A *Modulus:* 1.5MPa	--	--	*EOA:* 1.97-2.11cm^2 *Regurgitation:* 5.0-6.8%
(Chen et al. 2023)				
NiTi-reinforced UHMWPE/PET mesh	*Bending modulus*: 4-40 MPa	--	--	*EOA* > 1.60 cm^2 *Mean diff. pressure:* <15.00 mmHg *Regurgitation: >10%*
(Choi et al. 2024)				
Nylon mesh-reinforces PDMS	--	Successful visual functionality	--	
(Giaretta et al. 2024)				
Dip coated PSU, 3D-printed PCU fibre reinforcement	*Elongation: 250-300%* *UTS: 25-30 MPa*	--	--	*Regurgitation: <20%* *EOA: >2.25cm^2*
(Guo et al. 2025)				
Multilayered UHMWPE fibres embedded in TSPCU film	*Modulus: 60 MPa* *Tensile strength: 50 MPa*	Tested up to 200m cycles, no significant wear observed	--	*EOA: 2.44*±0.13 cm^2 Regurgitation: 5.11 ± 2.18%

With great advancements in material science at the beginning of the new century, polymer valve development has been revived. At the time of writing, there are at least five valve designs working their way towards commercialisation: TRISKELE valve, Polynova valve, Endurance valve, a heparinised polyurethane valve (Strait Access Technologies), and the Tria valve (Foldax).

TRISKELE is a self-expanding, fully retrievable and repositionable TAVR device constructed from polyhedral oligomeric sisequioxanes poly(carbonate-urea) urethane (POSS-PCU), see **Figure 2-20** (Rahmani et al. 2012, 2016, 2017) . This device is manufactured through an automated dip-coating procedure and attached to a Nitinol frame; it also comes in three sizes: 23mm, 26mm, and 29mm diameter. POSS-PCU is a unique polymer as it combines a crystalline segment (POSS) with a softer, elastomeric component (PCU) that allows for its favourable mechanical properties along with calcification resistance, biocompatibility, and anti-thrombogenic surface (Kannan et al. 2005, 2007). Developed with the University College London (UCL) Cardiovascular Engineering Laboratory, this valve underwent an acute preclinical animal trial in an ovine model pre-2016. In this study, the device was shown to safely and reproducibly position and recapture the valve, and was shown to implant successfully (Rahmani et al. 2016). The following year in 2017, an in vitro hydrodynamic assessment was published, and showed comparable performance of all valve sizes versus the SAPIEN XT (Edwards Lifesciences, US) and CoreValve (Medtronic, US) (Rahmani et al. 2017). According to this study, the TRISKELE valve is now under preclinical investigation for durability and function in animal models.

Figure 2-20 *The TRISKELE valve detailing dimensions, components, and deployment. Adapted from Rahmani et al., 2016*

PolyNova TAVR valve is a vacuum compression-moulded device using poly(styrene-block-isobutylene-block-styrene) (xSIBS) with a novel, variable thickness leaflet design, see **Figure 2-21**. The company is currently operating out of the Long Island High Tech Incubator in Stony Brook, New York. Previous studies carried out by this group worked on development of a similar valve using SIBS, however they saw extensive material damage through work hardening and calcification, which lead to the next iteration of this device utilising the crosslinked version of SIBS, xSIBS (Claiborne, Xenos, et al. 2013; Wang et al. 2010). This valve underwent extensive *in vitro* durability testing, passing 900M AWT cycles (and counting) without failure, exhibiting significantly less deposition of calcium and phosphorus than commercial PERIMOUNT Magna Ease (Edwards Lifesciences, US), and showing no material damage after 8 weeks of crimping (Kovarovic et al. 2022; Rotman et al. 2020). Recently, a 2nd generation of this devices was reported, the PolyV-2 (Kovarovic et al. 2022). This updated design includes a sutureless moulding manufacturing procedure, along with an optimised frame that increases radial force while minimising material. Additionally, variable leaflet thickness has been optimised to improve valve hemodynamics and stress.

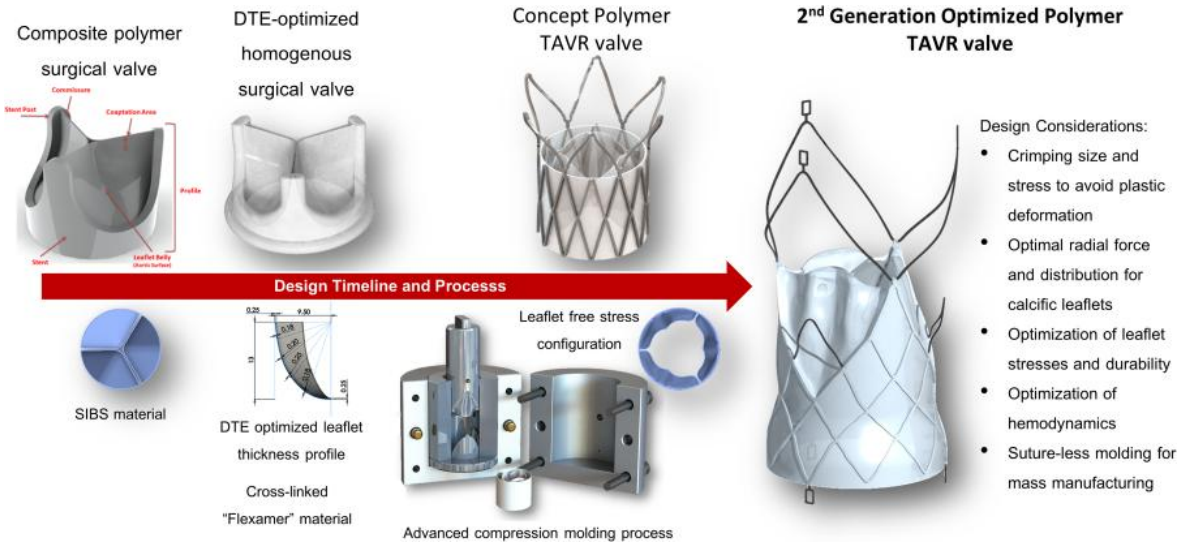

Figure 2-21 *Development of the PolyNova valve, from origin to current PolyV-2 iteration* (Kovarovic et al. 2023)

Operating out of Colorado State University, the Endurance valve is made from thermoformed hyaluronan liner low-density polyethylene (HA-LLDPE), see **Figure 2-22** (Bui, James, et al. 2021; Zwolak et al. 2018). This group has spent a great amount of time in recent years developing and assessing this material for *in vivo* use. Recently, they showed that this material is non-toxic and has reduced thrombogenicity compared to non-HA-reinforced LLDPE (Simon-Walker et al. 2018). In 2021, two abstracts on their valve work were released: one carrying out an FE analysis looking at durability optimisation through altering cusp height, and another assessing *in vitro* performance under pulsatile flow. In the first study, they found that an

increased cusp height and stent ratio decreased the peak stress on the valve leaflets (Bui, Ishrat, et al. 2021). The second study, an *in vitro* assessment of the current design, shows improves gradient and comparable effective orifice area (EOA) and regurgitation fraction to the Sapien 3 (Edwards Lifesciences, US) and the Evolut R (Medtronic, US) (Bui, James, et al. 2021).

Figure 2-22 *The Endurance valve* (Rotman et al. 2018)

Strait access technologies (SAT) is a company based in Cape Town, South Africa dedicated to the development of low-cost medical devices to treat heart valve disease in emerging countries. Their TAVI system is made from dip-coated, heparinised polyurethane mounted on to a balloon-expandable stent; it is non-occlusive, reducing the need for rapid ventricular pacing during surgery, see **Figure 2-23** (Bezuidenhout et al. 2017). In testing, the device has exceeded 500 million cycles, and it has been implanted in sheep for 5 months, returning good results of no structural degradation and a transvalvular gradient of 8.6 ± 5.38 mmHg (Scherman et al. 2019).

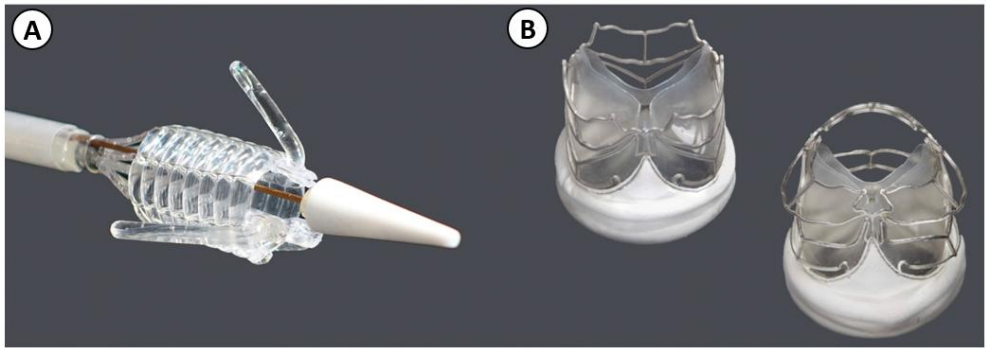

Figure 2-23 *(A) TAVR system and (B) valve developed by Strait Access Technolgies Bezuidenhout et al., 2017)*

Out of all the valves discussed here, the closest to gaining commercial approval is the Tria valve, developed by Foldax see **Figure 2-24**. This surgical valve is made from "LifePolymer": siloxane poly(urethane-urea) (SiPUU) and manufactured by a unique film fabrication technique in an automated robotic facility. After proving biostability and adequate performance, these valves are now undergoing a preclinical study (Jenney et al. 2020). Correspondence of the results from 15 patients at 1 year shows promising results, with an EOA

of 2.0cm^2 and gradient of 9.5 mmHg (Kereiakes et al. 2021) (Kereiakes et al. 2021). Of the 15 patients operated on, one was withdrawn intraoperatively, and two died of causes unrelated to the valve or procedure (60- and 90-days post-operation). Among the surviving patients, one experienced lacunar stroke at 172 days, and another had acute myocardial infarction at 92 days due to thrombus forming on the valve sewing ring. After three months on warfarin, the patient exhibited no thrombus. Preclinical trials with this valve are still ongoing.

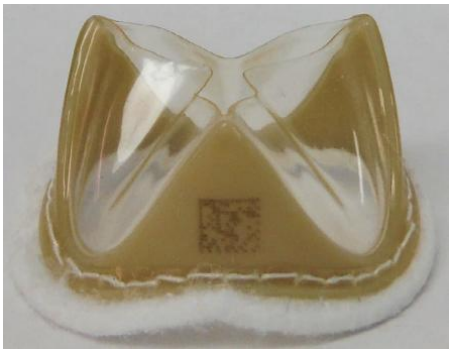

Figure 2-24 *Tria valve developed by Foldax* (Jenney et al. 2020)

Although it is not close to commercial development, a valve developed by Coulter et al. should also be discussed, see **Figure 2-25** (Coulter et al. 2019; Zeugin et al. 2024). This device is a 3D-printed, bioinspired, fibre-reinforced valve made from silicone. It stands out from the previously described devices due to its mode of manufacture (spraying and direct ink writing), and particularly its bioinspired fibre additions informed through finite element modelling. In their design workflow, this group used finite element tools to evaluate stress within the leaflet under four different design specifications: 200µm leaflets, 300µm leaflets, 200µm leaflets with stiff fibre reinforcement in the circumferential directions, and 200µm leaflets with bioinspired stiff fibres at 30° across the leaflet. They were able to show that the addition of stiff, 0.5mm-wide fibres across the belly of the leaflet would take on the majority of stress, particularly in the commissural regions, and allow for a thinner leaflet design. After manufacturing the valves in the non-reinforced, 0° fibres, and 30° fibres configurations, they showed that the valves have an EOA of 2.11-1.97cm^2 and a regurgitation of 5.0-6.8%, depending on the design. These results are all comparable to the commercial devices that were tested: Medtronic Advantage, Edwards Sapien 3, and St. Jude Trifecta. This valve design is unique to previous valves as it looks to optimise the geometry of the device, inspired by the biological structure of native aortic valve leaflets, rather than relying solely on polymer development to achieve optimal performance.

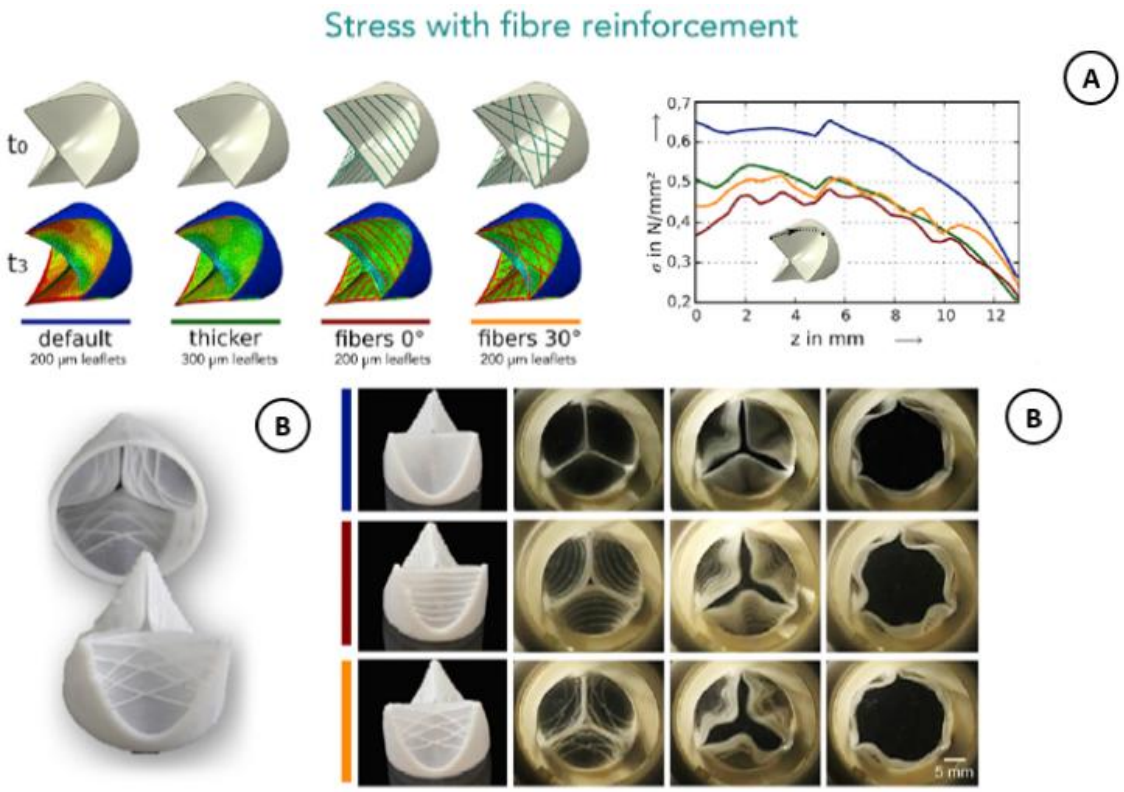

Figure 2-25 *(A) Finite element modelling of fibrous reinforcements with plot showing reduction in stress along commissural region, (b) 3D-printed valve construct, (c) leaflet coaptation in a pulse duplicator. Adapted from* (Coulter et al. 2019)

Another notable area in polymer valve development, although also not close to commercialisation, is the growing field of tissue engineered heart valves (TEHVs). These typically include the manufacture of a sacrificial or resorbable matrix onto which new tissue can grow and remodel to the local environment. Recent development in this space has focused on the creation of bioinspired structures to mimic the native leaflet structure and material response. Notable devices are presented in **Table 2-6**.

Table 2-6 *Bioinspired TEHVs, manufactured to replicate structure of native heart valve leaflets*

Material and manufacturing	About	Images
(Saidy et al. 2019, 2022)		
MEW PCL embedded in fibrin gel	*-Serpentine-like structure to mimic native leaflet anisotropy* *-Gradient:* 2.45 ± 0.36 mmHg *-EOA*: 3.3 cm^2 ± 0.26	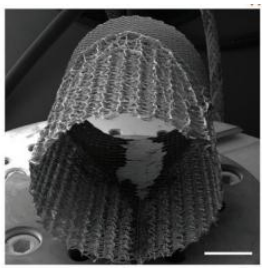 
(Snyder and Jana 2023b, 2023a)		
Trilayer, electrospun PCL/PTMC	*-Trilayer electrospun scaffold* *-Variable tensile response for each layer structure and anisotropic response*	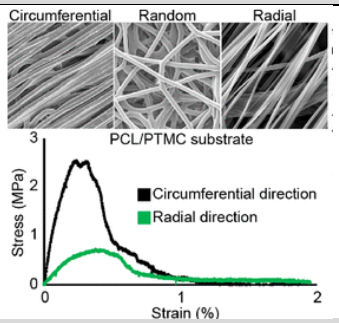
(Boehm et al. 2023)		
Solution electrospun PCL reinforced with PVDF fibres	*-Gradient*: 3.02 ± 0.26 mmHg *-EOA*: 2.12 ± 0.22 cm^2	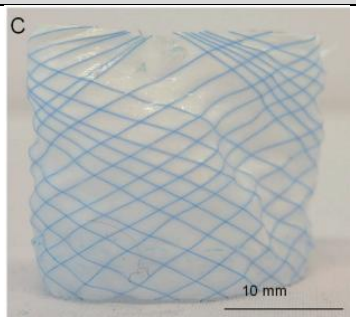
(De Jesus Morales et al. 2024)		
Hydrogel (GelMA/PEGDA) reinforced with PCL sheet	*-Multilayered structure to replicate native leaflets*	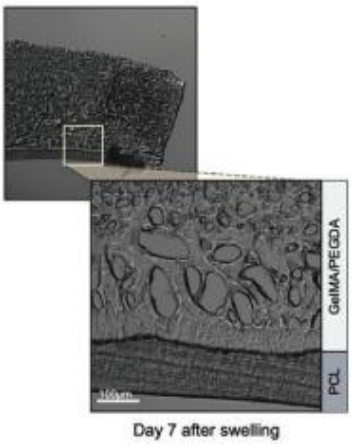

2.3 Finite element modelling in polymer valve development

Finite element (FE) modelling is a useful, versatile tool that is used widely to aid the assessment of leaflets and valves, providing insights into the expected behaviour before performing lengthy and expensive in vitro, and ultimately in vivo, tests.

In polymer valves, it has typically been used to assess and already-existing leaflet or material. In the case of the PolyNova Valve, Claiborne et al. used FE modelling to assess the impact of new materials and a variable thickness design on leaflet stress while under pressure (Claiborne, Sheriff, et al. 2013b). Recently, the group has used similar methods to optimise the leaflet shape and thickness in their newest iteration of the valve, see **Figure 2-26** (Kovarovic et al. 2022).

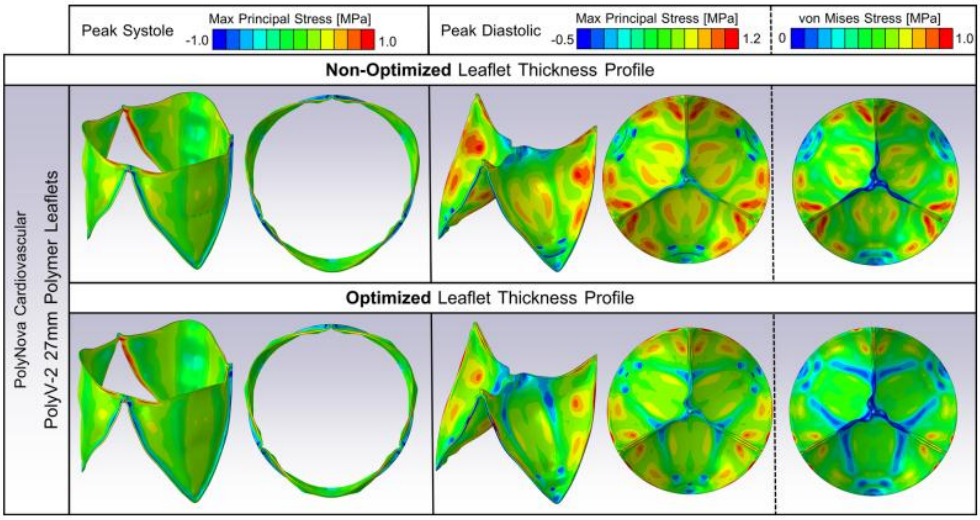

Figure 2-26 *Optimisation of PolyNova valve leaflet shape and thickness (Kovarovic et al., 2022)*

Similarly, Masheane et al. investigated the influence of belly thickness and free edge shape on leaflet stress, strain, and coaptation (Masheane et al. 2024). In this, the authors found that increased thickness of the leaflet belly reduces material stresses, but negatively impacts the valve opening and closing behaviour. Additionally, they found that adding curvature to the edges increases the pressure required to open the valve. With the insights gained from this work, the group will manufacture the best option indicated from these models and perform further testing.

In the development of a 3D-printed bioinspired fibre reinforcement structure, Coulter et al. used FE to assess stress differences in the leaflets with varying thickness and fibre reinforcement structure, see **Figure 2-25** (Coulter et al. 2019).

Chen et al. studied the effect of adding radially-aligned NiTi fibres within the leaflets on the material stress. Through this, the authors were able to show how the addition of NiTi fibres reduce peak leaflet stress in key points throughout the cycle, as well as promote tighter coaptation of the leaflets, see **Figure 2-27**.

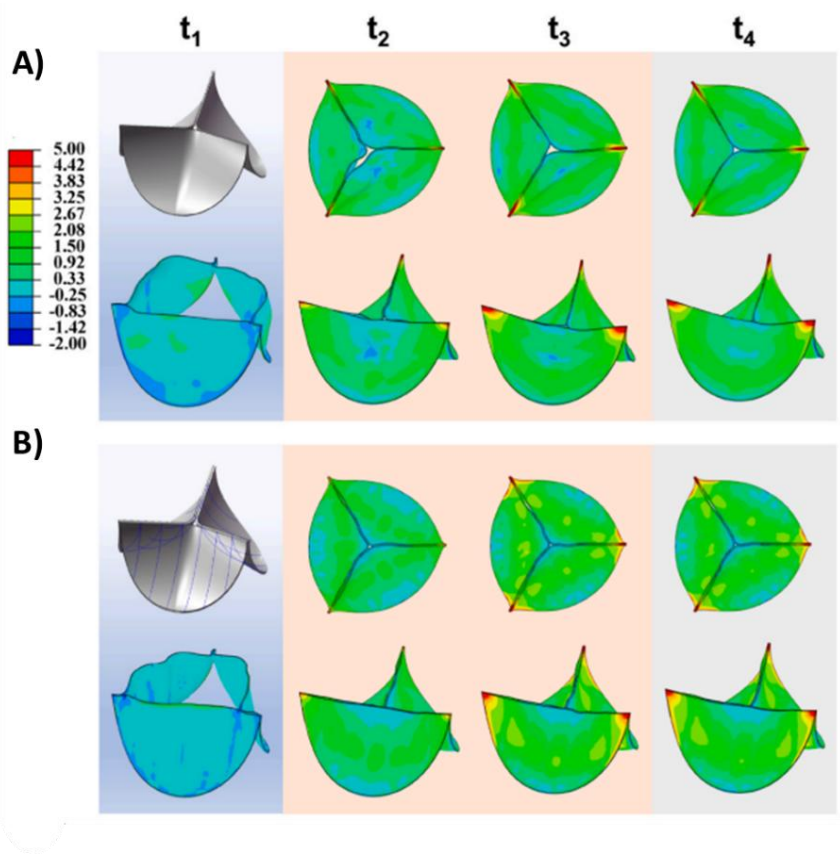

Figure 2-27 *Finite element modelling of mesh valve leaflets (A) without and (B) with NiTi fibre reinforcement in the radial direction. T1, T2, T3, and T4 correspond to times of interest across the cycle; legend refers to stress in MPa (Chen et al., 2023)*

In another study into fibre reinforcement, Khair et al. investigated the impact of fibre reinforcement to overcome tearing at the leaflet commissures (Khair et al. 2025). This work lead to the addition of a circumferential fibre reinforcement strip at the leaflet commissures to reduce stresses and improve valve opening behaviour.

Finally, in a different approach, Serrani et al. designed and implemented a fibre reorientation algorithm to determine an optimal reinforcement structure in the PoliValve (Serrani et al. 2016). The novel polymer in this valve is composed of blocks whose alignment can be controlled during manufacturing in order to support material stress and strain (Stasiak et al. 2014). In this work, the authors applied an algorithm to their FE models to determine optimum fibre alignment within the leaflet, see **Figure 2-28**. This design could then be used to inform future valve development.

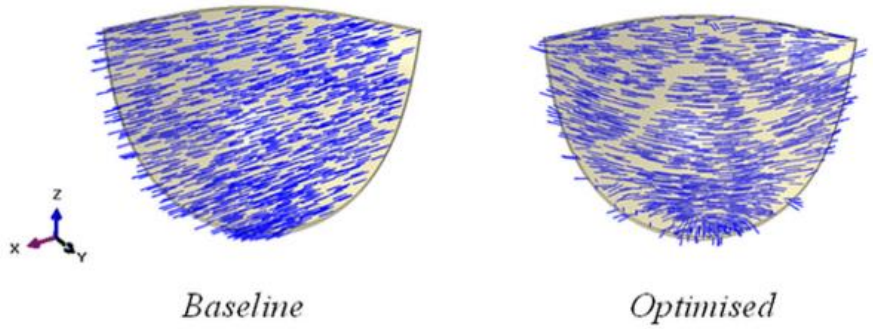

Figure 2-28 *Fibre orientations in FE model of the PoliValve before and after reorientation algorithm applied to reduce leaflet stress (Serrani et al., 2016).*

2.4 Melt electrowriting (MEW)

A recent additive manufacturing approach gaining popularity in the biomedical engineering field is melt electrowriting (MEW). MEW is a form of electrospinning where, with the application of heat, pressure, and voltage, melted polymer is drawn from a syringe onto a grounded collector (Brown, Dalton, and Hutmacher 2016). With developing understanding of the principles that dictate the polymer jet from the syringe, extensive advancement in many applications has been made for this technology (Robinson, Hutmacher, and Dalton 2019).

A typical device used for melt electrowriting includes: a syringe to hold polymer, a heating system to melt the polymer, a pressure control system to apply a pressure on the melted polymer, a voltage application system to apply voltage to the needle of the syringe, a grounded collector on a stage that can move in both the x- and y-directions, and control software to manage the machine, see **Figure 2-29** (Brown et al. 2016; Eichholz and Hoey 2018). With the application of pressure and voltage, melted polymer will be continuously extruded onto the collector, and as the collector moves in a prescribed pattern defined by code written into the control software, the structure will be created.

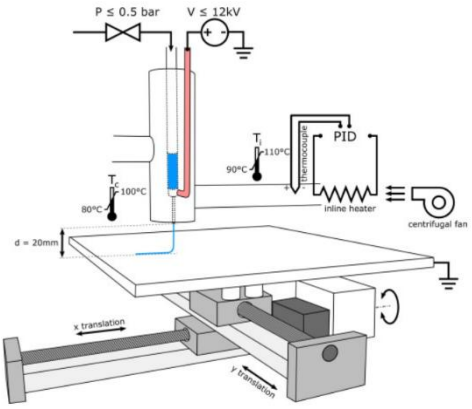

Figure 2-29 *A diagram of a typical MEW system (Eichholz & Hoey, 2018)*

MEW can be used with a wide range of materials, ranging from polypropylene to poly(ether-ether ketone) (PEEK) to poly(lactic acid)-based (PLA) polymers (Davachi et al. 2017; Govinna et al. 2019; Haigh, Dargaville, and Dalton 2017). However, poly(ε-caprolactone) (PCL) is regarded as the "gold standard" material (Hochleitner et al. 2016; Kade and Dalton 2021; Robinson et al. 2019). PCL is generally straightforward to use with MEW, which makes it the most widely used polymer in this space, giving it very well documented printing parameters. Studies have been carried out investigating its mechanical properties, three of which are presented in **Table 2-7**. It can be seen that PCL exhibits a stiff response in the initial portion of the curve, returning very high modulus values, before softening and maintaining a linear profile until breakage at strains over 100%.

Table 2-7 *Tensile mechanical properties of PCL manufactured by MEW*

Method	Modulus	Region for calculation	Extensibility	Stress/Strain plot
(Castilho et al. 2018)				
Micromechanical testing of single filament *Strain rate:* 1mm/min	363±21.2 MPa	1-3% strain	--	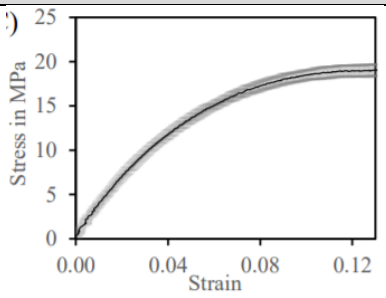
(Croisier et al. 2012)				
Uniaxial tensile testing of 3x0.5cm electrospun samples *Strain rate:* 5mm/min	3.8±0.8 MPa	Elastic deformation region	*Elongation at break:* 170±10%	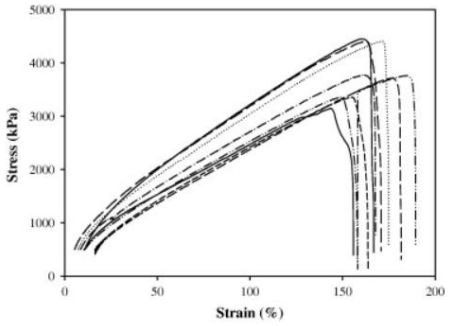
(Baker et al. 2016)				
Tested using AFM *Stretch rate:* 300 nm/s	*Initial:* 28±15 MPa *Final:* 3.9±3.7 MPa	--	*Lower limit for extensibility:* 98±30%	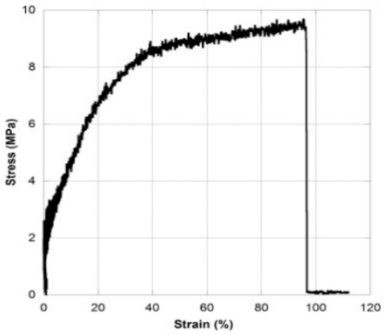

A key application for MEW is the biomedical engineering sector, in particular for manufacturing scaffolds used in tissue engineering applications. An emerging sector of this is related to heart valve repair.

Published in 2019, Saidy et al. used MEW to develop PCL leaflets for a polymer valve that could be seeded with cells and create a tissue-engineered prosthetic heart valve, see **Figure 2-30** (Saidy et al. 2019). This study used a unique serpentine-fibre pattern with different radii and fibre spacing to manufacture structures with comparable mechanical properties to native leaflets. By implementing curved fibres in the scaffold, they could mimic the characteristic j-shaped stress/strain curve exhibited by soft tissues, while also having control on material anisotropy, varying the stiffness in the x- and y-directions. Ultimately, they manufactured a material with very comparable properties to native leaflet tissue. In an expansion to this, on this, the leaflet structure was expanded to include an integrated tubular scaffold, with a seamless transition of fibre structure between the two components (Saidy et al. 2022).

Similarly, in a study published by Vernon et al., the researchers used MEW to create connected scaffolds of different structures with interfacing designed based on the native collagen structure in leaflets, see **Figure 2-31**.

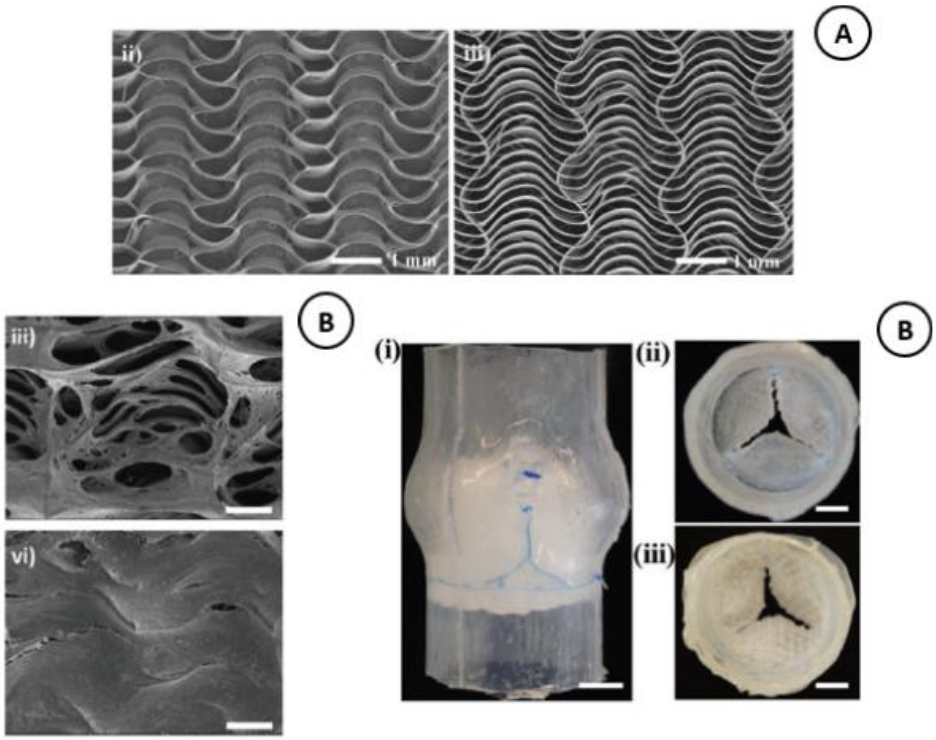

Figure 2-30 *(a) SEM images of two different MEW scaffolds, (b) SEM images of cell growth on scaffolds at iii. 1 and vi. 2 weeks, and (c) valve construct from i. side view, ii. Aortic view, and iii. Ventricular view. Adapted from (Saidy et al., 2019)*

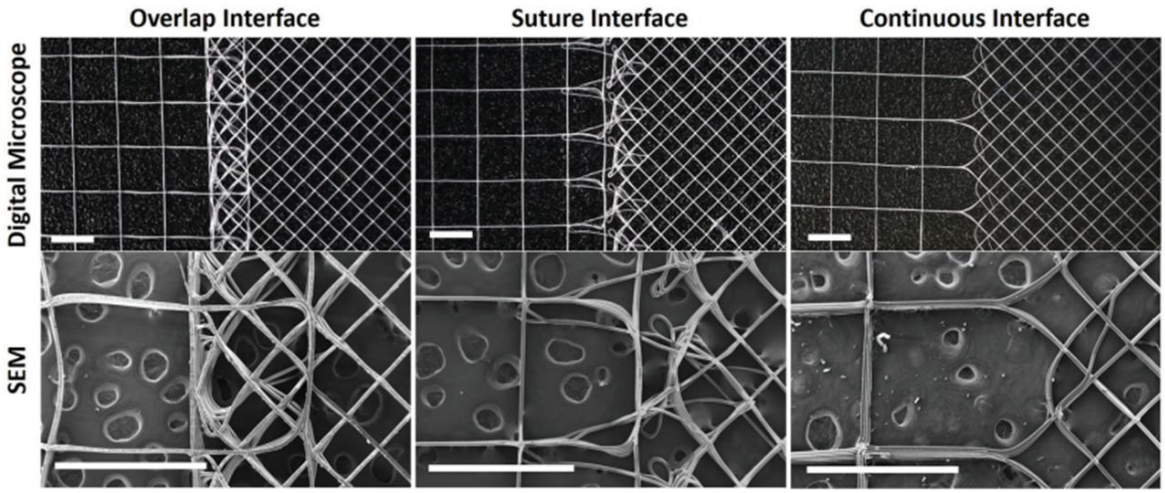

Figure 2-31 *Images of bioinspired interfacing between MEW meshes with different structures (Vernon et al. 2022). Scale = 1 mm*

2.5 Summary

Aortic stenosis is a prevalent disease of the aortic valve that leads to a high chance of mortality if left untreated. Current treatment is achieved through valve replacement, either with mechanical or bioprosthetic valves. Mechanical heart valves are long lasting and effective devices, however they require the need for lifelong, life-limiting anticoagulant therapy. On the other hand, bioprosthetic valves use either porcine or bovine pericardium to replicate the trileaflet structure of native valve leaflets, improving the local hemodynamic environment and reducing the need for anticoagulant therapy. Additionally, some of these valves are available for TAVR, which enables minimally-invasive implantation in patients not available for surgery; this has very quickly become the most popular valve implantation method. A major drawback of these devices, however, is the likelihood of early degeneration, requiring younger patients to require reintervention surgery later on in their lives.

To address the pitfalls of these bioprosthetic devices, polymer heart valves have been proposed as a solution that could emulate the native aortic valve leaflet structure in order to achieve enhanced durability compared to tissue valves. Polymer heart valves have been in development since the 1950s, but with the need for a new treatment option as well as new polymer knowledge, there has been a recent revival in the development of these devices. Notably, there are a handful of valves either in or close to entering clinical trials. However, with a wide variety of potential materials and structures to create, there is a need for a directed approach to enable efficient design and assessment of a variety of potential solutions. At the moment, polymer valve development has largely taken an ad-hoc approach, reducing the scope of design.

Through much of the polymer valve design and development, it has been shown that taking a bioinspired approach to design can improve material outcomes. This is through using materials with a similar mechanical response to native leaflets, as well as the inclusion and integration of a bioinspired fibre-reinforcement structure. Within the literature, however, there is incomplete information on these features of native aortic valve leaflets. In particular, there is a lack of mechanical testing data on the leaflets and their layers to describe the mechanical response of the tissue. While this has been investigated in literature, the mechanical testing approaches have largely been inconsistent, preventing adequate comparison between studies. Additionally, there is a need for a detailed characterisation of the collagen fibre microstructure to enable effective replication with synthetic materials.

Recent advances in manufacturing research have lead to the development of MEW, which is capable of manufacturing controllable, multi-layer structures with fibres at a biologically relevant scale. This has predominately been used for the creation of scaffolds to be used in tissue engineering applications. However, MEW has the potential to offer a useful method of manufacturing a bioinspired, fibre-reinforcement structure for a non-resorbable leaflet. Additional to this, FE modelling has been proven to be an invaluable tool for the assessment of valve design and performance, enabling a more efficient design process, but the crossover between FE and MEW has been limited. This thesis aims to provide a combination of these two methodologies that potentially could enable efficient design and optimisation of customised MEW-based fibre-reinforced leaflets.

Chapter 3 Aortic valve leaflet assessment to inform novel bioinspired materials

3.1 Introduction

As discussed in Chapter 2, the current valve replacement options are limited by their functionality, either requiring lifelong anticoagulant treatment or suffering from premature degeneration (Otto et al. 2021). An improved understanding of the native valve leaflets' structure and mechanical properties could help inform the next generation of implantable devices and treatments. By designing new prosthetic valves to mimic the native hemodynamic environment, these devices can achieve the superior function and durability needed from current commercial devices.

To be able to develop a truly "bioinspired" material for this application it is essential to have a detailed understanding of the native leaflet material and mechanical response, as well as the underlying microstructure determining this response. Currently, there is a lot of interest in developing this kind of biomimicking device, particularly in replicating the complex collagen fibre structure of the native aortic leaflets (Coulter et al. 2019; Saidy et al. 2019; Stasiak et al. 2020). However, across all of these studies it is clear that there is a need for a benchmark, both for the fibrous structure and the mechanical response of the material.

As mentioned earlier, the collagen fibre structure of native leaflets has been visualised using imaging techniques such as histology, SALS, and polarised light, but has not yet provided detailed information required for replicating this structure. SHG, on the other hand, presents a promising solution when paired with a clearing solution such as BABB (Sadeghinia et al. 2022; Schriefl et al. 2013). While aortic valve leaflets have frequently been a topic of study, there is a lack of detailed information on the collagen microstructure. Particularly, there is a gap in discerning the difference in structure between the fibrosa and ventricularis leaflet layers in intact leaflets. To better understand the microstructure, this work aims to draw inspiration from previous studies and use SHG to assist with quantifying fibre orientation and crimp in the commissure and belly regions of BABB-cleared porcine aortic valve leaflets.

Additionally, mechanical testing has been performed on aortic valve leaflets from both humans and animals. While there is a similar range in results through all of these studies, each uses different testing protocols and data processing methods, leading to inconsistent results that cannot be reliably compared or combined. In the screening of new materials, medical device companies and researchers require quick and effective methods, such as uniaxial

tensile testing, to characterise a decoupled mechanical response, and they need a reliable baseline to compare to. However, the current state of the art does not deliver on this need.

To supplement the structural information gained from imaging, the aim of this study is to perform uniaxial tensile testing on strips from whole porcine aortic valve leaflets as well as their fibrosa and ventricularis layers. By combining both imaging and mechanical testing on this tissue, we can develop a detailed profile of the mechanical behaviour of the leaflets and their individual layers and, importantly, understand how the underlying collagen microstructure governs this behaviour to ultimately provide key information for the development of novel, bioinspired materials for future prosthetic valves.

3.2 Methods

3.2.1 Tissue dissection and freezing

Sixteen porcine hearts from 6-month-old Large White Pigs were acquired from a local abattoir (N=10 for mechanical testing, N=3 for histology, and N=3 for SHG), with n=3 aortic valve leaflets available from each heart. Within three hours of slaughter, each leaflet was carefully dissected from the aortic root. After rinsing in phosphate buffered saline (PBS) (P5493, Sigma), each leaflet was cryopreserved in a tissue freezing medium containing Gibco RPMI medium (21875034, BioSciences), sucrose (S0389, Sigma), and dimethylsufoxide (PIER20688, VWR International) to -80°C at a controlled rate of 1°C/mm in a Mr. Frosty container (Nalgene, USA). Using dimethylsufoxide as a cryoprotectant prevents the formation of ice crystals during freezing that could possibly damage the tissue microstructure (Müller-Schweinitzer 2009). Rapid thawing of each sample occurred at room temperature within two months of freezing and each sample was rinsed in PBS immediately after thawing to remove excess solution.

3.2.2 Histology

To conduct histological analysis, porcine leaflets from N=3 animals (n=3 leaflets each) were cut into 2-3 mm sections along either the radial or circumferential direction and fixed in 0.6% glutaraldehyde solution overnight. Samples were stepwise dehydrated (Leica TP1020, semi-enclosed benchtop tissue processor, Germany), embedded in paraffin wax blocks, and sectioned in 8 µm-thick slices using Feather C35 microtome blades. This yielded cross sections in the radial and circumferential direction through the leaflet's thickness. Sections in each direction were stained using Verhoeff's elastin (VF) for elastin and both Picrosirius red (PSR) and Alcian blue (AB) for the combination of collagen and glycosaminoglycans (GAG) (Leica ST5010, Autostainer XL, Germany). Brightfield images were obtained using an Aperio

CS2 microscope with ImageScope software V12.3 (Leica Biosystems Imaging, Inc., Vista, California).

3.2.3 Second harmonic generation (SHG) imaging

3.2.3.1 Clearing protocol

Leaflets from N=3 animals were used for imaging to allow for n=3 left coronary (LC), n=3 right coronary (RC), and n=3 non-coronary (NC) leaflets, resulting in n=9 total leaflets imaged. After defrosting, the leaflets were fixed in 0.6% glutaraldehyde solution overnight; each sample was placed in a histology cassette and held secure between sponge sheets to ensure a flat surface for imaging and minimise shrinkage in the circumferential and radial directions. Tissue samples were chemically cleared according to a protocol described previously (Sadeghinia et al. 2022; Schriefl et al. 2013) using a 1:2 BABB solution. Briefly, samples were dehydrated in a series of graded alcohol solutions (50%, 75%, 95%, 95%, 100%, 100%) for 45 minutes at a time then submerged in a 1:1 solution of alcohol to BABB for 4 hours, before finally submerging in 100% BABB overnight (~18 hours). Samples were imaged within 2 days of clearing.

3.2.3.2 Imaging

SHG imaging was carried out using a Carl Zeiss 710 NLO Microscope (Carl Zeiss, Jena, Germany) and a laser wavelength of 840 nm. Z-stacks and tiled scans (5x5 tiles for belly region, 3x8 tiles for commissures) were taken at a magnification of 20x through the maximum thickness available, with a tile depth between 20 and 25 μm, depending on sample thickness. Each leaflet was imaged at both the belly region and a commissure, see **Figure 3-1**A.

3.2.3.3 Image processing

For image processing, tiles from each scan were selected for analysis. As the leaflets thickness is nonuniform, the number of images containing tissue differed by region. Therefore, for each stack, the topmost image with visible tissue was selected for analysis followed by each subsequent 3rd image until the tissue was no longer visible, see **Figure 3-1**B. This resulted in an analysed image every 60 to 75 μm over regions ranging from 200 to 900 μm in total thickness.

Image processing was carried out with FIJI software (Schindelin et al. 2012) using the NeuronJ plugin (Meijering et al. 2004) to measure fibre crimp as described by Rezahkaniha et al. and Whelan (Rezakhaniha et al. 2012; Whelan 2021). Crimp was measured by degree of fibre straightness (S), defined based on the length of the fibre (L_c) and the straight distance between the endpoints (L_0):

$$S = \frac{L_0}{L_c}$$

where S is bound between 0 and 1, with 1 representing a completely straight fibre. Straightness measurements (n=3) were taken per image, resulting in ~50 measurements per belly or commissure, see **Figure 3-1**B. In addition, measurements of the dominant fibre orientations (n=3) were taken for each image of the fibrosa. In total ~900 measurements of straightness and ~550 measurements of fibre angle were taken for analysis.

3.2.4 Uniaxial tensile testing

3.2.4.1 Tissue preparation

Uniaxial tensile testing was performed on test strips. Strips were prepared in either the circumferential (C) or radial (R) directions from whole leaflets (n=7C/10R), fibrosa layers (n=12C/11R), or ventricularis layers (n=8C/8R), see **Figure 3-1**C. To obtain fibrosa and ventricularis layers, the layers were separated by pinning the leaflet fibrosa side down onto a cardboard mat at 4-6 points, depending on the size of the sample, along the outer edge. Using forceps and a scalpel, the ventricularis was carefully removed from the fibrosa by scoring the spongiosa, starting from the belly edge of the leaflet until reaching the free edge, similar to previously described methods (Stella and Sacks 2007; Vesely and Noseworthy 1992).

Before testing, the samples were separated into 3-4 mm wide rectangular strips in either the circumferential or radial direction using a scalpel, see **Figure 3-1**C. After cutting, the tissue was free to stretch or contract in width, giving a resulting width for each sample between 1 and 3 mm. For each strip, thickness measurements were taken at three locations along the gauge length using a Mitutoyo LITEMATIC VL-50 thickness gauge (Mitutoyo (UK) Ltd., UK). This machine has an accuracy of 0.5 + h/1000 µm, where h is the height of the sample being measured.

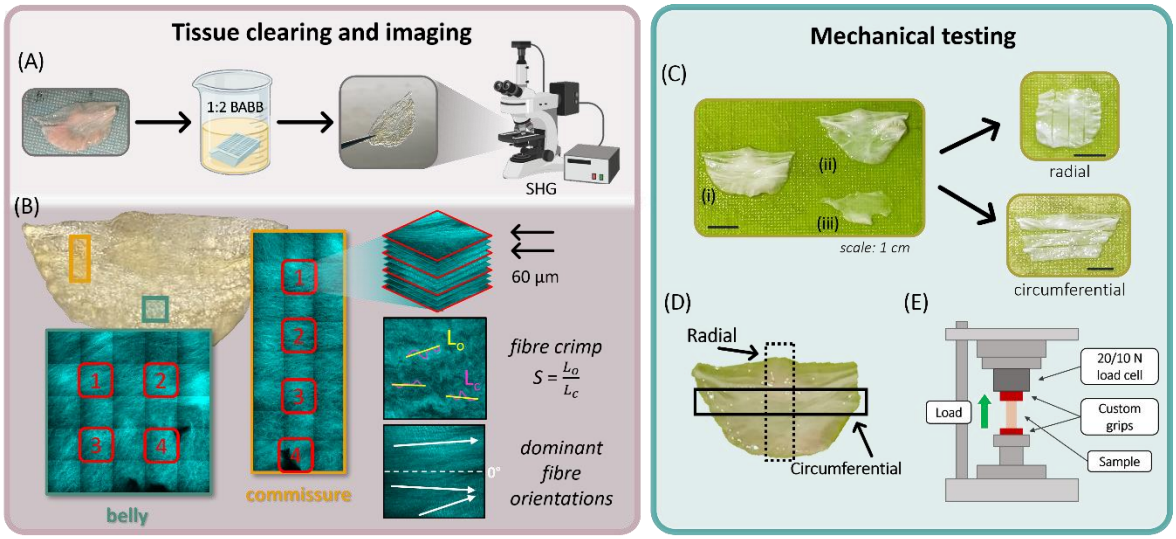

Figure 3-1 *Overview of methods used in this study. (A,B) Clearing porcine valve leaflets using 1:2 BABB and SHG imaging, (B) acquisition and analysis. (C) Separation of (i) whole leaflets into (ii) fibrosa and (iii) ventricularis layers, and further into strips in the radial and circumferential directions. (D) Diagram of radial and circumferential directions on intact leaflet and (E) diagram of uniaxial tensile testing setup.*

3.2.4.2 Mechanical testing

To prepare for testing, samples were loaded into custom-made grips and a holder used for preparation. Samples were held within grips lined with Velcro and secured at the very ends with a drop of superglue, with care taken to ensure glue did not get on the sample gauge length. Once in the grips, the samples were held taught within the holder and the width was measured at three points along the gauge length using an Absolute AOD Digimatic calliper (Mitutoyo (UK) Ltd., UK).

Each sample was uniaxially extended to failure using a Zwick uniaxial testing machine (Zwick Roell Group, Ulm, Germany) with either a 20 N (whole samples, fibrosa circumferential) or a 10 N load cell (ventricularis, fibrosa radial). With a strain rate of 20 mm/min, each sample was preconditioned for 5 cycles from 0.05 to 0.1 MPa and then loaded in tension until failure (defined as a 20% drop from maximum load reached), in line with previous testing performed within the group (Whelan et al. 2019). Sample displacement and load was measured using the Zwick crosshead output and a new reference configuration was recorded after preconditioning. Every sample was hydrated with PBS and tested at room temperature.

3.2.4.3 Mechanical characterisation

Each sample was characterised by its initial and final modulus, calculated from the slope of both the true stress and tension curves. True stress was defined as:

$$\sigma_t = \sigma_{eng}(1 + \varepsilon_{eng})$$

Where σ_{eng} is engineering stress and ε_{eng} is engineering strain, defined as:

$$\varepsilon_{eng} = \frac{\Delta l}{l_0}$$

Where Δl is crosshead displacement and l_0 is initial sample gauge length. True strain was defined as:

$$\varepsilon_t = ln(1 + \varepsilon_{eng})$$

Tension was defined as:

$$Tension = \frac{force}{sample\ width}$$

Modulus values were calculated using the slope formula:

$$m = \frac{y_2 - y_1}{x_2 - x_1}$$

With initial moduli taken as the slope for the initial part of the curve, which was defined as the region before a 5% increase from the starting slope as this was the point when the samples

typically began to stiffen. Final moduli were taken as the slope between failure and 80% of the failure load to obtain a robust determination of the slope at the end of the curve.

3.2.4.4 Data processing

All processing from raw, Zwick-output data was carried out using a custom MATLAB script to return true stress/strain, tension/strain, and slope values.

3.2.5 Statistics

All statistical analysis was performed using GraphPad Prism 9 (GraphPad Software, Inc., San Diego, California). Specific statistical tests for each dataset and sample sizes are specified in the results section. All numerical and graphical values are shown as mean ± standard deviation, and a $p \leq 0.05$ was considered significant.

3.3 Results

3.3.1 Histology

Histological images of leaflet samples sliced along either the circumferential or radial direction were obtained, see **Figure 3-2**. Combining PSR and AB allows the three layers of the leaflets to be distinguished, i.e. the fibrosa is on the top densely packed with collagen, the ventricularis on the bottom, with the spongiosa, rich in GAGs (blue), separating them. The coherent orientation of collagen fibres in the circumferential direction can be seen in the fibrosa, while there is no clear preference of collagen fibre orientation in the ventricularis layer, see **Figure 3-2**A, B. Looking at the VF-stained samples, the elastin in the leaflets is primarily located in the ventricularis, in what look like sheets somewhat more preferentially aligned along the radial direction of the leaflet, see **Figure 3-2**C,D.

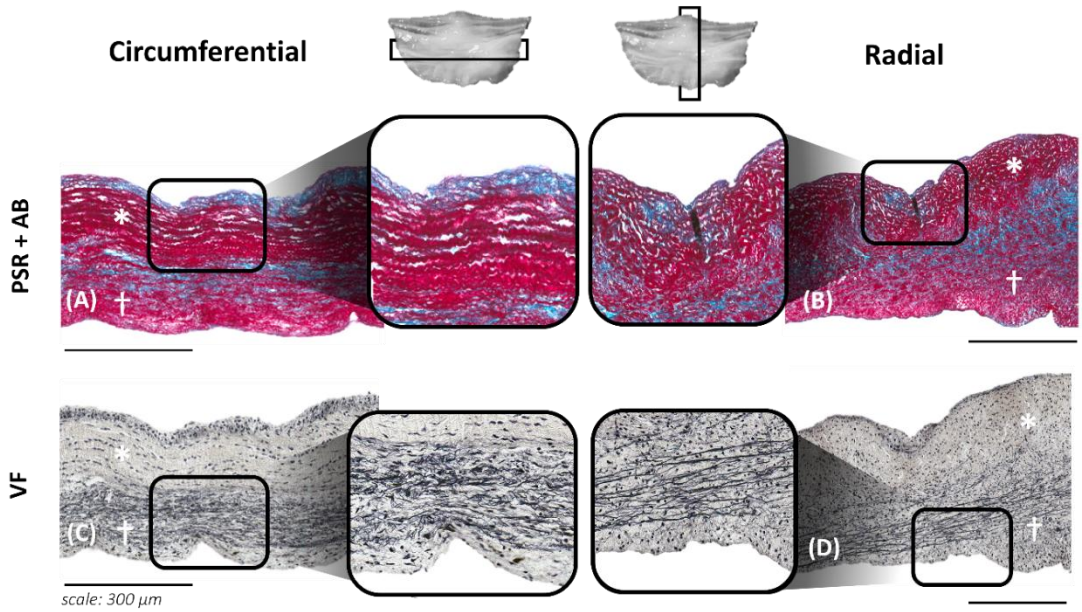

Figure 3-2 *Representative histology images of sample slices in the circumferential and radial directions stained with PSR and AB for collagen (red) and GAG (blue) (A, B), and the slices from the same samples stained with Verhoeff's for elastin (black) (C, D). Samples are oriented with the fibrosa layer (*) at the top and ventricularis (†) at the bottom.*

3.3.2 SHG imaging

3.3.2.1 Qualitative analysis

Figure 3-3 shows the images of the collagen fibre structure throughout the leaflet thickness at the belly and commissure regions across the three leaflet types; the number of image tiles differed based on the total sample thickness. In all leaflets, the collagen microstructure in the fibrosa appears dense and organised around one or two primary directions. Moving through the leaflet thickness this structure becomes sparser and more dispersed in the ventricularis, with random alignment of collagen fibres.

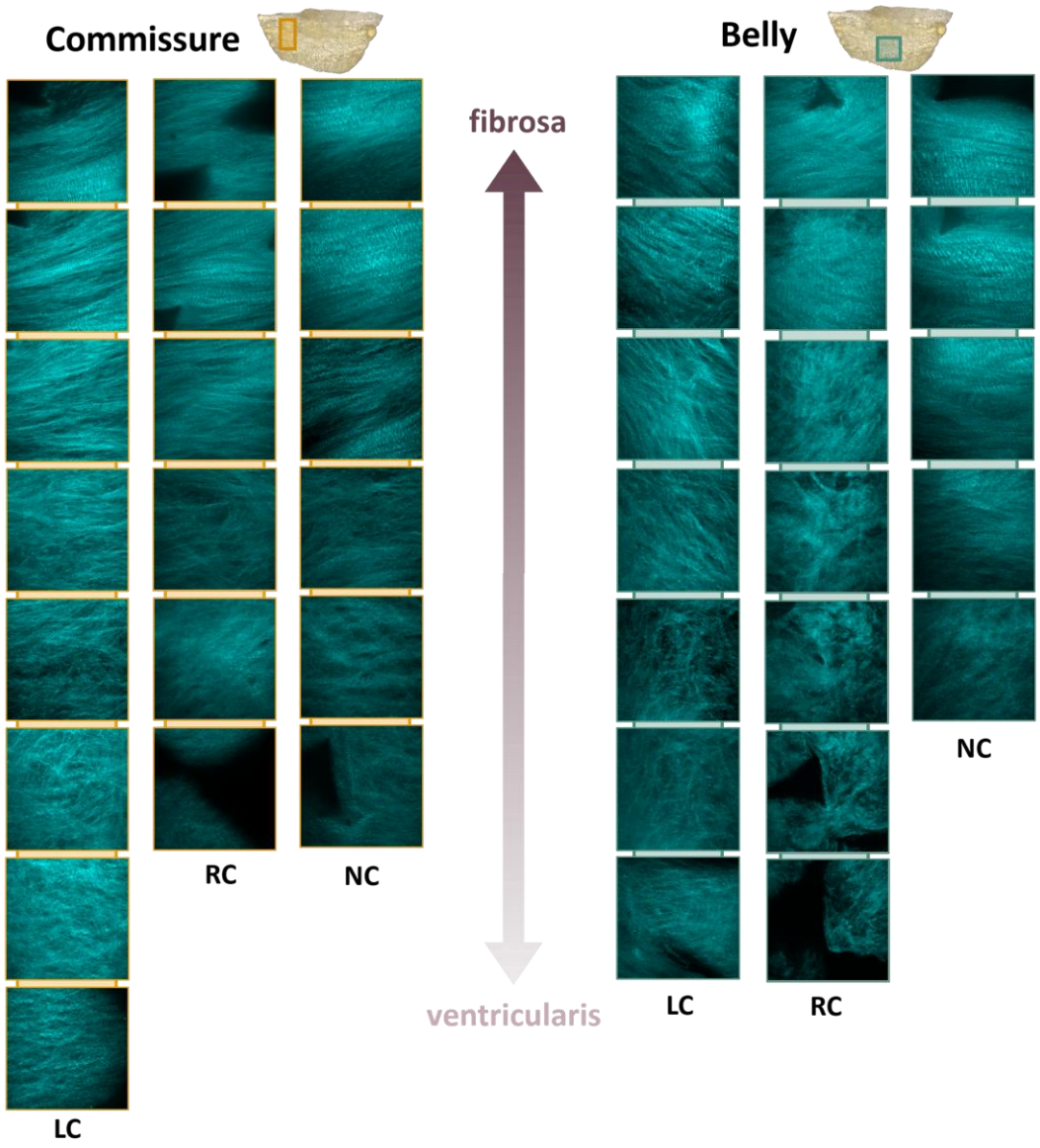

Figure 3-3 *Representative SHG images from each leaflet type (left coronary, LC; right coronary, RC; and non-coronary, NC) at both the commissure and belly regions. Each column shows a single tile view of the collagen microstructure from the fibrosa layer down through the thickness to the ventricularis. Distance between individual tiles: 60-75 μm. Tile size: 425 x 425 μm. More sample images in supplementary.*

3.3.2.2 Fibre straightness

Across all the leaflets studied, collagen fibres are more crimped in the fibrosa than the ventricularis, see **Figure 3-4**B. Overall, for all of the leaflets together, the level of fibre straightness remains consistent within each layer across the regions studied (fibrosa belly/commissure: 0.68 ± 0.12 /0.68 ± 0.13; ventricularis belly/ commissure: 0.79 ± 0.10/ 0.78± 0.10).

When grouping the results based on animal (PAV 1, 2, and 3) or leaflet type (LC, RC, NC), there is no trend to suggest that fibres are more or less straight based on either of these factors, and the fibrosa remains more crimped than the ventricularis, see **Figure 3-4**C-F. For detailed straightness measurements, see supplementary material.

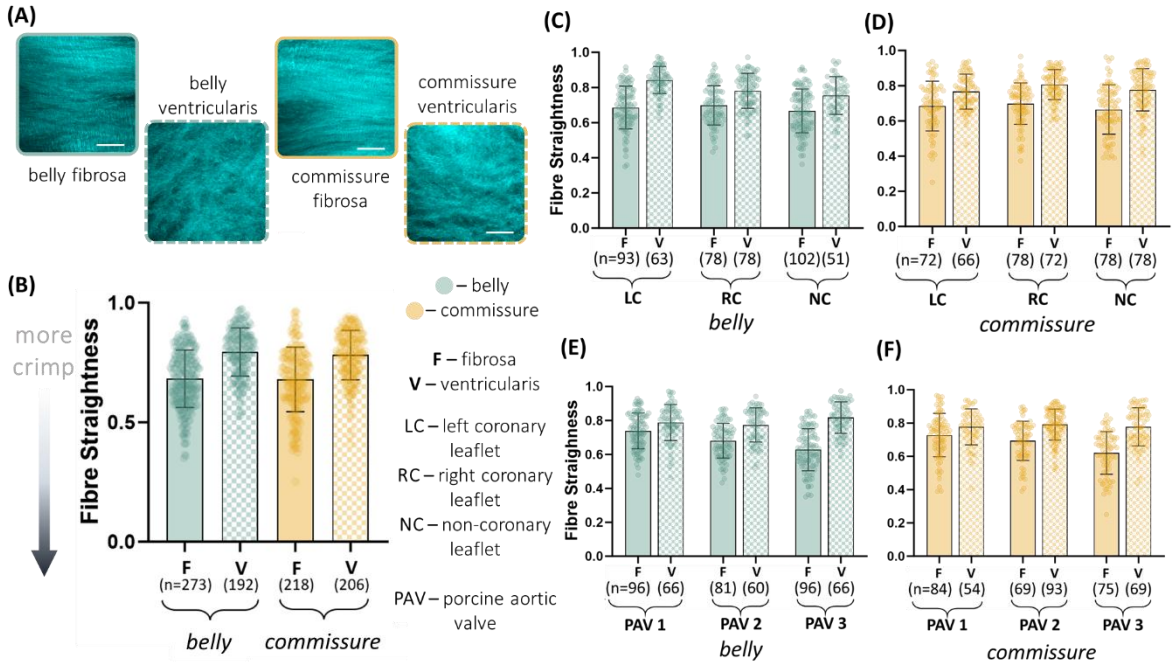

Figure 3-4 *Overview of fibre crimp analysis measured using fibre straightness, with (A) representative SHG images for each location and layer. (B) All straightness measurements organised by layer and location, (C) for the belly region separated by layer and leaflet type, (D) for commissure region separated by layer and leaflet type, (E) for belly regions separated by layer and animal, (F) for commissure region separated by layers and animal. Scale: 100 µm; n refers to number of measurements from N=3 valves.*

These results are presented to appreciate the overall distribution of fibre crimp across all leaflets and animals. While the number of observations are high (n=54-273), this represents a small population of animals (N=3). To avoid pseudoreplication inflating statistical significance, the results presented here do not include statistical analysis (Lazic 2010). For this analysis, see Appendix A1

3.3.2.3 Fibre orientation

Dominant collagen fibre orientations were measured in the fibrosa layer of the leaflets, shown in **Figure 3-5**A-D. The ventricularis was not considered in the orientation analysis due to the

high degree of disorganisation of the fibres in this layer resulting in no clear dominant alignment. There is a larger spread of angles in the belly portion of the leaflet compared to the commissure region, with the suggestion of a bimodal distribution at the belly region, see **Figure 3-5**A, B. For the belly, the angles are centred around -10 and +15 degrees while in the commissure the angles are normally distributed around -11 degrees.

Looking at differences in fibre orientation between valves and leaflet type in both the belly (B) and commissure (C) regions, the mean fibre orientations differ more between leaflet types than between animals, suggesting that fibre orientation is dependent upon leaflet type rather than animal, see **Figure 3-5**C,D.

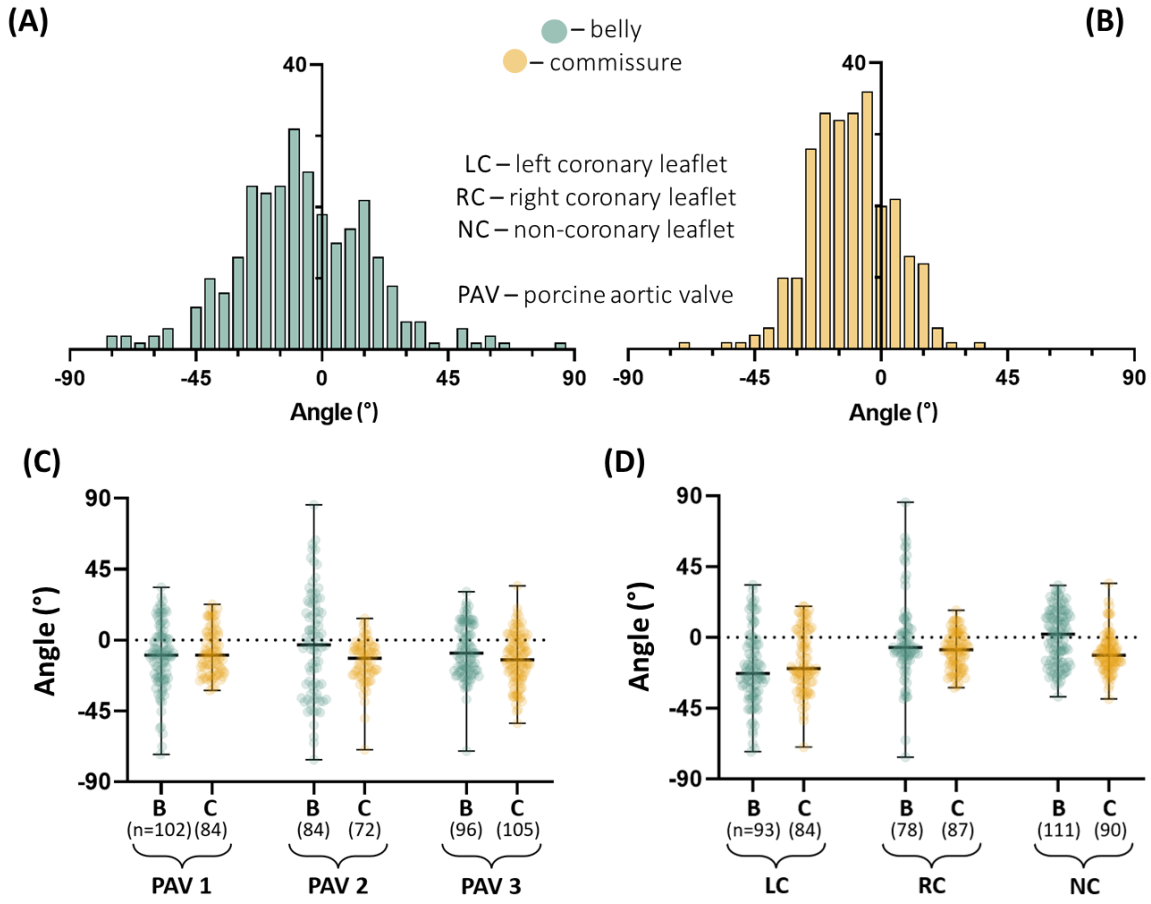

Figure 3-5 *Fibre orientation analysis in fibrosa layer. Histograms of fibre orientations in (A) belly and (B) commissure regions, for both plots bin width: 5°. Fibre orientations separated by (C) leaflet region and valve, (D) leaflet region and type. n refers to number of measurements from N=3 valves.*

3.3.3 Uniaxial tensile testing

3.3.3.1 Leaflet and layer thickness

Fibrosa samples were significantly thicker than ventricularis samples (0.33 ± 0.13, n=23 and 0.06 ± 0.03 mm, n=15, respectively; p=0.0002), and both groups were significantly thinner than the whole, intact samples (0.53 ± 0.15 mm, n=17; p=0.0165 for fibrosa and p<0.0001 for ventricularis), see **Figure 3-6**A.

3.3.3.2 Stress and tension response

For each group, an increase in mean modulus was observed between the initial and final portions of the curve, see **Figure 3-6**B-D. Generally, the circumferential samples had a stiffer response than the radial samples, although only the fibrosa exhibited a statistically significant difference between the two orientations in both the initial (5.70 ± 0.09, n=5 and 1.28 ± 1.69 MPa, n=7 for circumferential and radial, respectively) and final (26.6 ± 12.09, n=6 and 2.07 ± 0.92 MPa, n=7 for circumferential and radial, respectively) portions of the curve. Across the board, there was no statistically significant differences between the fibrosa, ventricularis, and whole leaflet samples tested in the circumferential direction, in either portion of the curve. This also remained the case for the radial direction. Unexpectedly, for samples tested in the circumferential direction, no significant difference was found between the ventricularis and either the fibrosa or whole leaflet, with the mean modulus values remaining above the others for both the initial (28.44 ± 36.6 MPa, n=6) and final (42.48 ± 14.81 MPa, n=6) modulus values. This relationship was also seen in the radial direction for the final modulus (54.14 ± 30.75 MPa, n=6). It is worth noting, however, that in in both radial and circumferential groups there is a high amount of variability in the ventricularis response.

In addition to stress, tension was analysed to investigate the influence of sample thickness on the load bearing share of the tissue, see **Figure 3-6**E-G. By removing thickness from the calculation, tension gives a better representation than stress response for how the individual layers contribute to the overall leaflet load bearing. Here, we see greater differences between the groups tested. The fibrosa and whole leaflet groups exhibit significantly stiffer behaviour in their circumferential directions compared to radial in both the initial ($p=0.0001$ for FC and FR; $p=0.014$ for WC and WR) and final ($p<0.0001$ for RC and FR; $p=0.0015$ for WC and WR) regions. There was no statistical difference observed between the two ventricularis directions for either portion of the curve. Between the groups, for samples tested in the circumferential direction, the ventricularis was significantly less stiff than the fibrosa ($p=0.0093$) and whole leaflet ($p=0.0012$) in the initial region and remained significantly less stiff than the whole leaflet ($p=0.0243$) samples in the final region. Across all the groups and both regions, there were no statistically significant differences between any of the radial samples.

Due to a number of samples breaking at the grips, failure stress and strain are not reported, instead only initial and final moduli have been considered.

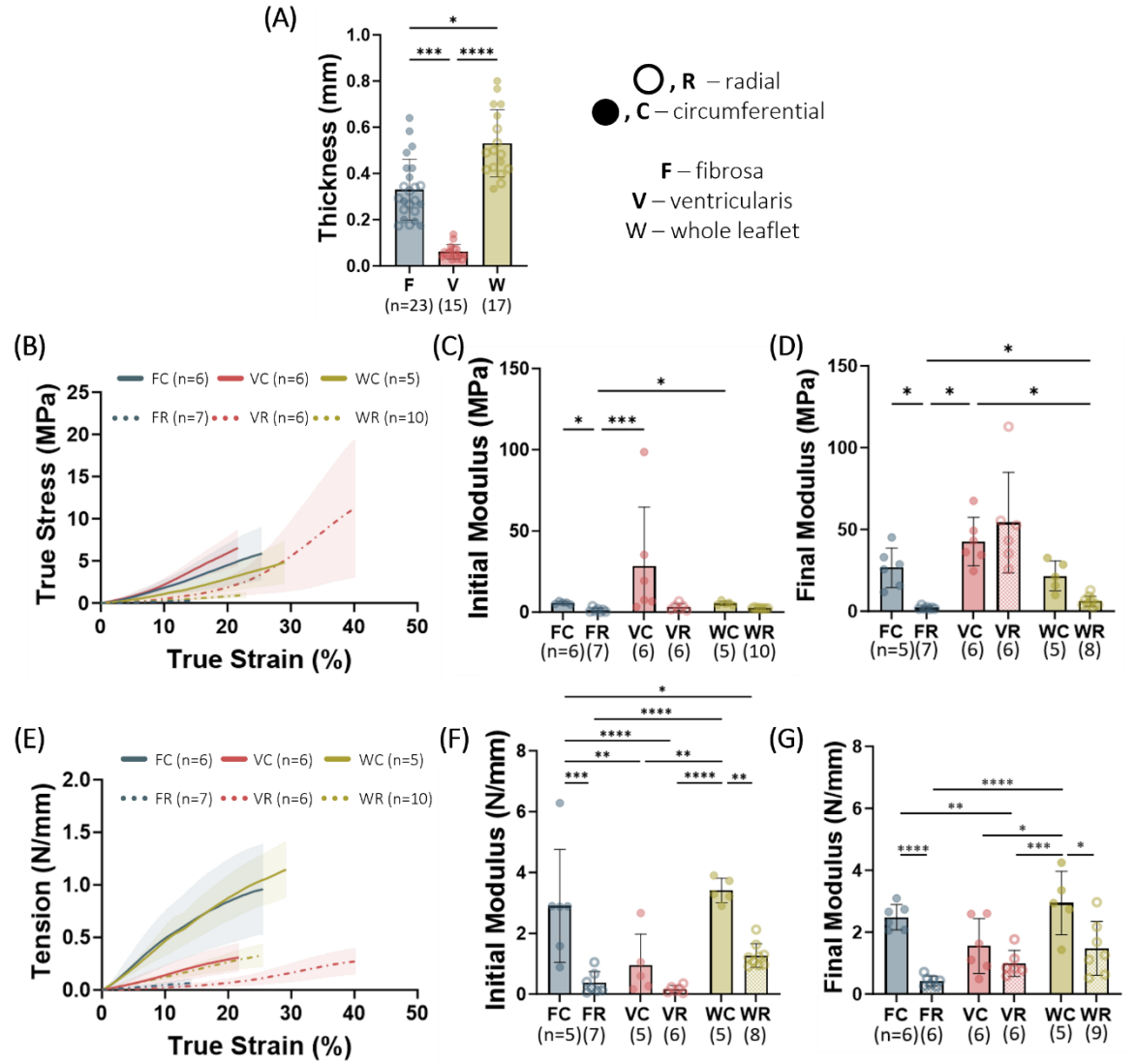

Figure 3-6 *Uniaxial tensile testing data overview. (A) Thickness measurements for all samples, significance tested using Kruskal-Wallis with Dunn's multiple comparisons test. (B) Average true stress and strain curves for all samples. (C) Initial stress modulus values, significance tested using Kruskal-Wallis with Dunn's multiple comparisons test; 3 outliers removed using ROUT (Q=1%). (D) Final stress modulus values, significance tested using Brown-Forsythe and Welch ANOVA tests with Dunnett's multiple comparisons. (E) Average tension and true strain curves for all samples. (F) Initial tension modulus values, significance tested using ordinary one-way ANOVA with Tukey's multiple comparisons; 2 outliers removed using ROUT (Q=1%). (G) Final tension modulus values, significance tested using ordinary one-way ANOVA with Tukey's multiple comparisons test. Normality tested for in all data using Shapiro-Wilk test; p*≤0.05, P**≤0.01, p***≤0.001, p****≤0.0001.*

3.4 Discussion

This study presented the use of histological imaging, SHG imaging, and uniaxial tensile testing to characterise the mechanical response and collagen microstructure of healthy, porcine aortic valve leaflets and their fibrosa and ventricularis layers with the aim of providing benchmarks for development of novel synthetic devices. This work presents, for the first time, the use of the chemical clearing agent BABB on aortic valve leaflets to allow for SHG imaging and detailed analysis of the collagen microstructure throughout the entire leaflet thickness, something which has previously been a challenge for imaging of valve leaflet tissue.

To effectively replicate native aortic leaflet tissue with synthetic materials, the collagen microstructure should be considered as the fibre orientation and organisation determine the tissue's function. Using SHG paired with BABB gave valuable insights into the collagen microstructure at key locations in the leaflets. Chemically clearing the leaflets with BABB solution allowed for full penetration of the leaflet thickness, up to 900 μm at some locations, while without clearing SHG depth is usually limited to less than 150 μm (Campion et al. 2021; Torun et al. 2023; Whelan, Williams, et al. 2021). This allowed for the ability to obtain detailed images of the collagen microstructure throughout the whole tissue thickness without the need for destructive wax embedding and slicing that comes with histology.

While this study investigates fibre orientation and crimp, the images obtained can be used to extract other useful characteristics of the microstructure. For example, Whelan et al. used SHG images to quantify collagen content in bovine pericardium (Whelan, Williams, et al. 2021) which could be applied to this workflow to extract potentially further differences between the fibrosa and ventricularis layers. Another application is in the development of more refined constitutive models to describe this tissue, such as in Sadeghinia et al. who utilised SHG on cleared mitral valve tissue (Sadeghinia et al. 2022). Ultimately, SHG imaging on cleared leaflet tissue can provide numerous insights into the tissue microstructure in a more robust and time efficient process than histology.

Collagen crimp is a key feature of tissue microstructure as it governs the tissue's strain-stiffening behaviour. With the aortic valve, the degree of crimp determines how much the leaflets are able to stretch under pressure when closed. To the authors' knowledge, these results have presented the most extensive quantification of collagen crimp to date in the fibrosa and ventricularis layers of the leaflet. We show that when the leaflet is flat, the collagen fibres in the ventricularis are straighter than in the fibrosa layers, see **Figure 3-4**B. Previously, Sacks et al. (Sacks, Smith, and Hiester 1997) used SALS to suggest that the fibres in the ventricularis layer are more crimped than the fibrosa due to lower fibre eccentricity measured compared to the fibrosa. With the new insights from our results, we can see that this particular phenomenon measured by Sacks et al. may not be due to less straight fibres, but most likely from to the higher degree of disorganisation of collagen fibres in this layer. These findings support the known function of the aortic valve: the ventricularis is held in tension to be able to provide elastic recoil to open the leaflet, while the fibrosa contains significant folding to allow leaflet deformation and effective closure of the valve. Throughout leaflet separation during mechanical testing this contrast between the two layers was evident with notable contraction of the ventricularis, particularly in the radial direction, and expansion of the fibrosa after separation (this can be seen in

C). This observation is supported by Stella and Sacks (Stella and Sacks 2007) who previously quantified the contraction of the ventricularis and expansion of the fibrosa after separation from each other.

Collagen fibre orientation in the fibrosa layer was quantified in both the commissure and belly regions and supported trends previously noted: there is a higher degree of alignment at the leaflet commissure with the origin of fibre bundles which fan out to a more dispersed overall alignment in the belly region (Misfeld and Sievers 2007; Rock et al. 2014; Sacks et al. 1998). Previously, studies have only been able to identify either overall fibre orientation in a particular region of interest which removed the ability to identify multiple families of fibres or have only visualised the large-scale fibre bundles across the leaflet (Mega et al. 2016; Rock et al. 2014). While previous work has been useful to understand the overall collagen fibre directions in the leaflet as a whole, a more detailed understanding of the range and variability of fibre orientations was needed and has now been uncovered from the results presented here. These results have been able to show orientation changes in the collagen fibres throughout the layers of the leaflet, something that has not been seen in detail with previously used imaging techniques (Hepfer et al. 2018; Liao et al. 2008; Martin and Sun 2012; Mega et al. 2016; Pierlot et al. 2015; Rock et al. 2014; Sacks et al. 1998). While fibre orientation was not measured in the ventricularis due to the high degree of disorganisation of the fibres, qualitative assessment of the images shows a stark contrast between the highly organised and dense collagen network in the fibrosa and a more sparse, non-uniform network in the ventricularis (see **Figure 3-3**).

Notably, these results have shown how fibre crimp and orientation change based on leaflet type and between valves. Collagen crimp was not seen to change from animal to animal, suggesting this feature is dependent upon the localised physiological environment of the individual leaflet. Meanwhile, fibre orientation was seen to depend on leaflet type, something that has only previously been seen on a macro scale (Mega et al. 2016; Rock et al. 2014). These results corroborate, at a microscale, what has been seen at a larger scale: predominant fibre orientation in the commissure points downwards towards the centre of the leaflet and belly region, and there is a greater range of fibre orientations in the belly spanning directions pointing upwards towards both commissures.

The native aortic valve leaflet is a complex structure whose function and mechanical response is dictated by its fibrosa and ventricularis layers. To understand and replicate the native leaflet through novel materials it is essential to characterise not only the leaflet as a whole but also its layers. Uniaxial tensile testing provided these unique insights into the mechanical and material response of the native aortic valve leaflets and their individual layers. In utilising uniaxial over biaxial tensile testing we were able to decouple the circumferential from radial

fibre orientations, allowing for the characterisation of the material with fibres predominately orientated either with or against the load. While biaxial testing provides insight into the behaviour of the leaflets in vivo, this does not necessarily directly translate to screenable characteristics in new materials for prosthetic leaflets. When screening new materials, medical device companies or researchers will use quick and reliable procedures like uniaxial testing to determine the mechanical response and anisotropy of the material, and they need to have accurate baseline data for assessment. To compare the groups, we looked at the stress and tension versus strain response curves as well as the initial and final modulus values for each of these. While all of the samples were loaded until failure, it was noted that many samples failed at the grips, suggesting high stress concentrations at these locations; for this reason, failure stress and strain have not been reported or considered in analysis. This is expected in strip samples are used over dog-bone samples (Pei et al. 2021).

In the whole, intact leaflets we saw that the tissue was stiffer in the circumferential direction than the radial direction, with a higher tensile modulus in both the initial and final loading regions. A handful of studies have previously investigated the uniaxial tensile response of this tissue before, looking at both porcine and human aortic valve tissue, and the results obtained in this current study fall within a similar range, see Figure A1-3 (Balguid et al. 2007; Kalejs et al. 2009; Mavrilas and Missirlis 1991; Stradins et al. 2004). Each of these studies employed a different testing protocol with varying stain rates and preloading conditions, so in order to reliably compare whole leaflet uniaxial behaviour to the individual layers it was necessary to repeat these tests.

By not only analysing the stress response of the tissue but also the tension response we used the initial and final moduli to show how the thickness of the layers impacts their mechanical contribution in the whole leaflet. Most notably, we see that the ventricularis as a material is very stiff, with many samples reaching higher stresses in both the radial and circumferential directions than the fibrosa. This high stiffness in both directions can be attributed to the disorganised nature of the collagen fibres, evident through histology and SHG imaging, allowing for a stiff response in all directions. Due to the tissue's small thickness, however, it does not dominate the leaflet's stress response in the circumferential direction. This is clearly shown in **Figure 3-6**B, E as the whole leaflet's stress and tension response more closely follow that of the fibrosa rather than the ventricularis in the circumferential direction. Due to its larger thickness and more specialised collagen fibres alignment, the fibrosa is the primary contributor to the leaflet's ability to withstand stress circumferentially.

Meanwhile, in the radial direction, it is the essential combination of both the ventricularis and fibrosa that provide the leaflet's mechanical response. These results further support

conclusions drawn previously from biaxial testing carried out by Stella and Sacks in 2007, where the researchers suggested that the ventricularis dominates the mechanical response of the native leaflet in the radial direction at high stress levels (Stella and Sacks 2007). While the ventricularis is able to withstand high stresses in the radial direction, due to the collagen fibres in the fibrosa having a predominantly circumferential alignment, it is unable to bear as high a load in the radial direction. It becomes the pairing of the two layers that gives the whole leaflet its stress response in this direction.

Additionally, the ventricularis contains elastin sheets/fibres with some preferential alignment radially. This is necessary for effective leaflet function as the high levels of stretching in the ventricularis in the radial direction allow the valve to close fully under diastolic pressure, while its subsequent elastic recoil ensures a fully open valve during systole (Sacks et al. 2009).

To the authors' knowledge no studies have presented both the mechanical and material response of this tissue, opting either to present a measure of tension or a measure of stress, but the consideration of both of these is needed for effective development of novel materials, especially when considering mimicking both the fibrosa and ventricularis layers. As mentioned, the specialised configuration of the two layers contains folding of the fibrosa and a stretched ventricularis. While this provides the leaflet with an enhanced ability to withstand load and quickly close, the overall stiffness of the leaflet can be described by the individual stiffnesses of the fibrosa and ventricularis layers (see Figure A1-4). When using synthetic materials to replicate the aortic leaflet in future prosthetic devices, it is essential to consider both the mechanical response of the material as well as how the union and combination of these materials may impact the leaflets' behaviour in vivo. The need for this structural and mechanical information is evident in publications attempting to mimic both the leaflet fibre microstructure and mechanical response, such as (Coulter et al. 2019; Saidy et al. 2019; Stasiak et al. 2020; Zeugin et al. 2024). Lack of a suitable tissue benchmark prevents adequate comparison of novel materials to native tissue. This study addresses this knowledge gap, providing future researchers with the necessary information to drive development of novel materials.

This study does contain a few limitations. The use of uniaxial tensile testing over biaxial tension removed the ability to measure the interaction between fibres in more than one direction. However, the results presented provide a detailed analysis of the mechanical response of the aortic valve leaflet layers and how these drive the response of the whole leaflet. In particular, we have used industrially-relevant methods to show the anisotropy of tissue response between the different orientations and provided quantifiable modulus values for ease of comparison with other materials. Secondly, SHG imaging was limited to the belly and

commissure regions of the leaflets. This was due to the knowledge that the collagen fibre bundles originate at the commissures and meet in the belly, providing two high-interest and contrasting regions, as well as the practicality of high imaging and data processing times. Additionally, characterising the fibre structure at the leaflet commissures could provide insight for future prosthetic valve development as the commissure region experiences high levels of stress, a factor known to exacerbate structural valve degeneration (Kostyunin et al. 2020; Stanova et al. 2024). Future work in this area should endeavour to gain the same degree of detailed understanding of the microstructure in the rest of the leaflet. Finally, this entire study was performed on porcine rather than human tissue. While human tissue is preferable, healthy human valve tissue is very difficult to obtain. Porcine tissue is commonly used in valve leaflet research and has been shown to be a good indicator of healthy human valve tissue while also being more readily available (Martin and Sun 2012).

This study presented an extensive evaluation of the aortic valve leaflet microstructure in combination with mechanical testing to provide further insights into the leaflet material. Overall, it has provided essential detail to support the current knowledge of the native aortic valve leaflets with the aim to aid the development of next generation bioinspired leaflet designs.

Chapter 4 Using design of experiments and finite element modelling to determine optimal bioinspired polymeric leaflet structural combinations

4.1 Introduction

Polymer heart valves offer an alternative to bioprosthetic or mechanical heart valves for the treatment of aortic stenosis with the potential to deliver durable and biocompatible leaflet material. There are a wide variety of polymer heart valves currently in development which have taken unique approaches to the creation of these next-generation devices. These approaches have primarily focused on developing novel polymer blends, such as the Tria valve (Dandeniyage et al. 2017; Jenney et al. 2020), PolyNova valve (Kovarovic et al. 2023; Rotman et al. 2020), PoliValve (Stasiak et al. 2020), Endurance valve (Khair et al. 2025), and Life Polymer (Scherman et al. 2019). However, some development has been focused on integrating a fibre-reinforcement structure. This is seen in the novel polymer used in the PoliValve with copolymer blocks that can be arranged to give a mechanical orientation (Stasiak et al. 2020) and in leaflet additions such as the 3D-printed valve developed by Coulter, et al. that has bioinspired fibre additions (Coulter et al. 2019; Zeugin et al. 2024) and in commissural and free edge fibre additions to new generations of the Endurance valve (Khair et al. 2025). Additionally, embedded leaflet reinforcement has been explored with NiTi fibres to support leaflet stress in the radial direction (Chen et al. 2023) and integration of a nylon fibre mesh (Choi et al. 2024). Many of these studies have shown a reduction of leaflet stress, strain, and improved hydrodynamic performance with these fibrous inclusions (Chen et al. 2023; Coulter et al. 2019; Giaretta et al. 2024; Khair et al. 2025).

On the other hand, there has been a great amount of development in bioinspired, tissue engineered valve leaflets (Boehm et al. 2023; De Jesus Morales et al. 2024; Saidy et al. 2019; Snyder and Jana 2023a). These devices will still require many years of development before they can be made commercially available; however, they have shown the potential for adopting manufacturing methods such as melt electrowriting (MEW), for the creation of a stiff, bioinspired, fibre reinforcement structure. For implementation in devices not tailored for tissue engineering, a fibre structure made from MEW can be embedded in a compliant elastomeric matrix to mimic the mechanical behaviour of the native aortic valve leaflets described previously in Chapter 3.

Finite element (FE) modelling is a useful and versatile tool that is used to aid the design and development of polymer valves. It has been used primarily to improve already-existing designs by modifying leaflet thickness, shape, or adding a simple reinforcement structure (Chen et al. 2023; Coulter et al. 2019; Khair et al. 2025; Kovarovic et al. 2022; Masheane et al. 2024). These tools have the potential to transform the design, development, and assessment process of these devices. By leveraging FE modelling as a tool, we can assess novel material combinations and structures in silico to guide future manufacture and bench testing. Implementation of these tools would dramatically decrease development time for these devices by reducing manufacturing and assessment time of potential material combinations.

Design of experiments, or DOE, is another valuable tool that can be leveraged in the development of novel leaflets. With a seemingly endless range of materials and structural features to choose from when designing leaflets, DOE can aid the process by providing a systematic approach to test the minimum number of combinations of features to allow sound statistical analysis of each feature's impact (Durakovic 2017).

The objective of this work is to develop an FE modelling and DOE approach for the design of novel, bioinspired, fibre-reinforced polymeric valve leaflets. Based on structures that can be manufactured using MEW, it aims to determine the best combination of printed fibre structural features embedded in a compliant elastomeric material. Additionally, it aims to verify the benefit of a fibre-reinforcement structure with bioinspired local orientations over other reinforcement types. Ultimately, this tool should be able to be used with any material combination to determine the best combination of structural features for a prosthetic aortic valve leaflet.

4.2 Methods

In order to simulate a fibre-reinforced leaflet, first a model with discrete fibre inclusions was developed to obtain the mechanical response of a MEW/ elastomer composite. This response is used to calibrate a hyperelastic, fibre-reinforced constitutive model to describe the material response and fibre orientations in a Trileaflet valve model. This methodology is first used to verify the benefit of bioinspired fibre orientations, and then it is used alongside a DOE approach to determine the best MEW and elastomer structural combination.

In this work, the materials simulated are Sylgard-184 (Dow Inc., MI, USA) PDMS at a 16:1 base to curing volume ratio embedded with a PEEK-like fibre structure.

4.2.1 Discrete fibre model

A dogbone-shaped model with discrete fibre inclusions was created in Abaqus (SIMULIA, Dassault Systèmes, 2022) to simulate the mechanical response of a MEW-embedded elastomer. Separately, a dogbone model and a MEW mesh were created. The dogbone sample had an 18 mm gauge length, 4.5 mm width, and variable thickness. A MEW mesh was created in SolidWorks (SolidWorks Corp., Dassault Systèmes, 2023) with an assumed circular fibre diameter of 20 µm. Layer number and fibre spacing were variable. All of the layers were modelled as a solid part, see **Figure 4-1**.

In Abaqus CAE, the two parts were merged together with boundaries retained. Each part was assigned unique material properties, and it was meshed as one solid part. For mesh generation, the part was seeded with an element size of 0.0625 mm for the fibres and 0.2 mm on the outside edges. It was meshed with 4-node linear tetrahedron elements. The matrix component, PDMS, was modelled as a first order Ogden material with a μ_1= 0.204 MPa, α_1= 2.504, and D=0; material parameters were calibrated from previous in-house uniaxial tensile testing. The fibres were modelled as a linear elastic material based on PEEK with a Young's modulus of 2,906 MPa and a Poisson's ratio of 0.45 (Shrestha et al. 2016). To simulate a uniaxial test, the bottom surface of the dogbone was fixed (U1=U2=U3=0) and the top surface was constrained using kinematic coupling to a reference point; all degrees of freedom were constrained (U1, U2, U3, UR1, UR2, UR3). A displacement boundary condition of 10 mm was applied to the reference point to deform the model (U2=10; U1=U3=0).

The stress/strain response of this material was calculated using force/displacement output from the reference point, and used to calibrate the in-built GOH model using MCalibrate (PolymerFEM, MA, USA) (Gasser, Ogden, and Holzapfel 2006).

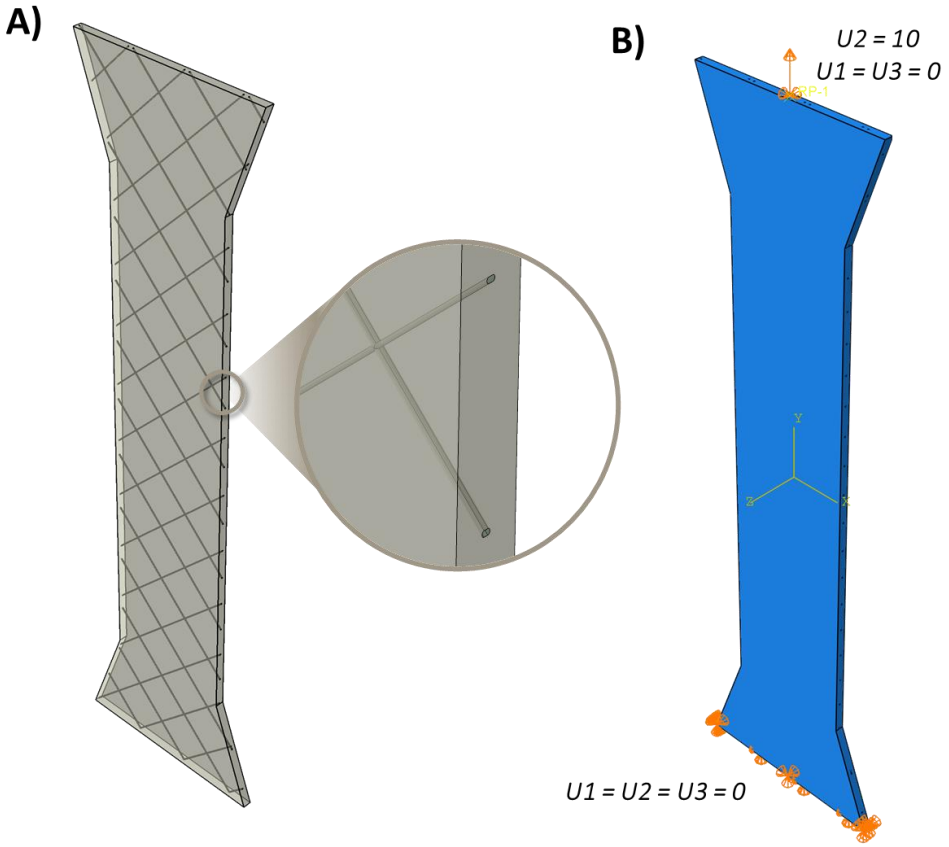

Figure 4-1 *Uniaxial dogbone model with discrete fibre inclusions showing (A) fibres embedded in matrix with different material assignments, and (B) model boundary conditions.*

4.2.2 Trileaflet valve model

A trileaflet valve model inspired by the ACURATE neo[2] Aortic Valve™ (Boston Scientific, Marlbourough, Minnesota, US) was developed to model the behaviour of MEW-embedded polymer leaflets in a simulated valve environment.

4.2.2.1 Geometry, mesh, material, and fibre orientations

For the valve model, the leaflet geometry was designed based on the large size ACCURATE neo2 Aortic Valve™. The geometry was drawn in Abaqus CAE and partitioned into 56 discrete rectangular regions to later assign local fibre orientations. After partitioning, the leaflet was exported as an STL file and imported into ANSA Beta (Beta CAE Systems, MI, USA) for uniform meshing into linear, full integration brick elements (C3D8), at which point it was imported back into Abaqus as an INP file. After performing a mesh convergence study (see Appendix A2), the optimum number of elements was selected at 22,715. Each of the 56 regions was assigned a unique local fibre orientation for two families of fibres, see **Figure 4-2**. These orientations were informed based on the measurements obtained in Chapter 3: orientations for the belly region were assigned to a partition in the same region on the leaflet model and the commissure orientations were assigned to a partition in the corresponding region. Fibre orientations were

extrapolated based on these for the rest of the leaflet, ensuring no family orientation differed by more than 5 degrees from its neighbouring regions. Material behaviour in the leaflet is described by the in-build HGO model, with parameters calibrated from the discrete fibre uniaxial model.

To simulate the frame and enable accurate leaflet "suturing", a surface part was created representing the geometry of the frame. This was meshed with 2,608 SFM3D4R elements. To assemble the whole model, three leaflets and three frame surface instances were brought in at 120° to each other to form a symmetrical valve. Local coordinate systems were defined for each leaflet-frame surface pairing in order to aid boundary condition definition.

4.2.2.2 Boundary conditions and steps

The valve was modelled using ABAQUS/Explicit solver. There are 8 steps total in the model comprised of four steps to suture the leaflet, one to move the frame out of contact, and three pressure steps (see **Figure 4-3**).

Steps 1, 2, and 3 moved the leaflet into contact with the frame, moved the edges close to the frame, and then pressurised the leaflet against the frame. Throughout these three steps the frame is fixed in place (U1=U2=U3=0). In Step 1, the entire leaflet moves towards the fame (U3= -1.3 mm) and is constrained in the other two directions (U1=U2=0). In Step 2, the sides of the leaflet move towards the frame (U3=-2 mm, U2=0) and the entire midline of the leaflet is fixed in place to stabilise the part (U1=U2=U3=0). For Step 3, a pressure is applied to the leaflet outer surface until it is fully in contact with the frame (p=0.005 MPa). To prevent vertical or side-to-side translation of the leaflet, a portion of the midline is constrained (U1=U2=0).

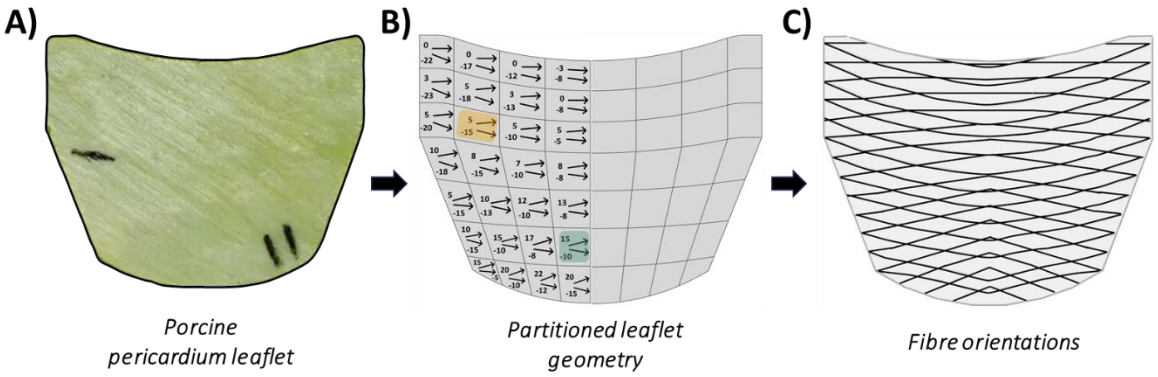

Figure 4-2 *Porcine pericardium leaflet from ACURATE neo2 aortic valve compared to (B) leaflet model including partitions and local fibre orientations, and (C) diagram of fibre orientations across leaflet. Orange and blue regions in (B) correspond to fibre orientations informed from imaging of native leaflets' commissures and belly regions.*

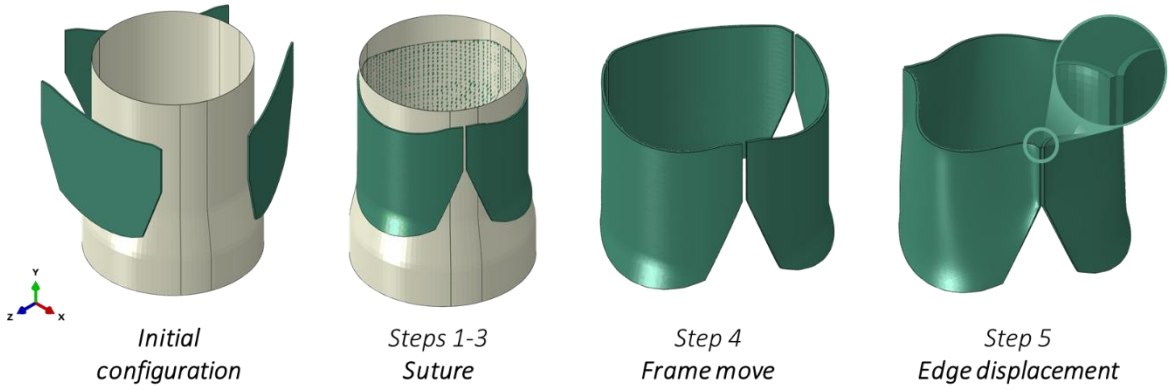

Figure 4-3 *Valve model setup steps before pressure application to simulate sutured leaflet.*

At this point, the frame is no longer needed and is moved away from the leaflet (U3=-20 mm).

To complete suturing, the inner edges of the leaflets should come into contact, as they would in a fully assembled valve. To simulate this, a displacement of total leaflet thickness in the X-direction is applied on these edges. Finally, the leaflets are in their sutured configuration and the pressure can be applied.

Pressure is applied as a dynamic load to simulate the opening and closing of the leaflets during a single cardiac cycle. The load is applied to the aortic and ventricular surfaces as shown in **Figure 4-4**A, these curves were provided by Boston Scientific, extracted from pulse duplicator testing on size large ACURATE neo2 devices. These were tested using a ViVitro Pulse Duplicator system (ViVitro Labs Inc., BC, Canada) under hypertensive pressure (peak trans-aortic pressure of 140 mmHg) and nominal flow conditions (70 bpm, 35% systolic duration, and 5 l/min) as outlined in ISO 5840. One full cycle lasts 0.857 seconds and is applied across a step. To ensure results are not impacted by the leaflets' initial conditions, three pressure cycles are applied in Steps 6, 7, and 8.

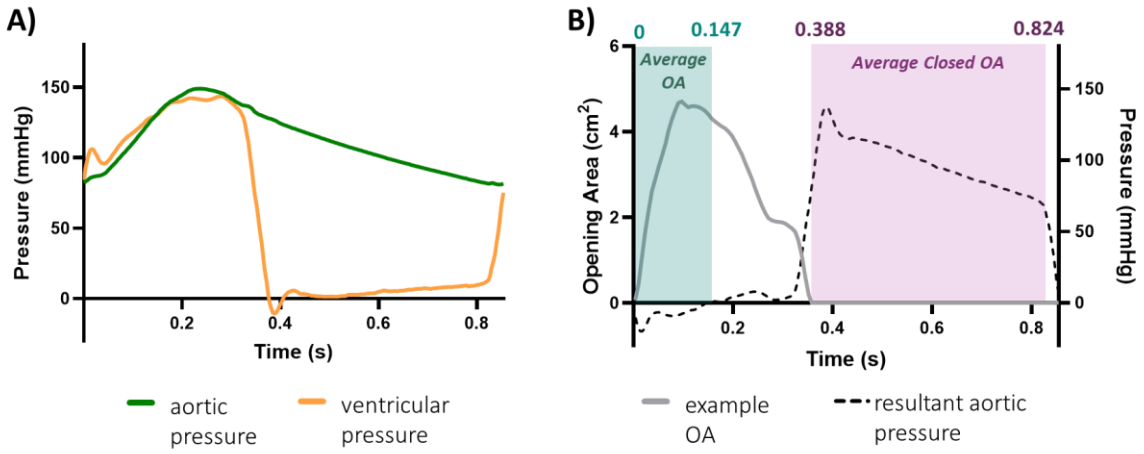

Figure 4-4 *(A) Pressure applied to aortic and ventricular surfaces across a step, and (B) diagram showing resultant aortic pressure alongside an example OA curve detailing the regions taken for average OA and average closed OA calculations.*

Contact throughout the model is defined using the general contact algorithm. It is defined for the leaflet-stent interaction as well as all of the leaflet-leaflet interactions. The same interaction property is assigned to all pairs: tangential behaviour is formulated using the penalty algorithm with a friction coefficient of 0.1, and normal behaviour is defined as "hard" contact with the default constraint enforcement method. Separation is allowed after contact.

4.2.2.3 Valve opening area extraction

A custom python script was created to extract images of the top view of the valve across the final cycle, amounting to 128 images each representing a time step of 0.0067 s. These were analysed in a custom MATLAB (MathWorks Inc. (2024), MA, USA) script that used edge detection to identify the open part of the valve and return the area within the valve, see **Figure 4-5**. Using the known dimensions of the valve, this value could be converted from pixels^2 to cm^2. With these outputs, a variety of parameters were calculated, see **Figure 4-4**B. First, maximum opening area (OA) across the entire cycle was extracted. However, since this is just one measurement taken from a period with varying areas, a secondary "average OA" was extracted to serve as a surrogate for effective orifice area (EOA). EOA is a clinical metric of valve opening performance derived from flow measures, and for valves of this size is required to be at least 1.7 cm^2 (ISO 5840-3). Average OA was taken as the mean OA during the time when ventricular pressure is higher than aortic pressure, which corresponded to 0-0.147 s. This aligns methods employed by Boston Scientific, where EOA during pulse duplicator testing is taken as an average output across this region. This measurement was validated by modelling porcine pericardium leaflets and comparing the average OA measurement to expected EOA values, which were aligned (see Appendix A2). Also extracted was a measure of closure, which was taken as an average OA across the end of the cycle (0.388 - 0.824 s). Finally, as a measure of valve "efficiency", the time from start of the cycle to maximum opening area was also assessed.

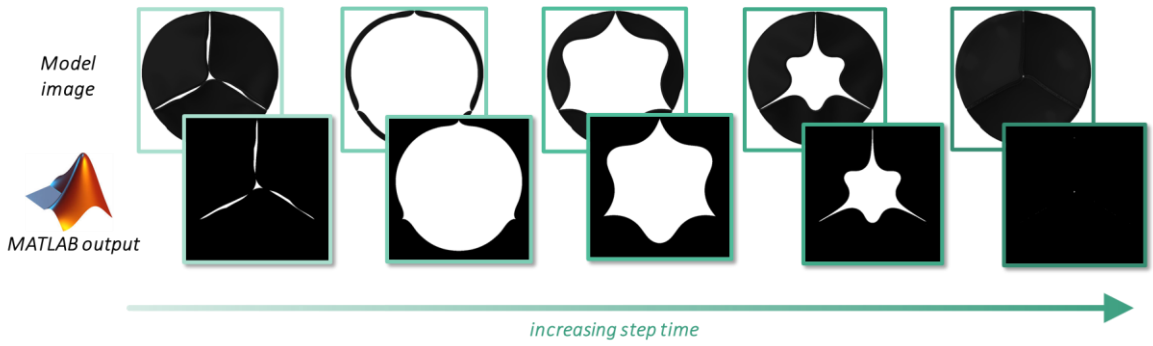

Figure 4-5 *diagram comparing image of valve from the top view extracted from Abaqus to the output from custom MATLAB script to determine valve opening area.*

4.2.3 Fibre orientation verification

In order to determine the impact of using bioinspired fibre orientations, an assessment was performed to compare the leaflet material and valve's response with different fibre reinforcement structures. For this, five models with different reinforcement structures were investigated: bioinspired fibre orientations, all circumferential, all radial, isotropically dispersed, and no fibres. The material models in all of the fibre reinforced structures were calibrated based on a 2-layered MEW structure with fibre spacing of 2 mm embedded in 0.3 mm of PDMS. The calibrated HGO parameters for this were: C10 = 0.07844 MPa; k1 = 0.1526 MPa; k2 = 0.109246. Dispersion, κ, was set to zero for all fibre models except for the isotropic model, where it was set to 0.333. For the model without fibres, a Neo Hookean material definition was used with C10 = 0.07844.

4.2.4 Design of experiments

Design of experiments (DOE) was used to identify the best combinations of structural components in the leaflet. Three structural features were identified: number of MEW layers (2, 5, 8, 10), fibre spacing (0.5, 1, 1.5, 2 mm), and silicone thickness (0.2, 0.3, 0.4, 0.5 mm). These parameters were chosen to represent the feasible manufacturable ranges. JMP (JMP Pro 18, NC, USA) was used to map the DOE runs; a response surface design was chosen with measured responses and targets shown in **Table 4-1**. 13 runs, 12 unique and 1 repeated combination, were identified to fully map this space, they are shown in **Table 4-2**.

Table 4-1 *Responses investigated using DOE, with objective for each and target, if applicable*

Response	**Objective**	**Target**	**Weight**
Average stress (belly and suture edge)	Minimise	--	1x
Average strain (belly and suture edge)	Minimise	--	1x
Maximum opening area	Maximise	Minimum: 1.7 cm^2	1x
Average opening area	Maximise	Minimum: 1.7 cm^2	2x
Average closed area	Minimise	0 cm^2	2x
Time to opening	Minimise	--	1x

Table 4-2 *Embedded MEW structure combination runs as indicated by DOE*

Number of layers	Fibre spacing (mm)	Thickness (mm)
2	0.5	0.5
2	0.5	0.2
2	1.5	0.3
2	2	0.5
5	1	0.4
5	1	0.4
5	2	0.2
8	0.5	0.3
8	1.5	0.5
8	1.5	0.3
10	0.5	0.5
10	1	0.2
10	2	0.4

4.2.5 Statistical analysis

All statistical analysis related to the DOE was performed within the JMP Pro software, and $p \leq 0.05$ was considered significant.

4.3 Results

4.3.1 Fibre orientation analysis

Stress and strain plots of the five different fibre-reinforced leaflets are shown in **Figure 4-6**. Across all the valves, there are high levels of strain and low levels of stress. Both the bioinspired and circumferential orientations result in leaflets that achieve full closure and minimal pinwheeling, meanwhile there is excessive leaflet deformation in the other three orientations. Notably, the unreinforced, matrix only leaflets reach a peak of 119.4% strain in the belly region, and the leaflets with radially aligned fibres reach 102.6% at the commissure edges. In the other three configurations, peak strains are far lower and all at the bottom suture edge, with the isotropic configuration reaching 74.6% maximum strain, circumferential reaching 69% maximum strain, and the bioinspired orientation reaching 66.4% maximum strain. Peak stresses in the leaflets occur in the same regions. The three leaflets with highest strain experience the lowest peak stresses (radial: 1.25 MPa; isotropic: 1.34 MPa; matrix only: 1.57 MPa) while the bioinspired (2.34 MPa) and circumferential (2.53 MPa) orientations experience higher peak stress.

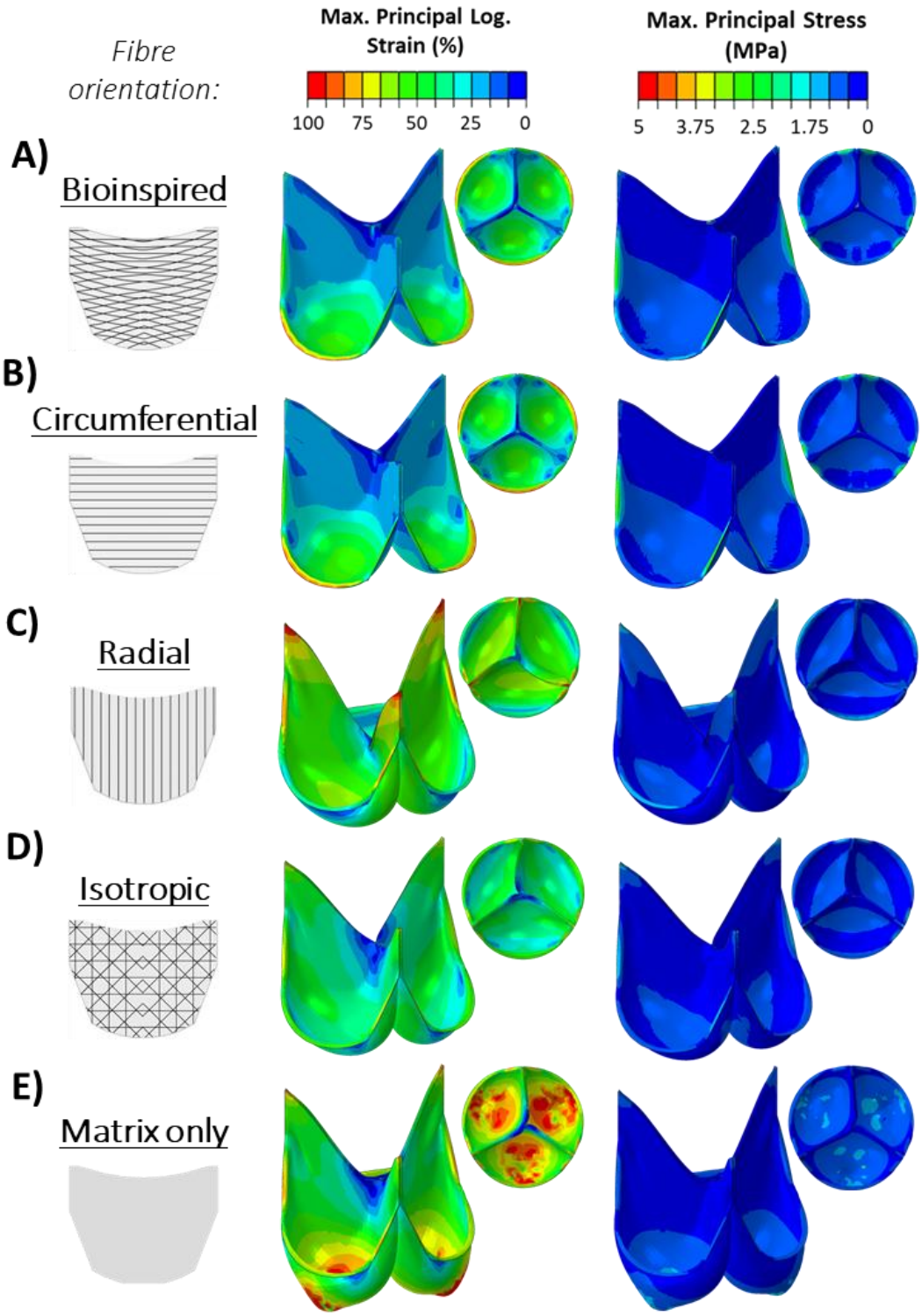

Figure 4-6 *Strain and stress outputs from fibre orientation analysis showing (A) bioinspired orientation, (B) circumferential, (C) radial, (D) isotropic, and (E) matric only with no fibre reinforcement.*

Average stress and strain in the three leaflet regions are shown in **Figure 4-6**. Stresses are highest in the belly region for all models, with the bioinspired, circumferential, and matrix only models reaching the highest average stress. In the free edge, the highest average stress is seen in the radial leaflets, while in the suture region all of the leaflet configurations experience similar levels of stress. Greater differences between the reinforcement configurations can be seen in the strain levels, with both the bioinspired and circumferential models experiencing lower strain than the other three models. In particular, the radial configuration and matrix only models experience greater strains across all three regions.

Strain in the leaflets is further investigated by organising into percent volume of elements within 10% strain bands, see **Figure 4-7**C-E. In the suture edge, the bioinspired and circumferential orientation models have a majority of the region experiencing less than 30% strain, while the other three configurations have a majority above 40%. Similar trends are seen in the free edge and the belly regions, where the bioinspired and circumferential models have more elements in the lower strain bands while the other three models have large volumes in the higher strain bands above 30 and 40%.

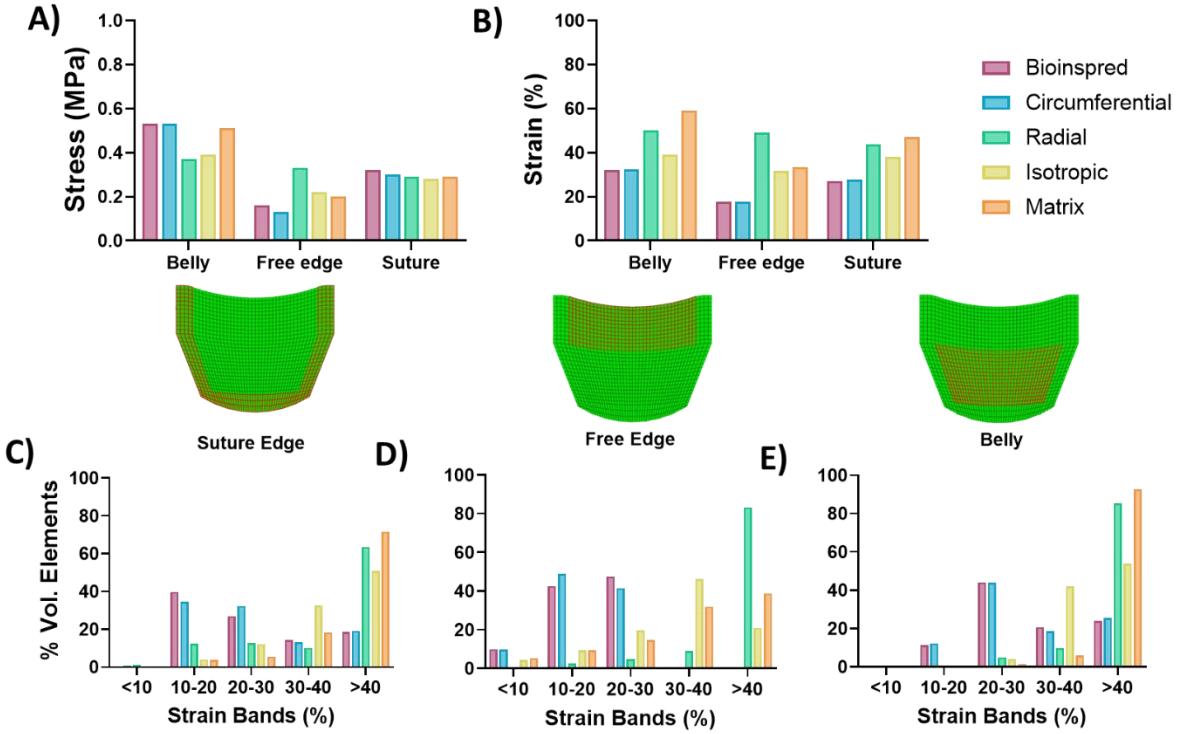

Figure 4-7 *Stress and strain values extracted from models with differing fibre reinforcement structures at three different regions. (A) Average stress for each model in each region, (B) average strain for each model in each region, and volume percent of elements in different strain bands for (C) suture edge, (D) free edge, and (E) belly.*

Opening areas across the cycle vary greatly between the models, with the bioinspired and circumferential configurations reaching the largest maximum OA and average OA, see **Figure 4-8**. The matrix only leaflets had the worst performance with the smallest maximum OA and average OA, with the radial configuration performing slightly better.

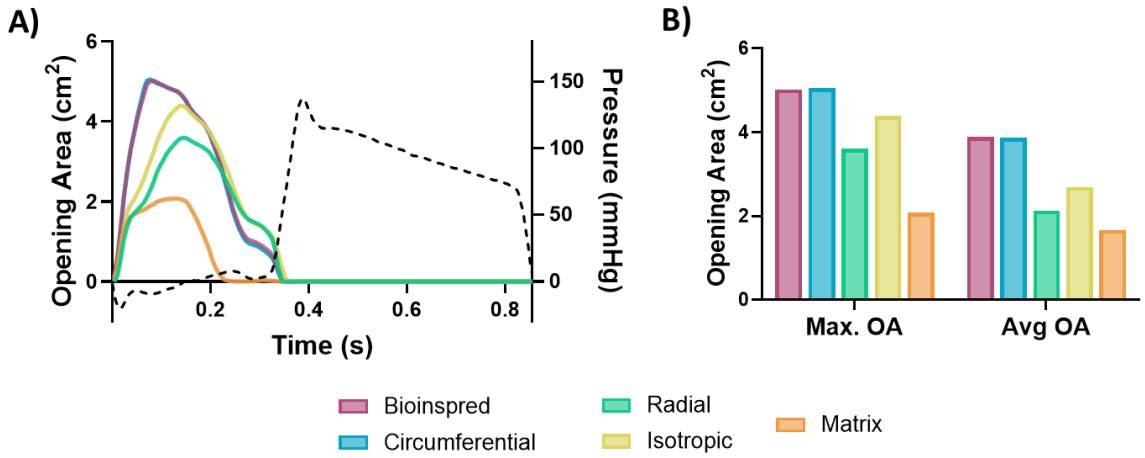

Figure 4-8 *Opening area analysis for valve models with different fibre reinforcement structures. (A) Opening area for each model throughout the cycles, and (B) maximum and average opening area values for each configuration.*

4.3.2 Design of experiments

4.3.2.1 Valve models

Figure 4-9A shows the stress/strain response of each combination of parameters and the corresponding valve opening area throughout the cycle. A wide range of stiffnesses were simulated across the 12 unique fibre/silicone structural combinations, leading to a variation of opening area responses. Looking at the stiffest combination (10 layers, 0.5 mm fibre spacing, and 0.5 mm thickness), there are high levels of stress at the suture edge with low strain across the leaflet (see F**igure4-9C**). Conversely, the most compliant combinations (2 layers, 2 mm fibre spacing, and 0.5 mm thickness) experienced low stress and high strain across the leaflet (see **Figure 4-9**D,E). Additionally, the more compliant material resulted in a larger maximum opening area (4.73 vs 4.20 cm^2) and achieved full closure, where the stiffer combination remains slightly open with an average closed area of 0.099 cm^2.

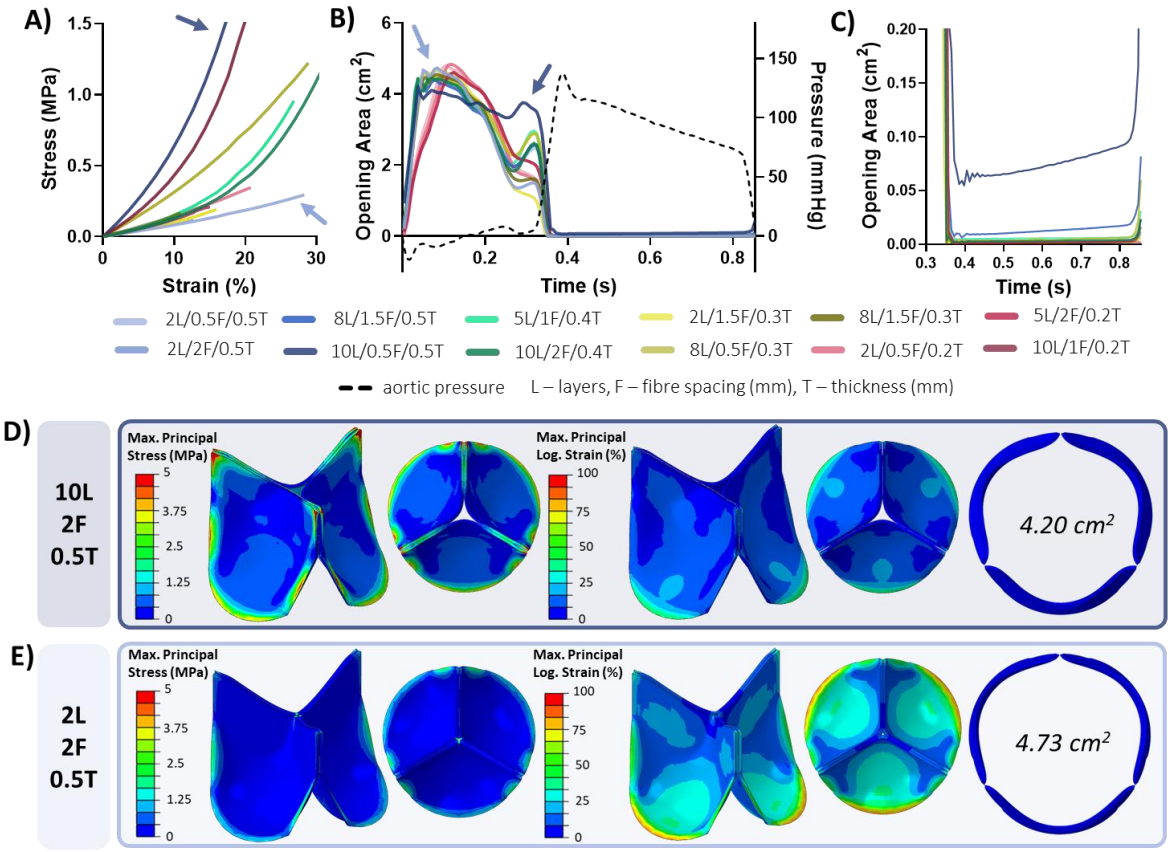

Figure 4-9 *Results of all models run in DOE analysis, showing (A) stress-strain curves from uniaxial model, (B) opening areas throughout the circle, (C) detailed view of closed opening areas, and detailed view of valve models with (D) stiffest material response and (E) most compliant material response. Arrows indicate response of two valve examples.*

4.3.2.2 DOE results

As seen in **Table 4-3**, the regression model was able to fit a good model for each response, with all R squared values over 0.95. Each factor on its own had numerous significant linear relationships with the responses, with the number of layers and fibre spacing significantly impacting the leaflet stress, strain, and maximum opening area. Fibre spacing also had a significant impact on the time to reach maximum opening area, and leaflet thickness had a strong significant impact on all responses except strain at the suture edge and the average closed opening area. There are fewer significant nonlinear relationships, with all having a less strong statistical significance than the linear fit except for leaflet thickness and strain in the suture edge: this is the only nonlinear relationship with a higher P-value than the linear fit.

Table 4-3 *Results of relationships between all input factors and the resulting response. Red numbers indicate a significant p-value less than 005, yellow numbers indicate a p-value less than 0.01.*

Response	Fit R^2	Factors								
		LN	LN^2	FS	FS^2	T	T^2	LN * FS	LN * T	FS * T
Suture edge stress	0.99	0.0005	*ns*	0.0009	*ns*	0.0001	0.0322	0.0021	*ns*	*ns*
Suture edge strain	0.96	0.0175	*ns*	0.0224	*ns*	*ns*	0.0369	*ns*	*ns*	*ns*
Belly stress	0.99	0.0046	0.0323	0.0326	*ns*	0.0002	0.0085	0.0137	*ns*	*ns*
Belly strain	0.98	0.0224	*ns*	0.0099	*ns*	0.0059	0.0159	*ns*	*ns*	*ns*
Max OA	0.99	<0.0001	*ns*	0.0002	0.0018	<0.0001	0.0008	0.0016	0.0003	*ns*
Avg. closed OA	0.96	*ns*	*ns*	*ns*	*ns*	*ns*	*ns*	0.0407	0.313	*ns*
Avg. positive OA	0.98	*ns*	*ns*	*ns*	*ns*	0.0047	0.0057	*ns*	*ns*	*ns*
Time to max OA	0.99	*ns*	*ns*	0.0439	*ns*	0.0016	0.0056	*ns*	0.0158	*ns*

Combining the factors also resulted in significant relationships in some cases, with the pairing of layer number and fibre spacing having a significant impact on stress in both regions of interest, as well as the maximum opening area and closed opening area. Number of layers and thickness together also has a significant effect on maximum opening area and closed opening area, as well as the time to reach maximum opening.

Figure 4-10 shows scatter plots for every factor and response pairing that had either a significant linear or nonlinear relationship. Stress in the two regions decreased with fewer layers, greater fibre spacing, and increased leaflet thickness (**Figure 4-10**A,C). A smaller fibre spacing and increased layers reduced average strain (**Figure 4-10**B, D). A significant relationship was found between maximum opening area and all three factors, but the change in opening area for every factor was very small (**Figure 4-10**E). Average opening area is increased with a larger thickness, increasing by 15.1% between 0.2 and 0.5 mm (**Figure 4-10**F). Notably, all of the maximum and average opening areas recorded were well above the 1.7 cm^2 target. Finally, the time to maximum opening area is reduced with a higher leaflet thickness and a smaller fibre spacing (**Figure 4-10**G).

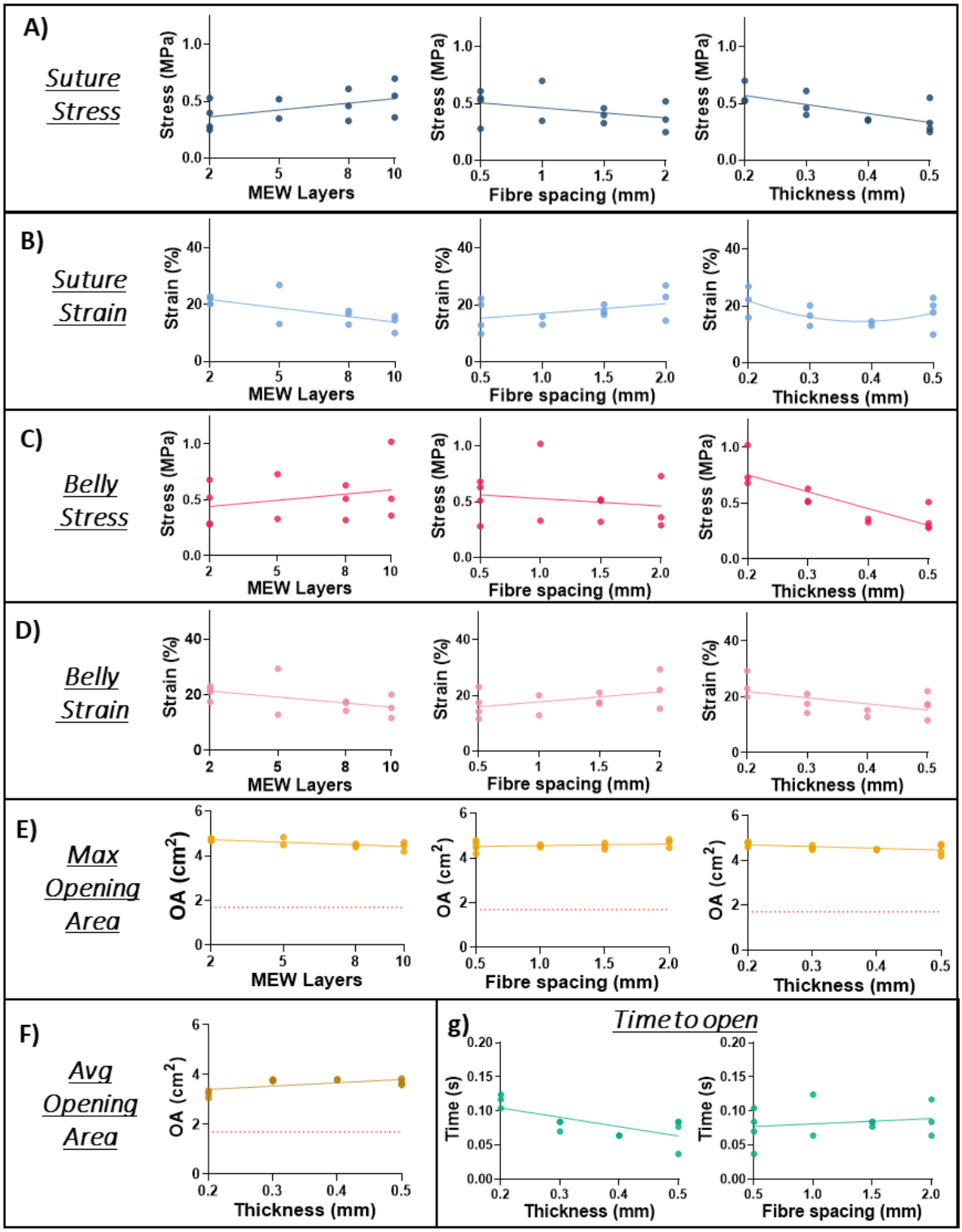

Figure 4-10 *Scatter plots for every factor and response with a statistically significant relationship with an indicative line of best fit. (A) Suture stress, (B) suture strain, (C) belly stress, (D) belly strain, (E) maximum opening area, (F) average opening area, and (G) time to open.*

Pairings of factors and their result on responses is shown in **Figure 4-11**. These follow the same relationships described previously, but showing an extra level of complexity in the response to these two factors. In both regions, stress is increased with more layers and a smaller fibre spacing, although it is greater when the fibre spacing is 1 mm than either 0.5 or 1.5 mm (see

Figure 4-11A,B). Maximum opening area is increased with fewer layers, a smaller thickness, and a larger fibre spacing (see **Figure 4-11**C). Time to maximum opening is reduced with a greater thickness and more layers (**Figure 4-11**D). Closed area is the only response to have a significant relationship with pairs of factors, showing a smaller area for a lower thickness, and generally fewer layers, although a large number of layers with a larger fibre spacing will also improve leaflet closure (**Figure 4-11**E). It should be noted, however, that all of the valves are effectively closed, and the recorded areas are a small number of pixels.

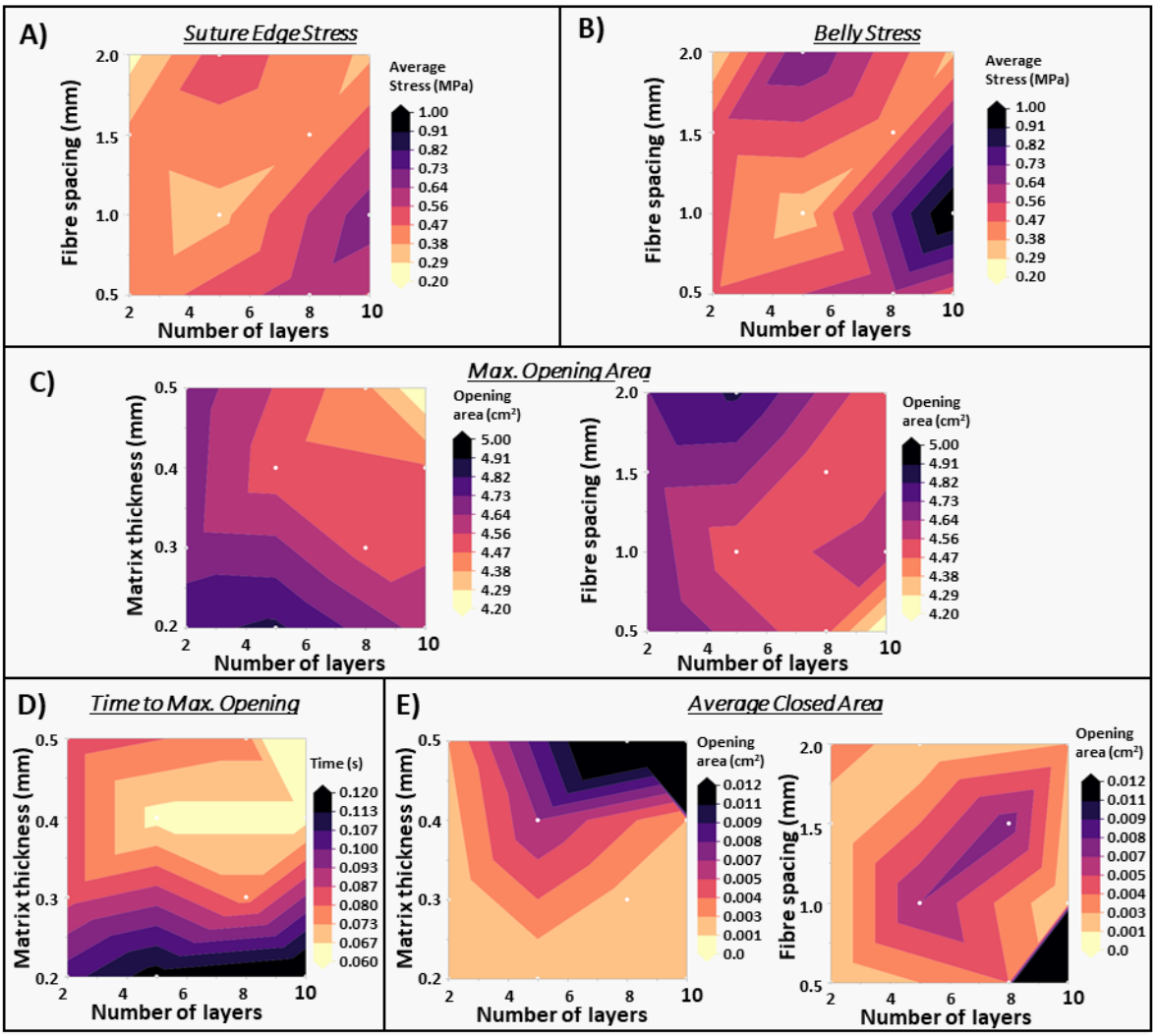

Figure 4-11 *Heatmaps of all paired factors and responses with statistically significant relationships. (A) Suture edge stress, (B) belly stress, (C) maximum opening area, (D) time to maximum opening, (E) average closed area.*

4.3.2.3 Most desirable combinations

From the results of all combinations, a "most desirable" combinations of 2 layers, 0.5 mm fibre spacing, and 0.4 mm thickness was identified (named MD04, desirability: 0.78), see **Figure 4-12**A. Due to the desire to maintain a low profile device, the most desirable combinations for 0.3 mm and 0.2 mm thickness were also identified: 2 layers, 0.5 mm fibre spacing, 0.3 mm thickness (MD03, desirability: 0.65); and 5 layers, 0.5 mm fibre spacing, and 0.2 mm thickness

(MD02, desirability: 0.1), see **Figure 4-12**B,C. These three combinations, not in the original DOE run, were created, run, and their results were compared to the software predictions. Average stresses in the leaflet suture edge and belly increased with decreasing thickness, while strain decreased in some regions and increased in others (see **Figure 4-12**D,E). These stress and strain measures were predicted well by the software, with each result falling within the predicted confidence intervals for each response. Additionally, the software correctly predicted an increase in stress in these regions with decreasing leaflet thickness. Strain levels in each of these regions also fall within or very close to the predicted intervals; however, MD02 experienced slightly lower average strain in these regions compared to MD04 and MD03 (MD02: 18.1% suture/20.1% belly, MD03: 21% suture, 20.9% belly, MD04: 21.5% suture/19.9% belly), where the software predicted the strain would be slightly higher than the other two combinations (MD02: 20.5% suture/21.74% belly, MD03: 17.22% suture/16.49% belly, MD04: 16.21% suture/14.37% belly).

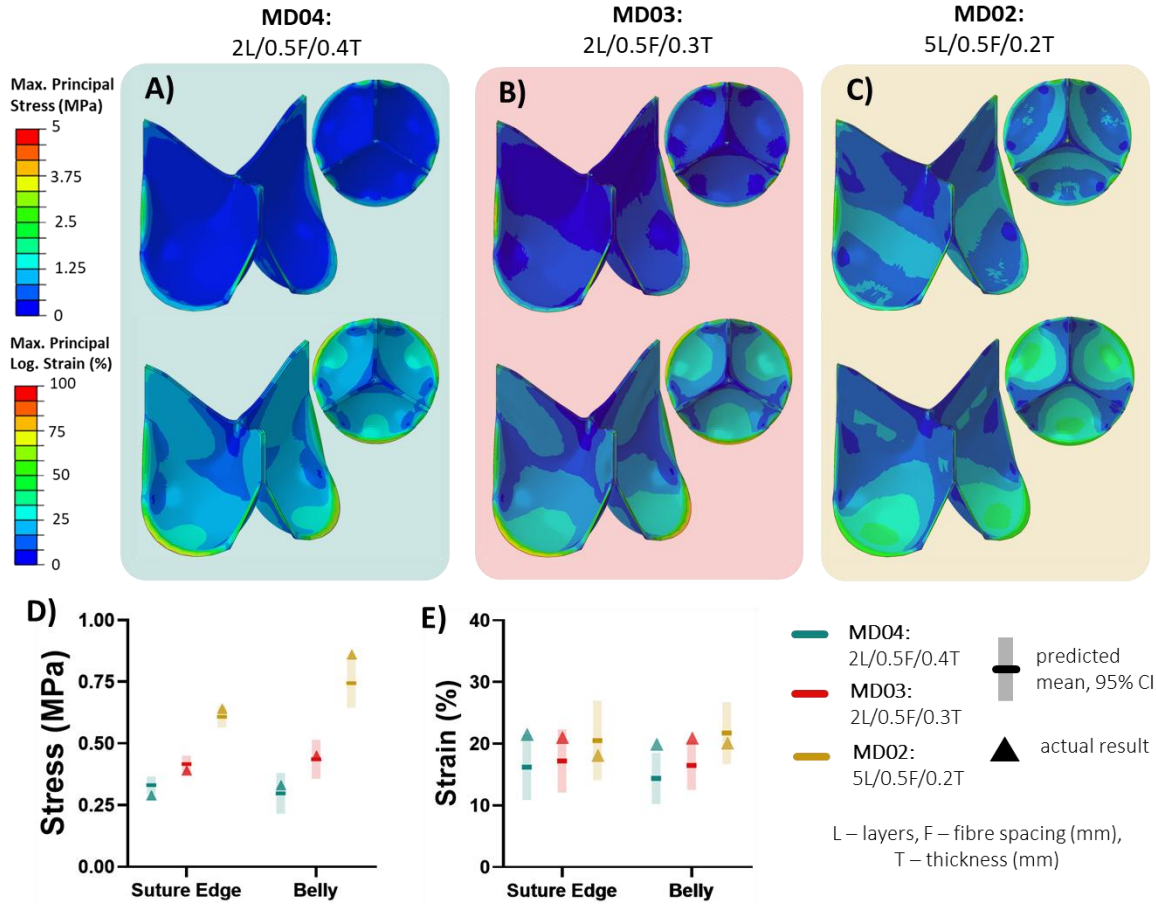

Figure 4-12 *Stress and strain results of three most desirable (MD) combinations: 2 layers, 0.5 mm fibre spacing, 0.4 mm thickness (MD04); 2 layers, 0.5 mm fibre spacing, 0.3 mm thickness (MD03); and 5 layers, 0.5 mm fibre spacing, 0.2 mm thickness (MD02). Visualisations of stress and strain in leaflets for (A) MD04, (B) MD03, and (C) MD02, as well as results compared to DOE predictions for (D) stress in the suture edge and belly regions, and (E) strain in the suture edge and belly regions for all combinations.*

Opening areas across the cycle for each most desirable combination are shown in **Figure 4-13**A. The maximum area reached is similar for each valve (MD04: 4.82 cm^2, MD03: 4.81 cm^2, MD02: 4.7cm^2), while MD02 has a lower average opening area than the other two combinations (MD04: 4.01 cm^2, MD03: 3.89 cm^2, MD02: 3.67 cm^2), see **Figure 4-13**B,C. Additionally, MD02 takes slightly longer than the other two combinations to completely open (MD04: 0.07 s, MD03: 0.084 s, MD02:0.097 s), see **Figure 4-13**D. All three valves reach full closure. These behaviours were predicted well, with all of the results for maximum opening area, average opening area, average closed area, and time to maximum opening falling within the predicted intervals and very close to the mean (see **Figure 4-13**B-D).

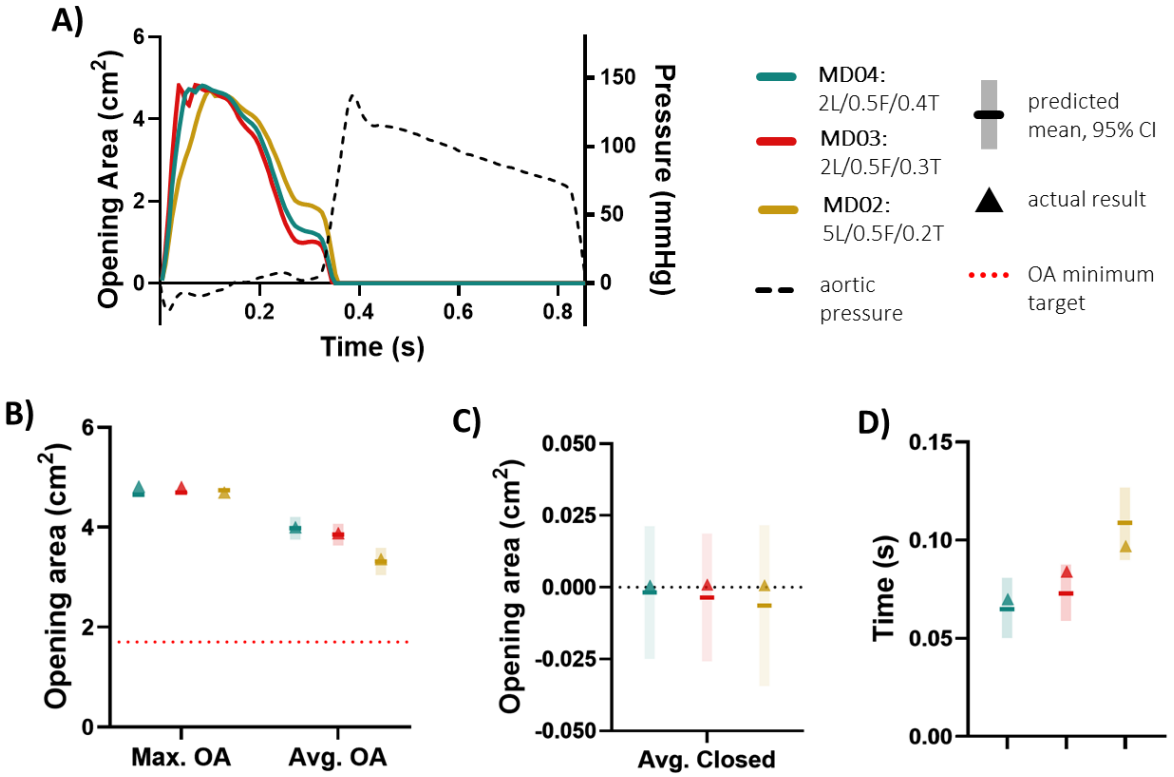

Figure 4-13 *Opening area results for the three most desirable combinations, showing (A) opening areas versus pressure for a cycle, (B) maximum and average opening area results versus predictions, (C) average closed areas versus predictions, and (D) time to maximum opening versus predictions.*

4.4 Discussion

This work presents the development of a trileaflet prosthetic aortic valve model framework to aid in the design of future polymeric aortic heart valves. Using a fibre-reinforcement structure inspired by MEW, we developed a methodology to obtain the mechanical behaviour of fibre-reinforced PDMS and simulate this material in the trileaflet valve model. After showing the positive impact of implementing a bioinspired fibre structure in this leaflet geometry, this methodology was used alongside DOE to determine the best structural combination of a PEEK-like fibre structure manufactured using MEW and embedded in PDMS.

The first step in this framework was to determine the stress/strain response of a fibre-reinforced PDMS in silico using a discrete fibre-reinforced dogbone model simulating a uniaxial tensile test. The response of this composite material is used to calibrate the relevant parameters of the HGO fibre-reinforced model, in-built into the software, which is implemented to describe fibres across the leaflets in the whole valve model. By taking this step and using a constitutive model to describe the fibres significantly reduces computational complexity and simulation time that would be implicated in including discrete fibre inclusions in the valve leaflets. For the load boundary conditions in the valve model, pressure was applied to the aortic and ventricular surfaces according to measurements taken from pulse duplicator testing of size large ACURATE neo2 valves. The pressure curves differ from the commonly referred Wiggers Diagram curve, previously shown in **Figure 2-4**, but they align with others seen in literature on bioprosthetic valves (Armfield et al. 2024; Wu et al. 2019).

We showed the flexibility of this model and the impact of fibre orientations on material response and valve performance by simulating leaflets with varying reinforcement configurations: bioinspired, circumferential, radial, isotropic, and no fibres. These results clearly showed the impact of varying the reinforcement structure, with the radial orientation, isotropic fibres, and matrix only leaflet models experiencing excessively high strains and failing to reach large opening areas quickly. While the bioinspired and circumferential orientation models performed similarly, the bioinspired orientation induced lower peak strain and stress at the suture edge which may help increase overall material lifetimes. Additionally, the results of changing the fibre orientations in the leaflet shows the positive impact of customised, local fibre reinforcement.

These insights into the impact of fibre orientation are corroborated by a study performed on similar leaflet geometry for porcine pericardium by Armfield, et al., where the authors showed higher leaflet displacement for radially aligned fibres compared to circumferentially aligned fibres (Armfield et al. 2024). Additionally, Serrani et al. found a reduction in overall and maximum leaflet strain with an optimised fibre reinforcement structure compared to an isotropic orientation (Serrani et al. 2016).

For the analysis of these valve models, an assessment framework was established to investigate material stress and strain as well as clinically-relevant valve performance metrics derived from the valve's opening area. By developing a set of custom scrips from Python and MATLAB, we were able to extract and process images of the valves allowing us a robust and repeatable methodology to analyse the valve opening area throughout the pressure cycle. Using these methods, the valve modelling framework provided broad insights into leaflet performance to enable future design choices.

Using DOE we were able to determine the impact of the three factors on leaflet and valve performance: fibre spacing (0.5, 1, 1.5, 2 mm), number of layers (2, 5, 8, 10), and overall thickness (0.2, 0.3, 0.4, 0.5 mm). A variety of responses were investigated, including both material behaviour (leaflet stress and strain in the suture and belly regions) and clinically-relevant performance indicators of opening area (maximum OA, average OA, average closed OA, time to maximum OA).

Notably, all of the models achieved good opening areas, far surpassing the 1.7 cm^2 minimum for this size valve in both the maximum OA and average OA (ISO5840-3). Additionally, all of the material combinations reached full closure except the stiffest combination (10 layers, 2 mm fibre spacing, and 0.5 mm thickness). While the material in each of these models may differ in its response, these opening areas suggest that this material at these ranges of stiffnesses are good candidates for enabling effective aortic valves.

Greater differences in the leaflet structural combinations were seen in the stress and strain results, particularly in the belly region. In order to ensure a durable and long lasting material, the stress and strain in the leaflet should be minimised. In addition, the models differed in their time to maximum opening area, particularly for the smaller thickness leaflets, suggesting poorer valve efficiency. Using the DOE results we can see that leaflet thickness had a significant impact on these responses, with a larger thickness leading to reduced stress, strain, and time to maximum opening area. Fibre spacing and number of layers also had a significant impact on the leaflet stress and strain, but in opposing ways: stress is decreased using fewer layers and a larger spacing, while strain is increased by those factors. A larger fibre spacing will also increase time to maximum valve opening.

Notably, there is not one independent factor that impacts valve performance and material response more than the others, all three elicit significant impacts on many of the responses.

Meanwhile, some responses are not impacted greatly by any of the factors. Almost all of the valves fully close, therefore none of the factors alone significantly impacted this. While two combinations of factors did result in a significant correlation to closed area, the actual values of closure are so small that these mean very little.

The overall complexity in how each of the factors contributed to the large number of responses argues for using this DOE approach as it is able to balance the interactions between each of these responses, the desired outcome for each of them (i.e. maximise or minimise), and the weighted importance of them to provide a "most desirable" combination.

We were able to identify the most desirable structural combinations for the leaflets based on the input criteria: minimise stress and strain, maximise maximum and average opening areas,

minimise average closed area, and minimise the time from the start of the cycle to maximum valve opening. Each of these were weighted equally, except for average opening area and average closed area, which were weighted at 2x. The combination with the highest desirability was MD04, with 2 layers, 0.5 mm fibre spacing, and 0.4 mm thickness, which has a desirability of 0.78. Due to the clinical need for a thinner leaflet to maintain a low profile device when crimped, we also identified the best combinations at the two smaller thicknesses: 0.3 and 0.2 mm. MD03 had the same MEW structure as MD04, 2 layers with 0.5 mm spacing, while MD02 had 5 MEW layers and a 0.5 mm spacing. MD03 also had a very high desirability, 0.65, while MD02 performed poorly with a desirability of 0.1.

These most desirable combinations were created, calibrated, and run in the dynamic valve model, and their results showed a close agreement with the software predictions. All of the responses fell within the 95% predicted confidence interval bands, and close to the mean, except for belly strain in the MD04 and MD03 models whose actual values were slightly above the maximum predicted. Additionally, while all other strain results fell within the bands, it was predicted that MD02 would experience higher strains than MD04 and MD03 which was not the case. Outside of strain, the rest of the responses were predicted very well, including both maximum and average opening area, average closed area, time to maximum area, and average stress.

Notably, the most desirable combination was 0.4 mm in thickness, which is thicker than porcine pericardium used in many self-expanding TAVR valves (Armfield et al. 2024; Bruschi et al. 2013). MD03 achieved similar but overall slightly worse results to MD04 across all categories, which suggests that in order to maintain a low device profile with thinner leaflets there is a necessary trade-off with the mechanical response of the material. From these results and taking into account the industrial need for thinner leaflets, the best combination from this dataset is likely MD03, as it is the thinnest option with the least compromise on material response.

An interesting observation throughout these models, not investigated in the DOE analysis, is the presence of a second opening area peak just before valve closing in some of the models. This secondary peak occurred in 8 of the 12 unique combinations and does not seem to be dependent solely on layer number, fibre spacing, or leaflet thickness. Its presence is due to an increase in applied ventricular pressure, dropping the resultant aortic pressure close to zero, before a drop in ventricular pressure which causes closure. This is possibly an artifact of the specific pressure curves used, but may indicate leaflet combinations that are more responsive to pressure changes, potentially indicating a more efficient valve. Looking at time to maximum

opening, all of the valves which opened in less than 0.084 s (the median opening time) experienced a notable second peak.

This work does contain limitations. First, there is no inclusion of a frame in the model. It is known that the frame displaces under leaflet loading, which would impact the stress and strain in the leaflets (Armfield et al. 2024). There is also a potential that this could impact the valve opening area and induce pinwheeling, but that would need to be studied. On the same theme, fluid is not included in the model, which is also likely to impact the same behaviours. While future work should investigate the impact of frame deflection and the difference with fluid inclusion, it is unlikely to change the DOE outcome as all the leaflet combinations are compared relative to each other. Second, the fibres were modelled as a linear elastic PEEK-like material with no yield included. While PEEK is a stiff polymer, it also has a low yield strain (Shrestha et al. 2016). Future work should look at the impact of this, and investigate using PCL as this is the most used and accessible material used for MEW. Additionally, the GOH model is used to describe the fibres in the leaflet material rather than including discrete fibres. This could impact the material behaviour, especially with combinations containing larger pore sizes as it will not be able to replicate local stiffening in one area and an unreinforced region elsewhere. However, using this material description greatly reduces model complexity and, more than likely, the average affect across the leaflet and valve is maintained. The use of this model requires further validation. On the DOE itself, some factor combinations would not be physically possible to manufacture. For example, while a 10-layered structure made of 20 μm-diameter fibres could theoretically be embedded within 0.2 mm of silicone, this would not be possibly physically using MEW due to the high peaks formed when fibres overlap, resulting in a total thickness in these regions of greater than 0.2 mm. This would also pose manufacturing challenges for structures with 8 layers at the same total leaflet thickness.

Overall, this framework proved to be a successful methodology for identifying the best combination of MEW-based structural features and leaflet thickness for the ranges investigated and materials used. By utilising a fully in silico approach, it removed the need for manufacturing leaflets, assembling valves, and testing these devices, significantly reducing time spent identifying the best combination. While these results only hold for the materials investigated in this study, the same methodology can be applied to different materials to identify the best structural combinations for a variety of material combinations. Ultimately, this is a highly valuable tool that can allow researchers the ability to probe potential material combinations to identify the best structures for in vitro testing. Additionally, its versatility allows the investigation of a variety of factors. While layers, fibre spacing, and thickness were investigated here, other factors can be explored such as fibre diameter, matrix stiffness, and

even MEW processing parameters. The value of linking FE methods with DOE allows for the exploration of numerous variables, while minimising time spent manufacturing and testing the chosen combinations.

Chapter 5 Optimisation of a fibre-reinforced polymer leaflet valves using a fibre reorientation algorithm

5.1 Introduction

In Chapter 4 we optimised the structural combination of silicone and MEW fibres, but we also highlighted another aspect of potential leaflet improvement: fibre orientation. It was seen that fibre orientation impacts the stress and strain induced in the leaflet, and that leaflet behaviour can be tailored by adjusting the local fibre structure. Favourable results were obtained with the customised, bioinspired fibre structure, but due to the structural differences between a native aortic valve leaflet and the commercial leaflet investigated here, there is likely to be a more effective reinforcement structure for this particular geometry.

Finite element modelling-based fibre remodelling algorithms have been used previously to accurately predict collagen fibre structure in leaflet tissue and tissue-engineered valves (Driessen et al. 2008; Loerakker et al. 2013; Sesa et al. 2023). In one set of studies, a remodelling algorithm was developed to understand collagen fibre deposition and remodelling under load in native aortic valve leaflets; this was subsequently used to predict collagen fibre deposition in tissue engineered heart valves (Driessen et al. 2007; Driessen, Bouten, and Baaijens 2005). A later iteration of this algorithm was used to closely predict the native aortic leaflet fibre structure and presence of multiple fibre families in the leaflet belly (Driessen et al. 2008). In a more recent study, Sesa et al. developed an algorithm to predict collagen growth over time in tissue engineered heart valves to inform future device development (Sesa et al. 2023).

These fibre remodelling algorithms identify the optimal reinforcement structure for the tissues and structures they are applied to, and, therefore, should be used to inform development of novel devices. While they have been used to predict the growth and remodelling of collagen over time, what they are typically doing is simply reorienting fibres within a material in response to an applied load. Knowing this, the same methods can be applied to identify an optimal reinforcement structure for prosthetic leaflets. Serrani, et al. published an application of a similar algorithm for the determination of optimal fibre reinforcement in a polymeric leaflet (Serrani et al. 2016). This valve, the PoliValve, is composed of a novel block copolymer whose

blocks provide mechanical support to the material when aligned with the principal stress. In this work, they presented a matlab-based procedure that determines the optimum load bearing direction throughout their leaflet design. However, this is only indicative of a single family of fibres, does not take into account dispersion, and cannot be extrapolated to another shape.

The aim of this work is to determine the optimum fibre-reinforcement structure in our polymeric leaflet by performing fibre reorientation using one of these algorithms. We also investigated the effect of fibre dispersion on this leaflet performance, as well as the application of a non-uniform orifice shape.

In this work we adapted and applied the code developed by Creane, et al., which was used to accurately predict fibre alignment and dispersion in carotid bifurcation models (Creane et al. 2011). The material description in this algorithm is based on the GOH model which is already used to define our fibre-reinforced polymer material, allowing seamless application of this procedure into the existing models. Using this fibre algorithm, we investigated fibre reorientation with two different methods, with and without fibre dispersion, and compared results to the dynamic bioinspired model. Additionally, we applied it to a leaflet model with an irregular orifice shape to investigate the utility of using this kind of method in patient-specific models.

5.2 Methods

5.2.1 Single leaflet model

To improve computational efficiency, the Trileaflet dynamic model introduced in Chapter 4 was simplified to a single leaflet with a static pressure applied. This model included the same leaflet and frame surface geometries previously described and all of the leaflet suturing steps were maintained. After suturing, a static pressure was applied to the aortic surface of the leaflet and maintained during fibre reorientation. To simulate the other two leaflets, two flat, symmetrical barriers were implemented; these were defined as surfaces and meshed with 765 SFM3D4 elements. After loading and fibre reorientation, pressure was removed and the leaflet underwent flattening steps to enable extraction and visualisation of the new fibre orientations. These flattening steps first pressurised the leaflet from the ventricular side to open it, then displaced the edges towards a plate, and finally pressurised the leaflet against a plate. Like the barriers, this plate was modelled with 2700 SFM3D4 elements and positioned at the leaflet starting point. Overall, the model included 8 steps: 3 to suture the leaflet, a pressure application step, fibre reorientation, and a further 3 steps to flatten the leaflet, see **Figure 5-1**.

.

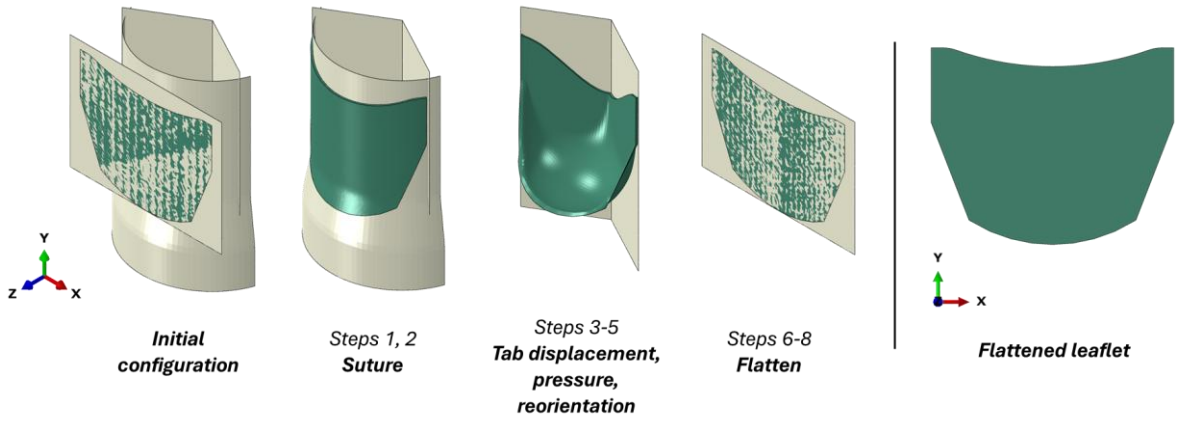

Figure 5-1 *Visualisation of leaflet suturing, pressurisation, reorientation, and flattening steps for single leaflet model.*

For material properties and geometry, we simulated the MD03 model described in 0: a 0.3 mm-thick silicone leaflet reinforced with a PEEK-like MEW mesh of 2 layers with a 0.5 mm fibre spacing. The material model parameters input were C10: 0.2 MPa, k1: 0.127 MPa, k2: 1.088. For pressure application, the dynamic implementation of this leaflet experienced the highest stress and strains when the resultant aortic pressure was 137.25 mmHg, or 0.0183 MPa. This pressure was applied in the pressure step and maintained for fibre reorientation.

The model was run using Abaqus/Standard solver, and each step was Dynamic, Implicit with Quasi-Static loading.

5.2.2 Reorientation algorithm

To perform fibre reorientation, the algorithm developed by Creane et al. was adapted and implemented (Creane et al. 2011). In brief, this procedure is applied to a fibre-reinforced material, and, under loading, the algorithm reorients the fibres in order to minimise strain. The material is described using an adjustment of the GOH model (Gasser et al. 2006), with the fibre orientation modelled as a 2D fan splay within a 3D continuum. The fibre family geometry, H_{fam_i}, is described by:

$$H_{fam_i} = \kappa\, I_{3D} + (1 - 2\kappa)\left(\overline{A_{fam_i}} \otimes \overline{A_{fam_i}}\right) - \kappa\left(\overline{B_{fam_i}} \otimes \overline{B_{fam_i}}\right)$$

$$0 \leq \kappa \leq \frac{1}{2}$$

Where κ is fibre dispersion, I_{3D} is the 3D identity matrix, A_{fam_i} is the unit vector of mean fibre orientation, and B_{fam_i} is a unit vector perpendicular to the plane of dispersion. H_{fam_i} can be visualised as an ellipsoid, described by its eigenvectors ($\boldsymbol{d}_i$) and eigenvalues (h_i) which form its principal axes:

$$H_{fam_i} = \sum_{i=1}^{3} h_i(\boldsymbol{d_i} \otimes \boldsymbol{d_i})$$

$$h_1 \geq h_2 \geq h_3$$

Mean fibre orientation, A_{fam_i} , is reoriented according to the strain in the material, see **Figure 5-2**A. The strain stimulus used here is the Green-Lagrangian strain tensor (E), which can be described by its eigenvectors (e_i) and eigenvalues (v_i):

$$E = \sum_{i=1}^{3} v_i(\boldsymbol{e_i} \otimes \boldsymbol{e_i})$$

$$v_1 \geq v_2 \geq v_3$$

During fibre reorientation, A_{fam_i} will be reoriented according to the directions and magnitude of the principal strain components. Optimum direction of fibres was defined using two different approaches, method 1 (M1) and method 2 (M2), which are described in sections 5.2.2.1 and 5.2.2.2.

Fibre reorientation is performed iteratively, with the rotation of fibres to the optimum direction in each iteration described by:

$$\frac{d\beta}{dt} = c[1 - \cos(\alpha)]$$

Where β is the rotation angle, t is an iteration, c is a rate constant, and α is the angle between the current principal direction and the optimum direction. The rate constant, c, is set by the user. Here, it is limited at 15 degrees as this was the largest change that could be applied without causing convergence problems in the model. Iteration number is set by the user also, and care should be taken to ensure sufficient number of iterations to achieve the correct solution. Here, 1,200 iterations enabled the reoriented fibre tensor components to fall within 5% of the optimum solution.

As part of the algorithm, fibre dispersion, κ, is also optimised; it is defined by:

$$\kappa = \frac{1}{2}\frac{v_2}{v_1}$$

The bounds of κ are 0 and ½, with 0 representing no dispersion of fibres and ½ as full dispersion, i.e. isotropic. All of the models were run both without (κ =0) and with dispersion.

As a starting point, the initial fibre orientations in the model were defined to be isotropic. To ensure the initial conditions would not impact the final solution, a model with an initial circumferential orientation was also run for comparison.

5.2.2.1 Reorientation method 1

The first reorientation method, M1, is defined in the original publication. In this method, the two optimised fibre families are oriented symmetrically about the direction of maximum principal strain at an angle, θ, determined by the magnitude of middle and maximum principal strain:

$$\theta = \tan^{-1}\frac{v_2}{v_1}$$

Where θ has a minimum value of 0° and maximum of 45°. This angle is used to calculate the new fibre vectors:

$$A_{fam_1} = \cos\theta e_1 + sin\theta e_2$$

$$A_{fam_2} = \cos\theta e_1 - sin\theta e_2$$

A visual depiction of these orientations is shown in **Figure 5-2**B.

5.2.2.2 Reorientation method 2

The second orientation method, M2, aligns fibres with the principal strain directions: family 1 is aligned with the maximum strain direction, while family 2 is aligned along the middle principal strain direction. These fibre orientations are visualised in **Figure 5-2**C.

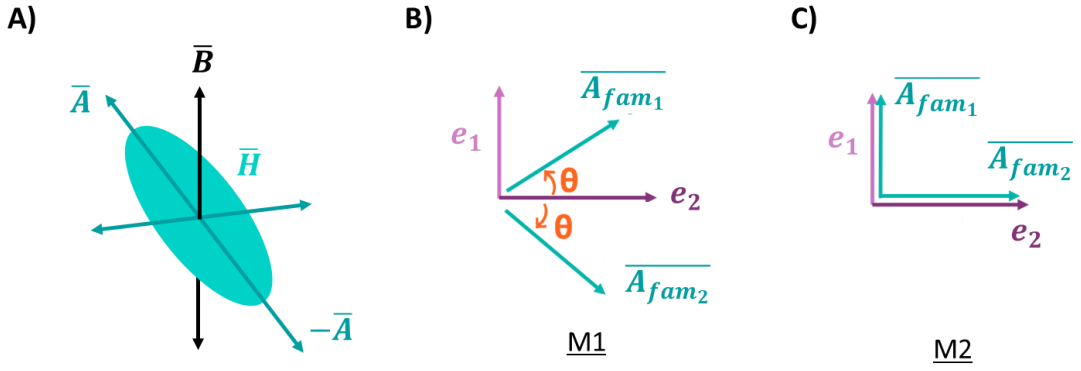

Figure 5-2 *Representation of fibres in reorientation algorithm showing A) visualisation of fibre splay and components, B) fibre orientations in reorientation method 1, and C) fibre orientations in reorientation method 2.*

5.2.3 Implementation in dynamic model

Reoriented fibre structures were applied in the dynamic valve model described in Chapter 4. To conform to that model, local fibre patterns were averaged within the 56 regions previously described.

5.2.4 Asymmetric orifice model

To evaluate wider applications and benefits of custom fibre reorientation, a model with a non-uniform orifice shape was developed to serve as an example of a diseased patient with

calcified tissue, as the calcifications would cause the device to take on an asymmetric shape. This was implemented by adjusting the single-leaflet model: a displacement (U1=2 mm) was applied to one side of the frame to perturb the shape, see **Figure 5-3**. Location of the barriers was also shifted to represent the new centre point of the valve. Pressurisation and reorientation were applied as normal.

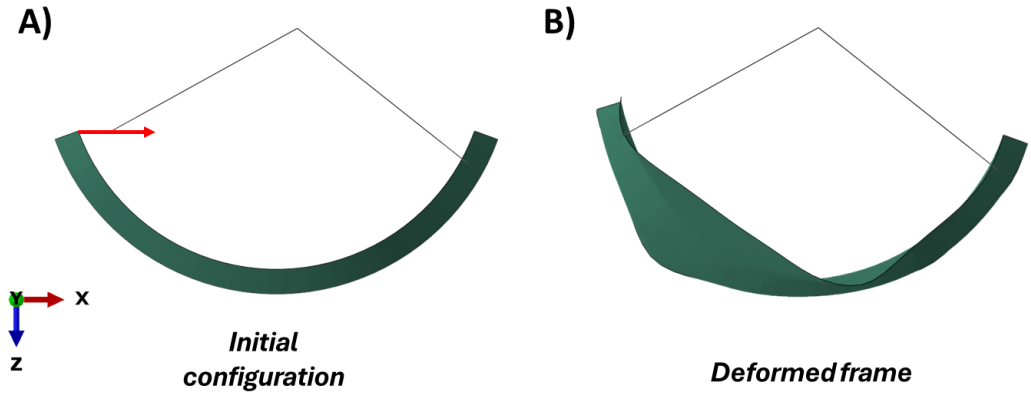

Figure 5-3 *Deformation of frame to form asymmetric orifice, showing A) initial frame shape and arrow indicating location of displacement boundary condition, and B) the frame shape after displacement.*

5.3 Results

5.3.1 Fibre reorientation

Fibre reorientation was performed on leaflets with isotropic and circumferential initial fibre configurations. After reorientation the percent difference in average stress and strain in these models was 3.03% and 3.10%, respectively, verifying an independence of the results from the initial conditions.

Figure 5-4 shows the visualisation of leaflet strain, stress, and fibre orientation from the two different reorientation methods, M1 and M2, with and without fibre dispersion. In both methods, leaflet strain is visibly decreased compared to the initial isotropic configuration. Stress visibly increases with fibre reorientation, but still remains low; high peak stresses can be seen at the bottom commissure edge.

After reorientation from M1, the configurations of the two families are very similar, with the most noticeable differences at the centre and belly of the leaflet. Both families are aligned in a predominately circumferential orientation at the sides that gradually becomes more radial towards the leaflet midline. Fibre family 1 resulting from M2 looks similar to the families in M1, while family 2 results in a completely different configuration. Notably, the fibres in the free edge towards the commissures — in the region where the leaflet is in contact with the barriers — are oriented out of plane, through the thickness of the leaflet. Additionally, where the fibres in family 1 take on a more circumferential configuration, the fibres in family 2 are predominately radial, and vice versa.

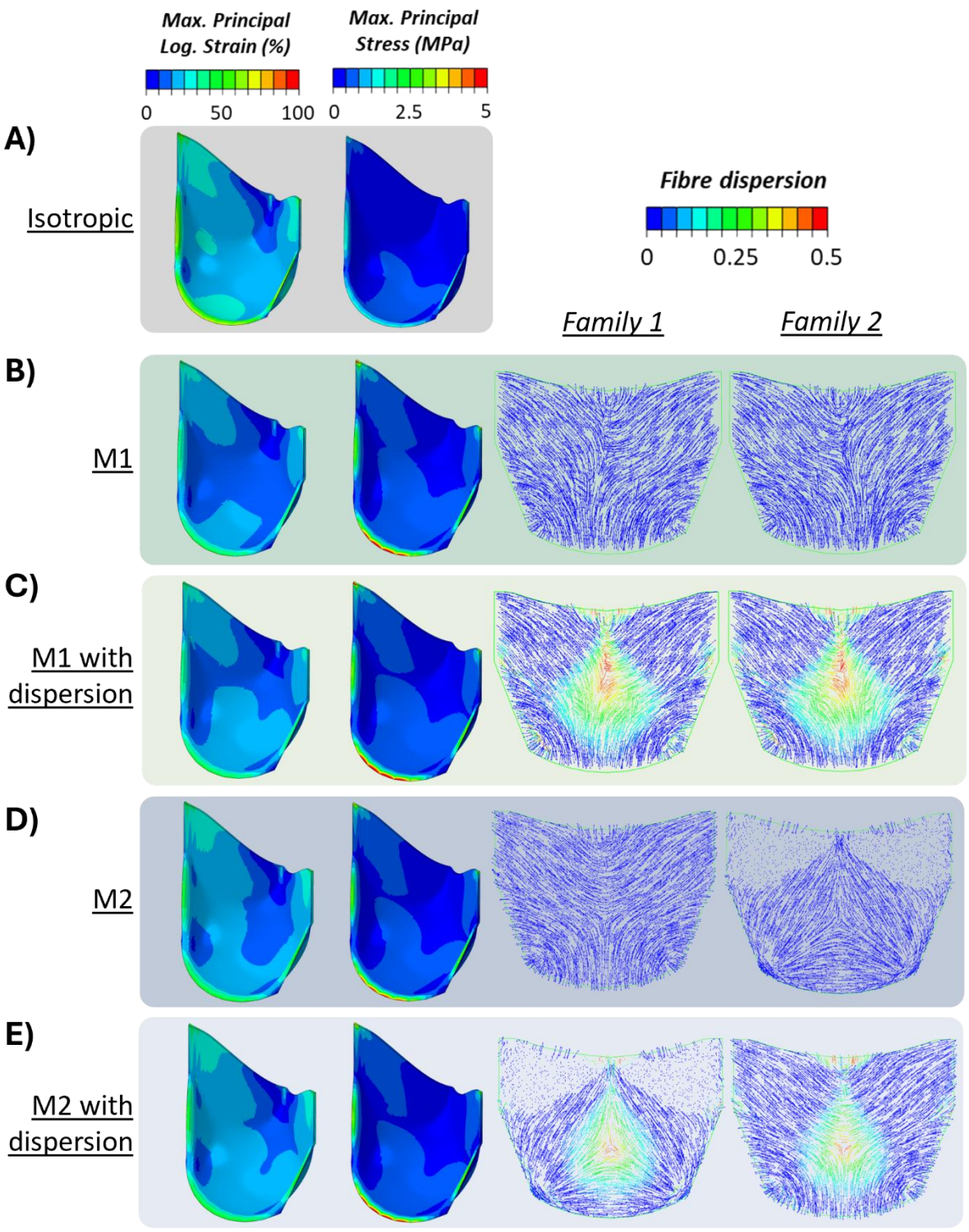

Figure 5-4 *Results of reorientated leaflet models, showing (A) stress and strain in the pressurised isotropic leaflet before reorientation, and stress, strain, and fibre orientations in (B) M1 without dispersion, (C) M1 with dispersion, (D) M2 without dispersion, and (E) M2 with dispersion.*

Where implemented, fibre dispersion was at its maximum (i.e. isotropic fibre alignment) in the centre of the leaflets and not present at the sides and sutured edges. Locations and magnitude of dispersion were similar in both methods, but the placement of the fully isotropic region was slightly higher in M1 than M2.

Additionally, both leaflets have an isotropic region in the centre of the free edge at the very edge elements. This location corresponds to where the leaflet is bent between the two barriers.

Average stress and strain in the leaflets is shown in **Figure 5-5**. Following what was seen visually, there is a decrease in strain from the isotropic configuration to the reorientated configurations. From isotropic (22.4% average strain) to M1 (16.1% average strain), there is a 28.4% decrease in strain magnitude, compared to an 18.5% decrease in M2 (18.3% average strain). Average stress increased in the reoriented models, with a 36.4% increase and 24.4% increase for M1 and M2, respectively (isotropic: 0.33 MPa; M1: 0.45 MPa; M2: 0.41 MPa).

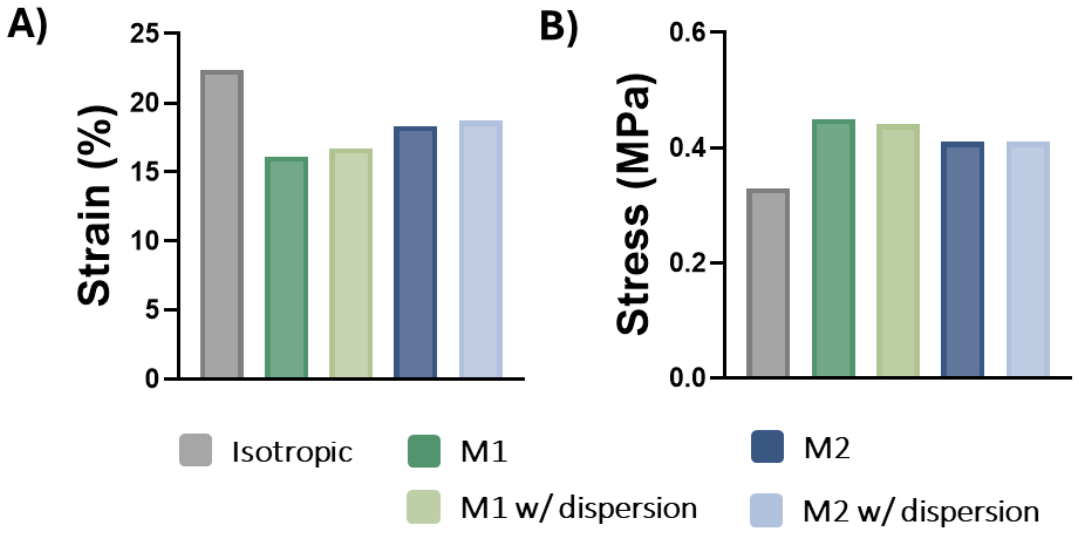

Figure 5-5 *Results of average (A) stress and (B) strain in the isotropic leaflet and all reorientation methods*

5.3.2 Dynamic implementation

Both M1 and M2 reoriented fibre patterns without dispersion were applied to the dynamic trileaflet valve model described in Chapter 4. Average fibre orientation within each partition was assigned. For fibre family 2 in the M2 configuration, the regions where the reoriented fibre direction was through the thickness of the sample were given the same fibre orientations as fibre family 1.

Results of the dynamic models and fibre orientations compared to the original bioinspired configuration are shown in **Figure 5-6**. Across the leaflet models, there is a clear visible decrease in strain between the bioinspired and reorientated structures, particularly in the

lower belly region. Stress visibly increased with leaflet reorientation, although maintained a low magnitude across the leaflet. Notably, the valves are still functional, achieving full closure and large opening areas. Difference in average OA was negligible between the three models, with the bioinspired, M1, and M2 models reaching 0.98 cm^2, 1.03 cm^2, and 1.00 cm^2, respectively.

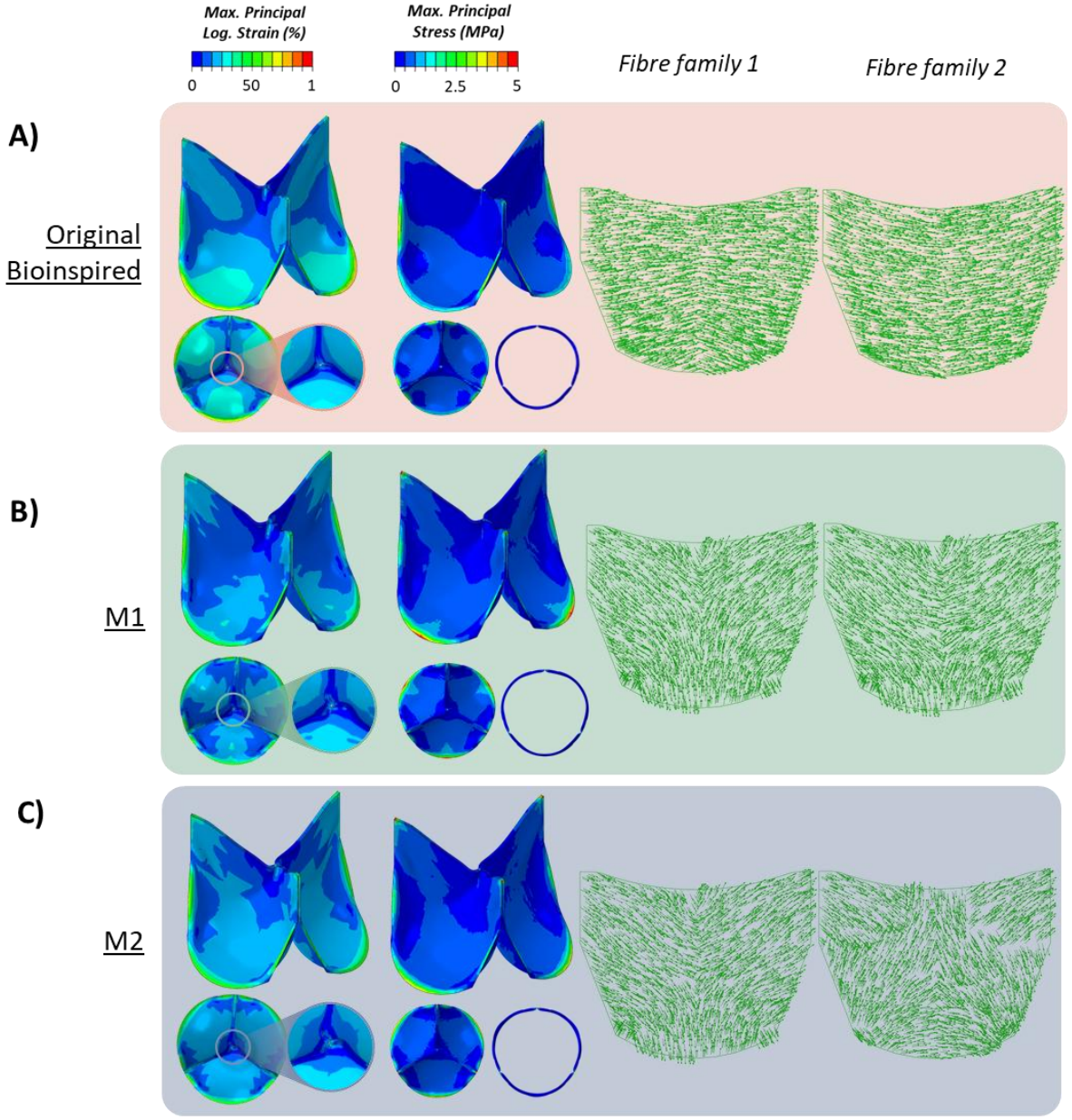

Figure 5-6 *Comparison of dynamic valve models' strain, stress, and fibre orientations in the (A) original bioinspired structure, (B) M1 structure, and (C) M2 structure.*

Looking at the average strain values across the leaflets, there was a decrease from the bioinspired orientation to the two reoriented ones, resulting in a 20.1% decrease in M1 and 11.1% decrease in M2, see **Figure 5-7**A. Strain distribution across the elements is similar in all three models, with M1 and M2 having slightly fewer elements reaching higher bands of strain (>30%) compared to the bioinspired configuration, see **Figure 5-7**B. Both reoriented configurations resulted in a 19.4% increase in average leaflet stress compared to the bioinspired leaflet, see **Figure 5-7**C. Additionally, the reoriented leaflets had more elements reaching high stresses (>0.6 MPa) compared to the bioinspired leaflet, see **Figure 5-7**D.

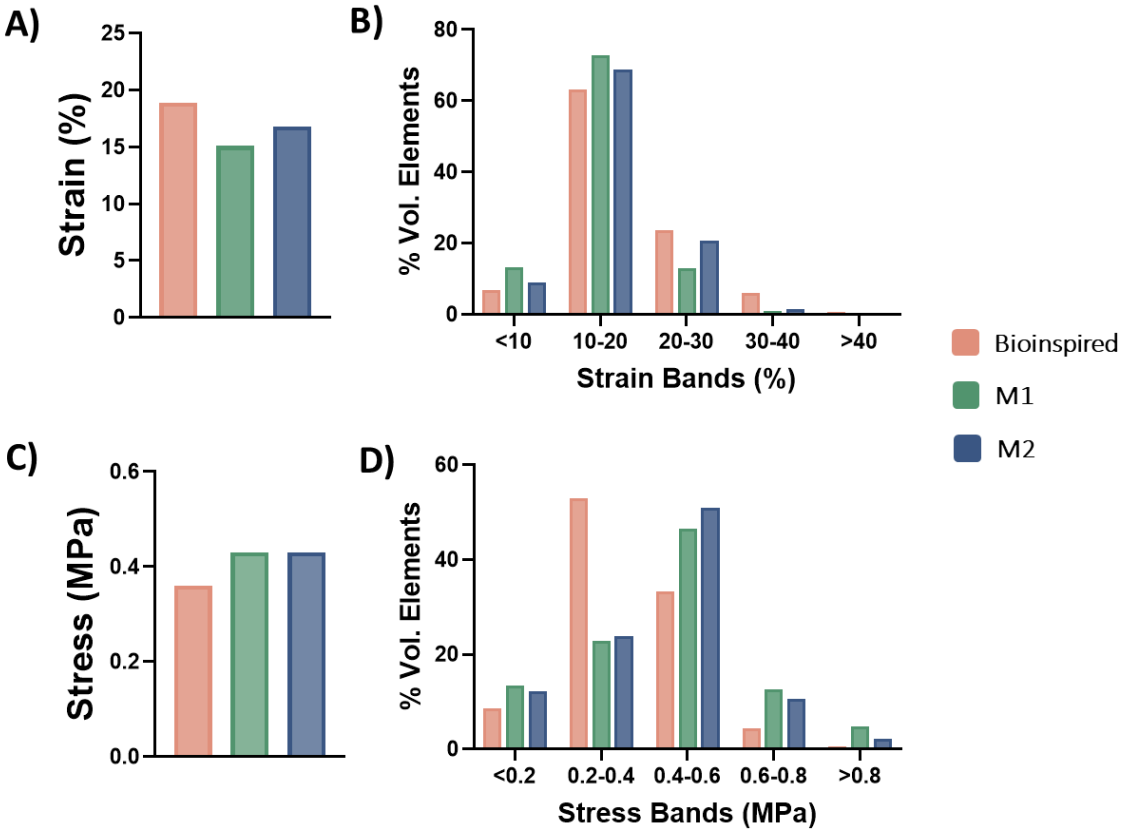

Figure 5-7 *Results from dynamic valve models showing A) average strain in the leaflet, B) volume percent of elements within various strain bands, C) average stress in the leaflet, and D) volume percent of elements within various stress bands.*

5.3.3 Asymmetric orifice model

Reorientation was applied to a single leaflet in an asymmetric orifice shape according to method M2 and including fibre dispersion. **Figure 5-8** shows the results of this model before and after fibre reorientation is applied. With a 2 mm displacement on one side of the frame, a clear perturbation in the leaflet strain was induced, and a slight asymmetry in the stress is apparent (see **Figure 5-8**A). After fibre reorientation, the strain field becomes much more symmetrical between the left and right sides of the leaflet (see **Figure 5-8**B). Strain magnitude in the leaflet also decreases by 16.2%, falling from an average strain of 24.5% to 20.6% in the

reoriented leaflet. On the other hand, stress in the leaflet maintains more apparent asymmetry, and the overall stress in the leaflet increases by 21.4% from 0.37 MPa to 0.45 MPa.

New fibres orientations are shown in **Figure 5-8**C. Visually, the orientations are similar to the symmetric model in most of the leaflet. However, at the bottom edge of the leaflet, there appears to be slight differences between the left and right sides, and the line of symmetry between the two sides has shifted slightly left.

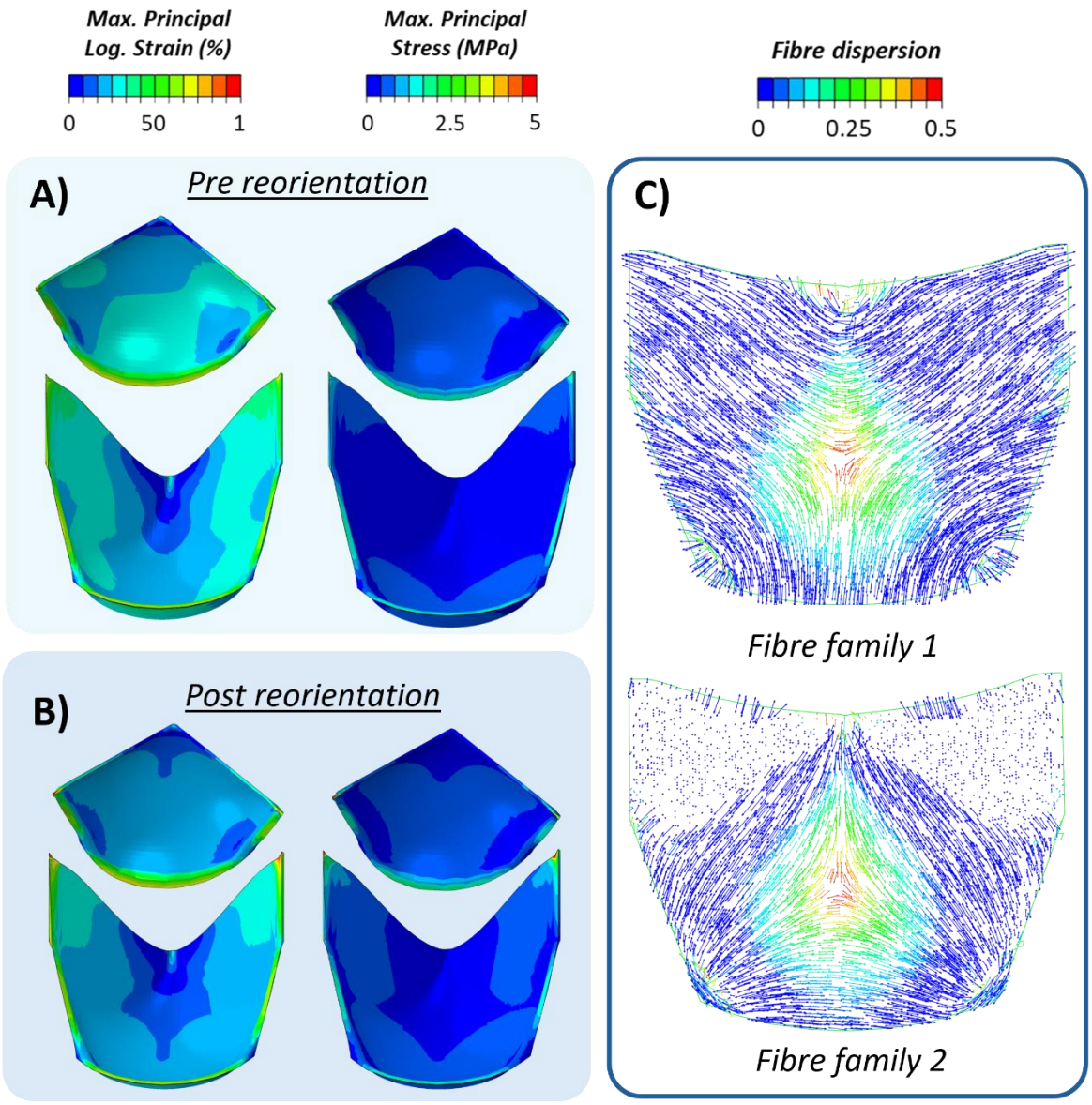

Figure 5-8 *Results of asymmetric orifice model, showing the stress and strain in the leaflet A) before and B) after fibre reorientation, and C) the optimised fibre orientations.*

5.4 Discussion

In this work, a fibre reorientation algorithm previously developed for carotid bifurcation geometries was successfully adapted and applied to a leaflet model to obtain an optimised fibre reinforcement structure (Creane et al. 2011). The objective of this algorithm was to minimise strain in the leaflet by reorienting fibres according to the principal strain directions. Two methods of reorientation of two fibre families were investigated: orientating symmetrically about the direction of maximum principal strain (M1), and orientating along the maximum and middle principal strain directions (M2). This work has shown the benefit of using this kind of optimisation approach, as well as the versatility of this algorithm. Using this methodology, we have optimised the fibre reinforcement structure in this leaflet shape, investigated the impact fibre dispersion on leaflet outcomes, and shown the benefit of using this kind of method in non-uniform orifice shapes.

The objective of this algorithm was to minimise strain in the material based on the assumption that regions of high strain will promote later failure of the material. While the material needs to deform enough to allow valve closure, too much deformation could lead to excessive pinwheeling or leaflet prolapse. As was discussed in Driessen et al 2008, a strain-based function is more likely to provide accurate results for this particular shape and loading. However, the results for this leaflet model are unlikely to change significantly with a stress-based approach as the directions of maximum principal stress are along the same lines as maximum principal strain.

To implement the reorientation algorithm, the trileaflet model was simplified to a single leaflet with barriers. This was to allow modelling using Abaqus/Standard solver as the reorientation algorithm code is compatible with this, and to increase computational efficiency. While simplification of the model removes the complex interactions between the three leaflets, it did not greatly affect the overall strain or stress in the leaflet, impacting the results of the isotropic leaflet by less than 5%. Using this model, we performed fibre reorientation according to the two methods. The algorithm worked as anticipated: the resulting strain after fibre reorientation was decreased in both methods.

Additionally, the impact of fibre dispersion was investigated. Dispersion was calculated and implemented according to the magnitude of middle to maximum principal strain: the more similar the magnitudes became, the higher the fibre dispersion. After applying the algorithm, in both methods the centre of the leaflet had dispersed fibres. In each there was a small region of fully isotropic fibres, due to the multiaxial loading of the leaflet in this area, which gradually became less dispersed towards the sides and bottom of the leaflet. However, the addition of

fibre dispersion did not greatly improve leaflet outcomes, instead leading to negligible increases and decreases in leaflet strain and stress, respectively. This has a positive impact on potential manufacturing as it will reduced complexity in the creation of fibre structures.

In M1, the two reoriented fibre patterns resemble what we know and have seen in the native leaflets in Chapter 3: at the commissures, fibres are aligned mostly circumferentially but with a tilt towards the middle and belly of the leaflet. However, we see a departure from the native leaflet structure in a shift to a radial alignment along the midline and at the bottom belly and suture edge. Fibres in family 1 from M2 have a very similar structure to both families from M1, but the second family in M2 is very different from the others. This disparity between methods is due to how the optimum directions are determined. In M1 the fibres align symmetrically about the direction of maximum principal strain, at an angle defined by the ratio of magnitude of middle to maximum principal strain. Since the maximum principal strain is much higher than the middle for most of the leaflet, the fibres will align very closely with this direction, which is also the direction assigned to the first family of M2. Fibre family 2 in M2 is aligned with middle principal strain which is normal to maximum strain, giving the results which are seen here.

While it may be logical to think that reinforcement of the leaflet structure in two different directions would provide improved support for the leaflet, it was seen in the single leaflet models that M2 did not reduce leaflet strain as much as M1, and did not decrease stress in the leaflet significantly compared to M1 either. This follows what we know about the native leaflet structure: although there is a variety of fibre orientations present, the fibres bundles are still usually aligned in similar directions. There is certainly a greater difference in fibre bundle orientations in the belly of the leaflet, but elsewhere the fibre families are much closer aligned.

The reoriented fibre patterns were implemented in the dynamic trileaflet model described in Chapter 4. To conform to that model, the local fibre patterns were averaged within the 56 regions previously described. Additionally, where fibres were defined to align out of plane, through the thickness of the leaflet in family 2 of M2, they were given the same orientation as the corresponding regions in family 1. This model is intended to predict the response of manufactured leaflets and fibres cannot be created in the through-thickness orientation described using MEW. Due to this limitation and the need of the model to have two fibre families present, the fibre orientations were adjusted in this way.

Comparing to the original bioinspired configuration in the dynamic model further confirms the benefit of using this fibre reorientation algorithm as the overall leaflet strains were reduced while the valves as a whole remained functional. Leaflet stress was increased with the new fibre configurations, but as was seen in the single leaflet model, the magnitude of average stress remained low. In M1, higher stress is seen around the bottom suture edge of the leaflet,

but, unlike much of the rest of the leaflet, this is reduced in M2. This may show that while on the whole the M2 configuration is less favourable than M1, having a more isotropic configuration of fibres at the edge may improve outcomes.

Leaflet calcification is a common feature of aortic stenosis and can severely impact valve functionality (Whelton et al. 2024; Willner et al. 2023). Due to the obstruction of the annulus, valve frames often do not take on a circular shape, as they are designed to, which can lead to poor outcomes such as paravalvular leakage (El Faquir et al. 2022; Musallam et al. 2022). The shape that the frame takes once implanted will ultimately impact the loading of the leaflets, potentially causing uneven deformation across the material, which could lead to earlier failure. In this work, we showed the potential benefit of using this fibre reorientation algorithm for designing patient-specific leaflets which account for an asymmetric orifice shape. By applying a deformation to one side of the frame, we showed the clear impact of a non-uniform orifice shape on the leaflet strain, causing an unbalanced deformation on one side of the leaflet. After applying the M2 fibre reorientation algorithm in this specific loading condition, the strains in the leaflet were reduced and balanced between the two sides, something which could potentially extend material lifetime. While the fibre structure appeared similar to the uniform leaflet, there were slight changes in the orientations at the bottom edge, which is the region impacted most by the orifice shape change.

This work has highlighted the benefit of optimising the fibre structure for specific leaflet shapes and orifice shapes. While designing a fibre structure based on the native leaflet provided a well-functioning valve, by optimising the fibres for this particular leaflet shape we were able to obtain an even better structure to potentially extend material lifetimes. Taking inspiration from the native leaflet structure provided a good baseline for design, but there are key differences in the native leaflet shape and structure that impact the loading and therefore optimal reinforcement configuration. First, the shape of the native leaflet is different from the commercial leaflet: where the free edge is convex, curving upwards, the commercial leaflet has a concave edge, curving in towards the centre of the leaflet. This edge structure impacts the fibre directions at the top of the leaflet and the commissures, because while the native leaflet has fibres that point upwards towards this edge, the commercial leaflet shape does not need this. Secondly, the native leaflet has a variable thickness, measuring upwards of 1 mm at the base and decreasing in thickness towards the free edge. The commercial leaflet is currently designed with a uniform thickness which would change the fibre patterns best for reinforcement. Finally, and importantly, native leaflets have a seamless connection to the aortic wall allowing efficient load transfer between the materials. In the case of this device, the commercial leaflets are sutured onto a frame, and in particular in these models, have a hard,

immovable boundary that would increase stress in this region. Due to this, the commercial leaflets may need a reinforcement structure to mitigate these high stresses and strains, where the native leaflet does not need this. This is seen in particular at the bottom suture edge of the leaflet, where the optimised patterns highlight a need for more radial fibre alignment which is not seen in native leaflets.

These differences are also seen in other studies applying fibre remodelling/reorientation on leaflets (Driessen et al. 2008; Serrani et al. 2016). In both of these leaflets, the optimised fibre orientations through the leaflet midline are far more circumferentially aligned than what was seen here. Particularly, in the structure optimised by Serrani et al. there are no radially aligned fibres in the belly of the leaflet. This clearly highlights the specific nature of fibre orientation optimisation and how much it can change between leaflet shapes, loading, and materials.

Ultimately, this approach can be used to tailor leaflet designs for specific leaflet and frame geometries, as well as an expansion to patient-specific designs. By creating leaflets that maintain functionality while maximising material lifetimes, next-generation prosthetic valve devices can be greatly improved.

This work does contain limitations. First, fibre reorientation is performed on a single leaflet model rather than the whole trileaflet valve. Here, the leaflet contact is simplified by using two static barriers, removing any potential impact from the two other. While this could potentially impact the reoriented fibre directions, it is unlikely to change significantly as we have seen there is a less than 5% difference in average stress or strain between the two configurations. Another limitation of this is the translation of reoriented fibre pattern from the single leaflet model to the trileaflet valve model: the fibre orientations were averaged over a local region rather than applied element by element. This was due to the setup of the dynamic model, which allows fibre definition for these discretised regions only, and to enable translation to future manufacturing of the fibre structure. Visually, the single-leaflet fibre orientations were well represented by the dynamic leaflet, and the average stress and strains in the leaflets were very similar. This, however, highlights an area for potential future study to investigate decreasing or increasing the size of the discretised regions. Finally, while it was assumed that reducing strain in the leaflet would increase material lifetimes, the long-term fatigue of this fibre-reinforced material is unknown and would need to be understood to generate any reliable conclusions on lifetime expectancy.

Chapter 6 Comparison of finite element predictions to benchtop testing of fibre-reinforced materials

6.1 Introduction

In earlier chapters we used finite element (FE) modelling to show the potential of a tuneable MEW fibre-reinforced elastomeric material for use in future polymeric heart valves. However, we have not yet explored the manufacturability of these materials, how well they are described by finite element modelling, or their availability for integration into current valve manufacturing procedures.

Melt electrowriting (MEW) is an additive manufacturing technique with growing popularity, particularly in tissue engineering (Mueller et al. 2024; O'Neill and Dalton 2023). It has been explored primarily for the creation of cell scaffolds, alone or embedded into hydrogels. Up to now, the ability to embed MEW meshes into silicones has not been explored in depth.

On the other hand, polydimethylsiloxane (PDMS) has been studied in a wide variety of biomedical applications and is used in numerous medical devices (Ariati et al. 2021). It is known that the mechanical response of this material can be tailored through its polymer to curing agent ratio, as well as the curing parameters, making it a popular material for its tuneability (Colombo et al. 2010; Hopf et al. 2016).

The aim of this chapter is to translate the learnings from FE modelling to real-world materials and leaflets. In this section, MEW-manufactured meshes are embedded into PDMS, mechanically assessed, and compared to finite element models. Polycaprolactone (PCL) is used to create the fibre structures as it is the current gold-standard material for MEW printing. While other materials can be explored in the future, starting with the most accessible and reliable polymer would be the prudent approach for determining the suitability of these procedures. For this reason Sylgard-184 PDMS is used as the matrix into which the MEW meshes are embedded.

These MEW-embedded materials are mechanically assessed using equibiaxial bulge loading to simulate a similar loading environment to prosthetic leaflets. This method of mechanical testing has been established for bovine pericardium (Whelan, O'Brien, et al. 2021), a material widely used in prosthetic heart valves, and had been used to calibrate constitutive models for pericardium (Whelan 2021) as well as Sylgard-184 (Bernardi et al. 2017; Hopf et al. 2016).

This work aims to establish the manufacturability of a MEW-embedded PDMS, as well as use mechanical assessment of the material to inform and improve our finite element models.

6.2 Methods

6.2.1 Sample manufacturing

6.2.1.1 Parameter selection

In Chapter 4 the most desirable combination of a PEEK-like MEW mesh embedded in PDMS was determined. In-house capability allows for printing of PCL, so the discrete fibre uniaxial model described earlier was used to determine a PCL-based MEW mesh with material properties that correspond to the MD03 combination. This was determined to be an 8-layer structure with 0.5 mm fibre spacing, embedded into 0.3 mm-thick PDMS.

6.2.1.2 Melt electrowriting (MEW)

PCL mesh structures were manufactured using MEW on a machine built in-house and previously described (Eichholz et al. 2022), see **Figure 6-1**. Briefly, polycaprolactone (PCL) (PURASORB® PC 12) was melted in a luer-lock syringe (Nordson 3cc) and extruded through a 22G needle (Nordson ¼") under a constant air pressure of 0.5 Bar. Temperature was maintained at 90°C around the syringe and a voltage of 6.5 kV (Heinzinger 30,000 LNC-Series) was applied to the needle. Extruded PCL fibres were deposited onto a grounded, aluminium collector plate. Movement of the plate was enabled using a 4-axis stepper motor (Arcus Technology). Plate movement, temperature, pressure, and voltage were controlled using Motion Perfect v4.4 (Trio Motion Technology, UK). The distance of the needle to the collector plate was maintained at 5 mm and plate speed was varied until accurate fibre deposition was achieved.

8-layer PCL meshes were manufactured with a fibre spacing of 0.5 mm. For mechanical testing, two types of structures with different fibre orientations were manufactured: 45° and 10° with respect to the horizontal direction. These orientations were chosen to represent isotropic and anisotropic structures.

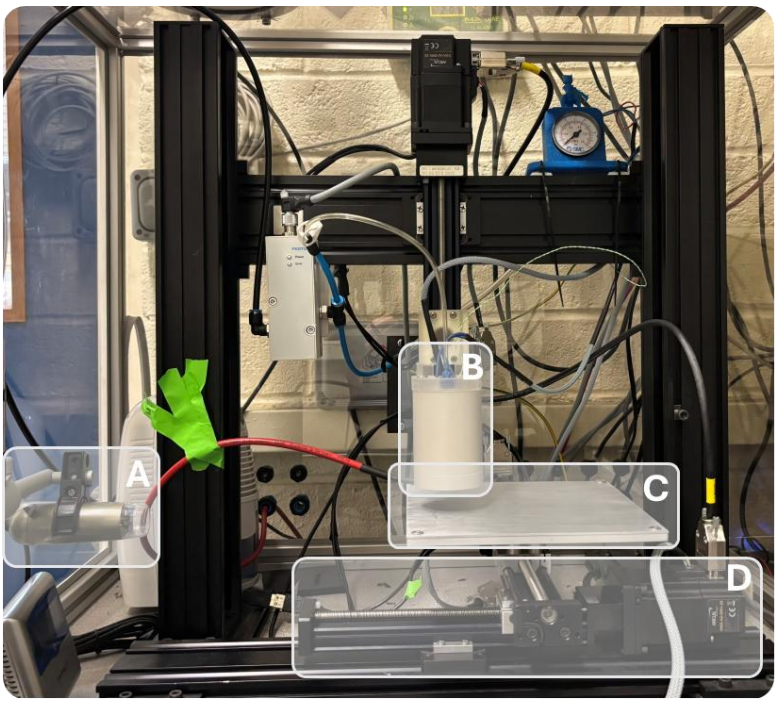

Figure 6-1 *Image of MEW printer highlighting (A) camera to monitor filament extrusion, (B) heated barrel containing polymer-filled syringe, (C) collector plate, (D) stepper motors to enable motion in the X- and Y-directions.*

6.2.1.3 PDMS embedding

MEW meshes were embedded within PDMS using a metallic mould developed by Aleesha Vahab, MSc, under my supervision. This mould consisted of two aluminium plates and four stainless steel shims: two each of 0.05 mm and 0.01 mm thickness to give a total sample thickness of 0.3 mm. The shims had a 30 x 30 mm hole cut from the centre into which PDMS was injected, and they were enclosed within the aluminium plates and secured with screws. PDMS could be injected using a syringe into one of two holes in the top plate, with a second hole allowing air to escape. MEW samples were secured within the mould between the four shims, with one shim of each thickness placed above and below the mesh. This arrangement maintained the mesh in the centre of the cured sample.

Sylgard-184 PDMS (Dow Inc., USA) was mixed at a 16:1 ratio of polymer to curing agent, loaded into a syringe, and degassed in a vacuum chamber (BINDER GmbH, Germany) for 10 minutes. After degassing, the polymer was slowly injected into the mould, then moulds were degassed for another 30 minutes. To cure, the moulds were placed in an oven at 40° for 36 hours.

Four (n=4) MEW-embedded samples were manufactured for each fibre orientation, and another four (n=4) PDMS only samples were created. Fibre bundle diameters and angles between bundles were measured using a Leica S6 D (Leica Microsystems) equipped with Zeiss Microscopy Camera (Axiocam 208 Colour), and sample thickness was measured using a Mitutoyo LITEMATIC VL-50 thickness gauge (Mitutoyo (UK) Ltd., UK). Measurements were taken at five points within the loaded region of the sample.

6.2.2 Flexural bulge testing

6.2.2.1 Sample preparation

After moulding, the corners of the samples were cut using a scalpel. To enable digital image correlation (DIC), a stochastic speckle patten was applied to the underside of the samples using white spray paint (Montana Colors, Spain).

6.2.2.2 Bulge testing

For equibiaxial bulge testing, an in-house multi-specimen pressure inflation rig, previously described in detail (Whelan, O'Brien, et al. 2021) was used, see **Figure 6-2**. In brief, this is a fully symmetric chamber that allows for pneumatic pressure-inflation of materials under physiological loads. Samples are alternately pressurised from above and below to simulate leaflet loading in vivo. Up to twenty circular samples with a total diameter of 30 mm and a loaded diameter of 20 mm can be tested at once. Air pressure is applied to reservoirs on the top and bottom of the rig, and is transferred to the saline-filled chambers via rubber diaphragms. These diaphragms have a limited volume that they can displace, so to ensure full loading of the samples, four (n=4) were tested at a time. The other sixteen holders were filled with blanks to prevent saline passing between chambers. Each group (PDMS only, 45°, and 10°) was tested individually. To replicate hypertensive pressure conditions, samples were loaded with a pressure amplitude of 150 mmHg at 1 Hz for the duration of testing. Prior to DIC imaging, samples were loaded at 80 mmHg for an hour to remove any air in the system.

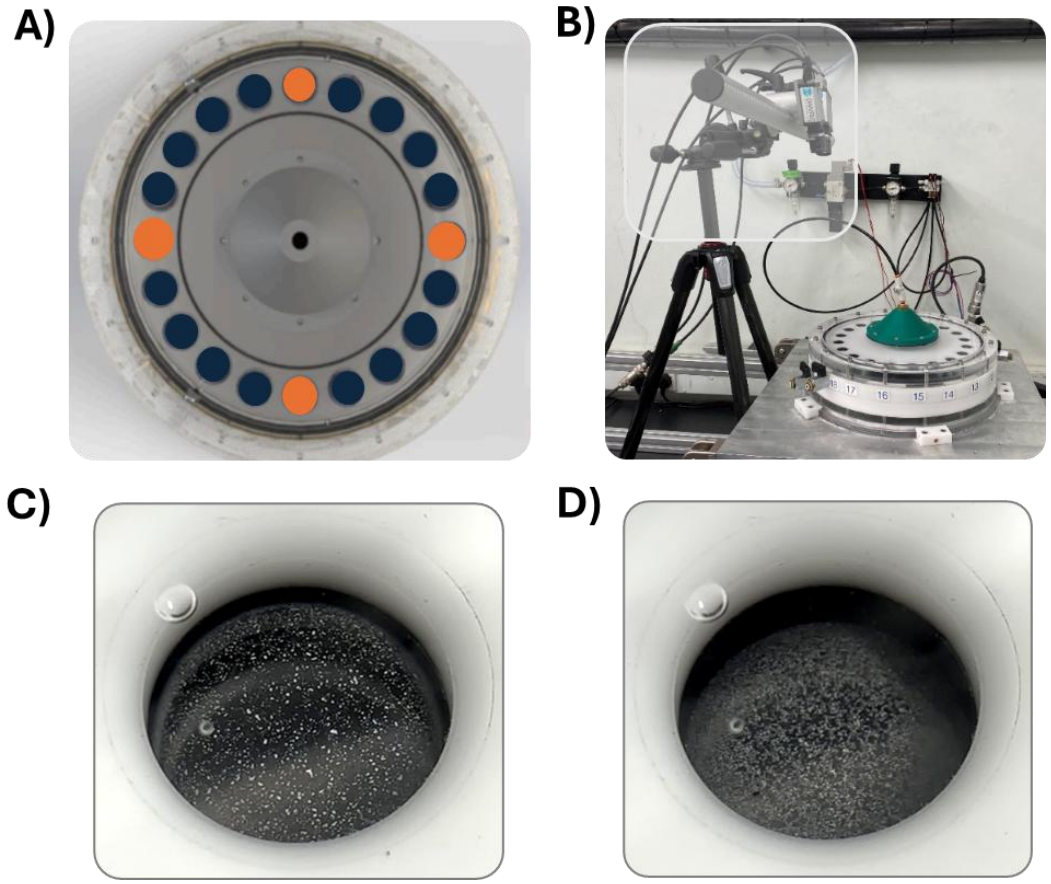

Figure 6-2 Flexural bulge loading rig. (A) Top view of rig showing locations of sample holders, orange circles indicate locations of test samples in this study. (B) Image of rig with DIC dual-camera setup highlighted. Example of sprayed PDMS sample (C) loaded and (D) unloaded. (A) and (B) adapted from Whelan et al., 2021.

6.2.2.3 Digital image correlation (DIC)

3D-DIC was performed on loaded samples to monitor displacement under pressure using a commercial system (DIC Q-400, Dantec Dynamics, Denmark). 200 images of each sample were taken at 15 Hz, capturing 13 full loading cycles. Post-processing was performed using Istra4D (Dantec Dynamics, Denmark); maximum and minimum z-displacement in the centre of each sample across all 200 images was extracted. To calculate the bulge height of the samples, the magnitude of all the maximum and minimum bulges were averaged.

6.2.3 Modelling

6.2.3.1 Bulge model

A model was created to simulate the experimental bulge loading in order to assess the material calibration. To mimic the samples, a 20 mm disc was created in Abaqus CAE and meshed with 8,320 C3D8 elements. Three models were created, one for each group tested (PDMS, 10°, and 45°), and the thickness for each was informed from measurements taken of the tested samples, described earlier. All edges of the disc were pinned (U1=U2=U3=0), and a pressure of 150 mmHg (19,998 Pa) was applied to the bottom surface, see **Figure 6-3**.

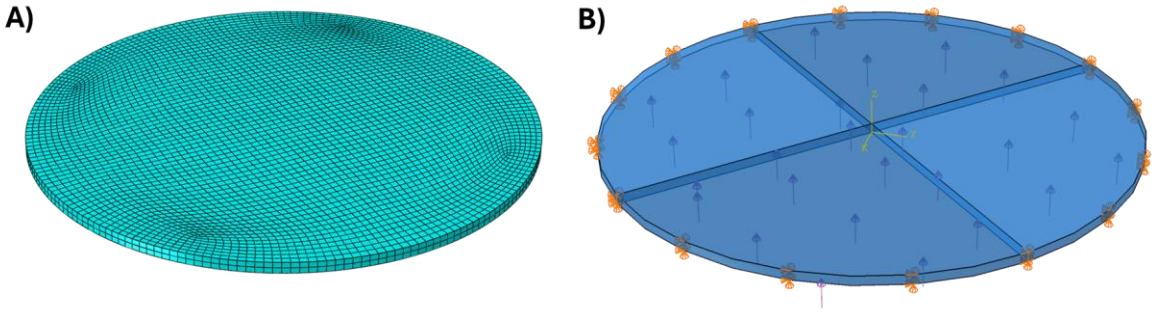

Figure 6-3 *Details of bulge model, (A) disc mesh and (B) boundary conditions showing pinned edge and pressure from below.*

6.2.3.2 Material calibration

For PDMS samples, an Ogden model was used to describe the material and calibration was performed using Abaqus CAE (Abaqus User Manual, 2024). The Ogden model is a form of strain energy potential used to describe hyperelastic material behaviour. For incompressible materials, it is defined in the Abaqus CAE software as:

$$U = \sum_{i=1}^{N} \frac{2\mu_i}{\alpha_i^2}\left(\lambda_1^{-\alpha_i} + \lambda_2^{-\alpha_i} + \lambda_3^{-\alpha_i} - 3\right)$$

Where λ_i are the principal stretches and μ_i and α_i are material parameters. μ_i is related to the shear modulus of the material according to:

$$\mu_0 = \sum_{i=1}^{N} \mu_i$$

A calibrated material description was applied to the bulge model and adjusted as necessary to reach a similar deformation seen experimentally. To stiffen the bulge, first a pseudo-biaxial dataset was generated by doubling the uniaxial curve's stiffness. After this, the material parameters were customised in order to reach the target bulge height. This was accomplished by maintaining the same shear modulus as earlier calibrations and increasing the α parameter.

For the MEW-embedded PDMS samples, discrete fibre uniaxial models were created and GOH material parameters were calibrated according to the methods described in Chapter 4. Fibre diameter and overall thickness were informed by the samples manufactured for bulge testing. PDMS material properties were applied based on calibration from uniaxial tensile data, and PCL was described using an elastic-plastic model, informed by Castilho, et al. (Castilho et al. 2018). Detailed material inputs can be found in Appendix A3.

6.2.4 Mechanical testing

Under my supervision, Aleesha Vahab, MSc, performed uniaxial tensile testing on PDMS and MEW-embedded PDMS. Some of these results are used for material calibration and model comparison here.

Dogbone samples with a width of 2.24 mm, gauge length of 12.5 mm, and thickness of 0.3 mm were uniaxially tensile tested to failure according to the procedure described in Chapter 3.

6.2.4.1 Statistical analysis

All statistical analysis was performed using GraphPad Prism 10 (GraphPad Software, Inc., San Diego, California) and results are presented as mean ± standard deviation. Specific statistical tests performed are detailed in figure captions and $p \leq 0.05$ was considered significant.

6.3 Results

6.3.1 Mesh embedding

Figure 6-4A and B shows representative images of both a 10° and a 45° embedded sample. Visually, both look to have embedded well with minimal disturbance to the fibre structure. Angle measurements for each sample are close to the target for both groups, see **Figure 6-4**C. Average angles between bundles for the 10° group were closer to the target (23.30 ± 1.48° vs 20°) compared to the 45° (95.20 ± 3.94° vs 90°). Fibre bundle diameters were more variable, with average diameters for each sample ranging between 20 and 40 µm, see **Figure 6-4**D. There was no statistically significant difference in diameters between the two groups (28.14 ± 6.21 µm for 10°; 31.75 ± 7.07 µm for 45°). In all three sample groups the average thickness was larger than the target 0.3 mm (0.36 ± 0.09 mm for 10°; 0.35 ± 0.02 mm for 45°; 0.36 ± 0.02 mm for PDMS), and there was no statistically significant different difference between the three groups, see **Figure 6-4**E.

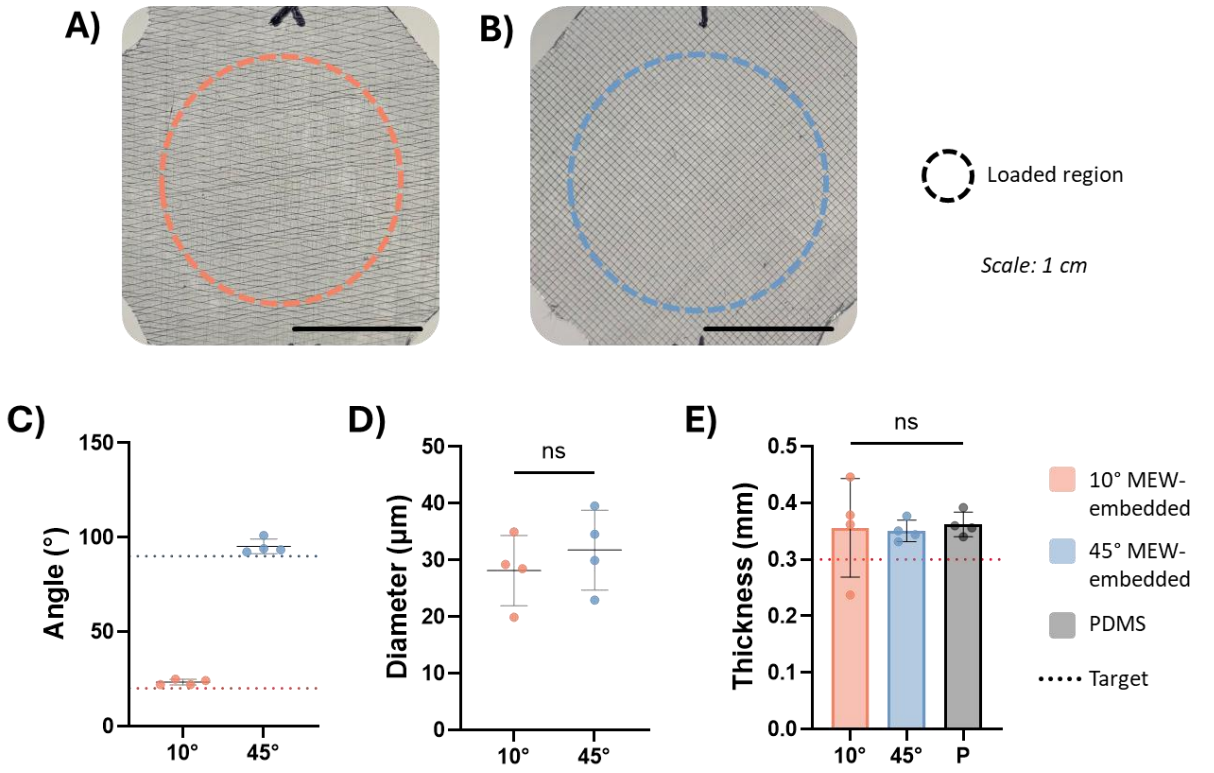

Figure 6-4 *Sample embedding details showing representative (A) 10° and (B) 45° embedded samples. (C) Measured angle between fibre bundles with target angle indicated by the dotted line. (D) Measured fibre diameters, normality tested using Shapiro-Wilk normality test and significance tested with unpaired t test. (E) Average thickness for each tested sample with target indicated by dotted line, normality tested using Shapiro-Wilk normality test and significance tested with Brown-Forsythe and Welch ANOVA test with Dunnett's T3 multiple comparisons test.*

6.3.2 Bulge testing

Displacements under bulge loading at 150 mmHg are shown in **Figure 6-5**A. Across all samples, the mean bulge height is around 5 mm (4.93 ± 0.55 mm for 10°; 5.71 ± 0.70 mm for 45°; 5.11 ± 0.35 mm for PDMS). One sample in the 45° group broke shortly after DIC imaging, and a second one appeared to be close to breaking during imaging. There were no statistically significant differences in bulge height between the three groups.

45° samples were also loaded and imaged at 100 mmHg and the bulge height was significantly smaller than at 150 mmHg (4.82 ± 0.59 mm), see **Figure 6-5**B.

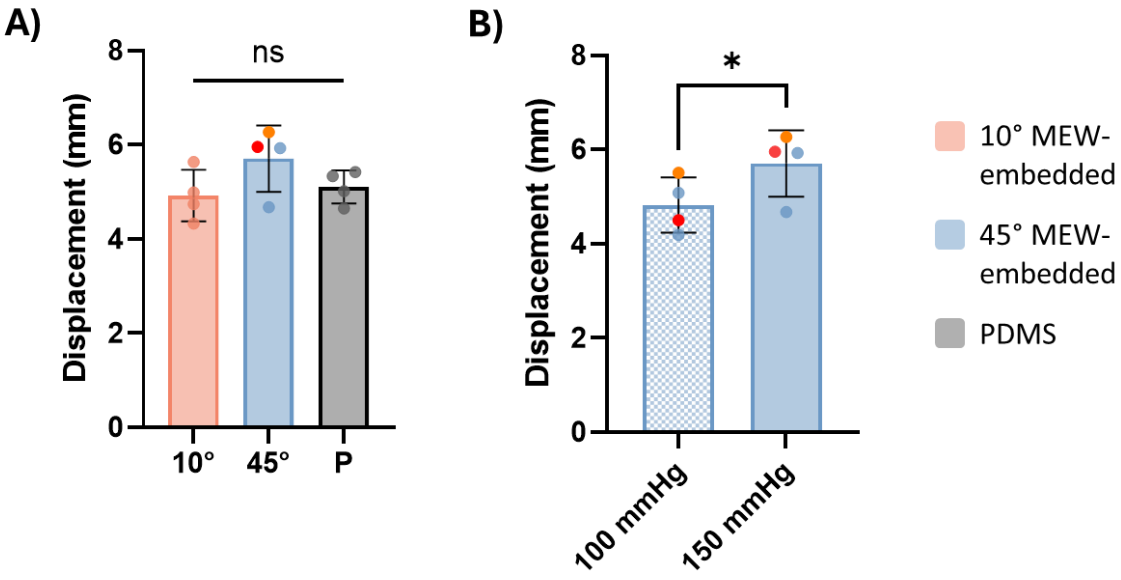

Figure 6-5 *Bulge testing results. (A) Displacement of all samples, significance tested using Brown-Forsythe and Welch ANOVA test. (B) Displacement of 45° samples for 100 and 150 mmHg pressure conditions, significance tested with a paired t test. Normality was tested for all data using Shapiro-Wilk normality test; p*≤0.05.*

6.3.3 PDMS calibration

Tensile test results of PDMS were used to calibrate an Ogden constitutive model implemented in Abaqus. This calibration was used in the bulge model and compared to experimental results. First, the uniaxial data alone was used to calibrate Ogden parameters and applied to the bulge model, resulting in a bulge height of 7.45 mm, see **Figure 6-6**A and B. To stiffen the bulge, a pseudo-biaxial dataset was generated which fit the uniaxial data well, reducing the bulge height to 6.20 mm, see **Figure 6-6**A and C. Finally, by applying a custom calibration with an increased α value, the bulge height was reduced to 5.14 mm, see **Figure 6-6**A and D. All Ogden model parameters and resulting bulge height are shown in **Table 6-1**.

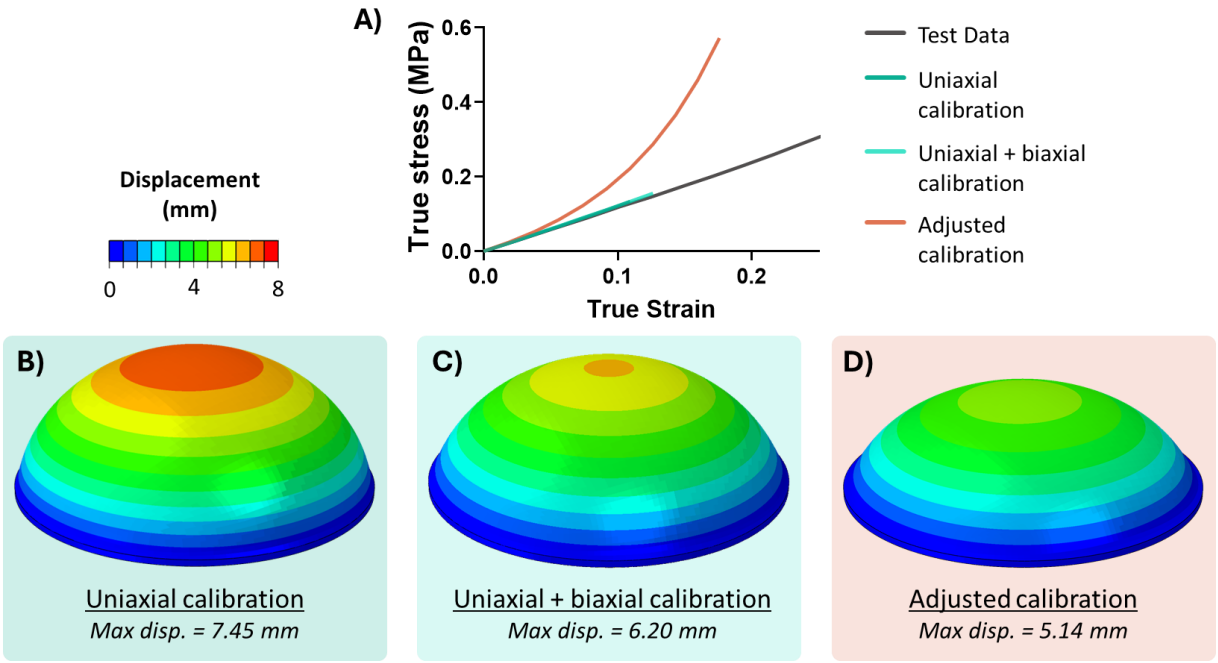

Figure 6-6 *Bulge modelling results of PDMS calibrations. (A) True stress-strain curves of each model compared to test data, and bulge displacements for (B) uniaxial calibration, (C) uniaxial + biaxial calibration, and (D) custom adjusted calibration.*

Table 6-1 *PDMS calibrations with their corresponding Ogden model parameters and maximum bulge height*

	μ (MPa)	**α**	**Bulge height (mm)**
Uniaxial	μ_1 = 0.356	α_1 = 2.033	7.45
Uniaxial + biaxial	μ_1 = -2.27 μ_2 = 1.092 μ_3 = 1.548	α_1 = 1.754 α_2 = 2.921 α_3 = 0.586	6.20
Custom	μ_1 = 0.37	α_1 = 12.75	5.13

6.3.4 MEW-embedded calibration

Before calibrating models for the samples, the dogbone size was altered to investigate impact on the stress-strain response. **Figure 6-7** shows the results of this, with the curve from the original-sized model and two scaled up versions: 1.5x and 2x. A stiffer response was seen in the larger models, although the two large models gave the same response. Moving forward, the 1.5x size model was used.

Stress-strain curves were obtained for the fibre-embedded materials and used to calibrate the parameters of the GOH model, which was subsequently used to model the sample bulge. With this calibration, both models reached smaller displacements than seen experimentally (2.37 mm vs 5.71 ± 0.70 mm for 45°, 2.33 mm vs 4.93 ± 0.55 mm for 10°), see **Figure 6-8**A and B.

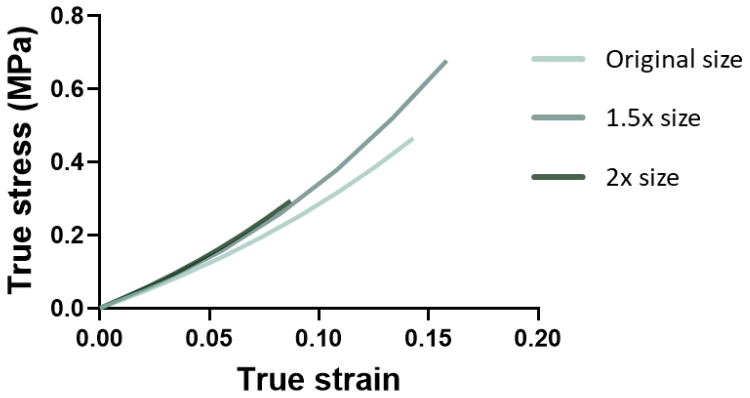

Figure 6-7 *True stress-strain curves for discrete fibre-embedded dogbone models of varying sizes.*

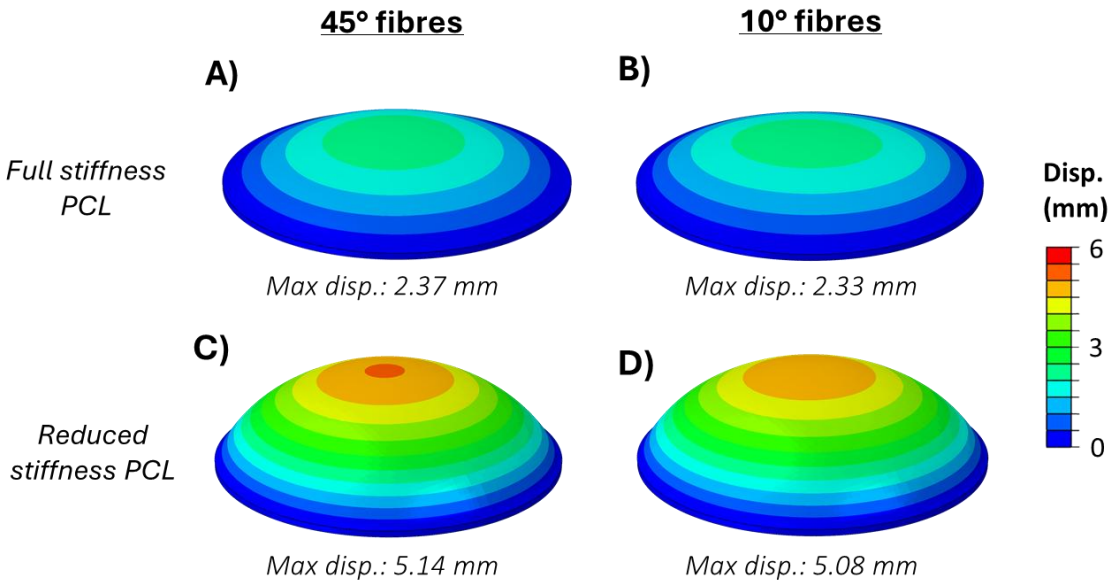

Figure 6-8 *Bulge results of MEW-embedded samples, showing samples calibrated with full stiffness PCL for (A) 45° and (B) 10° structures, and samples calibrated with reduced stiffness PCL for (C) 45° and (D) 10° structures.*

To obtain a more compliant material and increase bulge height, the stiffness of the PCL was reduced by 85%, from 343 MPa to 51.45 MPa. This resulted in a stress/strain response that, when used to calibrate an HGO model, resulted in bulge heights closer to what was seen experimentally (5.14 mm for 45°, 5.08 mm for 10°), see **Figure 6-8**C and D. GOH parameters are shown in **Table 6-2**. This model also predicted a similar bulge height for 45° samples loaded to 100 mmHg: experimentally, these samples reached 4.82 ± 0.59 mm, while the model predicted a bulge of 4.22 mm.

Table 6-2 *GOH model parameters for MEW-embedded materials.*

	C_{10} (MPa)	k_1 (MPa)	k_2	κ
Full stiffness PCL	0.33	4	2.995	0
Reduced stiffness PCL	0.28	0.03	2.995	0

6.3.5 Comparison to uniaxial data

Discrete fibre MEW-embedded uniaxial models were created based on mechanically tested samples and the stress/strain curves were compared for both models with original and reduced stiffness PCL. The results from these models are shown in **Figure 6-9**A and B. In the structure with fibres at 45°, 4 layers, and 1.5 mm spacing, the full stiffness model slightly overestimates the stress, while the reduced stiffness model falls within the range of the tested samples. On the other hand, in the sample with fibres at 80°, 10 layers, and 0.5 mm spacing, the full stiffness PCL reflects the experimental results well, while the more compliant PCL underestimates the curves.

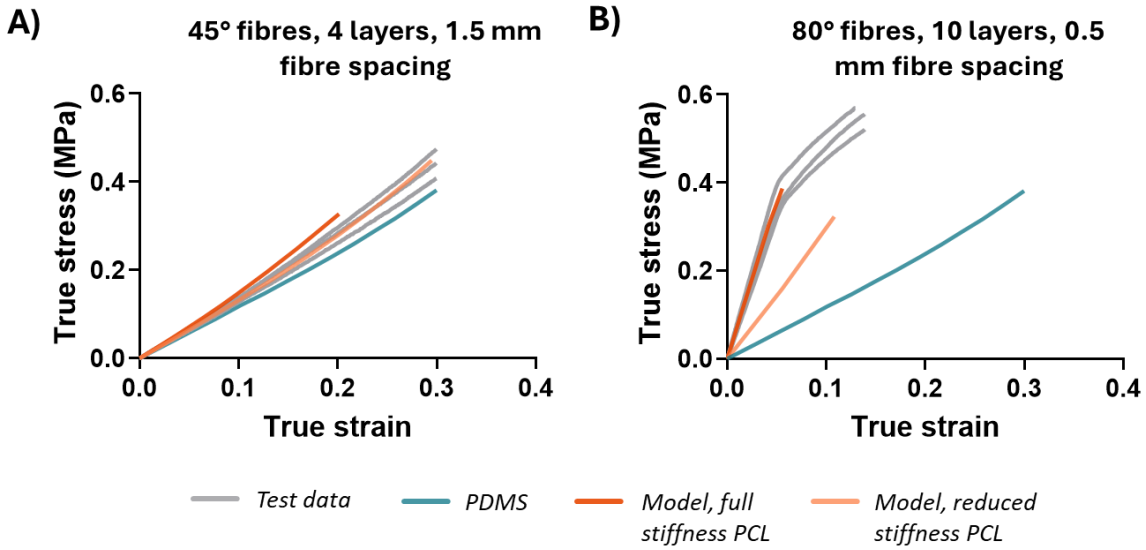

Figure 6-9 *Comparison of discrete fibre models to uniaxial testing data for PDMS embedded with (A) 45° fibres, 4 layers, and 1.5 mm spacing, and (B) 80° fibres, 10 layers, and 0.5 mm spacing.*

6.3.6 Valve models

All calibrated material models were implemented in the dynamic valve model described in Chapter 4: PDMS uniaxial, uniaxial + biaxial, and custom calibrations; MEW-embedded full and reduced stiffness PCL. The results from each of these models are shown in **Figure 6-9**. Both the uniaxial and uniaxial + biaxial PDMS leaflets experience high strains (average 22.8% uniaxial, 22.2% uniaxial + biaxial), resulting in a high degree of leaflet pinwheeling, see **Figure 6-10**A and B. Using the PDMS calibration customised to the experimental bulge results gave a

valve model with lower average leaflet strain (15.4%) and less pinwheeling. On the other hand, the fibre-based leaflet model using the full-stiffness PCL calibration had lower overall strains (13.3%), and consequently did not close fully. Using the reduced-stiffness PCL calibration gave a leaflet result much more similar to the PDMS bulge calibration in terms of average leaflet strain (17%) as well as closing behaviour.

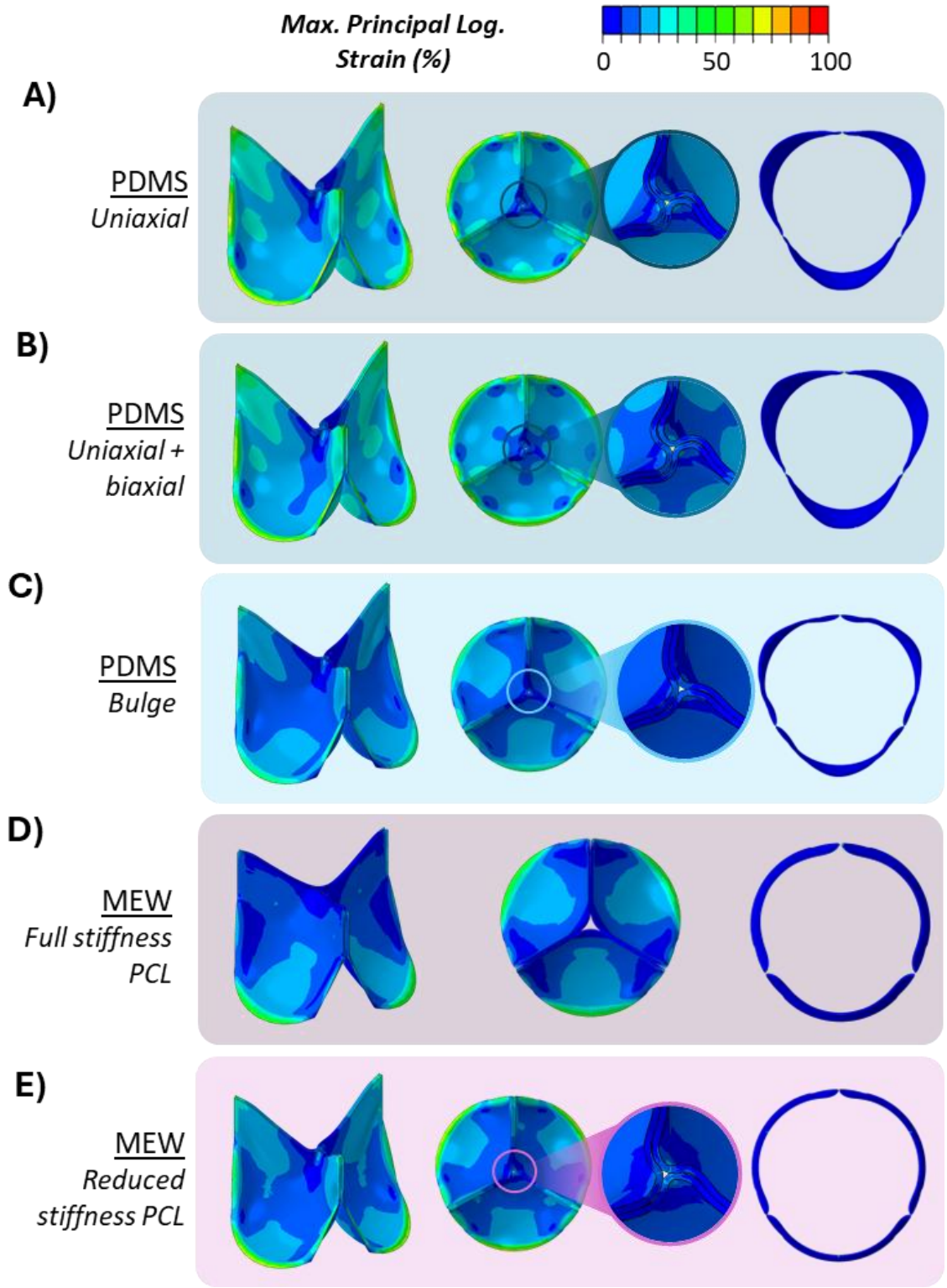

Figure 6-10 *Dynamic full valve models with different material calibrations for PDMS (A) uniaxial, (B) uniaxial + biaxial, (C) custom to bulge, and MEW-embedded with (D) full stiffness and (E) reduced stiffness PCL.*

6.4 Discussion

This work has shown the successful manufacture of MEW meshes and MEW-embedded PDMS which can be mechanically assessed to calibrate and improve finite element models.

Starting with moulding, all of the samples bar one 10° embedded sample had a larger thickness than intended. Although still close to the 0.3 target, the average thickness for each sample group was either 0.35 or 0.36 mm. The shims used in these moulds have been used before and have material residue on them from previous use which is likely what increased the overall thickness of these samples. Notably, the thickness of the MEW-embedded samples was not higher than the PDMS-only samples. This shows that the methodology of enclosing the mesh and shims between two plates sufficiently compresses the edges of the MEW structure; if this were not the case, the total sample thickness would be increased by the thickness of the MEW structure. Additionally, the fibre orientations within each sample remained relatively consistent, showing good reliability of this moulding method for not distorting of the mesh. On the other hand, while the fibre bundle diameters between the two groups were not significantly different, there was a high degree of variability within all of the samples, ranging from an average bundle size of 20 µm up to 40 µm. This indicates a need to investigate the independent fibre diameters and improve overall controllability of the bundle sizes. It should be highlighted also that only the total width of fibre bundles was measured, not individual fibre thickness, so the bundle size may be attributed more so to a lack of fibre coherence rather than individual fibre diameter.

The PDMS-only samples performed well under bulge loading with no breakages and showed a consistent bulge height. On the modelling side, the material had a stiffer response under bulge loading than what was predicted based on uniaxial tensile tests. Calibrating a material model based on the uniaxial tensile results, even adding a stiffer pseudo-biaxial curve, the predicted bulge height was still overestimated by more than a millimetre. This same behaviour was seen in a study performed by Hopf, et al. where the authors found that Sylgard-184 at a 10:1 ratio of polymer to curing agent had a much stiffer behaviour under bulge loading than a model calibrated on uniaxial or biaxial behaviour predicted (Hopf et al., 2016). By factoring the bulge behaviour into their calibrations, the authors were able to obtain a model which predicted all the deformation modes of the material with high accuracy. While their material performed similarly to what was tested here, it is known and well documented that the material properties of Sylgard are heavily dependent on mixing ratio and curing parameters (temperature, time, etc.). Due to this, it is important to perform our own mechanical assessment of this material instead of adopting material model parameters from other studies. Moving forward, to

characterise the material at this curing ratio and with these moulding procedures, we should perform more extensive mechanical assessment to adopt a more comprehensive calibration method. This testing procedure should include, at minimum, uniaxial testing and bulge loading over a range of pressures to determine a pressure-displacement curve. Using this data, inverse finite element methods using software such as Isight (SIMULIA, Dassault Systèmes) can be used to determine a more representative constitutive model to describe this material.

Looking at the MEW-embedded samples, we found that there is a size dependency of the mechanical response on the sample test size. This can inform future mechanical testing to ensure that the sample size is sufficient to obtain fully representative material behaviour of these embedded materials.

Calibrating a fibre-reinforced constitutive model based on the stress-strain curve from the discrete fibre model resulted in an overestimation of material stiffness under bulge loading. To obtain a bulge of the same height seen experimentally, the fibre stiffness needed be to reduced by 85%. After calibrating this reduced stiffness model to the bulge heights obtained at 150 mmHg, this model then better predicted the height of 45° samples loaded to 100 mmHg. Although the experimentally tested samples were slightly more compliant, this model seems to be a good predictor for the bulge behaviour of this combination of PCL mesh and PDMS. However, when we compare our models to uniaxial tensile data, we see that the full stiffness PCL provides a better match than the reduced stiffness PCL. While these samples were much smaller than what we have deemed to be a reliable dogbone test size, the experimental tests and simulations should provide similar results. What this has shown is the opposite to what was seen in the PDMS: the uniaxial response of this material over estimates what we see in the bulge loading condition.

It is important to highlight that in the case of the 45° sample group, one sample failed shortly after DIC imaging and another appeared close to failure through the propagation of cracks on the surface. Both of these samples exhibited large bulge heights around 6 mm, possibly indicating that imminent failure of the material decreased its stiffness. In the failed sample, the PDMS appeared to be ripping along the lines of embedded fibres, indicating that the interface between the PCL fibres and PDMS may have caused the eventual failure. This could be due to the mesh protruding through the surface after moulding, or, more likely, that peaks at fibre crossing points caused sites of high stress and later delamination between the materials. Cao et al. showed that this peak height can be affected by ambient temperature and humidity levels (Cao et al. 2021). By controlling these parameters when manufacturing, there is a potential to obtain a more uniform thickness mesh, which could improve the longevity of the embedded material.

Another factor leading to the bulge behaviour of the material being less stiff than predicted may be due to the fibre structure geometry. The PCL fibres embedded within the PDMS do not form a completely solid mesh, as they are modelled, instead there may be gaps between adjacent fibre layers (Cao et al., 2021; O'Neill and Dalton, et al. 2023). This would cause them to act individually rather than as a bundle under bulge loading, which could reduce the overall stiffness of the material.

With the materials studied here, more testing needs to be performed to fully understand their behaviour. However, we have seen that their mechanical response is heavily dependent on the type of loading applied. Due to this, since the ultimate aim is for these embedded materials to be used as leaflets in prosthetic valves, the best way to characterise their material response is as full leaflets. Applying the calibrated material models for both PDMS and PCL-embedded PDMS to the dynamic full valve models, we can see the variability between valve performance in all of the different models.

Most notably, in the PDMS bulge calibration and MEW reduced PCL calibration, both of which resulted in a bulge height of 5.14 mm, we can see different responses in the leaflets. The greatest difference between the two is seen in their opening behaviour, where the PDMS leaflets open past the suture edges of the leaflet, but the PCL-embedded leaflet edges stay within these bounds. Also, the fibre-reinforced leaflet experienced slightly higher average strain than the PDMS one. This clearly shows the impact of constitutive model choice in describing these materials, and the possible differences between them even when they give the same behaviour in the bulge model.

Overall, this work has shown the successful manufacture of MEW meshes, paired with a moulding method that can reliably produce embedded PDMS materials at a low thickness. While potential challenges have been highlighted, these manufacturing methods allow us to create samples which can be mechanically assessed to improve the validity of the FE models. Ultimately, however, the best way to asses these materials and inform our FE models will be to use them to manufacture and test full valves. Testing these valves in a pulse duplicator would provide the ultimate ground truth for validating the FE models.

Chapter 7 Manufacturing customised, fibre-reinforced polymer leaflets informed by finite element modelling

7.1 Introduction

As highlighted in Chapter 6, the most effective method to assess the embedded material and inform FE models is to perform testing on full valves with these polymer leaflets. However, the materials need to be assessed to determine their feasibility of integrating these methods into the current manufacturing procedures used by our partner company. A key feature to investigate is the material's ability to be sutured onto a frame. In the current devices, porcine pericardium leaflets are sutured to an inner skirt and then onto the frame[1]. In order to integrate with the currently used procedures, this material needs to be able to withstand suturing.

Additionally, Chapter 5 used fibre reorientation to identify optimal fibre orientations for these leaflets based on two different methods. This work aims to show the manufacturability of these highly customised fibre structures.

7.2 MEW-embedded leaflets, Iteration 1

7.2.1 MEW printing and embedding

Two-layered box structures with a fibre spacing of 1.5 mm and total dimensions of 45 x 35 mm were manufactured from PCL using MEW as described earlier. These structures were embedded into a target 0.3 mm-thickness Sylgard-184 using a prior iteration of the mould described earlier. This mould comprised two parts: a base which had a 0.15 mm recess and a top with a 0.15 mm thickness that had a hole in the centre, see **Figure 6-11**A. The recess and hole were both 40 x 30 mm, and the MEW sample was secured between the two parts. PDMS was prepared at a 16:1 ratio of polymer to curing agent, poured into the opening, and left to cure for 24 h at room temperature.

7.2.2 Leaflet manufacture

MEW-embedded PDMS structures were brought to Boston Scientific in Galway for a preliminary manufacturability assessment. Size L leaflets were cut using an in-house punch

[1] Personal communication with R&D engineer, Boston Scientific.

and suturing was performed by an operator. Polymer leaflets were sutured onto a rubber sheet using a single thread, following similar procedures used on site.

7.2.3 Insights

MEW-embedded PDMS sheets were successfully cut into leaflets with no hinderance from the MEW fibres, see **Figure 6-11**B. The presence of PCL fibres embedded within the silicone did not prevent clean cutting of the material and all three leaflets were cut easily on the first attempt. When manufacturing the ACURATE neo2 device, porcine pericardium leaflets are sutured together and then to the inner skirt, which is also made of porcine pericardium. Suturing is aided by using a fabric strip attached to the leaflet's edges which provides reinforcement during manufacture and loading. In this case, polymer leaflets were sewn directly to a rubber sheet, mimicking suturing to the inner skirt. The fabric reinforcement strip was not used due to the polymer leaflets having a larger thickness than porcine pericardium.

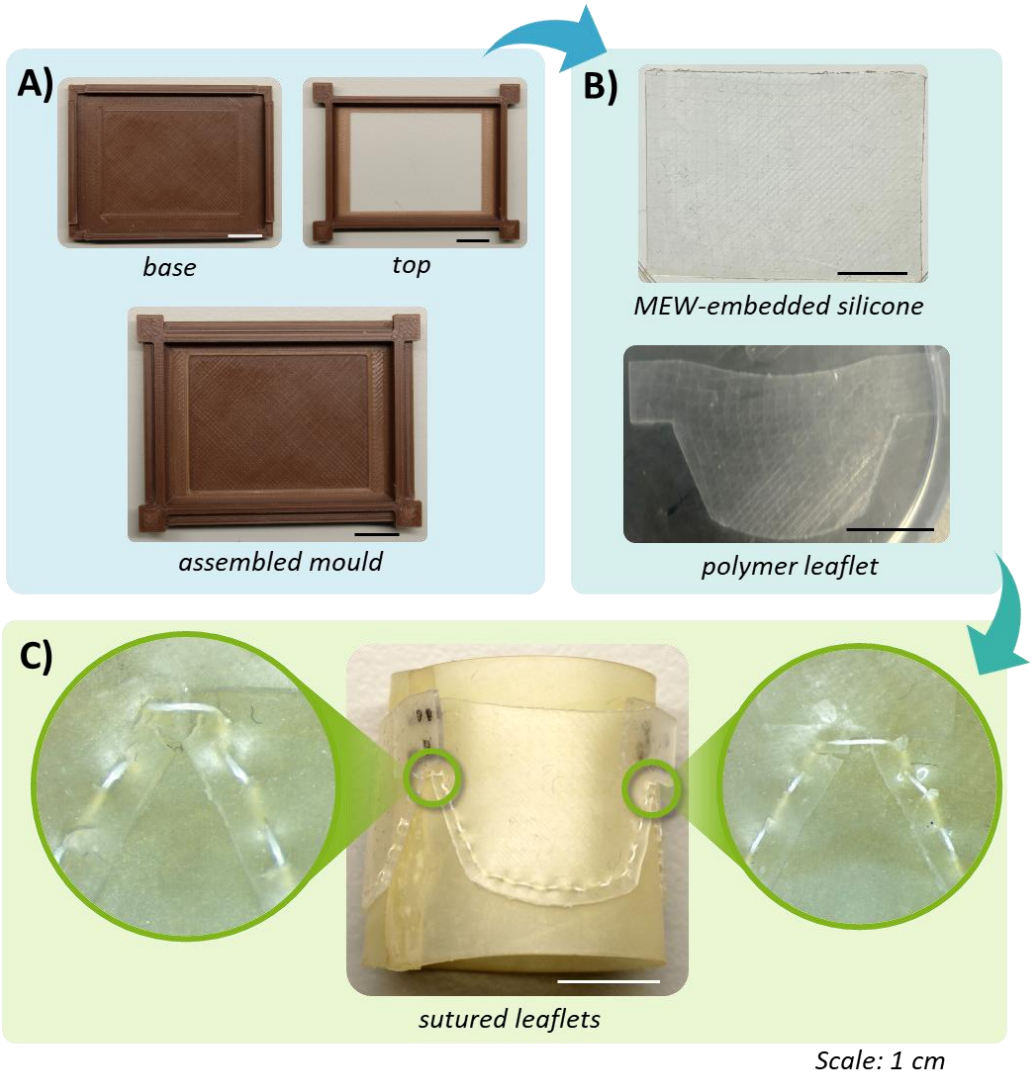

Figure 6-11 *Moulding and suturing of MEW-embedded polymer leaflets. (A) Open mould showing the base, top, and assembled mould. (B) Embedded silicone cured and removed from mould, and leaflet cut from silicone sheet. (C) Leaflets sutured onto rubber sheet with detailed view of sutures and tears.*

All three leaflets were successfully attached to the rubber sheet without major tearing or breaking; the suture was able to freely pass through the material with ease. While the material is tackier to touch than pericardium, this did not negatively impact the handling of the material. Small tears between a suture hole and leaflet edge appeared in regions connecting the two leaflets, see **Figure 6-11**C; however, these tears did not propagate inwards.

Overall, the initial suturing test of this material was successful: we were able to cleanly cut leaflets from larger sheets and suture them to a replica of an inner skirt in accordance with company protocols. This trial also provided insight for design changes that could improve suturability. In particular, since a reinforcement strip is typically used, it was proposed that we could implement an embedded structure around the edges to resist tearing from the sutures. This design change was implemented in the second leaflet iteration.

7.3 MEW embedded leaflets, Iteration 2

With the learnings from the initial leaflet suture test, a second leaflet design was created. The aim of this was twofold: assess manufacturability of a bioinspired fibre structure and integrate a MEW fibre-based reinforcement strip around the leaflet edges.

A bioinspired fibre structure was chosen based on the reoriented fibre structures presented in Chapter 5. M2, shown in **Figure 6-12**A, was chosen due to the diversity in fibre orientations between the two layers to showcase the flexibility of these design and manufacturing tools.

7.3.1 MEW fibre structure

The M2 fibre structure was recreated in SolidWorks (SolidWorks corp., Dassault Systèmes, 2023) with a target fibre spacing of 0.5 mm. This structure was based on that implemented in the dynamic valve model: fibre orientations were averaged within the discretised 56 regions. Each fibre was comprised of numerous straight components whose orientations shifted from region to region, ultimately forming a unique curved shape across the leaflet. The use of straight segments enabled an ease of translation to code for printing. In SolidWorks, the full toolpath for the machine was recreated and saved as a DXF file; this connected the individual fibres into an efficient path for each family. The sketch file was imported into cad2motion (Trio Motion Technology, UK) to generate the BASIC code for printing, the code used can be found in Appendix A4.

Additionally, an integrated reinforcement strip was added to a 2 mm border around the leaflet's suture edge. This reinforcement strip was made of parallel lines that traced the leaflet edge at 0.25 mm increments.

Before printing the fibres, an outline of the leaflet offset outwards by 0.25 mm was created. By design, the printed fibres extended past this boundary to ensure they were contained completely within the leaflet after cutting excess material. A single leaflet layer was comprised of one pass each of the outline, first fibre family, second fibre family, and the reinforcement strip. Each component started and finished at the same point on the collector plate to allow for easy editing or removal of a component without impacting the rest of the structure, see **Figure 6-12**B.

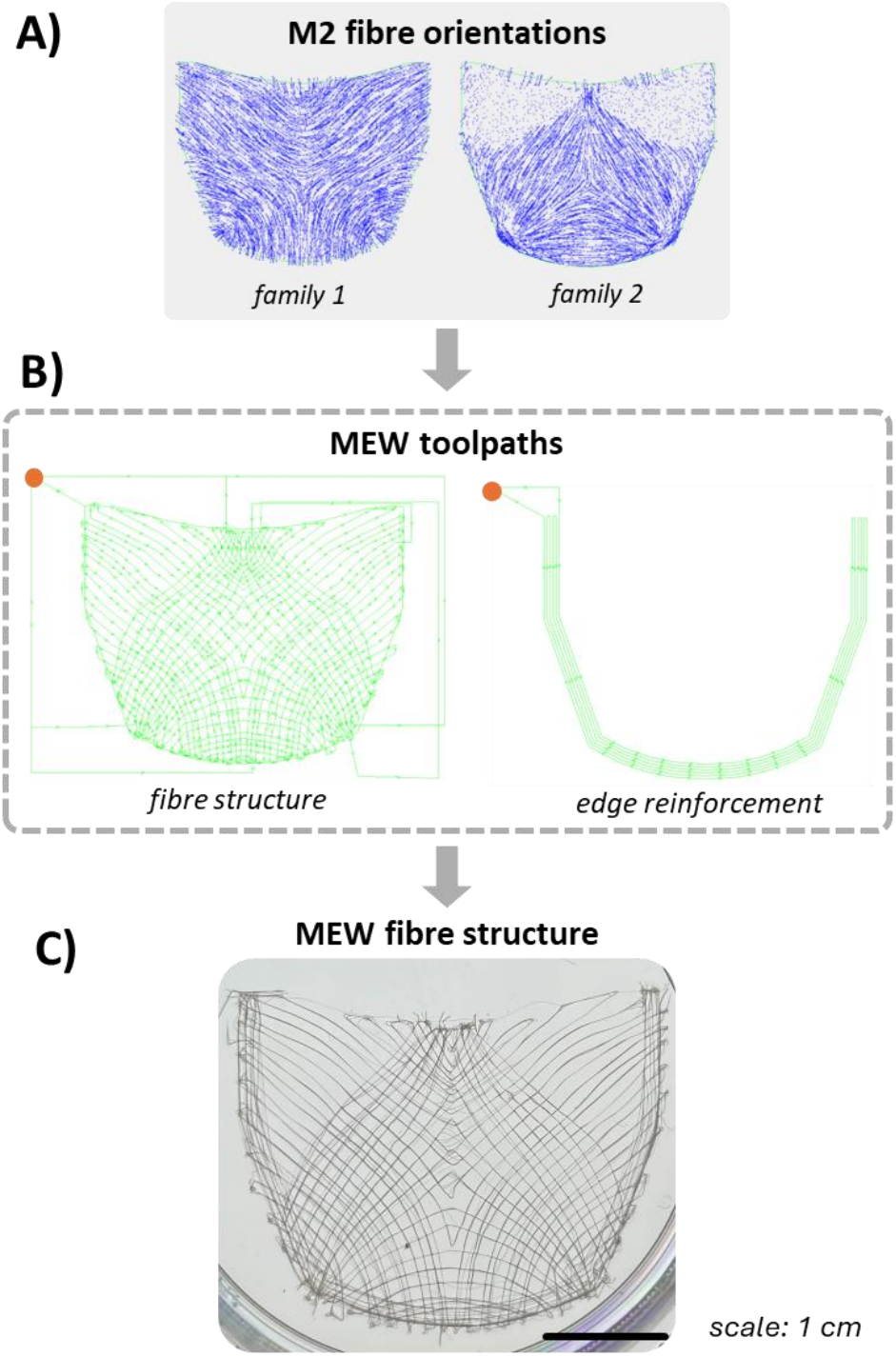

Figure 6-12 *Visualisation of fibre orientations translation from FE to printing. (A) Reoriented fibre families in the FE model. (B) Programmed toolpath for fibre structure and edge reinforcement strip, orange dot indicates start and end point for each section. (C) Final printed leaflet fibre structure.*

7.3.2 Results

A bioinspired fibre structure based on M2 in was successfully manufactured with an integrated reinforcement strip, see **Figure 6-12**C. Fibre coherence among layers was good with minimal divergence, and the ends of most fibres extended past the leaflet boundary as intended. Integration of a reinforcement strip was also successful, leading to a high density of dispersed fibres at the leaflet edges that could improve suture retention.

Using a plate speed of 7 mm/sec, the total print time for this leaflet was just over an hour.

7.4 Discussion

Adopting this iterative approach to leaflet manufacture and suturing demonstrated the flexibility in design and manufacture of these leaflets, as well as the potential for implementation into already-existing protocols within Boston Scientific. Through this, we were able to show the promising suturability and manufacturability of these MEW fibre-reinforced polymer leaflets.

In an initial suturability test, the material held well, experiencing only a few tears. This highlighted areas for improvement in design to enhance the suturability and potential suture retention of the material. Namely, this improvement was through the addition of fibre-based reinforcement around the leaflet edges.

Iteration 2 of the leaflet brought together learnings from the Iteration 1 as well as the bioinspired, reorientated fibre structure presented in Chapter 5. This showcased the FE-based leaflet design process as a whole: the trileaflet valve model, paired with fibre reorientation, defined a fibre reinforcement structure that was successfully translated to a 3D printed mesh using MEW. Within this structure, a reinforcement strip was also implemented.

The M2 reorientated fibre structure was chosen to be manufactured due to the difference in fibre orientation between the two families. This structure printed well on the first attempt, creating fibre layers which were mostly coherent, especially in regions with low fibre density. Divergence in placement was seen in regions of high fibre density (i.e. reinforcement strip) and where there were larger changes in fibre direction (i.e. leaflet midline, rounded fibres at corners). These observed divergences are due to both fibre bridging and polymer jet lag, two well-known and widely observed phenomena in MEW printing.

Fibre bridging occurs when the polymer jet interacts with the previously deposited filaments, both of which are charged (Cao et al. 2021; Ding et al. 2019; Kim et al. 2021). Typically, the fibre jet being deposited will “snap” to the fibres printed previously along that path. However, when the distance between the current path and nearby fibres becomes small, the adjacent fibres

can pull the jet off its course, causing bridging. This can be improved by increasing the space between adjacent fibre bundles or potentially though increasing the collector speed. As bridging was primarily seen in the reinforcement strip, though, removing it may not be necessary as a higher density of fibres could have the potential to improve suture retention. Allowing for a more random deposition of fibres around the edge, however, would reduce the size of fibre bundles, so this hypothesis requires testing to validate.

The lack of fibre coherence in certain regions can also be attributed to filament jet lag. This is another widely understood phenomenon in MEW, which is a spatial delay between the nozzle position and filament deposition (Hrynevich, Liashenko, and Dalton 2020; Shin, Kim, and Chang 2018). If not accounted for in the printing parameters or code, it can cause a divergence of fibre position from the predefined path. This behaviour is predominately determined by the collector speed, and it is exacerbated with increasing collector speeds much higher than the critical translation speed (CTS). However, as with many other MEW deposition behaviours, material flow rate and ambient conditions such as temperature and humidity can also play a role (Tourlomousis et al. 2017)). Lag can generally be reduced by decreasing the collector speed closer to the CTS and adding pauses at direction changes to allow the extruded filament to "catch up" to the nozzle. In this particular print, the speed used was 7 mm/s, which is only slightly faster than the typical CTS on this machine of around 6 mm/s with these printing parameters used. While slowing the speed could improve the lag, slowing it too much could begin to cause fibre buckling, leading to an unpredictable and, consequentially, undesirable deposition of the fibres. An alternative approach is to introduce pauses and slower regions where jet lag is an issue. In the current code, pauses of 600 ms are present where large shifts in direction occur, and these are accompanied by an acceleration of 500 m/s^2 and a deceleration of 1000 m/s^2. By adjusting the pause duration as well as acceleration and deceleration, the fibre lag can be improved in these regions. For more detail on the individual printed sections and location of pauses, see Appendix A4.

By using learnings from suture tests and implementing a bioinspired fibre reinforcement structure, the feasibility of manufacturing fully customised bioinspired, fibre-reinforced polymer leaflets was shown.

This iterative approach showed the flexibility and ease of design, with the MEW process allowing for the manufacture of a wide variety of fibre orientations and other design features, such as a reinforcement strip. It is also a fast process, with the longest print time for a leaflet at 60 minutes.

Overall, this chapter has investigated the real-world translation of these MEW fibre-reinforced structures from finite element models to customisable leaflets that can be sutured onto a valve frame. This work has clearly shown the translatability from finite element models to fully customised, fibre-reinforced polymer leaflets. While there are areas for improvement in the manufacturing, the procedures in place to identify, design, and manufacture polymer leaflets with fully flexible fibre orientations that can be customised based on patient needs.

Chapter 8 Final discussion

Aortic stenosis affects 4% of people over the age of 70 and carries a 50% chance of mortality within 2 years if left untreated (Ambrosy et al. 2023; Généreux et al. 2023). While valve replacement is an option through the use of prosthetic devices, these come with drawbacks such as the need for lifelong, life-limiting anticoagulant therapy or the risk of premature failure (Otto et al. 2021). With a growing demand for minimally invasive valve implantation, this carries the risk of valve degeneration or failure within a short timeframe, excluding younger patients, as well as patients with abnormal physiology (Coisne et al. 2023). Polymer heart valves provide a potential solution to these challenges by offering materials that could outlast current leaflet material, reduce production costs for companies, and enable flexibility in design for custom cases. To date, a wide range of polymer valves have been developed and investigated, including a variety of materials, manufacturing techniques, and valve geometries, which has shown the potential of this technology. Many of the leaflets created have been comprised of a single material and manufacturing method, limiting the scope of design. A handful of studies have used both experimental and finite element methods to show the benefit of introducing fibre reinforcement to the material, opening the possibility of combining materials and structure to design a functional, long-lasting device (Chen et al. 2023; Coulter et al. 2019; Khair et al. 2025). However, to date, development of these devices has largely been on an ad-hoc basis, manufacturing and assessing particular materials of a certain geometry within tight bounds. Additionally, for groups attempting to replicate the structure and material of native aortic valve leaflets, there is a lack of information on material and structural parameters to target (Hasan et al. 2014). This thesis aimed to aid the development and design of these novel polymeric devices in two ways. First, to determine baseline characteristics of native leaflets in order to inform materials and structure of bioinspired polymeric leaflets. The second aim was to create a valve design and assessment tool which uses finite element analysis to inform the design and development of next generation polymer heart valve devices. Finally, the predictions from these tools were compared to manufactured materials, and they were used to define the manufacture of a novel fibre reinforcement structure.

A key gap in the literature was a definitive assessment of the material properties of native leaflets and their layers, as well as the microstructure that drives these properties, for the purposes of informing future devices. Chapter 3 in this thesis aimed to address this by providing important information on the native aortic valve leaflets to establish a baseline for future material development. While previous studies have investigated the material response of leaflet tissue, no singular study has characterised the leaflet's layers as well as the whole

leaflets using the same procedure, or in a way that can be easily replicated and compared to new materials. Additionally, while some imaging has been performed to visualise the macroscale fibre structure in leaflets, little has been done to characterise the microstructure and its change through the thickness of the leaflet. This chapter used both imaging and mechanical assessment to inform key microstructural features of the leaflets as well as their material properties. By performing leaflet tissue clearing using BABB, SHG images of the collagen fibre structure were acquired throughout the thickness of the leaflet. A key finding was the quantification of collagen fibre crimp in both the fibrosa and ventricularis layers which showed that, when the leaflet is in a flat configuration, the fibres of the fibrosa are more crimped than the ventricularis. Additionally, the fibre orientations in key regions of the fibrosa layer were identified, and it was seen that the ventricularis fibres are much more disorganised than those in the fibrosa. Both of these findings have provided insight into fibre crimp and orientation which can be used to inform bioinspired fibre reinforcement in future materials.

On the other hand, uniaxial tensile testing was used to determine the mechanical and material response of the leaflets and their layers. Notably, it was seen that while the ventricularis on its own is a very stiff material, since its thickness is so small, the mechanical response of the whole leaflet is dominated by the fibrosa. However, in the radial direction, the response of the whole leaflet is a combination of both the fibrosa and ventricularis layers. Through this work, information on the material response of the tissue layers, as well as how they contribute to the leaflet as a whole, can be used as a baseline for material selection and comparison when developing novel devices.

Over the next two chapters, this work aimed to develop a finite element-based framework to aid with the design and assessment of bioinspired, fibre-reinforced polymer leaflets. With knowledge of the fibre orientations in native leaflets, Chapter 4 developed a finite element leaflet model with a bioinspired fibre structure. Through this, a procedure was developed to calibrate a fibre reinforced constitutive model to the behaviour of a fibre-embedded elastomer using a simulation of a discrete fibre reinforced dogbone loaded under uniaxial tension. By using the GOH model to describe a fibre-embedded material in the leaflets, computational complexity is reduced when simulating a full trileaflet valve. The trileaflet valve model provided a platform to assess and compare different leaflet structures, starting with fibre orientation. Using this model, it was seen how a tailored fibre structure can improve the material response by reducing overall strain and improve the whole valve's performance. Importantly, this showcased the value and flexibility of this model for assessing different leaflet designs.

Next, this model was used in combination with design of experiments (DOE) to determine the best combination of key structural features for the two materials of interest. Pairing DOE with

finite element modelling in this way allowed us to investigate the impact of leaflet thickness, number of layers, and fibre spacing on the material response of the leaflets as well as whole valve performance. Through this, it was noted that all three factors contribute to the leaflet response in different ways. For example, number of layers and fibre spacing have a strong correlation with leaflet stress and strain, but have less impact on opening behaviour compared to leaflet thickness. Meanwhile, leaflet thickness also contributes to material stress and strain. Using DOE showed not just the impact of the factors investigated, but also enabled the identification of the most desirable combinations of factors based on design targets. Most importantly, it was able to predict the results of untested combinations of factors. By creating models of the best combinations and comparing their results to predictions from the software, it was seen that the model results aligned very well with the predicted results. This showed the value of using FE and DOE tools together: FE modelling already increases the assessment time of various material combinations compared to in vitro testing, and DOE further increases the efficiency of the process. With the factors of interest, a total of 64 different combinations were possible, but through DOE the design space was able to be mapped and predicted with only 12 unique combinations. Using these methods can aid the device design process significantly by indicating the best combinations to test, reducing testing time and materials spent on manufacturing.

A key point highlighted in Chapter 4 was how impactful fibre orientation was on the leaflet material response and overall performance of the valve model. It showed that optimising the fibre orientations for this particular leaflet shape could improve outcomes in terms of opening characteristics and material stress and strain. This was explored in Chapter 5, where fibre orientations were optimised using a fibre reorientation algorithm (Creane et al. 2011). By reorienting the fibres based on the principal strain directions in the leaflet, the overall strain in the material was reduced compared to the isotropic configuration. Also, strain was reduced in comparison to the bioinspired configuration developed in Chapter 4. A significant observation in this work was the dependence of optimal fibre orientation on leaflet geometry and optimisation strategy. Other research has used similar fibre reorientation or remodelling methods to identify optimal structural reinforcement in leaflets (Driessen et al. 2008; Serrani et al. 2016), but the structures identified by each of these procedures are unique to the investigated leaflet shape. Additionally, in this work, two different reorientation methods were employed. Each oriented the fibres with respect to the principal strain directions, but M1 oriented the two fibre families symmetrically about the maximum principal direction, while M2 oriented the families with either the maximum or middle principal direction. Strain reduction in the leaflets shows that M1 was more favourable in this particular leaflet shape and loading.

Finally, this chapter also looked at a specialised case of a non-circular orifice shape and how reorientation might be able to improve material response in this case. By optimising the fibre structure, the strains on either side of the leaflet became more uniform and symmetrical. This showcased the flexibility of this method to inform design not just for idealised, symmetrical orifice geometries, but also for patient-specific applications.

These models did not include the presence of fibre crimp or investigate inclusion of multiple layers. Notable crimp of collagen fibres was seen and quantified in the native porcine leaflets, indicating significance of this feature for leaflet function, but this was not included in the design of these fibre-reinforced leaflets. While it is possible to manufacture serpentine fibre structures using MEW (Saidy et al. 2019)**,** the inclusion of this feature would introduce even more independent variables to the design framework as well as potential manufacturing challenges. Thus, the fibre reinforcement structure remained simple, comprised of linear fibres. Inclusion of crimp should be investigated in future iterations of this fibre-reinforced leaflet. For the same reasons, the leaflet was maintained as a single layer, but the addition and use of multiple layers should be a key direction of future development.

Chapters 4 and 5 together form an in silico framework for the design, development, and assessment of a bioinspired, fibre-reinforced polymer leaflet valve. Here, they were used to identify the best combination of a PEEK-like fibre reinforcement structure, manufactured using MEW, embedded within a compliant PDMS. After this, the fibre reinforcement structure was optimised for this particular leaflet shape based on the ACURATE neo2 Aortic Valve. While these materials were used on this particular leaflet shape, the value of using FE-based methods for this is that they can be applied to any materials or valve shape of interest. Additionally, the parameters of the DOE explored in Chapter 4 can be expanded to look at a wider range of structural features or even other characteristics. These can include fibre diameter, different fibre or matrix materials, and leaflet shape, as well as fibre crimp and layers as mentioned earlier. These methods can be used to identify the best candidates for further in vitro testing, allowing less time to be spent manufacturing and testing different combinations. Ultimately, this can improve the valve development process and enable researchers to assess a wider range of materials and structures in a shorter timeframe.

Chapters 6 and 7 looked at the translatability of the methods used and insights gained throughout the FE valve design framework. In Chapter 6, the manufacturability of a MEW fibre-embedded PDMS was tested along with calibration and validation of the FE material modelling. First, MEW meshes were manufactured using PCL, the gold-standard material used with this technique. These were successfully embedded within Sylgard-184 PDM cured at a 16:1 ratio of polymer to curing agent using a custom-built, enclosed metal mould. This moulding system

contains low-thickness shims to control the overall sample thickness, and enables customisation of the overall thickness by varying the combinations of shims. Additionally, they ensure that the mesh is maintained at the centre of the sample after curing. It was seen that the overall thickness of the manufactured samples was larger than intended, likely due to the reuse of the shims. However, there was no increase in thickness of the samples with a MEW structure embedded, showing that the final thickness is not impacted by the addition of a MEW structure up to 8 layers. The moulded samples were mechanically tested in a custom-made flexural bulge loading rig that has been use for the mechanical characterisation and FE model calibration of bovine pericardium (Whelan 2021; Whelan, O'Brien, et al. 2021). FE models were created of the embedded structures and compared to the bulge loading. Additionally, models were created to be compared to uniaxial tensile testing previously performed. Unexpectedly, it was seen that for both PDMS and MEW-embedded materials the bulge behaviour was not well predicted using models based on the uniaxial tensile response of the material. However, the uniaxial tensile response of both PDMS and MEW-embedded samples were well described with FE models. This phenomenon was seen before in PDMS (Hopf et al. 2016), where the bulge inflation of the material resulted in a stiffer response than what was predicted by uniaxial tensile testing. On the other hand, the bulge behaviour of MEW-embedded PDMS gave a more compliant response than what was predicted from uniaxial tensile testing. In order to achieve a bulge height of a similar magnitude, the PCL stiffness needed to be reduced by 85% in the uniaxial model. What this has shown is that in order to obtain a constitutive model calibrated to these materials, a more comprehensive mechanical testing protocol and calibration procedure should be adopted.

All of the variations of materials calibrated during this work were implemented in the dynamic trileaflet valve model used in the previous chapters. Through this, a wide variability in leaflet and valve responses were seen. Notably, the calibrations for PDMS and MEW-embedded PDMS that best matched the experimental bulge testing were the two valves with the most favourable leaflet response. However, even though the models predicted near identical bulge height for the two models, the valves differed in their strain and opening behaviour. The key takeaway from this is that to obtain a comprehensive and representative ground truth for these materials to enable accurate calibration for the FE models, these materials should be used to manufacture valves. Only through pulse duplicator assessment of valves with this material will we be able to reliably characterise the material in this application.

Finally, Chapter 7 investigated the suturability of MEW-embedded PDMS, looking to assess how well the material could be integrated into current valve manufacturing procedures. In the first iteration of a leaflet, an initial suturing test closely mimicking the in-house leaflet suturing

procedures showed promising suturability of the material. The three leaflets were tied together and into a rubber sheet to mimic the valve's inner skirt with minimal complications. Small tears between the suture and leaflet edge appeared at leaflet corners, particularly in places where earlier knots were created to hold the leaflets in place, but notably these tears did not propagate between suture holes or into the leaflet belly. Additionally, PDMS is tackier than the porcine pericardium used, and it was a concern that this could make them difficult to handle, but that was not the case. This first suturability assessment showed the potential of this material to be implemented into the current manufacturing procedures, and highlighted areas for improvement.

A second leaflet design was created that implemented solutions to tearing, as well as bringing in a customised, reoriented fibre reinforcement structure informed from Chapter 5. This iteration showcased the flexibility and customisability of using MEW for making the fibre reinforcement structure, as there is a wide freedom of design. The M2 reinforcement structure was made in order to show the manufacturability of two very different fibre structures. Also, a reinforcement strip around the edge of the leaflet was added in between fibre layers to improve suture retention.

Through these last two chapters, the polymer leaflet design framework was brought full circle, showing the manufacturability of customised fibre-reinforced PDMS leaflets. Within this in silico and manufacturing framework, a wide range of materials can be investigated and, ultimately, manufactured for future assessment.

8.1 Future directions

This work has established an FE-based framework for the design and development of novel, fibre-reinforced polymer leaflets for future prosthetic valves, and has resulted in the realisation of design outputs into manufactured leaflets. While it has shown its benefit so far, there is availability for improvements and future applications:

- Full valve testing of the fibre-reinforced PDMS leaflets by pulse duplicator testing should be performed in order to effectively calibrate and validate the FE full valve models. A number of combinations of materials should be investigated to fully cover the range of possible materials, including just PDMS leaflets, the most desirable combination highlighted from the DOE study, one combination that is much more stiff, and another that is much less stiff.

- Suturability testing of leaflets should be performed to determine the most effective edge reinforcement, and ensure that the suture retention of the leaflets is adequate to

not induce failure during the device lifetime. Suture retention can be tested according to ISO 7198.

- The trileaflet valve model described here uses a non-deformable boundary condition on the leaflet edges and assumes equal pressure distribution across the leaflets. These assumptions should be investigated and accounted for by implementing a model with either a deformable frame or a simplified deformable boundary condition at the leaflet edges. Further, the impact of fluid on the leaflet deformation should be studied by implementing a fluid-structure integration model.

- MEW printing parameters should be optimised for the creation of fibre reinforcement structures in order to improve fibre coherence. Additionally, this should be investigated to control for fibre diameter. Further, the impact of ambient temperature and humidity can be explored to improve inter-layer bonding and result in a more solid final structure.

- Scaling of manufacturing procedures can be explored to improve the industrial feasibility of these leaflets. This can include printing multiple leaflet structures at once, using larger moulds, as well as investigating the ability to print a MEW structure directly onto PDMS. As the MEW machine is built in-house, it is customisable to allow for implementation of a larger collector plate or other equipment that may be needed.

- Implementation of crimp into the fibre-reinforcement structure could enable more customisability of leaflet material response and potentially improve localised stress peaks in the leaflet to protect against material failure. This should be informed based on crimp quantification in Chapter 3. MEW has been used to manufacture wavy structures, and a combination of crimped and non-crimped fibres may improve overall valve performance (Olvera et al. 2020; Saidy et al. 2019, 2022).

- Throughout the modelling work, the MEW fibre diameter was assumed to be 20 μm, while in manufacturing meshes this diameter was seen to be very variable. Future development in this should perform fibre diameter verification to ensure consistent and predictable fibre diameters.

- Leaflet design can be expanded to include multiple layers or a curved shape, more closely replicating the native aortic valve leaflet structure. Using MEW, different fibre structures can be manufactured to replicate the fibrosa or ventricularis collagen structures. Additionally, the inclusion of a spongiosa-like layer should be considered;

this may require further mechanical assessment of the native spongiosa, as well as exploration of suitable materials to replicate this. By adjusting the collector plate, MEW fibres can be printed on a curved surface (Peiffer et al. 2020). Inducing a non-flat geometry may have implications on the permanent strain accumulation in the material, as well as potentially induce a pre-stressed state that could allow for a more efficient valve design (Kovarovic et al. 2022).

- The fatigue behaviour of the material should be investigated to determine suitability for long-term use. Performing long-term fatigue tests, such as accelerated wear testing, should be used. Additionally, insight from these could be used to inform a damage-based FE model to improve future design criteria (Ghasemi, Nolan, and Lally 2018; Whelan 2021).

- This tool should be used to investigate alternative material combinations. A wide range of novel elastomeric polymers are available and could potentially be more suitable to this application than those currently explored.

- The FE framework should be packaged into a simple tool that can be integrated into current industrial design processes with limited technical background. Ideally, it should enable a user to input materials of interest or specific design requirements, and output a customised material combination and specialised fibre reinforcement structure. Additionally, it could be integrated with other tools to output the gcode needed for MEW printing (Devlin et al. 2024).

- Applications of this design framework beyond valves can and should be explored. For example, this type of structure and design approach could deliver novel, mechanically optimised materials to replace the current non-resorbable transvaginal mesh used to treat pelvic organ prolapse and stress urinary incontinence (Ruffolo et al. 2023). In addition, this framework can offer insights to fibre-reinforcement structures manufactured using procedures other than MEW. Possible manufacturing methods could include laser cut structures, textiles, or other novel additive manufacturing techniques such as filament-based MEW (F-MEW) (Mueller et al. 2023).

Chapter 9 Concluding remarks

The overall aims of this thesis were to provide necessary baseline information on native aortic leaflet tissue to drive development of future bioinspired valve devices, along with developing a finite element-based framework to enable this device creation, optimisation, and assessment. Ultimately, this findings presented here can aid future polymeric valve development, as well as development of other specialised fibre reinforcement structures for other applications. The primary findings and outputs are summarised here:

- Key structural and material parameters of native porcine aortic leaflets were determined in order to direct development of future bioinspired leaflet materials. This includes collagen fibre crimp quantification in both the fibrosa and ventricularis, as well as collagen fibre orientation assessment in the commissure and belly of leaflets. Additionally, the mechanical and material response of the whole leaflet, fibrosa, and ventricularis layers were characterised, along with both initial and final stiffness, showing the contributions of the two layers in the whole leaflet.

- A trileaflet dynamic valve model based on the ACURATE neo2 Aortic Valve was developed with the ability to define local fibre orientations and material properties, as well as customising leaflet geometry. Alongside this, a methodology to assess leaflet and valve functionality was established through determination of material stress and strain, as well as valve opening area and efficiency. This enables the assessment of a variety of materials and leaflet structures to assess leaflet candidates.

- A methodology of using DOE alongside FE was established in order to quantify the impact of varying structural features in a MEW fibre reinforcement structure on valve and leaflet performance. This also enables the prediction of untested parameter combinations to inform future manufacturing and testing. Ultimately, this will reduce time and resources manufacturing and testing possible candidates, and allows for the exploration of a wider variety of parameters.

- Fibre reorientation was used to optimise the fibre structure within a FE leaflet model, decreasing overall leaflet strains while maintaining valve function, potentially leading to extended material lifetimes. Using this will allow for the creation of customised fibre reinforcement structures based on leaflet and frame shapes, as well as local patient anatomy.

- The feasibility of creating fully customised MEW fibre-reinforcement structures, informed by FE models and embedded within a PDMS matrix was established. This enables full flexibility in the design of future fibre-reinforced polymer leaflets using these manufacturing techniques.

- Suturability of the fibre-reinforced materials was explored, showing strong potential of integrating these leaflets into existing valve manufacturing methods. Additionally, the flexibility of manufacturing a fibre structure enables customisation of suture reinforcement around the leaflet edge.

References

Ambrosy, Andrew P., Alan S. Go, Thomas K. Leong, Elisha A. Garcia, Alex J. Chang, Justin J. Slade, Edward J. McNulty, Jacob M. Mishell, Andrew N. Rassi, Ivy A. Ku, David C. Lange, Femi Philip, Benjamin Z. Galper, Natalia Berry, and Matthew D. Solomon. 2023. "Temporal Trends in the Prevalence and Severity of Aortic Stenosis within a Contemporary and Diverse Community-Based Cohort." *International Journal of Cardiology* 384(April):107–11. doi: 10.1016/j.ijcard.2023.04.047.

Ariati, Ronaldo, Flaminio Sales, Andrews Souza, Rui A. Lima, and João Ribeiro. 2021. "Polydimethylsiloxane Composites Characterization and Its Applications: A Review." *Polymers* 13(23):1–21. doi: 10.3390/polym13234258.

Armfield, Dylan, Sam Boxwell, Laoise McNamara, Scott Cook, Shane Conway, Mert Celikin, and Philip Cardiff. 2024. "Effect of Bioprosthetic Leaflet Anisotropy on Stent Dynamics of Transcatheter Aortic Valve Replacement Devices." *Journal of the Mechanical Behavior of Biomedical Materials* 157(July):106650. doi: 10.1016/j.jmbbm.2024.106650.

Attmann, Tim, Ulrich Steinseifer, Jochen Cremer, and Georg Lutter. 2006. "Percutaneous Valve Replacement: A Novel Low-Profile Polyurethane Valved Stent." *European Journal of Cardio-Thoracic Surgery* 30(2):379. doi: 10.1016/j.ejcts.2006.04.035.

Baker, Stephen R., Soham Banerjee, Keith Bonin, and Martin Guthold. 2016. "Determining the Mechanical Properties of Electrospun Poly-ε-Caprolactone (PCL) Nanofibers Using AFM and a Novel Fiber Anchoring Technique." *Materials Science and Engineering: C* 59:203–12. doi: 10.1016/J.MSEC.2015.09.102.

Balguid, Angelique, Mirjam P. Rubbens, Anita Mol, Ruud A. Bank, Ad J. J. C. Bogers, Jorge P. Van Kats, Bas A. J. M. De Mol, Frank P. T. Baaijens, and Carlijn V. C. Bouten. 2007. "The Role of Collagen Cross-Links in Biomechanical Behavior of Human Aortic Heart Valve Leaflets - Relevance for Tissue Engineering." *Tissue Engineering* 13(7):1501–11. doi: 10.1089/ten.2006.0279.

Beaver, Thomas, Joseph E. Bavaria, Bartley Griffith, Lars G. Svensson, Philippe Pibarot, Michael A. Borger, Omar M. Sharaf, David A. Heimansohn, Vinod H. Thourani, Eugene H. Blackstone, and John D. Puskas. 2024. "Seven-Year Outcomes Following Aortic Valve Replacement with a Novel Tissue Bioprosthesis." *Journal of Thoracic and Cardiovascular Surgery* 168(3):781–91. doi: 10.1016/j.jtcvs.2023.09.047.

Bernacca, Gillian M., T. G. Mackay, R. Wilkinson, and D. J. Wheatley. 1997. "Polyurethane Heart Valves: Fatigue Failure, Calcification, and Polyurethane Structure." *Journal of*

Biomedical Materials Research 34(3):371–79. doi: 10.1002/(SICI)1097-4636(19970305)34:3<371::AID-JBM12>3.0.CO;2-J.

Bernacca, Gillian M., Ian Straub, and David J. Wheatley. 2002. "Mechanical and Morphological Study of Biostable Polyurethane Heart Valve Leaflets Explanted from Sheep." *Journal of Biomedical Materials Research* 61(1):138–45. doi: 10.1002/jbm.10149.

Bernardi, L., R. Hopf, A. Ferrari, A. E. Ehret, and E. Mazza. 2017. "On the Large Strain Deformation Behavior of Silicone-Based Elastomers for Biomedical Applications." *Polymer Testing* 58:189–98. doi: 10.1016/j.polymertesting.2016.12.029.

Bezuidenhout, Deon, David F. Williams, Chima Ofoegbu, Jacques Scherman, and Peter Zilla. 2017. "TAVI for Low to Middle Income Countries." *European Heart Journal* 38(16):1182–84. doi: 10.1093/eurheartj/ehx169.

Biancari, Fausto, Paola D'Errigo, Marco Barbanti, Gabriella Badoni, Corrado Tamburino, Gianluca Polvani, Giuliano Costa, Giovanni Baglio, and Stefano Rosato. 2024. "Ten-Year Outcomes after Transcatheter or Surgical Aortic Valve Replacement in Low-Risk Patients: The OBSERVANT Study." *IJC Heart and Vasculature* 55(July):101545. doi: 10.1016/j.ijcha.2024.101545.

Billiar, K. L., and M. S. Sacks. 2000. "Biaxial Mechanical Properties of the Natural and Glutaraldehyde Treated Aortic Valve Cusp - Part I: Experimental Results." *Journal of Biomechanical Engineering* 122(1):23–30. doi: 10.1115/1.429624.

Boehm, Christian A., Christine Donay, Andreas Lubig, Stephan Ruetten, Mahmoud Sesa, Alicia Fernández-Colino, Stefanie Reese, and Stefan Jockenhoevel. 2023. "Bio-Inspired Fiber Reinforcement for Aortic Valves: Scaffold Production Process and Characterization." *Bioengineering* 10(9). doi: 10.3390/bioengineering10091064.

Boretos, John W., and William S. Pierce. 1967. "Segmented Polyurethane: A New Elastomer for Biomedical Applications." *Science* 158(3807):1481–82. doi: 10.1126/science.158.3807.1481.

Bouma, B. J., R. B. A. Van den Brink, J. H. P. Van der Meulen, H. A. Verheul, E. C. Cheriex, H. P. M. Hamer, E. Dekker, K. I. Lie, and J. G. P. Tijssen. 1999. "To Operate or Not on Elderly Patients with Aortic Stenosis: The Decision and Its Consequences." *Heart* 82(2):143–48. doi: 10.1136/hrt.82.2.143.

Bourguignon, Thierry, Anne Lorraine Bouquiaux-Stablo, Pascal Candolfi, Alain Mirza, Claudia Loardi, Marc Antoine May, Rym El-Khoury, Michel Marchand, and Michel Aupart. 2015. "Very Long-Term Outcomes of the Carpentier-Edwards Perimount Valve in Aortic

Position." *Annals of Thoracic Surgery* 99(3):831–37. doi: 10.1016/j.athoracsur.2014.09.030.

Bourguignon, Thierry, R. El Khoury, P. Candolfi, C. Loardi, A. Mirza, J. Boulanger-Lothion, AL Bouquiaux-Stablo-Duncan, F. Espitalier, M. Marchand, and M. Aupart. 2015. "Very Long-Term Outcomes of the Carpentier-Edwards Perimount Aortic Valve in Patients Aged 60 or Younger." *The Annals of Thoracic Surgery* 100(3):853–59. doi: 10.1016/J.ATHORACSUR.2015.03.105.

Broom, N. D. 1978. "The Observation of Collagen and Elastin Structures in Wet Whole Mounts of Pulmonary and Aortic Leaflets." *The Journal of Thoracic and Cardiovascular Surgery* 75(1):121–30.

Brown, Toby D., Paul D. Dalton, and Dietmar W. Hutmacher. 2016. "Melt Electrospinning Today: An Opportune Time for an Emerging Polymer Process." *Progress in Polymer Science* 56:116–66. doi: 10.1016/j.progpolymsci.2016.01.001.

Brubert, Jacob, Stefanie Krajewski, Hans Peter Wendel, Sukumaran Nair, Joanna Stasiak, and Geoff D. Moggridge. 2016. "Hemocompatibility of Styrenic Block Copolymers for Use in Prosthetic Heart Valves." *Journal of Materials Science: Materials in Medicine* 27(2):1–12. doi: 10.1007/s10856-015-5628-7.

Bruschi, Giuseppe, Federico De Marco, Luigi Martinelli, and Silvio Klugmann. 2013. "CoreValve® Transcatheter Self-Expandable Aortic Bioprosthesis." *Expert Review of Medical Devices* 10(1):15–26. doi: 10.1586/erd.12.64.

Bui, Hieu, Amina Ishrat, Susan James, and Lakshmi Prasad Dasi. 2021. "Durability Optimization of Novel Hyaluronic Acid Enhanced Polymeric Transcatheter Aortic Valves." *Journal of the American College of Cardiology* 77(18):3236. doi: 10.1016/s0735-1097(21)04590-3.

Bui, Hieu, Susan James, and Lakshmi Dasi. 2021. "TCT-326 In Vitro Performance of Thermoformed Polymeric Transcatheter Heart Valves." *Journal of the American College of Cardiology* 78(19):B133. doi: 10.1016/j.jacc.2021.09.1179.

Cacciola, G., G. W. M. Peters, and F. P. T. Baaijens. 2000. "A Synthetic Fiber-Reinforced Stentless Heart Valve." *Journal of Biomechanics* 33(6):653–58. doi: 10.1016/S0021-9290(00)00003-8.

Campagnola, P. J., and C. Y. Dong. 2011. "Second Harmonic Generation Microscopy: Principles and Applications to Disease Diagnosis." *Laser and Photonics Reviews* 5(1):13–26. doi: 10.1002/lpor.200910024.

Campion, Greg, Kylie Hershberger, Alix Whelan, Jack Conroy, Caitríona Lally, and Bruce P. Murphy. 2021. “A Biomechanical and Microstructural Analysis of Bovine and Porcine Pericardium for Use in Bioprosthetic Heart Valves.” *Structural Heart* 5(5):486–96. doi: 10.1080/24748706.2021.1938317.

Cao, Kai, Fucheng Zhang, Ahmadreza Zaeri, Ralf Zgeib, and Robert Change. 2021. “A Charge-Based Mechanistic Study into the Effect of Collector Temperature on Melt.” *Advanced Materials Technologies* 6. doi: 10.1002/admt.202100251.

Carroll, John D., Michael J. Mack, Sreekanth Vemulapalli, Howard C. Herrmann, Thomas G. Gleason, George Hanzel, G. Michael Deeb, Vinod H. Thourani, David J. Cohen, Nimesh Desai, Ajay J. Kirtane, Susan Fitzgerald, Joan Michaels, Carole Krohn, Frederick A. Masoudi, Ralph G. Brindis, and Joseph E. Bavaria. 2020. “STS-ACC TVT Registry of Transcatheter Aortic Valve Replacement.” *Journal of the American College of Cardiology* 76(21):2492–2516. doi: 10.1016/j.jacc.2020.09.595.

Castilho, Miguel, Gernot Hochleitner, Wouter Wilson, Bert Van Rietbergen, Paul D. Dalton, Jürgen Groll, Jos Malda, and Keita Ito. 2018. “Mechanical Behavior of a Soft Hydrogel Reinforced with Three-Dimensional Printed Microfibre Scaffolds.” *Scientific Reports 2018 8:1* 8(1):1–10. doi: 10.1038/S41598-018-19502-Y.

Chaikof, Elliot L. 2009. “The Development of Prosthetic Heart Valves — Lessons in Form and Function.” *Https://Doi.Org/10.1056/NEJMp078175* 357(14):1368–71. doi: 10.1056/NEJMP078175.

Chen, Shiping, Bowen Zhang, Jingyi Hu, Xiaofan Zheng, Siyu Qin, Chaojing Li, Shengzhang Wang, Jifu Mao, and Lu Wang. 2023. “Bioinspired NiTi-Reinforced Polymeric Heart Valve Exhibiting Excellent Hemodynamics and Reduced Stress.” *Composites Part B: Engineering* 255(November 2022):110615. doi: 10.1016/j.compositesb.2023.110615.

Chen, Xiyi, Oleg Nadiarynkh, Sergey Plotnikov, and Paul J. Campagnola. 2012. “Second Harmonic Generation Microscopy for Quantitative Analysis of Collagen Fibrillar Structure.” *Nature Protocols* 7(4):654–69. doi: 10.1038/nprot.2012.009.

Chetta, G. E., and J. R. Lloyd. 1980. “The Design, Fabrication and Evaluation of a Trileaflet Prosthetic Heart Valve.” *Journal of Biomechanical Engineering* 102(1):34–41. doi: 10.1115/1.3138196.

Choi, Peter J., Hugo Zazueta, John A. Acevedo, Philip Park, Rio Grande, Citation Peter J. Choi, Hugo Zazueta, John A. Acevedo, and Philip Park Struc-. 2024. “Structural Fiber Mesh Reinforcement of a Polymeric Heart Valve : Improving Valve Durability and Leaflet

Closure Effectiveness.” 48317–26. doi: 10.26717/BJSTR.2024.56.008885.

Claiborne, Thomas E., Jawaad Sheriff, Maximilian Kuetting, Ulrich Steinseifer, Marvin J. Slepian, and Danny Bluestein. 2013a. “In Vitro Evaluation of a Novel Hemodynamically Optimized Trileaflet Polymeric Prosthetic Heart Valve.” *Journal of Biomechanical Engineering* 135(2):1–8. doi: 10.1115/1.4023235.

Claiborne, Thomas E., Jawaad Sheriff, Maximilian Kuetting, Ulrich Steinseifer, Marvin J. Slepian, and Danny Bluestein. 2013b. “In Vitro Evaluation of a Novel Hemodynamically Optimized Trileaflet Polymeric Prosthetic Heart Valve.” *Journal of Biomechanical Engineering* 135(2). doi: 10.1115/1.4023235.

Claiborne, Thomas E., Michalis Xenos, Jawaad Sheriff, Wei Che Chiu, Joao Soares, Yared Alemu, Shikha Gupta, Stefan Judex, Marvin J. Slepian, and Danny Bluestein. 2013. “Toward Optimization of a Novel Trileaflet Polymeric Prosthetic Heart Valve via Device Thrombogenicity Emulation.” *ASAIO Journal* 59(3):275–83. doi: 10.1097/MAT.0b013e31828e4d80.

Coisne, Augustin, Patrizio Lancellotti, Gilbert Habib, Madalina Garbi, Jordi Sanchez Dahl, Marco Barbanti, Mani A. Vannan, Vassilios S. Vassiliou, Dariusz Dudek, Ovidiu Chioncel, Johannes L. Waltenberger, Victoria L. Johnson, Ruggero De Paulis, Rodolfo Citro, and Philippe Pibarot. 2023. “ACC/AHA and ESC/EACTS Guidelines for the Management of Valvular Heart Diseases: JACC Guideline Comparison.” *Journal of the American College of Cardiology* 82(8):721–34. doi: 10.1016/j.jacc.2023.05.061.

Colombo, A., H. Zahedmanesh, D. M. Toner, P. A. Cahill, and C. Lally. 2010. “A Method to Develop Mock Arteries Suitable for Cell Seeding and In-Vitro Cell Culture Experiments.” *Journal of the Mechanical Behavior of Biomedical Materials* 3(6):470–77. doi: 10.1016/j.jmbbm.2010.04.003.

Coulter, Fergal B., Manuel Schaffner, Jakob A. Faber, Ahmad Rafsanjani, Robin Smith, Harish Appa, Peter Zilla, Deon Bezuidenhout, and André R. Studart. 2019. “Bioinspired Heart Valve Prosthesis Made by Silicone Additive Manufacturing.” *Matter* 1(1):266–79. doi: 10.1016/j.matt.2019.05.013.

Creane, Arthur, Eoghan Maher, Sherif Sultan, Niamh Hynes, Daniel J. Kelly, and Caitríona Lally. 2011. “Prediction of Fibre Architecture and Adaptation in Diseased Carotid Bifurcations.” *Biomechanics and Modeling in Mechanobiology* 10(6):831–43. doi: 10.1007/s10237-010-0277-8.

Cribier, Alain, Helene Eltchaninoff, Assaf Bash, Nicolas Borenstein, Christophe Tron, Fabrice

Bauer, Genevieve Derumeaux, Frederic Anselme, François Laborde, and Martin B. Leon. 2002. “Percutaneous Transcatheter Implantation of an Aortic Valve Prosthesis for Calcific Aortic Stenosis: First Human Case Description.” *Circulation* 106(24):3006–8. doi: 10.1161/01.CIR.0000047200.36165.B8.

Cribier, Alain, Hélène Eltchaninoff, Christophe Tron, Fabrice Bauer, Carla Agatiello, Laurent Sebagh, Assaf Bash, Danielle Nusimovici, P. Y. Litzler, Jean Paul Bessou, and Martin B. Leon. 2004. “Early Experience with Percutaneous Transcatheter Implantation of Heart Valve Prosthesis for the Treatment of End-Stage Inoperable Patients with Calcific Aortic Stenosis.” *Journal of the American College of Cardiology* 43(4):698–703. doi: 10.1016/j.jacc.2003.11.026.

Croisier, F., A. S. Duwez, C. Jérôme, A. F. Léonard, K. O. Van Der Werf, P. J. Dijkstra, and M. L. Bennink. 2012. “Mechanical Testing of Electrospun PCL Fibers.” *Acta Biomaterialia* 8(1):218–24. doi: 10.1016/J.ACTBIO.2011.08.015.

Czer, L. S., A. Chaux, J. M. Matloff, M. A. DeRobertis, S. A. Nessim, D. Scarlata, S. S. Khan, T. P. Tsai, and C. Blanche. 1990. “Ten-Year Experience with the St. Jude Medical Valve for Primary Valve Replacement.” *Journal of Thoracic and Cardiovascular Surgery* 100(1):discussion 54-55.

D’Souza, Marissa, Nicholas A. Macdonald, Julian L. Gendreau, Pate J. Duddleston, Austin Y. Feng, and Allen L. Ho. 2019. “Graft Materials and Biologics for Spinal Interbody Fusion.” *Biomedicines* 7(4):75. doi: 10.3390/biomedicines7040075.

Daebritz, Sabine H., Bernd Fausten, Benita Hermanns, Andreas Franke, Joerg Schroeder, Jan Groetzner, Ruediger Autschbach, Bruno J. Messmer, and Jörg S. Sachweh. 2004. “New Flexible Polymeric Heart Valve Prostheses for the Mitral and Aortic Positions.” *Heart Surgery Forum* 7(5):371–78. doi: 10.1532/HSF98.20041083.

Daebritz, Sabine H., Bernd Fausten, Benita Hermanns, Joerg Schroeder, Jan Groetzner, Ruediger Autschbach, Bruno J. Messmer, and Jörg S. Sachweh. 2004. “Introduction of a Flexible Polymeric Heart Valve Prosthesis with Special Design for Aortic Position.” *European Journal of Cardio-Thoracic Surgery* 25(6):946–52. doi: 10.1016/j.ejcts.2004.02.040.

Dandeniyage, Loshini S., Raju Adhikari, Mark Bown, Robert Shanks, Benu Adhikari, Christopher D. Easton, Thomas R. Gengenbach, David Cookson, and Pathiraja A. Gunatillake. 2019. “Morphology and Surface Properties of High Strength Siloxane Poly(Urethane-Urea)s Developed for Heart Valve Application.” *J Biomed Mater Res Part B: Appl Biomater* 107(1):112–21. doi: 10.1002/jbm.b.34101.

Dandeniyage, Loshini S., Pathiraja A. Gunatillake, Raju Adhikari, Mark Bown, Robert Shanks, and Benu Adhikari. 2017. “Development of High Strength Siloxane Poly(Urethane-Urea) Elastomers Based on Linked Macrodiols for Heart Valve Application.” *J Biomed Mater Res Part B: Appl Biomater* 106:1712–20. doi: 10.1002/jbm.b.33970.

Davachi, Seyed Mohammad, Behzad Shiroud Heidari, Iman Hejazi, Javad Seyfi, Erfan Oliaei, Arman Farzaneh, and Hamid Rashedi. 2017. “Interface Modified Polylactic Acid/Starch/Poly ε-Caprolactone Antibacterial Nanocomposite Blends for Medical Applications.” *Carbohydrate Polymers* 155:336–44. doi: 10.1016/J.CARBPOL.2016.08.037.

Devlin, Brenna L., Shahak Kuba, Patrick C. Hall, Audrey B. McCosker, Edmund Pickering, Paul D. Dalton, Travis J. Klein, Maria A. Woodruff, and Naomi C. Paxton. 2024. “A Melt Electrowriting Toolbox for Automated G-Code Generation and Toolpath Correction of Flat and Tubular Constructs.” *Advanced Materials Technologies* 2400419:1–14. doi: 10.1002/admt.202400419.

Ding, Houzhu, Kai Cao, Fucheng Zhang, William Boettcher, and Robert C. Chang. 2019. “A Fundamental Study of Charge Effects on Melt Electrowritten Polymer Fibers.” *Materials and Design* 178:107857. doi: 10.1016/j.matdes.2019.107857.

Driessen, Niels J. B., Carlijn V. C. Bouten, and Frank P. T. Baaijens. 2005. “A Structural Constitutive Model for Collagenous Cardiovascular Tissues Incorporating the Angular Fiber Distribution.” *Journal of Biomechanical Engineering* 127(3):494–503. doi: 10.1115/1.1894373.

Driessen, Niels J. B., Martijn A. J. Cox, Carlijn V. C. Bouten, and Frank P. T. Baaijens. 2008. “Remodelling of the Angular Collagen Fiber Distribution in Cardiovascular Tissues.” *Biomechanics and Modeling in Mechanobiology* 7(2):93–103. doi: 10.1007/s10237-007-0078-x.

Driessen, Niels J. B., Anita Mol, Carlijn V. C. Bouten, and Frank P. T. Baaijens. 2007. “Modeling the Mechanics of Tissue-Engineered Human Heart Valve Leaflets.” *Journal of Biomechanics* 40(2):325–34. doi: 10.1016/j.jbiomech.2006.01.009.

Durakovic, Benjamin. 2017. “Design of Experiments Application, Concepts, Examples: State of the Art.” *Periodicals of Engineering and Natural Sciences* 5(3):421–39. doi: 10.21533/pen.v5i3.145.

Eichholz, Kian F., Inês Gonçalves, Xavier Barceló, Angelica S. Federici, David A. Hoey, and Daniel J. Kelly. 2022. “How to Design, Develop and Build a Fully-Integrated Melt

Electrowriting 3D Printer." *Additive Manufacturing* 58(June). doi: 10.1016/j.addma.2022.102998.

Eichholz, Kian F., and David A. Hoey. 2018. "Mediating Human Stem Cell Behaviour via Defined Fibrous Architectures by Melt Electrospinning Writing." *Acta Biomaterialia* 140–51. doi: 10.1016/j.actbio.2018.05.048.

El Faquir, Nahid, Quinten Wolff, Rafi Sakhi, Ben Ren, Zouhair Rahhab, Sander van Weenen, Patrick Geeve, Ricardo P. J. Budde, Eric Boersma, Joost Daemen, Nicolas M. van Mieghem, and Peter P. de Jaegere. 2022. "Distribution of Aortic Root Calcium in Relation to Frame Expansion and Paravalvular Leakage After Transcatheter Aortic Valve Implantation (TAVI): An Observational Study Using a Patient-Specific Contrast Attenuation Coefficient for Calcium Definition and I." *Journal of Cardiovascular Imaging* 30(4):292–304. doi: 10.4250/jcvi.2021.0141.

De Gaetano, Francesco, Marta Serrani, Paola Bagnoli, Jacob Brubert, Joanna Stasiak, Geoff D. Moggridge, and Maria Laura Costantino. 2015. "Fluid Dynamic Characterization of a Polymeric Heart Valve Prototype (Poli-Valve) Tested under Continuous and Pulsatile Flow Conditions." *International Journal of Artificial Organs* 38(11):600–606. doi: 10.5301/ijao.5000452.

Gasser, T. Christian, Ray W. Ogden, and Gerhard A. Holzapfel. 2006. "Hyperelastic Modelling of Arterial Layers with Distributed Collagen Fibre Orientations." *Journal of the Royal Society Interface* 3(6):15–35. doi: 10.1098/rsif.2005.0073.

Gaul, R. T., D. R. Nolan, and C. Lally. 2017. "Collagen Fibre Characterisation in Arterial Tissue under Load Using SALS." *Journal of the Mechanical Behavior of Biomedical Materials* 75:359–68. doi: 10.1016/J.JMBBM.2017.07.036.

Généreux, Philippe, Nicolo Piazza, Maria C. Alu, Tamim Nazif, Rebecca T. Hahn, Philippe Pibarot, Jeroen J. Bax, Jonathon A. Leipsic, Philipp Blanke, Eugene H. Blackstone, Matthew T. Finn, Samir Kapadia, Axel Linke, Michael J. Mack, Raj Makkar, Roxana Mehran, Jeffrey J. Popma, Michael Reardon, Josep Rodes-Cabau, Nicolas M. Van Mieghem, John G. Webb, David J. Cohen, and Martin B. Leon. 2021. "Valve Academic Research Consortium 3: Updated Endpoint Definitions for Aortic Valve Clinical Research." *Journal of the American College of Cardiology* 77(21):2717–46. doi: 10.1016/j.jacc.2021.02.038.

Généreux, Philippe, Rahul P. Sharma, Robert J. Cubeddu, Lucy Aaron, Omar M. Abdelfattah, Konstantinos P. Koulogiannis, Leo Marcoff, Mostafa Naguib, Samir R. Kapadia, Rajendra R. Makkar, Vinod H. Thourani, Benjamin S. van Boxtel, David J. Cohen, Michael Dobbles, Glenn R. Barnhart, Michelle Kwon, Philippe Pibarot, Martin B. Leon, and Linda D. Gillam.

2023. “The Mortality Burden of Untreated Aortic Stenosis.” *Journal of the American College of Cardiology* 82(22):2101–9. doi: 10.1016/j.jacc.2023.09.796.

Ghasemi, Milad, David R. Nolan, and Caitríona Lally. 2018. “An Investigation into the Role of Different Constituents in Damage Accumulation in Arterial Tissue and Constitutive Model Development.” *Biomechanics and Modeling in Mechanobiology* 17(6):1757–69. doi: 10.1007/s10237-018-1054-3.

Ghista, Dhanjoo N. 1976. “Toward an Optimum Prosthetic Trileaflet Aortic-Valve Design.” *Medical & Biological Engineering* 14(2):122–29. doi: 10.1007/BF02478737.

Ghista, Dhanjoo N., and Helmut Reul. 1977. “Optimal Prosthetic Aortic Leaflet Valve: Design Parametric and Longevity Analyses: Development of the Avcothane-51 Leaflet Valve Based on the Optimum Design Analysis.” *Journal of Biomechanics* 10(5–6):313–24. doi: 10.1016/0021-9290(77)90004-5.

Giaretta, Jacopo, Matthew Crago, Thanh Phuong Hoang, Xinying Liu, Aeryne Lee, Yiqi Wang, Syamak Farajikhah, David Frederick Fletcher, Fariba Dehghani, David Scott Winlaw, and Sina Naficy. 2024. “Structural Reinforcements as a Strategy toward Durable Polymeric Heart Valves.” *Cell Reports Physical Science* 5(3):101870. doi: 10.1016/j.xcrp.2024.101870.

Gott, Vincent L., Diane E. Alejo, and Duke E. Cameron. 2003. “Mechanical Heart Valves: 50 Years of Evolution.” *Annals of Thoracic Surgery* 76(6):S2230–39. doi: 10.1016/j.athoracsur.2003.09.002.

Govinna, Nelaka Dilshan, Thomas Keller, Christoph Schick, and Peggy Cebe. 2019. “Melt-Electrospinning of Poly(Ether Ether Ketone) Fibers to Avoid Sulfonation.” *Polymer* 171:50–57. doi: 10.1016/J.POLYMER.2019.03.041.

Gross, L., and M. A. Kugel. 1931. “Topographic Anatomy and Histology of the Valves in the Human Heart.” *The American Journal of Pathology* 7(5):445-474.7.

Guo, Xu Nan, Rui Lin, Kun Zhang, Hui Na Zhang, Ning Zhang, and Guang Yuan Song. 2025. “Biomimetic Multilayered Polymeric Heart Valve Featuring Ultra-Thin Thickness and Exceptional Durability.” *Biochemical and Biophysical Research Communications* 756:151609. doi: 10.1016/j.bbrc.2025.151609.

Haigh, Jodie N., Tim R. Dargaville, and Paul D. Dalton. 2017. “Additive Manufacturing with Polypropylene Microfibers.” *Materials Science and Engineering: C* 77:883–87. doi: 10.1016/J.MSEC.2017.03.286.

Hale, Conor. 2020. “FDA TAVR Approval.” Retrieved July 21, 2020

(https://www.fiercebiotech.com/medtech/fda-opens-up-medtronic-s-tavr-system-to-younger-low-risk-heart-patients-new-approval).

Harken, Dwight E. 1986. “The Emergence of Cardiac Surgery: I. Personal Recollections of the 1940s and 1950s.” *The Journal of Thoracic and Cardiovascular Surgery* 98(5):805–13. doi: 10.1016/S0022-52233(19)34256-4.

Hasan, Anwarul, Kim Ragaert, Wojciech Swieszkowski, Šeila Selimović, Arghya Paul, Gulden Camci-Unal, Mohammad R. K. Mofrad, and Ali Khademhosseini. 2014. “Biomechanical Properties of Native and Tissue Engineered Heart Valve Constructs.” *Journal of Biomechanics* 47(9):1949–63. doi: 10.1016/j.jbiomech.2013.09.023.

Hepfer, R. Glenn, Peng Chen, Kelvin G. M. Brockbank, Alyce L. Jones, Amanda K. Burnette, Zhen Chen, Elizabeth D. Greene, Lia H. Campbell, and Hai Yao. 2018. “The Impact of Heat Treatment on Porcine Heart Valve Leaflets.” *Cardiovascular Engineering and Technology* 9(1):32–41. doi: 10.1007/s13239-017-0334-x.

Hilbert, S. L., V. J. Ferrans, Y. Tomita, E. E. Eidbo, and M. Jones. 1987. “Evaluation of Explanted Polyurethane Trileaflet Cardiac Valve Prostheses.” *Journal of Thoracic and Cardiovascular Surgery* 94(3):419–29. doi: 10.1016/s0022-5223(19)36257-9.

Hochleitner, Gernot, Almoatazbellah Youssef, Andrei Hrynevich, Jodie N. Haigh, Tomasz Jungst, Jürgen Groll, and Paul D. Dalton. 2016. “Fibre Pulsing during Melt Electrospinning Writing.” *BioNanoMaterials* 17(3–4):159–71. doi: 10.1515/BNM-2015-0022/ASSET/GRAPHIC/J_BNM-2015-0022_FIG_010.JPG.

Hopf, R., L. Bernardi, J. Menze, M. Zündel, E. Mazza, and A. E. Ehret. 2016. “Experimental and Theoretical Analyses of the Age-Dependent Large-Strain Behavior of Sylgard 184 (10:1) Silicone Elastomer.” *Journal of the Mechanical Behavior of Biomedical Materials* 60:425–37. doi: 10.1016/j.jmbbm.2016.02.022.

Hørsted Thyregod, Hans Gustav, Troels Højsgaard Jørgensen, Nikolaj Ihlemann, Daniel Andreas Steinbrüchel, Henrik Nissen, Bo Juel Kjeldsen, Petur Petursson, Ole De Backer, Peter Skov Olsen, and Lars Søndergaard. 2024. “Transcatheter or Surgical Aortic Valve Implantation: 10-Year Outcomes of the NOTION Trial.” *European Heart Journal* 45(13):1116–24. doi: 10.1093/eurheartj/ehae043.

Hrynevich, Andrei, Ievgenii Liashenko, and Paul D. Dalton. 2020. “Accurate Prediction of Melt Electrowritten Laydown Patterns from Simple Geometrical Considerations.” *Advanced Materials Technologies* 5(12). doi: 10.1002/admt.202000772.

Hutson, Heather N., Taylor Marohl, Matthew Anderson, Kevin Eliceiri, Paul Campagnola, and

Kristyn S. Masters. 2016. “Calcific Aortic Valve Disease Is Associated with Layer-Specific Alterations in Collagen Architecture.” *PLoS ONE* 11(9):1–18. doi: 10.1371/journal.pone.0163858.

Imamura, E., and M. P. Kaye. 1977. “Function of Expanded-Polytetrafluoroethylene Laminated Trileaflet Valves in Animals.” *Mayo Clinic Proceedings* 52(12):770–75.

Imamura, E., M. P. Kaye, and G. D. Davis. 1977. “Radiographic Assessment of Leaflet Motion of Gore-Tex Laminate Trileaflet Valves and Hancock Xenograft in Tricuspid Position of Dogs.” *Circulation* 56(6):1053–58. doi: 10.1161/01.CIR.56.6.1053.

Ionescu, Marian Ion. 2014. “In the Beginning...” Pp. 1–35 in *Pericardial Heart Valve: The Odyssey of a Continuously evolving Concept*. Society for Cardiothoracic Surgery in Great Britan and Ireland.

Jansen, J., and H. Reul. 1992. “A Synthetic Three-Leaflet Valve.” *Journal of Medical Engineering and Technology* 16(1):27–33. doi: 10.3109/03091909209021954.

Jansen, J., S. Willeke, B. Reiners, P. Harbott, H. Reul, and G. Rau. 1991. “New J-3 Flexible-Leaflet Polyurethane Heart Valve Prosthesis with Improved Hydrodynamic Performance.” *International Journal of Artificial Organs* 14(10):655–60. doi: 10.1177/039139889101401009.

Jenney, Chris, Peter Millson, David W. Grainger, Robert Grubbs, Pathiraja Gunatillake, Simon J. Mccarthy, James Runt, and Jason Beith. 2020. “Assessment of a Siloxane Poly(Urethane-Urea) Elastomer Designed for Implantable Heart Valve Leaflets.” doi: 10.1002/anbr.202000032.

De Jesus Morales, Kenneth J., Utari Santosa, Olga Brazhkina, Pranshu Rajurkar, Hanjoong Jo, and Michael E. Davis. 2024. “A Biomimetic Leaflet Scaffold for Aortic Valve Remodeling.” *Advanced Healthcare Materials* 2303972:1–11. doi: 10.1002/adhm.202303972.

Joyce, Erinn M., Jun Liao, Frederick J. Schoen, John E. Mayer, and Michael S. Sacks. 2009. “Functional Collagen Fiber Architecture of the Pulmonary Heart Valve Cusp.” *Annals of Thoracic Surgery* 87(4):1240–49. doi: 10.1016/j.athoracsur.2008.12.049.

Kade, Juliane C., and Paul D. Dalton. 2021. “Polymers for Melt Electrowriting.” *Advanced Healthcare Materials* 10(1):2001232. doi: 10.1002/ADHM.202001232.

Kalejs, Martins, Peteris Stradins, Romans Lacis, Iveta Ozolanta, Janis Pavars, and Vladimir Kasyanov. 2009. “St Jude Epic Heart Valve Bioprostheses versus Native Human and Porcine Aortic Valves - Comparison of Mechanical Properties.” *Interactive Cardiovascular and Thoracic Surgery* 8(5):553–56. doi: 10.1510/icvts.2008.196220.

Kannan, Ruben Y., Henryk J. Salacinski, Peter E. Butler, and Alexander M. Seifalian. 2005. “Polyhedral Oligomeric Silsesquioxane Nanocomposites: The next Generation Material for Biomedical Applications.” *Accounts of Chemical Research* 38(11):879–84. doi: 10.1021/ar050055b.

Kannan, Ruben Y., Henryk J. Salacinski, Jalal-edin Ghanavi, Ashish Narula, Marianne Odlyha, Habiballah Peirovi, Peter Buter, and Alexander M. Seifalian. 2007. “Silsesquioxane Nanocomposites as Tissue Implants.” *Plastic and Reconstructuve Surgery* 119(6):1653–62. doi: 10.1097/01.prs.0000246404.53831.4c.

Kereiakes, Dean J., Geoff A. Answini, Steven J. Yakubov, Balaj Rai, J. Michael Smith, Steven Duff, Francis L. Shannon, Marc Sakwa, Jason Beith, and David Heimansohn. 2021. “Preliminary Evaluation of a Novel Polymeric Valve Following Surgical Implantation for Symptomatic Aortic Valve Disease.” *JACC: Cardiovascular Interventions* 14:2754–56. doi: 10.1016/j.

Khair, Nipa, Sanchita Bhat, Sakhawat Hossan Robel, Srujana Joshi, Katie Vinterella, Lakshmi Dasi, and Susan James. 2025. “Parametric Finite Element Modeling of Reinforced Polymeric Leaflets for Improved Durability.” *Journal of the Mechanical Behavior of Biomedical Materials* 163(August 2024):106884. doi: 10.1016/j.jmbbm.2024.106884.

Kim, Jaehyeon, Ezgi Bakirci, Kelly L. O’Neill, Andrei Hrynevich, and Paul D. Dalton. 2021. “Fiber Bridging during Melt Electrowriting of Poly -Caprolactone and the Influence of Fiber Diameter and Wall Height.” *Macromolecular Materials and Engineering* 306. doi: 10.1002/mame.202000685.

Koh, Masahiro, Toshikatsu Yagihara, Hideki Uemura, Koji Kagisaki, Ikuo Hagino, Toru Ishizaka, and Soichiro Kitamura. 2005. “Long-Term Outcome of Right Ventricular Outflow Tract Reconstruction Using a Handmade Tri-Leaflet Conduit *.” doi: 10.1016/j.ejcts.2005.01.060.

Kostyunin, Alexander E., Arseniy E. Yuzhalin, Maria A. Rezvova, Evgeniy A. Ovcharenko, Tatiana V Glushkova, and Anton G. Kutikhin. 2020. “Degeneration of Bioprosthetic Heart Valves : Update 2020.” *Journal of the American Heart Association* 1–19. doi: 10.1161/JAHA.120.018506.

Kovarovic, Brandon, Ryan Helbock, Kyle Baylous, Oren M. Rotman, Marvin J. Slepian, and Danny Bluestein. 2022. “Visions of TAVR Future: Development and Optimization of a Second Generation Novel Polymeric TAVR.” *Journal of Biomechanical Engineering* 144(6). doi: 10.1115/1.4054149.

Kovarovic, Brandon J., Oren M. Rotman, Puja B. Parikh, Marvin J. Slepian, and Danny Bluestein. 2020. “Patient-specific in Vitro Testing for Evaluating TAVR Clinical Performance.” *Artificial Organs* 45:E41–52. doi: 10.1111/aor.13841.

Kovarovic, Brandon J., Oren M. Rotman, Puja B. Parikh, Marvin J. Slepian, and Danny Bluestein. 2023. “Mild Paravalvular Leak May Pose an Increased Thrombogenic Risk in Transcatheter Aortic Valve Replacement (TAVR) Patients-Insights from Patient Specific In Vitro and In Silico Studies.” *Bioengineering* 10(2). doi: 10.3390/bioengineering10020188.

Lange, Ruediger, Sabine Bleiziffer, Domenico Mazzitelli, Yacine Elhmidi, Anke Opitz, Marcus Krane, Marcus Andre Deutsch, Hendrik Ruge, Gernot Brockmann, Bernhard Voss, Christian Schreiber, Peter Tassani, and Nicolo Piazza. 2012. “Improvements in Transcatheter Aortic Valve Implantation Outcomes in Lower Surgical Risk Patients: A Glimpse into the Future.” *Journal of the American College of Cardiology* 59(3):280–87. doi: 10.1016/j.jacc.2011.10.868.

Lazic, Stanley E. 2010. “The Problem of Pseudoreplication in Neuroscientific Studies: Is It Affecting Your Analysis?” *BMC Neuroscience* 11:1–17. doi: 10.1186/1471-2202-11-5.

Leat, M. E., and J. Fisher. 1994. “A Synthetic Leaflet Heart Valve with Improved Opening Characteristics.” *Medical Engineering and Physics* 16(6):470–76. doi: 10.1016/1350-4533(94)90071-X.

Leat, M. E., and J. Fisher. 1995. “The Influence of Manufacturing Methods on the Function and Performance of a Synthetic Leaflet Heart Valve.” *Proceedings of the Institution of Mechanical Engineers, Part H: Journal of Engineering in Medicine* 209(1):65–69.

Lee, Chung Hao, Will Zhang, Jun Liao, Christopher A. Carruthers, Jacob I. Sacks, and Michael S. Sacks. 2015. “On the Presence of Affine Fibril and Fiber Kinematics in the Mitral Valve Anterior Leaflet.” *Biophysical Journal* 108(8):2074–87. doi: 10.1016/j.bpj.2015.03.019.

Leon, MB, CR Smith, M. Mack, DC Miller, JW Moses, and LG Svensson. 2010. “Transcatheter Aortic-Valve Implantation for Aortic Stenosis in Patients Who Cannot Undergo Surgery.” *New England Journal of Medicine* 61(2010):61–67. doi: 10.1056/NEJMoa1008232.

Li, Richard L., Jonathan Russ, Costas Paschalides, Giovanni Ferrari, Haim Waisman, Jeffrey W. Kysar, and David Kalfa. 2019. “Mechanical Considerations for Polymeric Heart Valve Development: Biomechanics, Materials, Design and Manufacturing.” *Biomaterials* 225(April):119493. doi: 10.1016/j.biomaterials.2019.119493.

Liao, Jun, Erinn M. Joyce, and Michael S. Sacks. 2008. “Effects of Decellularization on the Mechanical and Structural Properties of the Porcine Aortic Valve Leaflet.” *Biomaterials*

29(8):1065–74. doi: 10.1016/j.biomaterials.2007.11.007.

Lindblom, D., V. O. Bjork, and B. K. Semb. 1986. “Mechanical Failure of the Bjork-Shiley Valve. Incidence, Clinical Presentation, and Management.” *Journal of Thoracic and Cardiovascular Surgery* 92(5):894–907.

Lindblom, D., L. Rodriguez, and V. O. Bjork. 1989. “Mechanical Failure of the Bjork-Shiley Valve. Updated Follow-up and Considerations on Prophylactic Replacement.” *Journal of Thoracic and Cardiovascular Surgery* 97(1):95–97.

Lo, H. B., M. Herold, H. Reul, H. Muckter, K. Taguchi, M. Surman, K. H. Hildingers, H. Lambertz, H. De Haan, S. Handt, G. Hollweg, B. J. Messmer, and G. Rau. 1988. “A Tricuspid Polyurethane Heart Valve as an Alternative to Mechanical Prosthesis or Bioprostheses.” *Trans Am Soc Artif Intern Organs* 34.

Loerakker, S., G. Argento, C. W. J. Oomens, and F. P. T. Baaijens. 2013. “Effects of Valve Geometry and Tissue Anisotropy on the Radial Stretch and Coaptation Area of Tissue-Engineered Heart Valves.” *Journal of Biomechanics* 46(11):1792–1800. doi: 10.1016/j.jbiomech.2013.05.015.

MacIsaac, Sarah, Iqbal H. Jaffer, Emilie P. Belley-Côté, Graham R. McClure, John W. Eikelboom, and Richard P. Whitlock. 2019. “How Did We Get Here?: A Historical Review and Critical Analysis of Anticoagulation Therapy Following Mechanical Valve Replacement.” *Circulation* 140(23):1933–42. doi: 10.1161/CIRCULATIONAHA.119.041105.

Mackay, T. G., D. J. Wheatley, G. M. Bernacca, A. C. Fisher, and C. S. Hindle. 1996. “New Polyurethane Heart Valve Prosthesis: Design, Manufacture and Evaluation.” *Biomaterials* 17(19):1857–63. doi: 10.1016/0142-9612(95)00242-1.

Manji, Rizwan A., Whayoung Lee, and David K. C. Cooper. 2015. “Xenograft Bioprosthetic Heart Valves: Past, Present and Future.” *International Journal of Surgery* 23:280–84. doi: 10.1016/j.ijsu.2015.07.009.

Marco, Russo, Taramasso Maurizio, Guidotti Andrea, Pozzoli Alberto, Nietilspach Fabian, Von Segesser Ludwig, and Maisano Francesco. 2017. “The Evolution of Surgical Valves.” *Cardiovascular Medicine 2017 :12* 20(12):285–92. doi: 10.4414/CVM.2017.00532.

Martin, Caitlin, and Wei Sun. 2012. “Biomechanical Characterization of Aortic Valve Tissue in Humans and Common Animal Models.” *Journal of Biomedical Materials Research - Part A* 100 A(6):1591–99. doi: 10.1002/jbm.a.34099.

Masheane, Lebohang, Willie Preez, and Jacques Combrinck. 2024. “Analysis of the Influence

of Belly Thickness and Free Edge Curves on the Hemodynamic Performance of a Polymer Heart Valve." 406:08001. doi: 10.1051/matecconf/202440608001.

Masheane, Ronald, Jacques Combrinck, and Lebohang Masheane. 2023. "Development of a Compression Moulding Process for the Manufacturing of Artificial Polymer Heart Valves." *MATEC Web of Conferences* 388:06002. doi: 10.1051/matecconf/202338806002.

Mavrilas, Dimosthenis, and Yannis Missirlis. 1991. "An Approach to the Optimization of Preparation of Bioprosthetic Heart Valves." *Journal of Biomechanics* 24(5):331–39. doi: 10.1016/0021-9290(91)90351-M.

Mega, Mor, Gil Marom, Rotem Halevi, Ashraf Hamdan, Danny Bluestein, and Rami Haj-Ali. 2016. "Imaging Analysis of Collagen Fiber Networks in Cusps of Porcine Aortic Valves: Effect of Their Local Distribution and Alignment on Valve Functionality." *Computer Methods in Biomechanics and Biomedical Engineering* 19(9):1002–8. doi: 10.1080/10255842.2015.108800.

Meijering, E., M. Jacob, J. C. F. Sarria, P. Steiner, H. Hirling, and M. Unser. 2004. "Design and Validation of a Tool for Neurite Tracing and Analysis in Fluroescence Microscopy Images." *Cytometry* 58A(2):167–76. doi: 10.5040/9781474229050.0007.

Merryman, W. David, Hsiao Ying Shadow Huang, Frederick J. Schoen, and Michael S. Sacks. 2006. "The Effects of Cellular Contraction on Aortic Valve Leaflet Flexural Stiffness." *Journal of Biomechanics* 39(1):88–96. doi: 10.1016/j.jbiomech.2004.11.008.

Metzner, Anja, Kenji Iino, Ulrich Steinseifer, Anselm Uebing, Wiebke de Buhr, Jochen Cremer, and Georg Lutter. 2010. "Percutaneous Pulmonary Polyurethane Valved Stent Implantation." *Journal of Thoracic and Cardiovascular Surgery* 139(3):748–52. doi: 10.1016/j.jtcvs.2009.08.013.

Misfeld, Martin, and Hans Hinrich Sievers. 2007. "Heart Valve Macro- and Microstructure." *Philosophical Transactions of the Royal Society B: Biological Sciences* 362(1484):1421–36. doi: 10.1098/rstb.2007.2125.

Missirlis, Y. F., and C. D. Armeniades. 1977. "Ultrastructure of the Human Aortic Valve." *Acta Anatomica* 98(2):199–205. doi: 10.1159/000144794.

Mueller, Kilian Maria Arthur, Annika Hangleiter, Sarah Burkhardt, Diana M. Rojas-González, Christina Kwade, Sebastian T. Pammer, Stefan Leonhardt, and Petra Mela. 2023. "Filament-Based Melt Electrowriting Enables Dual-Mode Additive Manufacturing for Multiscale." *Small* 3(8). doi: doi.org/10.1002/smsc.202300021.

Mueller, Kilian Maria Arthur, Salma Mansi, Elena M. De-Juan-Pardo, and Petra Mela. 2024.

"Advances in Melt Electrowriting for Cardiovascular Applications." *Frontiers in Bioengineering and Biotechnology* (September):1–9. doi: 10.3389/fbioe.2024.1425073.

Müller-Schweinitzer, Else. 2009. "Cryopreservation of Vascular Tissues." *Organogenesis* 5(3):97–104. doi: 10.4161/ORG.5.3.9495.

Musallam, Anees, Kyle D. Buchanan, Charan Yerasi, Aaphtaab Dheendsa, Cheng Zhang, Corey Shea, Brian C. Case, Brian J. Forrestal, Lowell F. Satler, Itsik Ben-Dor, Rebecca Torguson, Toby Rogers, and Ron Waksman. 2022. "Impact of Left Ventricular Outflow Tract Calcification on Outcomes Following Transcatheter Aortic Valve Replacement." *Cardiovascular Revascularization Medicine* 35:1–7. doi: 10.1016/j.carrev.2021.07.010.

Nicoloff, D. M., R. W. Emery, K. V Arom, W. F. Northrup 3rd, C. R. Jorgensen, Y. Wang, and W. G. Lindsay. 1981. "Clinical and Hemodynamic Results with the St. Jude Medical Cardiac Valve Prosthesis. A Three-Year Experience." *Journal of Thoracic and Cardiovascular Surgery* 82(2):674–83.

Nistal, F., V. Garcia-Martinez, E. Arbe, D. Fernandez, E. Artinano, F. Mazorra, and I. Gallo. 1990. "In Vivo Experimental Assessment of Polytetrafluoroethylene Trileaflet Heart Valve Prosthesis." *Journal of Thoracic and Cardiovascular Surgery* 99(6). doi: 10.1016/s0022-5223(20)31464-1.

O'Neill, Kelly L., and Paul D. Dalton. 2023. "A Decade of Melt Electrowriting." *Small Methods* 7(7):1–16. doi: 10.1002/smtd.202201589.

Olvera, Dinorath, Mina Sohrabi Molina, Gillian Hendy, and Michael G. Monaghan. 2020. "Electroconductive Melt Electrowritten Patches Matching the Mechanical Anisotropy of Human Myocardium." *Advanced Functional Materials* 30(44):1–10. doi: 10.1002/adfm.201909880.

Otto, Catherine M. 2000. "Timing of Aortic Valve Surgery." *Heart* 84(2):211–18. doi: 10.1136/heart.84.2.211.

Otto, Catherine M., Bonnie K. Lind, Dalane W. Kitzman, Bernard J. Gersh, and David S. Siscovick. 1999. "Association of Aortic-Valve Sclerosis with Cardiovascular Mortality and Morbidity in the Elderly." *New England Journal of Medicine* 341(3):142–47. doi: 10.1056/NEJM199907153410302.

Otto, Catherine M., Rick A. Nishimura, Robert O. Bonow, Blase A. Carabello, John P. Rwin, Federico Gentile, Hani Jneid, ric V. Krieger, Michael Mack, Christopher McLeod, Patrick T. O'Gara, Vera H. Rigolin, Thoralf M. Sundt, Annemarie Thompson, and Christopher Toly. 2021. "2020 ACC/AHA Guideline for the Management of Patients With Valvular Heart

Disease: A Report of the American College of Cardiology/American Heart Association Joint Committee on Clinical Practice Guidelines." *Circulation* 143(5):E72–227. doi: 10.1161/CIR.0000000000000923.

Palareti, G., C. Manotti, A. DAngelo, V. Pengo, N. Erba, M. Moia, N. Ciavarella, G. Devoto, M. Berrettini, N. Leali, M. Poggi, C. Legani, S. Musolesi, and S. Coccheri. 1997. "Thrombotic Events during Oral Anticoagulant Treatment: Results of the Inception-Cohort, Prospective, Collaborative ISCOAT Study Group (Italian Study on Complications of Oral Anticoagulant Therapy)." *Journal of Thrombosis and Haemostasis* 78(6):1438–43.

Palatianos, George M., Axel M. Laczkovics, Paul Simon, Jose Luis Pomar, Dietrich E. Birnbaum, Hans H. Greve, and Axel Haverich. 2007. "Multicentered European Study on Safety and Effectiveness of the On-X Prosthetic Heart Valve: Intermediate Follow-Up." *The Annals of Thoracic Surgery* 83(1):40–46. doi: 10.1016/J.ATHORACSUR.2006.08.010.

Pei, Ming, Donghua Zou, Yong Gao, Jianhua Zhang, and Ping Huang. 2021. "The Influence of Sample Geometry and Size on Porcine Aortic Material Properties from Uniaxial Tensile Tests Using Custom-Designed Tissue Cutters , Clamps and Molds." *PLOS One* 1–19. doi: 10.1371/journal.pone.0244390.

Peiffer, Quentin C., Mylène de Ruijter, Joost van Duijn, Denis Crottet, Ernst Dominic, Jos Malda, and Miguel Castilho. 2020. "Melt Electrowriting onto Anatomically Relevant Biodegradable Substrates: Resurfacing a Diarthrodial Joint." *Materials and Design* 195:1–9. doi: 10.1016/j.matdes.2020.109025.

Piatti, Filippo, Francesco Sturla, Gil Marom, Jawaad Sheriff, Thomas E. Claiborne, Marvin J. Slepian, Alberto Redaelli, and Danny Bluestein. 2015. "Hemodynamic and Thrombogenic Analysis of a Trileaflet Polymeric Valve Using a Fluid-Structure Interaction Approach." *Journal of Biomechanics* 48(13):3641–49. doi: 10.1016/j.jbiomech.2015.08.009.

Pierlot, Caitlin M., Andrew D. Moeller, J. Michael Lee, and Sarah M. Wells. 2015. "Biaxial Creep Resistance and Structural Remodeling of the Aortic and Mitral Valves in Pregnancy." *Annals of Biomedical Engineering* 43(8):1772–85. doi: 10.1007/s10439-014-1230-2.

Prawel, David A., Harold Dean, Marcio Forleo, Nicole Lewis, Justin Gangwish, Ketul C. Popat, Lakshmi Prasad Dasi, and Susan P. James. 2014. "Hemocompatibility and Hemodynamics of Novel Hyaluronan-Polyethylene Materials for Flexible Heart Valve Leaflets." *Cardiovascular Engineering and Technology* 5(1):70–81. doi: 10.1007/s13239-013-0171-5.

Rahmani, Benyamin, Spyridon Tzamtzis, Hossein Ghanbari, Gaetano Burriesci, and Alexander

M. Seifalian. 2012. “Manufacturing and Hydrodynamic Assessment of a Novel Aortic Valve Made of a New Nanocomposite Polymer.” *Journal of Biomechanics* 45(7):1205–11. doi: 10.1016/j.jbiomech.2012.01.046.

Rahmani, Benyamin, Spyros Tzamtzis, Rose Sheridan, Michael J. Mullen, John Yap, Alexander M. Seifalian, and Gaetano Burriesci. 2016. “A New Transcatheter Heart Valve Concept (the TRISKELE): Feasibility in an Acute Preclinical Model.” *EuroIntervention* 12(7):901–8. doi: 10.4244/EIJV12I7A148.

Rahmani, Benyamin, Spyros Tzamtzis, Rose Sheridan, Michael J. Mullen, John Yap, Alexander M. Seifalian, and Gaetano Burriesci. 2017. “In Vitro Hydrodynamic Assessment of a New Transcatheter Heart Valve Concept (the TRISKELE).” *Journal of Cardiovascular Translational Research* 10(2):104–15. doi: 10.1007/s12265-016-9722-0.

Rezakhaniha, R., A. Agianniotis, J. T. C. Schrauwen, A. Griffa, D. Sage, C. V. C. Bouten, F. N. Van De Vosse, M. Unser, and N. Stergiopulos. 2012. “Experimental Investigation of Collagen Waviness and Orientation in the Arterial Adventitia Using Confocal Laser Scanning Microscopy.” *Biomechanics and Modeling in Mechanobiology* 11(3–4):461–73. doi: 10.1007/s10237-011-0325-z.

Robinson, Thomas M., Dietmar W. Hutmacher, and Paul D. Dalton. 2019. “The Next Frontier in Melt Electrospinning: Taming the Jet.” *Advanced Functional Materials* 29(44). doi: 10.1002/adfm.201904664.

Rock, Christopher A., Lin Han, and Todd C. Doehring. 2014. “Complex Collagen Fiber and Membrane Morphologies of the Whole Porcine Aortic Valve.” *PLoS ONE* 9(1):1–9. doi: 10.1371/journal.pone.0086087.

Roe, B. B. 1969. “Late Follow-up Studies on Flexible Leaflet Prosthetic Valves.” *The Journal of Thoracic and Cardiovascular Surgery* 58(1):59–61. doi: 10.1016/s0022-5223(19)42628-7.

Roe, B. B. 1989. “A Compression-Molded Leaflet Prosthetic Valve.” *The Annals of Thoracic Surgery* 48(3 SUPPL.). doi: 10.1016/0003-4975(89)90626-7.

Roe, B. B., J. W. Owsley, and P. C. Boudoures. 1958. “Experimental Results with a Prosthetic Aortic Valve.” *The Journal of Thoracic Surgery* 36(4):563–70. doi: 10.1016/s0096-5588(20)30134-3.

Rogers, Kara. 2011. *The Cardiovascular System*. edited by K. Rogers. Britannica Educational Publishing.

Ross, D. N. 1962. “Homograft Replacement of the Aortic Valve.” *The Lancet* 280(7254):487. doi: https://doi.org/10.1016/S0140-6736(62)90345-8.

Rotman, Oren M., Matteo Bianchi, Ram P. Ghosh, Brandon Kovarovic, and Danny Bluestein. 2018. “Principles of TAVR Valve Design, Modelling, and Testing.” *Expert Review of Medical Devices* 15(11):771–91. doi: 10.1080/17434440.2018.1536427.

Rotman, Oren M., Brandon Kovarovic, Matteo Bianchi, Marvin J. Slepian, and Danny Bluestein. 2020. “In Vitro Durability and Stability Testing of a Novel Polymeric Transcatheter Aortic Valve.” *ASAIO Journal* 66(2):190–98. doi: 10.1097/MAT.0000000000000980.

Rotman, Oren M., Brandon Kovarovic, Wei Che Chiu, Matteo Bianchi, Gil Marom, Marvin J. Slepian, and Danny Bluestein. 2019. “Novel Polymeric Valve for Transcatheter Aortic Valve Replacement Applications: In Vitro Hemodynamic Study.” *Annals of Biomedical Engineering* 47(1):113–25. doi: 10.1007/s10439-018-02119-7.

Ruffolo, Alessandro Ferdinando, Marine Lallemant, Sophie Delplanque, and Michel Cosson. 2023. “The Transvaginal Mesh: An Overview of Indications and Contraindications for Its Use.” *Expert Review of Medical Devices* 20(5):393–400. doi: 10.1080/17434440.2023.2199926.

Sachweh, Joerg S., and Sabine H. Daebritz. 2006. “Novel ‘Biomechanical’ Polymeric Valve Prostheses with Special Design for Aortic and Mitral Position: A Future Option for Pediatric Patients?” *ASAIO Journal* 52(5):575–80. doi: 10.1097/01.mat.0000237695.87457.2a.

Sacks, Michael S., W. David Merryman, and David E. Schmidt. 2009. “On the Biomechanics of Heart Valve Function.” *Journal of Biomechanics* 42(12):1804–24.

Sacks, Michael S., David B. Smith, and Erik D. Hiester. 1997. “A Small Angle Light Scattering Device for Planar Connective Tissue Microstructural Analysis.” *Annals of Biomedical Engineering* 25(4):678–89. doi: 10.1007/BF02684845.

Sacks, Michael S., David B. Smith, and Erik D. Hiester. 1998. “The Aortic Valve Microstructure: Effects of Transvalvular Pressure.” *Journal of Biomedical Materials Research* 41(1):131–41. doi: 10.1002/(SICI)1097-4636(199807)41:1<131::AID-JBM16>3.0.CO;2-Q.

Sadeghinia, Mohammad Javad, Bjørn Skallerud, Gerhard A. Holzapfel, and Victorien Prot. 2022. “Biomechanics of Mitral Valve Leaflets: Second Harmonic Generation Microscopy, Biaxial Mechanical Tests and Tissue Modeling.” *Acta Biomaterialia* 141(15):244–54. doi: 10.1016/j.actbio.2022.01.003.

Saidy, Navid T., Frederic Wolf, Onur Bas, Hans Keijdener, Dietmar W. Hutmacher, Petra Mela, and Elena M. De-Juan-Pardo. 2019. “Biologically Inspired Scaffolds for Heart Valve Tissue Engineering via Melt Electrowriting.” *Small* 15(24):1–15. doi: 10.1002/smll.201900873.

Saidy, Navid Toosi, Alicia Fernández-Colino, Behzad Shiroud Heidari, Ross Kent, Michael Vernon, Onur Bas, Shane Mulderrig, Andreas Lubig, José Carlos Rodríguez-Cabello, Barry Doyle, Dietmar W. Hutmacher, Elena M. De-Juan-Pardo, and Petra Mela. 2022. "Spatially Heterogeneous Tubular Scaffolds for In Situ Heart Valve Tissue Engineering Using Melt Electrowriting." *Advanced Functional Materials* 32(21). doi: 10.1002/adfm.202110716.

Sauren, A. A. H. J. (. 1981. "The Mechanical Behaviour of the Aortic Valve." (1981):159. doi: 10.6100/IR94978.

Scherman, Jacques, Chima Ofoegbu, Adriaan Myburgh, Justiaan Swanevelder, Braden van Breda, Harish Appa, Paul Human, David Williams, Deon Bezuidenhout, and Peter Zilla. 2019. "Preclinical Evaluation of a Transcatheter Aortic Valve Replacement System for Patients with Rheumatic Heart Disease." *EuroIntervention* 15(11):E975–82. doi: 10.4244/EIJ-D-18-01052.

Schindelin, Johannes, Ignacio Arganda-Carreras, Erwin Frise, Verena Kaynig, Mark Longair, Tobias Pietzsch, Stephan Preibisch, Curtis Rueden, Stephan Saalfeld, Benjamin Schmid, Jean Yves Tinevez, Daniel James White, Volker Hartenstein, Kevin Eliceiri, Pavel Tomancak, and Albert Cardona. 2012. "Fiji: An Open-Source Platform for Biological-Image Analysis." *Nature Methods* 9(7):676–82. doi: 10.1038/nmeth.2019.

Schoen, Frederick J. 2012. "Mechanisms of Function and Disease of Natural and Replacement Heart Valves." *Annual Reviews of Pathology: Mechanisms of Disease* 7:161–83. doi: 10.1146/ANNUREV-PATHOL-011110-130257.

Schoen, Frederick J., and W. D. Edwards. 2001. "Valvular Heart Disease: General Principles and Stenosis." Pp. 402–42 in *Cardiovascular pathology*, edited by M. Silver, A. I. Gotlieb, and F. J. Schoen. Churchill Livingstone, New York.

Schoen, Frederick J., and Avrum I. Gotlieb. 2016. "Heart Valve Health, Disease, Replacement, and Repair: A 25-Year Cardiovascular Pathology Perspective." *Cardiovascular Pathology* 25(4):341–52. doi: 10.1016/j.carpath.2016.05.002.

Schoen, Frederick J., and Richard D. Levy. 2020. "Bioprosthetic Heart Valve Calcification: Clinicopathologic Correlations, Mechanisms, and Prevention." in *Cadriovascular Calcificaation and Bone Mineralization*, edited by E. Aikawa and J. D. Hutcheson. Humana Press.

Schriefl, Andreas J., Heimo Wollinski, Peter Regitnig, Sepp D. Kohlwein, and Gerhard A. Holzapfel. 2013. "An Automated Approach for Three-Dimensional Quantification of Fibrillar Structures in Optically Cleared Soft Biological Tissues." *Journal of the Royal*

Society Interface 10(80). doi: 10.1098/rsif.2012.0760.

Serrani, M., J. Brubert, J. Stasiak, F. De Gaetano, A. Zaffora, M. L. Costantino, and G. D. Moggridge. 2016. "A Computational Tool for the Microstructure Optimization of a Polymeric Heart Valve Prosthesis." *Journal of Biomechanical Engineering* 138(6):16–20. doi: 10.1115/1.4033178.

Sesa, Mahmoud, Hagen Holthusen, Lukas Lamm, Christian Böhm, Tim Brepols, Stefan Jockenhövel, and Stefanie Reese. 2023. "Mechanical Modeling of the Maturation Process for Tissue-Engineered Implants: Application to Biohybrid Heart Valves." *Computers in Biology and Medicine* 167(September):107623. doi: 10.1016/j.compbiomed.2023.107623.

Sevre, Knut. 2006. *Handbook of Cardiac Anatomy, Physiology, and Devices*. Vol. 15.

Shin, Dongwoon, Jonghyun Kim, and Jiyoung Chang. 2018. "Experimental Study on Jet Impact Speed in Near-Field Electrospinning for Precise Patterning of Nanofiber." *Journal of Manufacturing Processes* 36(March):231–37. doi: 10.1016/j.jmapro.2018.10.011.

Shrestha, Rakish, Jutima Simsiriwong, Nima Shamsaei, and Robert D. Moser. 2016. "Cyclic Deformation and Fatigue Behavior of Polyether Ether Ketone (PEEK)." *International Journal of Fatigue* 82:411–27. doi: 10.1016/j.ijfatigue.2015.08.022.

Simon-Walker, Rachael, John Cavicchia, David A. Prawel, Lakshmi Prasad Dasi, Susan P. James, and Ketul C. Popat. 2018. "Hemocompatibility of Hyaluronan Enhanced Linear Low Density Polyethylene for Blood Contacting Applications." *Journal of Biomedical Materials Research - Part B Applied Biomaterials* 106(5):1964–75. doi: 10.1002/jbm.b.34010.

Snyder, Yuriy, and Soumen Jana. 2023a. "Electrospun Elastomeric Leaflet Substrates That Structurally and Mechanically Mimic Human Aortic Valve Leaflets." *ACS Applied Polymer Materials* 5(5):3749–61. doi: 10.1021/acsapm.3c00385.

Snyder, Yuriy, and Soumen Jana. 2023b. "Trilayer Anisotropic Structure versus Randomly Oriented Structure in Heart Valve Leaflet Tissue Engineering." *Bio-Design and Manufacturing* 6(4):423–38. doi: 10.1007/s42242-023-00237-3.

Standardization, International Organization for. 2021. "ISO 5840-3:2021 Cardiovascular Implants - Cardiac Valve Prostheses."

Stanova, Viktoria, Regis Rieu, Lionel Thollon, Erwan Salaun, Josep Rodes-Cabau, Nancy Cote, Diego Mantovani, and Philippe Pibarot. 2024. "Leaflet Mechanical Stress in Different Designs and Generations of Transcatheter Aortic Valves: An in Vitro Study." *Structural*

Heart 8. doi: 10.1016/j.shj.2023.100262.

Starr, A., and M. L. Edwards. 1961. “Mitral Replacement: Clinical Experience with a Ball-Valve Prosthesis.” *Annals of Surgery* 154(4):726–40. doi: 10.1097/00000658-196110000-00017.

Stasiak, J., J. Brubert, M. Serrani, A. Talhat, F. De Gaetano, M. L. Costantino, and G. D. Moggridge. 2015. “Structural Changes of Block Copolymers with Bi-Modal Orientation under Fast Cyclical Stretching as Observed by Synchrotron SAXS.” *Soft Matter* 11(16):3271–78. doi: 10.1039/c5sm00360a.

Stasiak, Joanna, Jacob Brubert, Marta Serrani, Sukumaran Nair, Francesco De Gaetano, Maria Laura Costantino, and Geoff D. Moggridge. 2014. “A Bio-Inspired Microstructure Induced by Slow Injection Moulding of Cylindrical Block Copolymers.” *Soft Matter* 10(32):6077–86. doi: 10.1039/c4sm00884g.

Stasiak, Joanna, Geoff D. Moggridge, Adriano Zaffora, Anna Pandolfi, and Maria L. Costantino. 2010. “Engineering Orientation in Block Copolymers for Application to Prosthetic Heart Valves.” *Functional Materials Letters* 3(4):249–52. doi: 10.1142/S1793604710001342.

Stasiak, Joanna R., Marta Serrani, Eugenia Biral, James V. Taylor, Azfar G. Zaman, Samantha Jones, Thomas Ness, Francesco De Gaetano, Maria Laura Costantino, Vito D. Bruno, Saadeh Suleiman, Raimondo Ascione, and Geoff D. Moggridge. 2020. “Design, Development, Testing at ISO Standards and: In Vivo Feasibility Study of a Novel Polymeric Heart Valve Prosthesis.” *Biomaterials Science* 8(16):4467–80. doi: 10.1039/d0bm00412j.

Stella, John A., and Michael S. Sacks. 2007. “On the Biaxial Mechanical Properties of the Layers of the Aortic Valve Leaflet.” *Journal of Biomechanical Engineering* 129(5):757–66. doi: 10.1115/1.2768111.

Stradins, Peteris, Romans Lacis, Iveta Ozolanta, Biruta Purina, Velta Ose, Laila Feldmane, and Vladimir Kasyanov. 2004. “Comparison of Biomechanical and Structural Properties between Human Aortic and Pulmonary Valve.” *European Journal of Cardio-Thoracic Surgery* 26(3):634–39. doi: 10.1016/j.ejcts.2004.05.043.

Tadros, Rami, and Sepehr Shakib. 2010. “Warfarin -- Indications, Risks and Drug Interactions.” *Australian Family Physician* 39(7):476–79.

Torun, Su Guvenir, Pablo de Miguel Munoz, Hanneke Crielaard, Hence J. M. Verhagen, Gert Jan Kremers, Antonius F. W. van der Steen, and Ali C. Akyildiz. 2023. “Local Characterization of Collagen Architecture and Mechanical Failure Properties of Fibrous Plaque Tissue of Atherosclerotic Human Carotid Arteries.” *Acta Biomaterialia* 164:293–302. doi:

10.1016/j.actbio.2023.04.022.

Tourlomousis, Filippos, Houzhu Ding, Dilhan M. Kalyon, and Robert C. Chang. 2017. “Melt Electrospinning Writing Process Guided by a ‘Printability Number.’” *Journal of Manufacturing Science and Engineering, Transactions of the ASME* 139(8). doi: 10.1115/1.4036348.

Ueda, Hiroki R., Hans-Ulrich Dodt, Pavel Osten, Michael N. Economo, Jayaram Chandrashekar, and Philipp J. Keller. 2020. “Whole-Brain Profiling of Cells and Circuits in Mammals by Tissue Clearing and Light-Sheet Microscopy.” *Neuron* 106(3):369–87. doi: 10.1016/j.neuron.2020.03.004.

Vanhaverbeke, Maarten, Philippe Nuyens, Pernille Steen Bække, Pasi Ensio Maaranen, Xi Wang, Gintautas Bieliauskas, Ole De Backer, and Lars Sondergaard. 2022. “Temporal Trends in Survival Rates After Transcatheter Aortic Valve Replacement.” *JACC: Cardiovascular Interventions* 15(13):1391–93. doi: 10.1016/j.jcin.2022.04.038.

Vernon, Michael J., Jason Lu, Benjamin Padman, Christopher Lamb, Ross Kent, Petra Mela, Barry Doyle, Abdul Rahman Ihdayhid, Shirley Jansen, Rodney J. Dilley, and Elena M. De-Juan-Pardo. 2022. “Engineering Heart Valve Interfaces Using Melt Electrowriting: Biomimetic Design Strategies from Multi-Modal Imaging.” *Advanced Healthcare Materials* 11(24):1–17. doi: 10.1002/adhm.202201028.

Vesely, Ivan. 1997. “The Role of Elastin in Aortic Valve Mechanics.” *Journal of Biomechanics* 31(2):115–23. doi: 10.1016/S0021-9290(97)00122-X.

Vesely, Ivan, and Derek Boughner. 1989. “Analysis of the Bending Behaviour of Porcine Xenograft Leaflets and of Natural Aortic Valve Material: Bending Stiffness, Neutral Axis and Shear Measurements.” *J. Biomechanics* 22(617).

Vesely, Ivan, and Ronald Noseworthy. 1992. “Micromechanics of the Fibrosa and the Ventricularis in Aortic Valve Leaflets.” *Journal of Biomechanics* 25(1). doi: 10.1016/0021-9290(92)90249-Z.

Virani, Salim S., Alvaro Alonso, Hugo J. Aparicio, Emelia J. Benjamin, Marcio S. Bittencourt, Clifton W. Callaway, April P. Carson, Alanna M. Chamberlain, Susan Cheng, Francesca N. Delling, Mitchell S. V. Elkind, Kelly R. Evenson, Jane F. Ferguson, Deepak K. Gupta, Sadiya S. Khan, Brett M. Kissela, Kristen L. Knutson, Chong D. Lee, Tené T. Lewis, Junxiu Liu, Matthew Shane Loop, Pamela L. Lutsey, Jun Ma, Jason Mackey, Seth S. Martin, David B. Matchar, Michael E. Mussolino, Sankar D. Navaneethan, Amanda Marma Perak, Gregory A. Roth, Zainab Samad, Gary M. Satou, Emily B. Schroeder, Svati H. Shah,

Christina M. Shay, Andrew Stokes, Lisa B. VanWagner, Nae-Yuh Wang, Connie W. Tsao, and On behalf of the American Heart Association Council on Epidemiology and Prevention Statistics Committee and Stroke Statistics Subcommittee. 2021. “Heart Disease and Stroke Statistics—2021 Update.” *Circulation* E254–743. doi: 10.1161/CIR.0000000000000950.

Virtanen, Marko P. O., Markku Eskola, Maina P. Jalava, Annastiina Husso, Teemu Laakso, Matti Niemelä, Tuomas Ahvenvaara, Tuomas Tauriainen, Pasi Maaranen, Eeva Maija Kinnunen, Sebastian Dahlbacka, Jussi Jaakkola, Tuija Vasankari, Juhani Airaksinen, Vesa Anttila, Stefano Rosato, Paola D’Errigo, Mikko Savontaus, Tatu Juvonen, Mika Laine, Timo Mäkikallio, Antti Valtola, Peter Raivio, and Fausto Biancari. 2019. “Comparison of Outcomes After Transcatheter Aortic Valve Replacement vs Surgical Aortic Valve Replacement Among Patients With Aortic Stenosis at Low Operative Risk.” *JAMA Network Open* 2(6):e195742. doi: 10.1001/jamanetworkopen.2019.5742.

Vyas, Payal, Joshua D. Hutcheson, and Elena Aikawa. 2018. “Calcific Aortic Valve Disease: Pathobiology, Basic Mechanisms, and Clinical Strategies.” *Advances in Heart Valve Biomechanics: Valvular Physiology, Mechanobiology, and Bioengineering* 153–79. doi: 10.1007/978-3-030-01993-8_7.

Vyavahare, Naren, and Hobey Tam. 2018. “Bioprosthetic Heart Valves: From a Biomaterials Perspective” edited by M. Sacks and J. Liao. *Advances in Heart Valve Biomechanics: Valvular Physiology, Mechanobiology, and Bioengineering* 337–84. doi: 10.1007/978-3-030-01993-8_2.

Wang, Mansen, Anthony P. Furnary, Hsin Fang Li, and Gary L. Grunkemeier. 2017. “Bioprosthetic Aortic Valve Durability: A Meta-Regression of Published Studies.” *Annals of Thoracic Surgery* 104(3):1080–87. doi: 10.1016/j.athoracsur.2017.02.011.

Wang, Qiang, Anthony J. McGoron, Richard Bianco, Yasushi Kato, Leonard Pinchuk, and Richard T. Schoephoerster. 2010. “In-Vivo Assessment of a Novel Polymer (SIBS) Trileaflet Heart Valve.” *Journal of Heart Valve Disease* 19(4):499–505. doi: 10.1002/jbm.a.32562.

Wang, Tim. 2015. *Mizuho Industry Focus*.

Wheatley, D. J., L. Raco, G. M. Bernacca, I. Sim, P. R. Belcher, and J. S. Boyd. 2000. “Polyurethane: Material for the next Generation of Heart Valve Prostheses?” *European Journal of Cardio-Thoracic Surgery* 17(4):440–48. doi: 10.1016/S1010-7940(00)00381-X.

Whelan, Alix. 2021. “Investigation into the Collagen Fibre-Mediated Fatigue Mechanics of

Bovine Pericardium for Use in Bioprosthetic Heart Valves." Trinity College Dublin.

Whelan, Alix, J. Duffy, R. T. Gaul, D. O'Reilly, D. R. Nolan, P. Gunning, C. Lally, and B. P. Murphy. 2019. "Collagen Fibre Orientation and Dispersion Govern Ultimate Tensile Strength, Stiffness and the Fatigue Performance of Bovine Pericardium." *Journal of the Mechanical Behavior of Biomedical Materials* 90(April 2018):54–60. doi: 10.1016/j.jmbbm.2018.09.038.

Whelan, Alix, Gordon O'Brien, Anna Szagdaj, David O'Reilly, and Caitríona Lally. 2021. "Investigation into Early Stage Fatigue-Damage Accumulation in Glutaraldehyde-Fixed Bovine Pericardium Using a Novel Equibiaxial Bulge Inflation System." *Journal of the Mechanical Behavior of Biomedical Materials* 121:104588. doi: 10.1016/J.JMBBM.2021.104588.

Whelan, Alix, Elizabeth Williams, David Nolan, Bruce Murphy, Paul Gunning, David O'Reilly, and Caitríona Lally. 2021. "Bovine Pericardium of High Fibre Dispersion Has High Fatigue Life and Increased Collagen Content; Potentially an Untapped Source of Heart Valve Leaflet Tissue." *Annals of Biomedical Engineering* 49:1022–32. doi: 10.1007/s10439-020-02644-4.

Whelton, Seamus P., Kunal Jha, Zeina Dardari, Alexander C. Razavi, Ellen Boakye, Omar Dzaye, Dhiran Verghese, Sanjiv Shah, Matthew J. Budoff, Kunihiro Matsushita, J. Jeffery Carr, Ramachandran S. Vasan, Roger S. Blumenthal, Khalil Anchouche, George Thanassoulis, Xiuqing Guo, Jerome I. Rotter, Robyn L. McClelland, Wendy S. Post, and Michael J. Blaha. 2024. "Prevalence of Aortic Valve Calcium and the Long-Term Risk of Incident Severe Aortic Stenosis." *JACC: Cardiovascular Imaging* 17(1):31–42. doi: 10.1016/j.jcmg.2023.02.018.

Whitaker, Robert H. 2018. "Anatomy of the Heart." *Medicine (United Kingdom)* 46(8):423–26. doi: 10.1016/j.mpmed.2018.05.010.

Willner, Nadav, Graeme Prosperi-Porta, Lawrence Lau, Angel Yi Nam Fu, Kevin Boczar, Anthony Poulin, Pietro Di Santo, Rudy R. Unni, Sarah Visintini, Paul E. Ronksley, Kwan Leung Chan, Luc Beauchesne, Ian G. Burwash, and David Messika-Zeitoun. 2023. "Aortic Stenosis Progression: A Systematic Review and Meta-Analysis." *JACC: Cardiovascular Imaging* 16(3):314–28. doi: 10.1016/j.jcmg.2022.10.009.

Wiseman, C. B., W. S. Pierce, J. H. Donachy, W. E. Pae, J. L. Myers, and G. A. Prophet. 1982. "A Polyurethane Trileaflet Cardiac Valve Prosthesis: In Vitro and In Vivo Studies." *Trans Am Soc Artif Intern Organs* 28.

Wu, Changfu, Neelakantan Saikrishnan, Aaron J. Chalekian, Rob Fraser, Ornella Ieropoli, Stephen M. Retta, Russell Joseph, Shouyan Lee, Salvador Marquez, David Mester, Ning Pan, Sepehr Vatanpour, Craig Weinberg, and Ulrich Steinseifer. 2019. “In-Vitro Pulsatile Flow Testing of Prosthetic Heart Valves: A Round-Robin Study by the ISO Cardiac Valves Working Group.” *Cardiovascular Engineering and Technology* 10(3):397–422. doi: 10.1007/s13239-019-00422-5.

Zeugin, Till, Fergal B. Coulter, Utku Gülan, André R. Studart, and Markus Holzner. 2024. “In Vitro Investigation of the Blood Flow Downstream of a 3D-Printed Aortic Valve.” *Scientific Reports* 14(1):1–12. doi: 10.1038/s41598-024-51676-6.

Zwolak, Pawel, Jan Farei-Campagna, Thorsten Jentzsch, Brigitte von Rechenberg, and Clément M. Werner. 2018. “Local Effect of Zoledronic Acid on New Bone Formation in Posterolateral Spinal Fusion with Demineralized Bone Matrix in a Murine Model.” *Archives of Orthopaedic and Trauma Surgery* 138(1):13–18. doi: 10.1007/s00402-017-2818-4.

Appendix A1

This section includes supplementary material for Chapter 3.

Supplementary Material

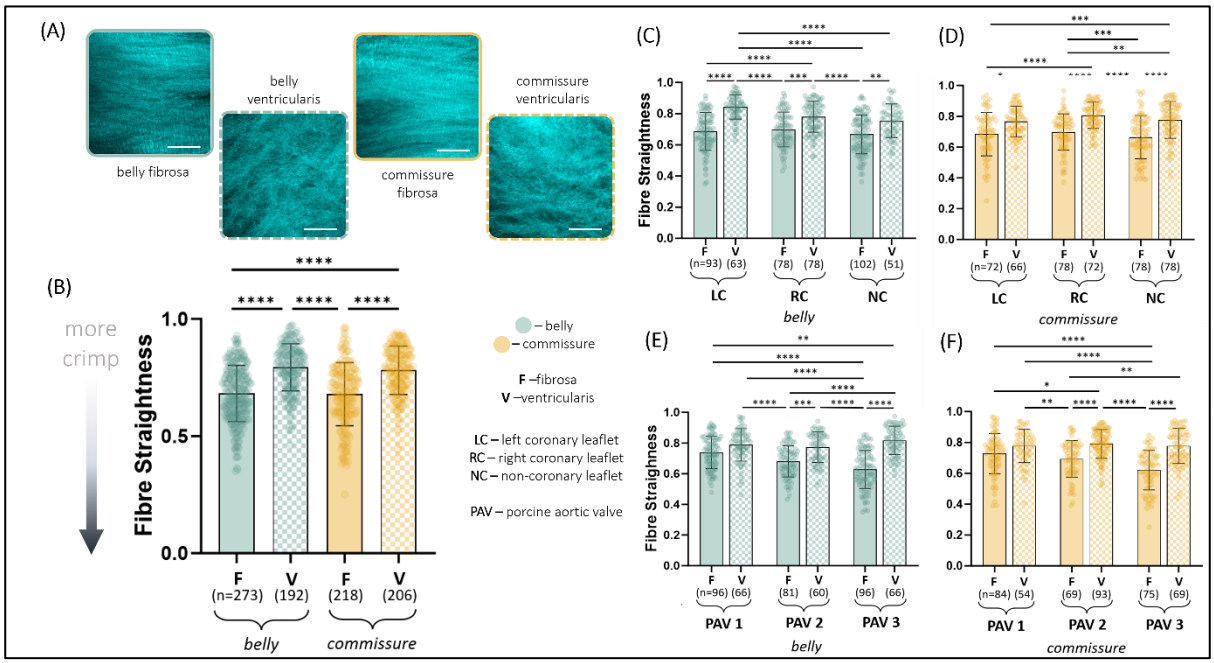

Figure A1-1 *Repetition of Figure 4 including statistical analysis. Overview of fibre crimp analysis with (A) representative SHG images for each location and layer. (B) All crimp measurements organised by layer and location, (C) crimp measurements for the belly region separated by layer and leaflet type, (D) crimp measurements for commissure region separated by layer and leaflet type, (E) crimp measurements for belly regions separated by layer and animal, (F) crimp measurements for commissure region separated by layers and animal. For all data sets: Shapiro-Wilk normality test and Kruskal-Wallis with Dunn's multiple comparisons test; p*≤0.05, P**≤0.01, p***≤0.001, p****≤0.0001.*

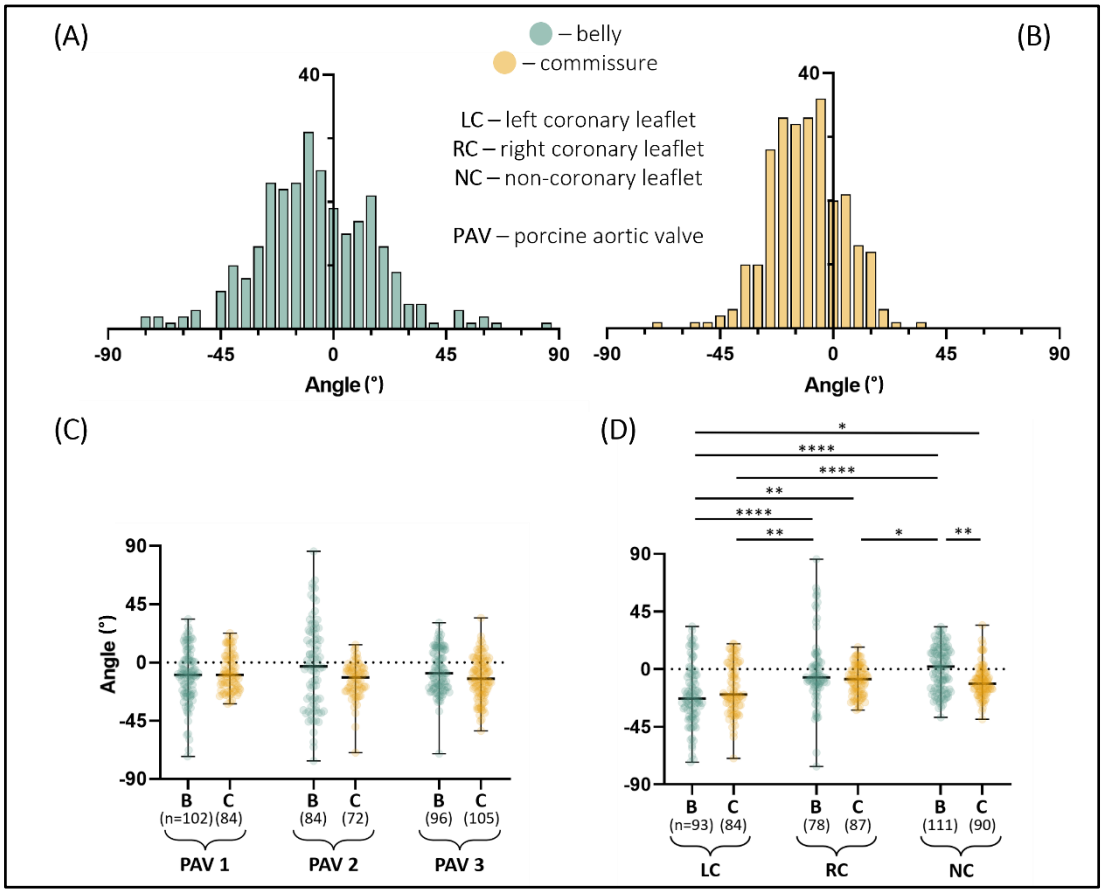

Figure A1-2 *Repetition of Figure 5 including statistical analysis. Fibre orientation analysis. Histograms of fibre orientations in (A) belly and (B) commissure regions, for both plots bin width: 5°. (C) fibre orientations separated by region and animal, (D) fibre orientations separated by region and leaflet type, using Shapiro-Wilk normality test and Kruskall-Wallis test with Dunn's multiple comparisons; p*≤0.05, P**≤0.01, p***≤0.001, p****≤0.0001.*

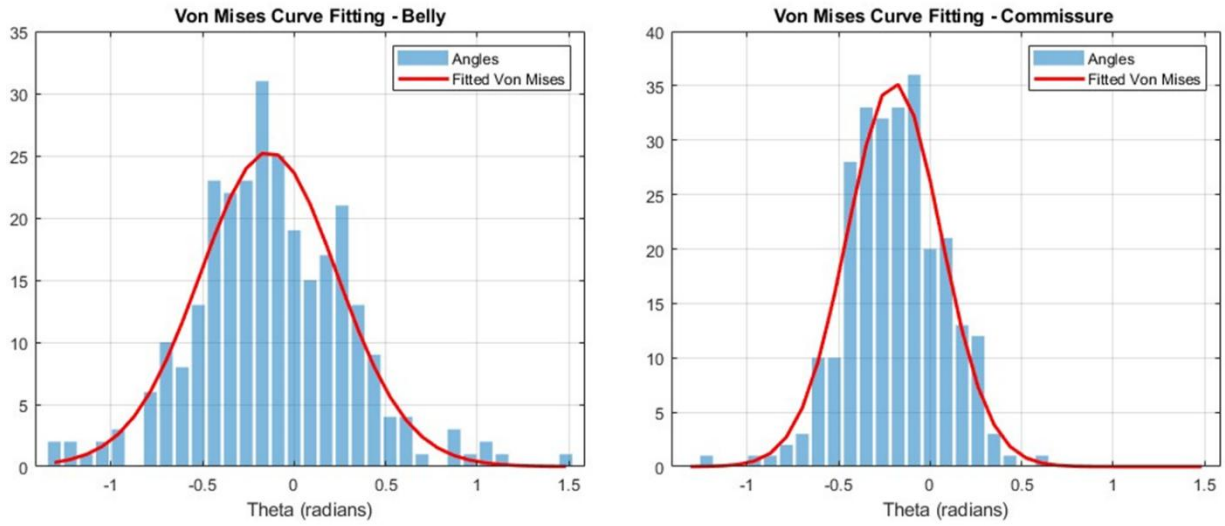

Figure A1-3 *Von Mises distributions fitted to angle data*

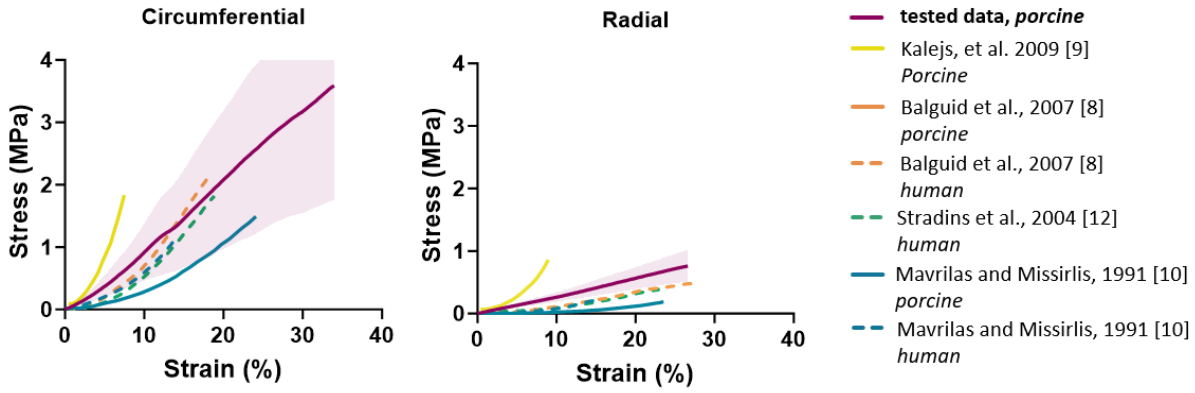

Figure A1-4 *Plots of stress/strain behaviour of porcine aortic valve leaflets in the circumferential and radial directions compared to human and porcine tissue cited in literature.*

Table A1-1 *Initial and final stress modulus values for all tested tissue groups*

	INITIAL MODULUS (MPA)	FINAL MODULUS (MPA)
FC	5.70 ± 0.87	26.60 ± 12.09
FR	1.28 ± 1.27	2.07 ± 0.92
VC	28.44 ± 36.30	42.48 ± 14.81
VR	3.17 ± 2.10	54.16 ± 30.75
WC	5.43 ± 1.24	21.55 ± 9.21
WR	2.48 ± 0.30	6.00 ± 3.32

Table A1-2 *Initial and final tension modulus values for all tested tissue groups*

	INITIAL MODULUS (N/MM)	FINAL MODULUS (N/MM)
FC	2.90 ± 1.86	2.49 ± 0.42
FR	0.37 ± 0.37	0.42 ± 0.17
VC	0.95 ± 1.02	1.55 ± 0.89
VR	0.16 ± 0.12	0.99 ± 0.42
WC	3.41 ± 0.40	2.94 ± 1.02
WR	1.27 ± 0.39	1.48 ± 0.87

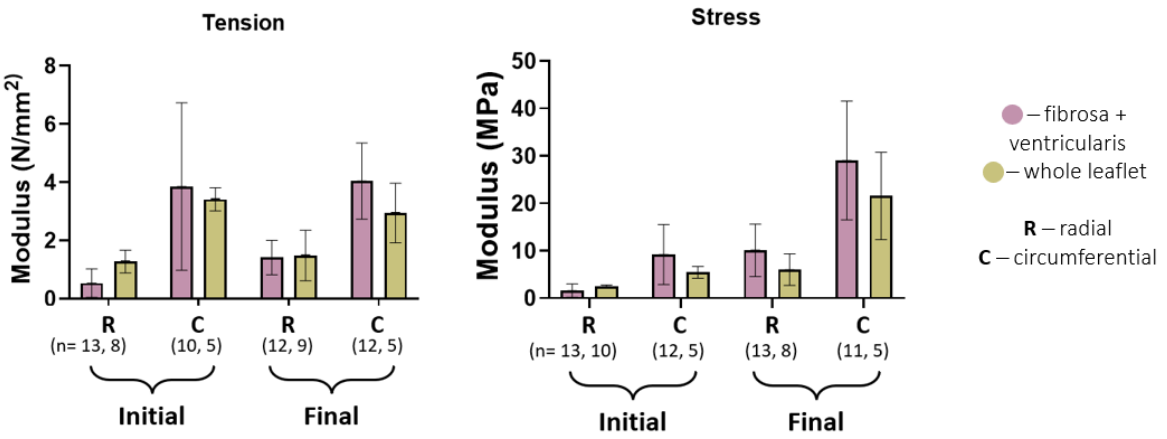

Figure A1-5 *Combined results for fibrosa and ventricularis stiffness compared to whole leaflet stiffness for both tension and stress results. 2-way ANOVA with Šídák's multiple comparisons; all pairings returned no statistically significant differences. For stress calculations, the fibrosa and ventricularis are expected to be 84.6% and 15.4% of total leaflet thickness, respectively, and the results are scaled and added accordingly.*

Table A1-3 *Fibre straightness by region, layer, leaflet type, and animal.*

	BELLY		**COMMISSURE**	
	F	***V***	***F***	***V***
All Leaflets	0.68 ± 0.12	0.79 ± 0.10	0.68 ± 0.13	0.78 ± 0.10
LC	0.69 ± 0.12	0.84 ± 0.14	0.68 ± 0.14	0.77 ± 0.10
RC	0.70 ± 0.11	0.78 ± 0.10	0.70 ± 0.12	0.81 ± 0.08
NC	0.67 ± 0.12	0.75 ± 0.11	0.66 ± 0.14	0.78 ± 0.12
PAV1	0.74 ± 0.11	0.79 ± 0.11	0.73 ± 0.13	0.78 ± 0.11
PAV2	0.68 ± 0.10	0.77 ± 0.10	0.69 ± 0.12	0.79 ±0.09
PAV3	0.63 ± 0.12	0.81 ± 0.09	0.62 ± 0.13	0.78 ± 0.11

Table A1-4 *Fibrosa fibre orientations by region, leaflet type, and valve.*

	BELLY (°)	COMMISSURE (°)
ALL LEAFLETS	-6.86 ± 24.33	-11.06 ± 15.02
LC	-19.96 ± 23.39	-15.01 ± 19.61
RC	-1.45 ± 27.76	-8.51 ± 11.46
NC	0.30 ± 17.26	-9.84 ± 12.3
PAV1	-10.43 ± 20.64	-7.67 ± 14.16
PAV2	-2.51 ± 33.56	-13.43 ± 13.82
PAV3	-6.88 ± 16.84	-12.16 ± 16.11

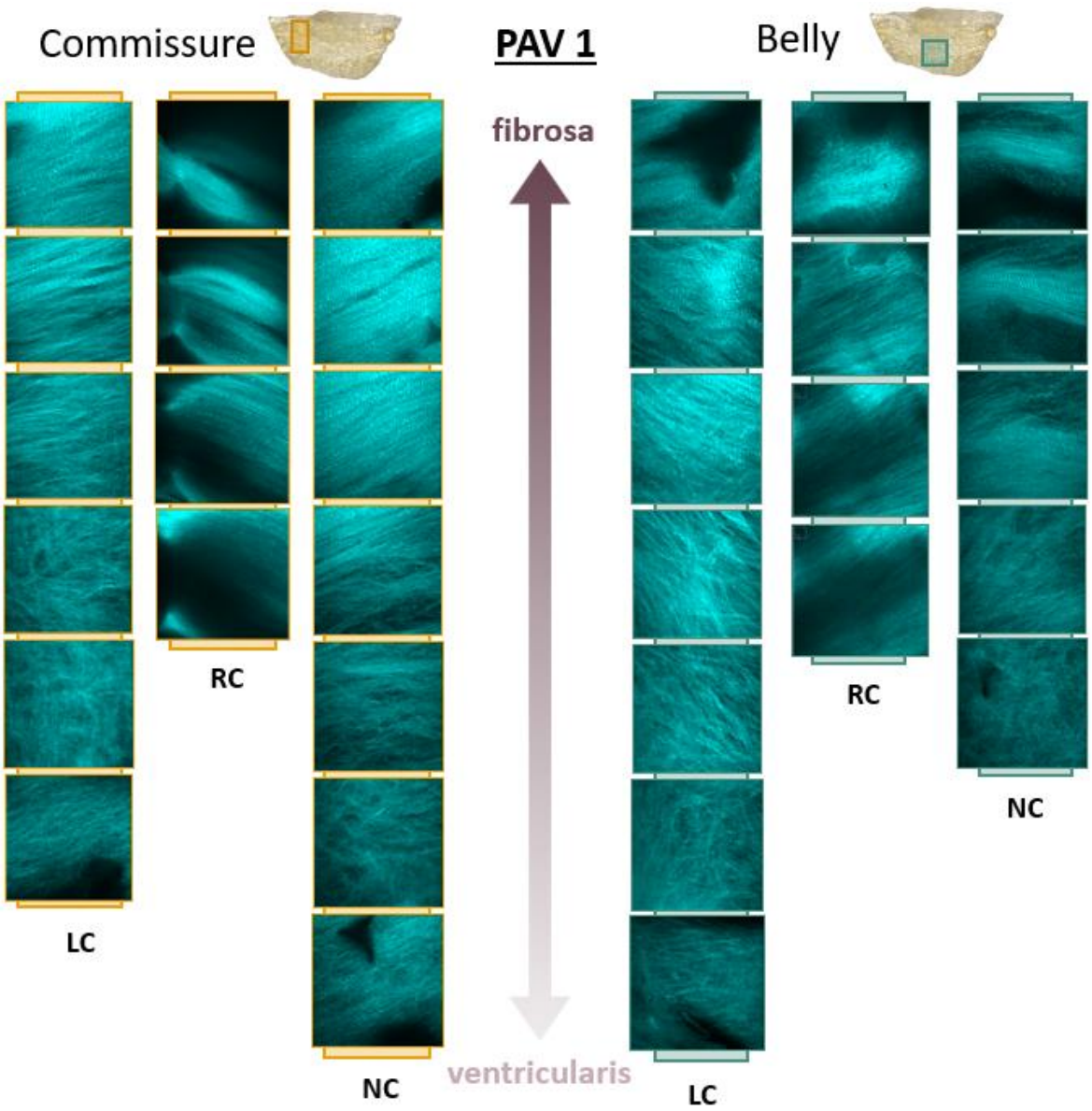

Figure A1-6 *SHG images of PAV 1 from both the commissure and belly regions across the three leaflets*

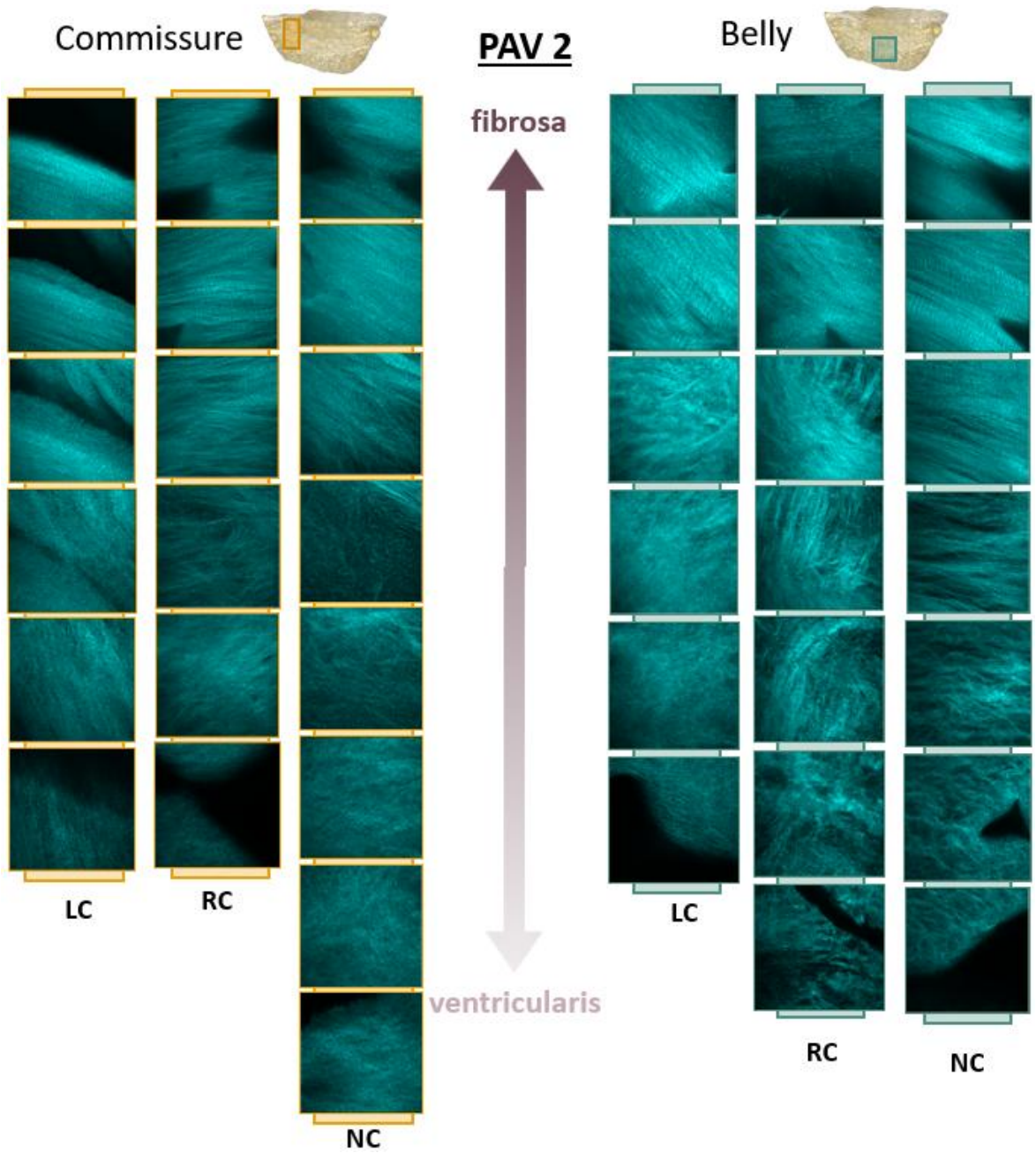

Figure A1-7 *SHG images of PAV 2 from both the commissure and belly regions across the three leaflets*

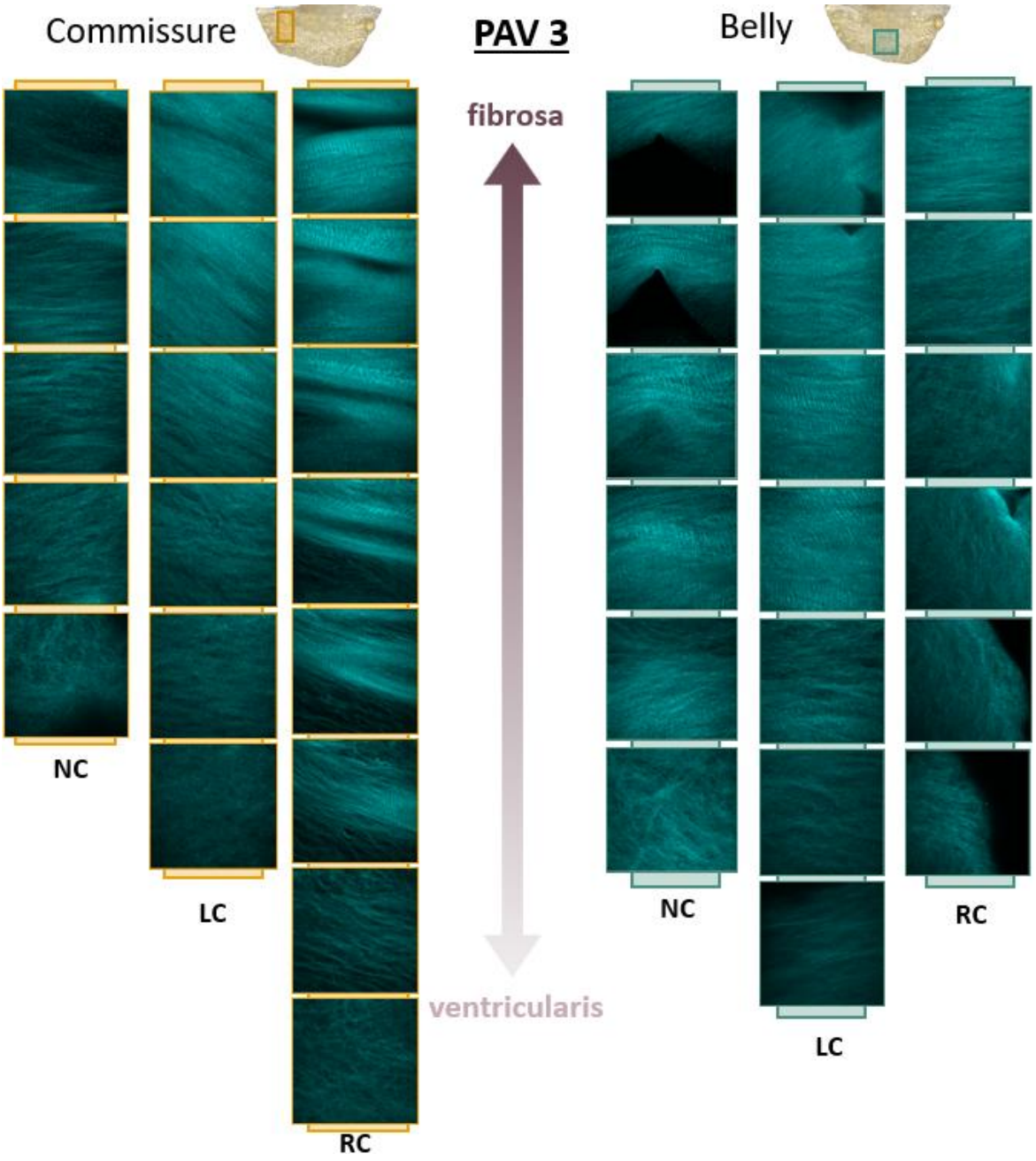

Figure A1-8 *SHG images of PAV 3 from both the commissure and belly regions across the three leaflets*

Appendix A2

This section includes supplementary material for Chapter 4.

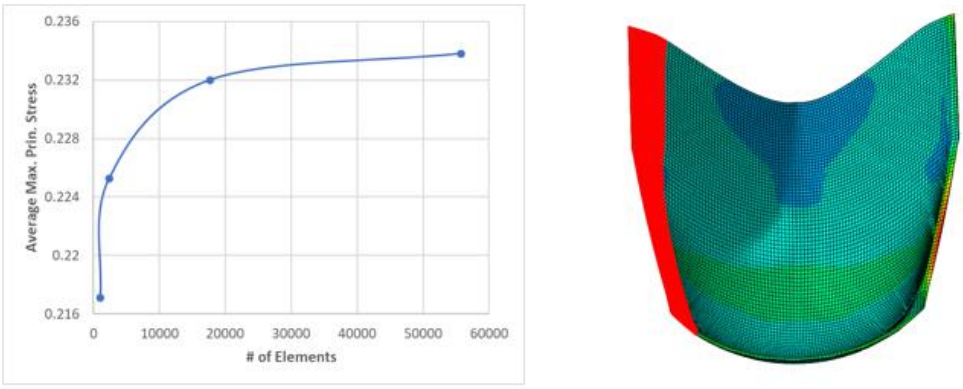

Figure A2-1 Mesh size sensitivity analysis.

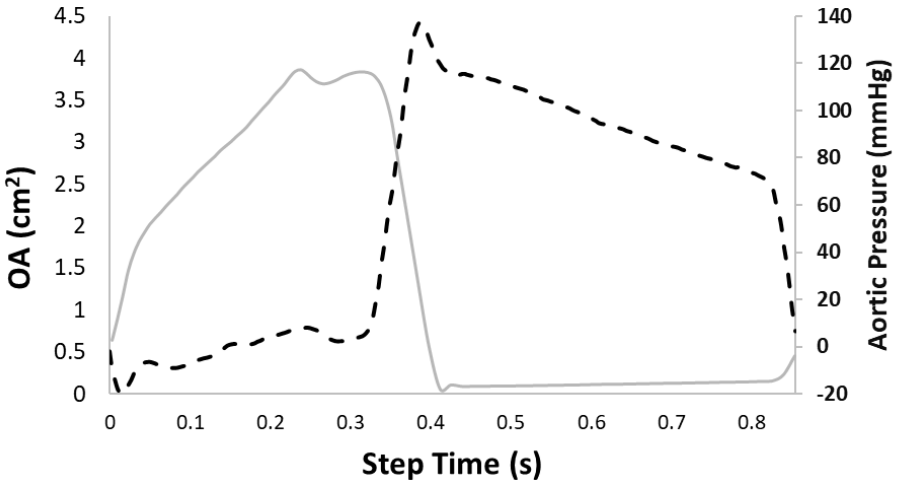

Figure A2-2 Opening area of porcine pericardium model compared to resultant aortic pressure.

Material properties of highly-dispersed porcine pericardium were applied to the trileaflet valve model and the average OA was compared to expected EOA ranges provided by Boston Scientific to validate the comparability of these outputs. It was found that the valve model accurately predicted measured EOA valves, with the average OA reaching 2.14 cm^2 compared to the expected range of 2.0-2.9 cm^2.

Appendix A3

This section includes supplementary material for Chapter 7.

Table A3-1 PCL material properties

Young's modulus (MPa)	Poisson's ratio
343	0.45

Yield stress (MPa)	Plastic strain
9.20	0
13.98	0.006
18.50	0.021
20.91	0.043
21.77	0.070
22.41	0.097
23.06	0.123
23.70	0.149
25.73	0.225
27.63	0.291

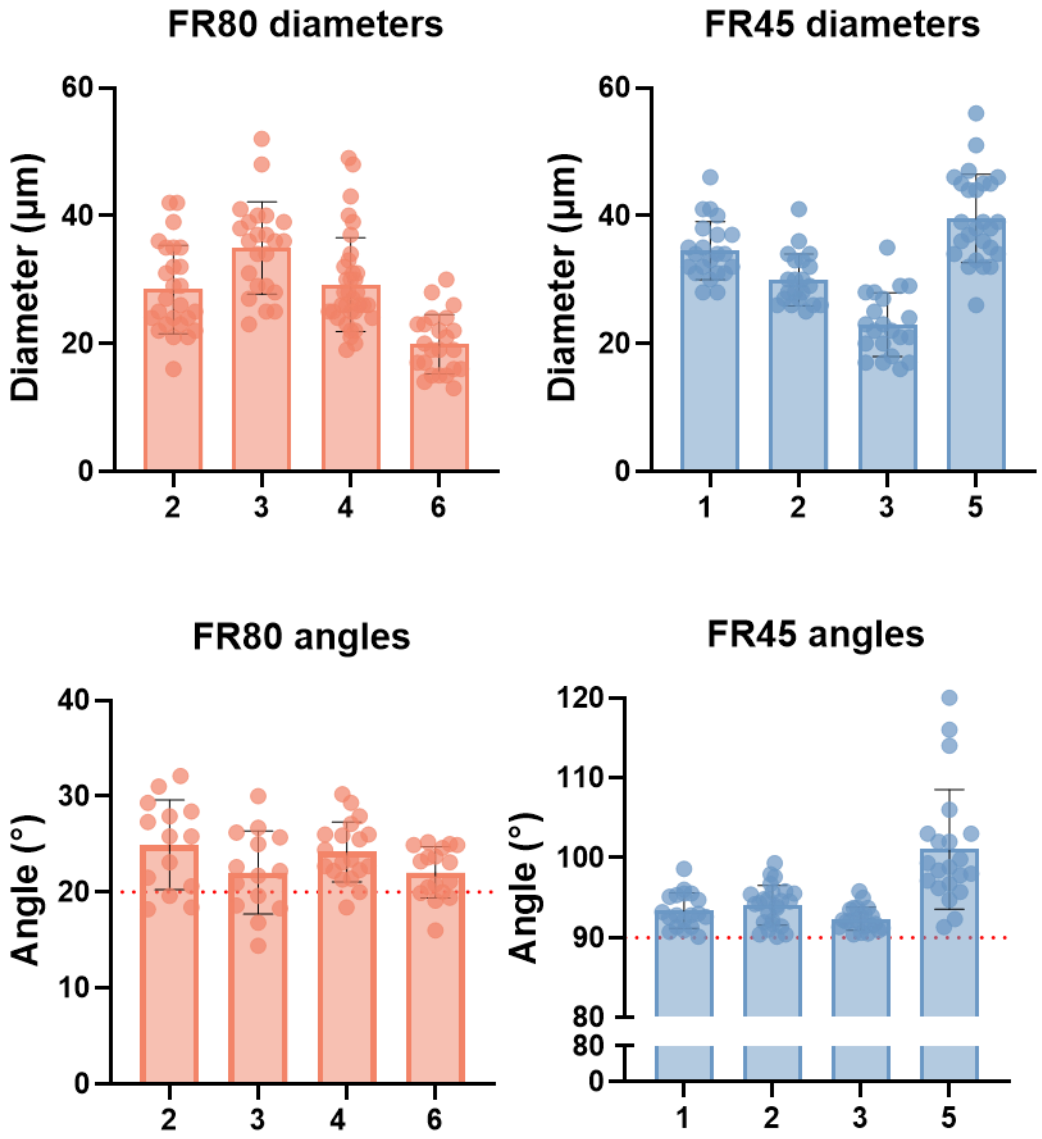

Figure A3-1 Detailed measurements of measured fibre bundle angles and diameters.

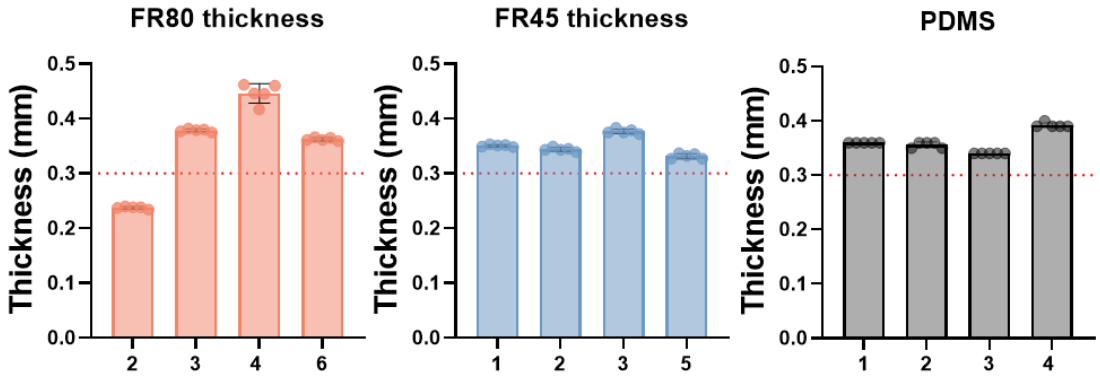

Figure A3-2 Detailed measurements of sample thicknesses

Appendix A4

This appendix includes supplementary material for Chapter 8.

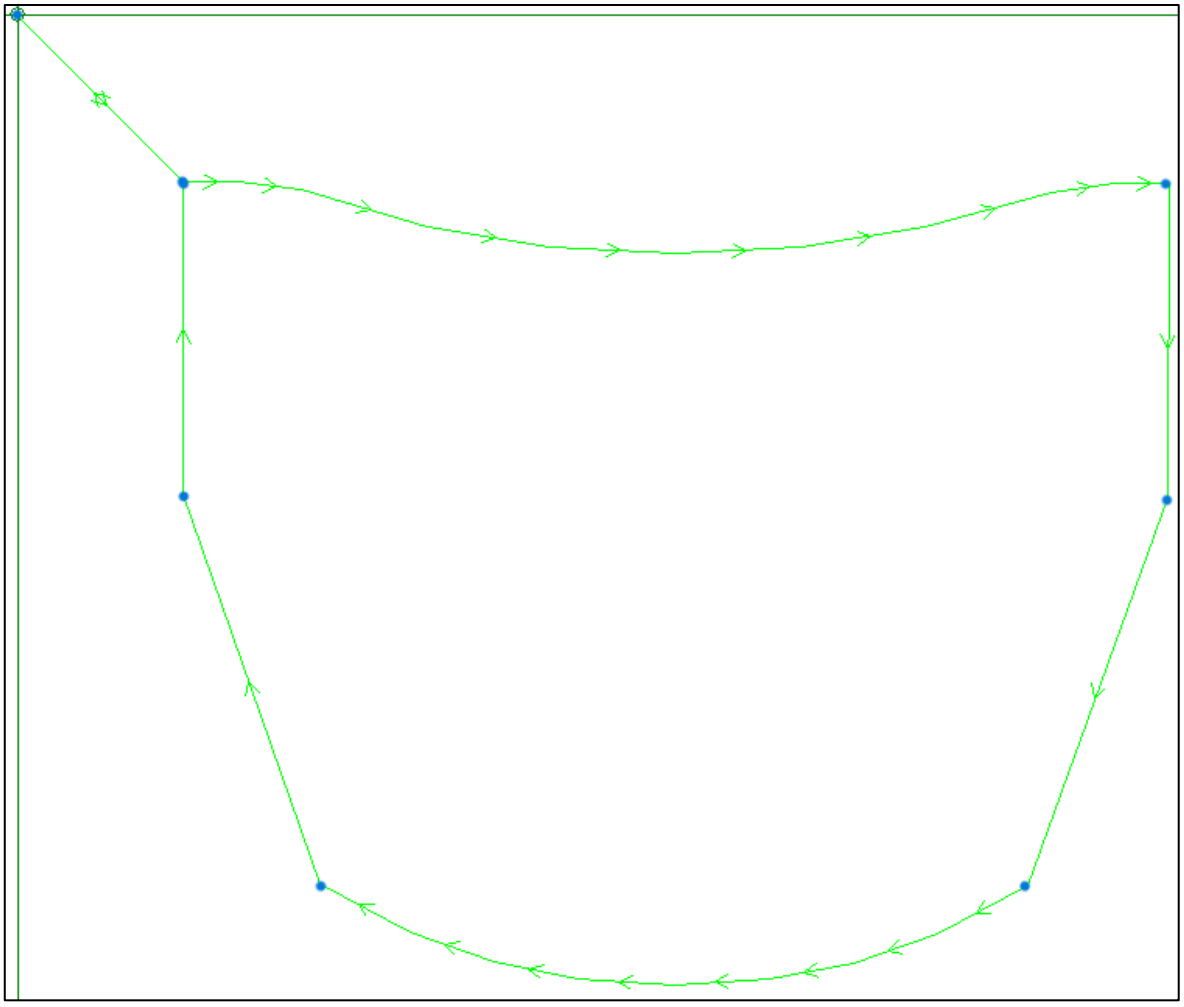

Figure A4-1 Gcode path for leaflet outline with blue dots indicating pauses

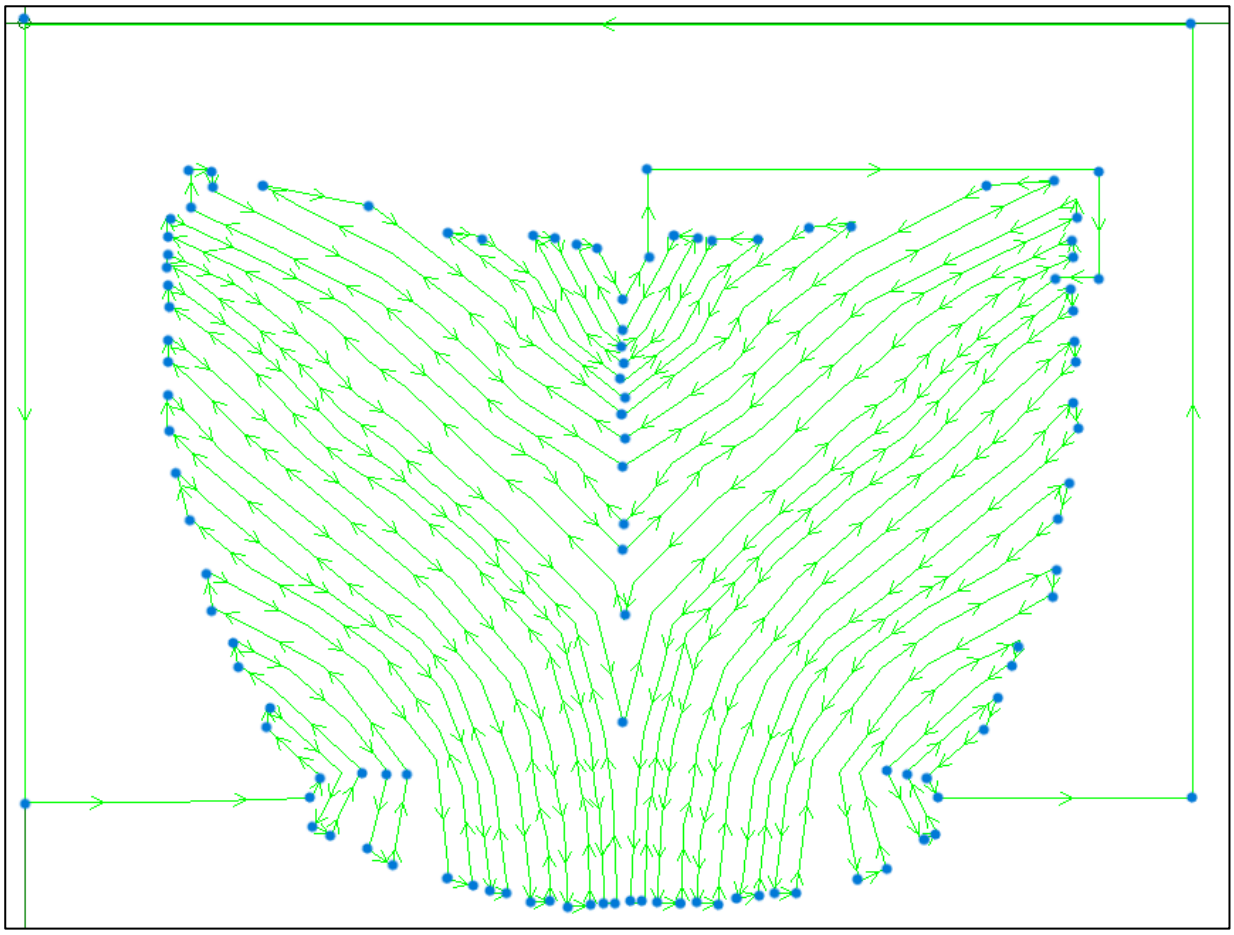

Figure A4-2 Gcode path for fibre family 1 with blue dots indicating pauses

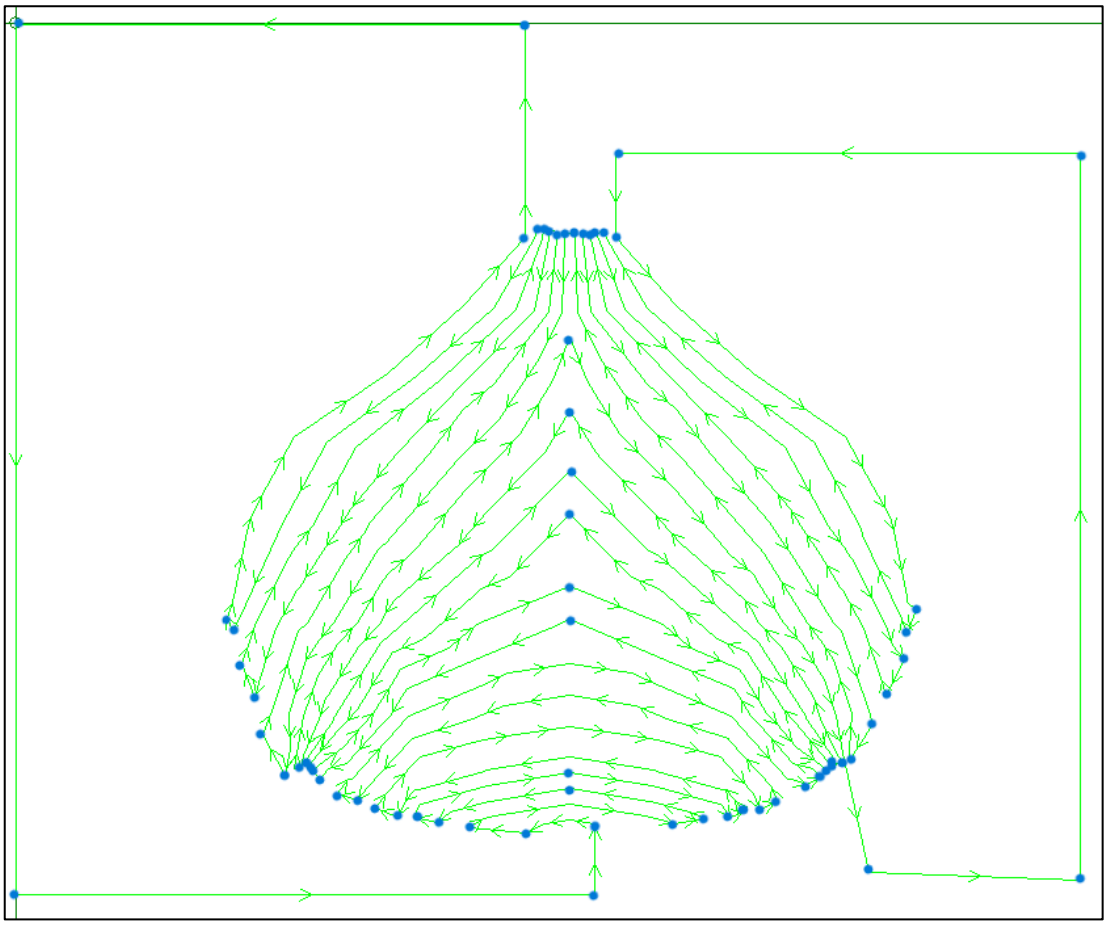

Figure A4-3 Gcode path for fibre family 2 with dots indicating pauses

Printing gcode for fibre reinforced leaflet

```
'Axis 4 = pressure
SERVO AXIS(4)=OFF
pressure=0.7 'Bar
DAC AXIS(4)=(pressure/10)*2048

'Axis 5 = voltage
SERVO AXIS(5) = OFF
initial_voltage=6.5 'kV
voltage=initial_voltage
DAC AXIS(5)=(voltage/30)*2048

'Axis 6 = current (3mA max) scale:0-2048
SERVO AXIS(6)=OFF
DAC AXIS(6)=10

raster_speed=7 '(mm/s)
raster_accel=500 '(mm/s/s)
raster_decel=1000
pause=600 '(ms)
layer_number=8

FWD_IN AXIS(0)=1
REV_IN AXIS(0)=0
FWD_IN AXIS(1)=2
REV_IN AXIS(1)=3
FWD_IN AXIS(2)=4
REV_IN AXIS(2)=5

BASE(0)
ATYPE=43
SPEED=raster_speed
ACCEL=raster_accel
DECEL=raster_decel

BASE(1)
ATYPE=43
SPEED=raster_speed
ACCEL=raster_accel
DECEL=raster_decel
WDOG=ON

BASE(0,1,2) 'set base array

layer=0

'border
MOVE(-1.5312,0)
WAIT IDLE
WA(pause)
MOVE(0,-35.5753)
WAIT IDLE
WA(pause)
MOVE(38.6202,0)
WAIT IDLE
WA(pause)
MOVE(0,38.5663)
WAIT IDLE
WA(pause)
MOVE(-37.089,0)
WAIT IDLE
WA(pause)
MOVE(0,-2.991)
WAIT IDLE
WA(pause)

'outline
MOVE(4.5,-4.5)
WAIT IDLE
WA(pause)
MOVE(1.493,0)
MOVE(1.7639,-0.2461)
MOVE(3.4343,-0.9896)
MOVE(3.4044,-0.5746)
MOVE(3.4321,-0.1905)
MOVE(3.4331,0.1711)
MOVE(3.4076,0.5554)
MOVE(3.4398,0.9702)
MOVE(1.7652,0.2362)
MOVE(1.493,-0.0084)
WAIT IDLE
WA(pause)
MOVE(-0.0484,-8.5857)
WAIT IDLE
WA(pause)
MOVE(-3.8335,-10.6429)
WAIT IDLE
WA(pause)
MOVE(-2.4717,-1.2968)
MOVE(-2.3022,-0.8031)
MOVE(-2.3023,-0.4583)
MOVE(-2.637,-0.1362)
MOVE(-2.6362,0.1511)
MOVE(-2.2997,0.4713)
MOVE(-2.2977,0.816)
MOVE(-2.4643,1.3107)
WAIT IDLE
WA(pause)
MOVE(-3.7735,10.6643)
WAIT IDLE
WA(pause)
MOVE(0,8.5859)
WAIT IDLE
WA(pause)
MOVE(-4.5,4.5)
WAIT IDLE
WA(pause)

REPEAT
        'family 2
        MOVE(0,-28.2493)
        WAIT IDLE
        WA(pause)
        MOVE(18.7999,0)
        WAIT IDLE
        WA(pause)
        MOVE(0,1.5623)
```

MOVE(0,0.7328)
WAIT IDLE
WA(pause)
MOVE(-0.7999,0.1277)
MOVE(-0.7999,-0.1277)
MOVE(-0.5953,-0.3265)
WAIT IDLE
WA(pause)
MOVE(-1.8886,0.1796)
WAIT IDLE
WA(pause)
MOVE(0.4758,0.2927)
MOVE(0.2008,0.056)
MOVE(0.1351,0.0377)
MOVE(2.4721,0.3946)
MOVE(2.4721,-0.3946)
MOVE(0.1351,-0.0377)
MOVE(0.2008,-0.056)
MOVE(0.5793,-0.1458)
WAIT IDLE
WA(pause)
MOVE(0.986,0.1458)
WAIT IDLE
WA(pause)
MOVE(-0.4919,0.22)
MOVE(-1.2369,0.3447)
MOVE(-0.0655,0.0183)
MOVE(-2.579,0.4117)
WAIT IDLE
WA(pause)
MOVE(-2.579,-0.4117)
MOVE(-0.0655,-0.0183)
MOVE(-1.2369,-0.3447)
MOVE(-0.4371,-0.3345)
WAIT IDLE
WA(pause)
MOVE(-0.7797,0.1705)
MOVE(0.173,0.3922)
WAIT IDLE
WA(pause)
MOVE(0.0849,0.0236)
MOVE(2.1545,0.6003)
MOVE(0.0041,0.0007)
MOVE(2.6817,0.4281)
WAIT IDLE
WA(pause)
MOVE(2.6817,-0.4281)
MOVE(0.0041,-0.0007)
MOVE(2.1545,-0.6003)
MOVE(0.0849,-0.0236)
MOVE(0.2881,-0.3765)
MOVE(0.4501,0.1598)
WAIT IDLE
WA(pause)
MOVE(-0.3177,0.366)
MOVE(-0.2993,0.3359)
MOVE(-0.1173,0.0327)
MOVE(-2.1364,0.5953)
MOVE(-0.0743,0.0119)
MOVE(-2.7184,0.434)
MOVE(-2.7184,-0.434)
MOVE(-0.0743,-0.0119)
MOVE(-2.1364,-0.5953)
MOVE(-0.1173,-0.0327)
MOVE(-0.2993,-0.3359)
MOVE(-0.2389,-0.5416)
WAIT IDLE
WA(pause)
MOVE(-0.7165,0.3094)
WAIT IDLE
WA(pause)
MOVE(0.3449,0.4489)
MOVE(0.8776,0.985)
MOVE(0.1936,0.2172)
MOVE(1.8786,0.5235)
MOVE(0.2147,0.0343)
MOVE(1.0155,0.1621)
MOVE(1.7761,0.2823)
MOVE(1.7761,-0.2823)
MOVE(1.0155,-0.1621)
MOVE(0.2147,-0.0343)
MOVE(1.8786,-0.5235)
MOVE(0.1936,-0.2172)
MOVE(0.8776,-0.985)
MOVE(0.1998,-0.4876)
WAIT IDLE
WA(pause)
MOVE(0.5592,0.2291)
WAIT IDLE
WA(pause)
MOVE(-0.1485,0.4753)
MOVE(-1.3533,1.5189)
MOVE(-0.0723,0.0811)
MOVE(-2.1175,0.6827)
MOVE(-0.1724,0.0729)
MOVE(-0.724,0.3064)
MOVE(-2.1272,0.3381)
MOVE(-2.1272,-0.3381)
MOVE(-0.724,-0.3064)
MOVE(-0.1724,-0.0729)
MOVE(-2.1175,-0.6827)
MOVE(-0.0723,-0.0811)
MOVE(-1.3533,-1.5189)
MOVE(-0.3626,-0.4336)
WAIT IDLE
WA(pause)
MOVE(-0.6087,0.2168)
MOVE(0.3393,0.4658)
MOVE(0.1173,0)
MOVE(1.4968,1.68)
MOVE(0.2478,0.2781)
MOVE(0.1056,0.1185)
MOVE(2.3105,0.9779)
MOVE(0.9268,0.3923)
MOVE(1.9938,0.3169)
MOVE(1.9938,-0.3169)
MOVE(0.9268,-0.3923)
MOVE(2.3105,-0.9779)

MOVE(0.1056,-0.1185)
MOVE(0.2478,-0.2781)
MOVE(1.4968,-1.68)
MOVE(0.1173,0)
MOVE(0.4976,-0.1568)
WAIT IDLE
WA(pause)
MOVE(0.4474,0.2329)
WAIT IDLE
WA(pause)
MOVE(-0.2768,0.2793)
MOVE(-0.631,0.1779)
MOVE(-1.0799,1.212)
MOVE(-0.2869,0.322)
MOVE(-0.3989,0.6335)
MOVE(-0.1698,0.2696)
MOVE(-2.3141,0.9794)
MOVE(-2.621,1.1093)
MOVE(-0.3652,0.1464)
WAIT IDLE
WA(pause)
MOVE(-0.3652,-0.1464)
MOVE(-2.621,-1.1093)
MOVE(-2.3141,-0.9794)
MOVE(-0.1698,-0.2696)
MOVE(-0.3989,-0.6335)
MOVE(-0.2869,-0.322)
MOVE(-1.0799,-1.212)
MOVE(-0.631,-0.1779)
MOVE(-0.229,-0.3393)
WAIT IDLE
WA(pause)
MOVE(-0.2671,0.2671)
WAIT IDLE
WA(pause)
MOVE(0.2194,0.2194)
MOVE(0.7567,0.5526)
MOVE(0.6718,0.754)
MOVE(0.316,0.3547)
MOVE(0.798,1.2672)
MOVE(0.1101,0.1645)
MOVE(1.574,0.6662)
MOVE(0.3409,0.2955)
MOVE(0.5129,0.4446)
MOVE(0.1145,0.0992)
MOVE(2.9488,1.1818)
WAIT IDLE
WA(pause)
MOVE(2.9488,-1.1818)
MOVE(0.1145,-0.0992)
MOVE(0.5129,-0.4446)
MOVE(0.3409,-0.2955)
MOVE(1.574,-0.6662)
MOVE(0.1101,-0.1645)
MOVE(0.798,-1.2672)
MOVE(0.316,-0.3547)
MOVE(0.6718,-0.754)
MOVE(0.7567,-0.5526)
MOVE(0.223,-0.2503)
WAIT IDLE
WA(pause)
MOVE(0.1405,0.1252)
WAIT IDLE
WA(pause)
MOVE(-0.1405,0.2438)
MOVE(-0.8287,0.9559)
MOVE(-0.2637,0.2959)
MOVE(-0.3451,0.3873)
MOVE(-1.1831,1.8787)
MOVE(-0.0167,0.0071)
MOVE(-0.8944,0.3786)
MOVE(-0.0611,0.0529)
MOVE(-0.0548,0.0475)
MOVE(-1.5829,1.3721)
MOVE(-0.2273,0.197)
MOVE(-0.923,0.3699)
MOVE(-0.7969,0.8198)
MOVE(-1.1889,1.223)
WAIT IDLE
WA(pause)
MOVE(-1.1889,-1.223)
MOVE(-0.7969,-0.8198)
MOVE(-0.923,-0.3699)
MOVE(-0.2273,-0.197)
MOVE(-1.5829,-1.3721)
MOVE(-0.0548,-0.0475)
MOVE(-0.0611,-0.0529)
MOVE(-0.8944,-0.3786)
MOVE(-0.0167,-0.0071)
MOVE(-1.1831,-1.8787)
MOVE(-0.3451,-0.3873)
MOVE(-0.2637,-0.2959)
MOVE(-0.8287,-0.9559)
MOVE(-0.1288,-0.2658)
WAIT IDLE
WA(pause)
MOVE(-0.0949,0.1472)
WAIT IDLE
WA(pause)
MOVE(0.046,0.2131)
MOVE(0.8481,1.2078)
MOVE(0.0312,0.0926)
MOVE(0.0102,0.0304)
MOVE(1.5152,2.4061)
MOVE(0.3073,0.2664)
MOVE(2.6231,2.2738)
MOVE(0.3401,0.2948)
MOVE(0.3141,0.1259)
MOVE(2.5549,2.6282)
WAIT IDLE
WA(pause)
MOVE(2.5549,-2.6282)
MOVE(0.3141,-0.1259)
MOVE(0.3401,-0.2948)
MOVE(2.6231,-2.2738)
MOVE(0.3073,-0.2664)
MOVE(1.5152,-2.4061)
MOVE(0.0102,-0.0304)

MOVE(0.0312,-0.0926)
MOVE(0.8481,-1.2078)
MOVE(0.1134,-0.2131)
WAIT IDLE
WA(pause)
MOVE(0.2038,0.1084)
WAIT IDLE
WA(pause)
MOVE(-0.1858,0.1746)
MOVE(-0.5276,1.2063)
MOVE(-0.2201,0.6529)
MOVE(-0.0554,0.088)
MOVE(-1.0006,1.5889)
MOVE(-0.7223,0.7749)
MOVE(-0.1933,0.3141)
MOVE(-0.2549,0.4141)
MOVE(-1.8904,1.6387)
MOVE(-0.2138,0.1853)
MOVE(-0.3135,0.3644)
MOVE(-0.6348,0.738)
MOVE(-1.5705,1.6156)
MOVE(-0.248,0.2551)
MOVE(-0.8305,1.3564
WAIT IDLE
WA(pause)
MOVE(-0.8305,-1.3564)
MOVE(-0.248,-0.2551)
MOVE(-1.5705,-1.6156)
MOVE(-0.6348,-0.738)
MOVE(-0.3135,-0.3644)
MOVE(-0.2138,-0.1853)
MOVE(-1.8904,-1.6387)
MOVE(-0.2549,-0.4141)
MOVE(-0.1933,-0.3141)
MOVE(-0.7223,-0.7749)
MOVE(-1.0006,-1.5889)
MOVE(-0.0554,-0.088)
MOVE(-0.2201,-0.6529)
MOVE(-0.5276,-1.2063)
MOVE(-0.0929,-0.4302)
WAIT IDLE
WA(pause)
MOVE(-0.1874,0)
MOVE(0.0945,0.529)
MOVE(0.2114,1.1835)
MOVE(0.4035,1.1968)
MOVE(0.1508,0.2394)
MOVE(0.5614,0.8915)
MOVE(0.6062,0.6761)
MOVE(0.7995,1.2991)
MOVE(0.1879,0.3052)
MOVE(0.7383,0.6399)
MOVE(0.1906,0.2215)
MOVE(1.6247,1.8888)
MOVE(0.9304,0.9571)
MOVE(0.8317,0.8556)
MOVE(0.9365,1.5295)
MOVE(0.1225,0.2001)
MOVE(0.5662,1.4119)
WAIT IDLE
WA(pause)
MOVE(0.5662,-1.4119)
MOVE(0.1225,-0.2001)
MOVE(0.9365,-1.5295)
MOVE(0.8317,-0.8556)
MOVE(0.9304,-0.9571)
MOVE(1.6247,-1.8888)
MOVE(0.1906,-0.2215)
MOVE(0.7383,-0.6399)
MOVE(0.1879,-0.3052)
MOVE(0.7995,-1.2991)
MOVE(0.6062,-0.6761)
MOVE(0.5614,-0.8915)
MOVE(0.1508,-0.2394)
MOVE(0.4035,-1.1968)
MOVE(0.2114,-1.1835)
MOVE(0.8452,-3.8949)
WAIT IDLE
WA(pause)
MOVE(6.8653,-0.2424)
WAIT IDLE
WA(pause)
MOVE(0,23.5922)
WAIT IDLE
WA(pause)
MOVE(-15.1013,0)
WAIT IDLE
WA(pause)
MOVE(0,-2.7293)
WAIT IDLE
WA(pause)
MOVE(1.9894,-2.2094)
MOVE(2.4808,-2.199)
MOVE(3.0013,-2.0623)
MOVE(0.8968,-1.6139)
MOVE(0.5356,-0.9638)
MOVE(0.1392,-0.4691)
MOVE(0.4232,-2.1412)
MOVE(0.0321,-0.1625)
MOVE(0.2861,-0.2961)
WAIT IDLE
WA(pause)
MOVE(-0.2861,-0.7592)
WAIT IDLE
WA(pause)
MOVE(-0.2096,0.4631)
MOVE(-1.2475,2.7565)
MOVE(-0.0649,0.2188)
MOVE(-1.5463,2.7827)
MOVE(-2.8888,2.1306)
MOVE(-2.5161,2.2174)
MOVE(-1.3227,2.291)
MOVE(-0.0686,0.2045)
WAIT IDLE
WA(pause)
MOVE(-0.2477,-0.039)
WAIT IDLE
WA(pause)

MOVE(0.0667,-0.1794)
MOVE(0.842,-2.3135)
MOVE(2.4614,-2.2796)
MOVE(2.7366,-2.1985)
MOVE(1.4084,-2.5345)
MOVE(0.5375,-0.6774)
MOVE(0.2218,-0.3604)
MOVE(0.0266,-0.0431)
MOVE(1.0948,-2.1893)
MOVE(0.2105,-0.6244)
MOVE(0.3852,-0.4717)
WAIT IDLE
WA(pause)
MOVE(-0.5743,-1.1585)
WAIT IDLE
WA(pause)
MOVE(-0.1891,0.5611)
MOVE(-0.5467,1.6216)
MOVE(-0.6809,1.2231)
MOVE(-0.0714,0.1159)
MOVE(-0.6557,1.0655)
MOVE(-0.6557,0.9054)
MOVE(-0.33,0.5939)
MOVE(-0.4775,0.5552)
MOVE(-1.0916,1.2691)
MOVE(-2.1154,2.2507)
MOVE(-2.2909,2.3461)
MOVE(-0.4951,2.3293)
MOVE(-0.0686,0.1932)
WAIT IDLE
WA(pause)
MOVE(-0.2028,0)
WAIT IDLE
WA(pause)
MOVE(0.0218,-0.2071)
MOVE(0.246,-2.3402)
MOVE(1.8256,-2.3637)
MOVE(0.9641,-0.8185)
MOVE(1.1473,-1.4911)
MOVE(1.8775,-2.1828)
MOVE(0.1365,-0.2457)
MOVE(0.658,-0.9376)
MOVE(1.2775,-2.0757)
MOVE(0.2669,-0.2569)
MOVE(0.8829,-2.6189)
MOVE(0.1323,-0.4116)
WAIT IDLE
WA(pause)
MOVE(-0.75,-1.1982)
WAIT IDLE
WA(pause)
MOVE(0,0.3944)
MOVE(0.0632,1.1385)
MOVE(-0.5869,1.7408)
MOVE(-0.2461,0.3908)
MOVE(-0.1749,0.2777)
MOVE(-0.4528,0.5186)
MOVE(-1.3904,2.2592)
MOVE(-0.1208,0.1963)
MOVE(-0.0886,0.0768)
MOVE(-0.0614,0.0532)
MOVE(-2.3909,2.7796)
MOVE(-1.3099,1.274)
MOVE(-0.74,1.0971)
MOVE(-0.6153,0.9122)
MOVE(-0.7173,1.4707)
MOVE(-0.082,2.3469)
MOVE(0,0.2209)
WAIT IDLE
WA(pause)
MOVE(-0.3495,0)
WAIT IDLE
WA(pause)
MOVE(0,-0.2209)
MOVE(-0.082,-2.3469)
MOVE(-0.7173,-1.4707)
MOVE(-0.6153,-0.9122)
MOVE(-0.74,-1.0971)
MOVE(-1.3099,-1.274)
MOVE(-2.3909,-2.7796)
MOVE(-0.0614,-0.0532)
MOVE(-0.0886,-0.0768)
MOVE(-0.1208,-0.1963)
MOVE(-1.3904,-2.2592)
MOVE(-0.4528,-0.5186)
MOVE(-0.1749,-0.2777)
MOVE(-0.2461,-0.3908)
MOVE(-0.5869,-1.7408)
MOVE(0.0632,-1.1385)
MOVE(-0.1847,-0.8711)
WAIT IDLE
WA(pause)
MOVE(-0.7311,1.322)
WAIT IDLE
WA(pause)
MOVE(0.2981,0.7645)
MOVE(0.8829,2.6189)
MOVE(0.2669,0.2569)
MOVE(1.2775,2.0757)
MOVE(0.658,0.9376)
MOVE(0.1365,0.2457)
MOVE(1.8775,2.1828)
MOVE(1.1473,1.4911)
MOVE(0.9641,0.8185)
MOVE(1.8256,2.3637)
MOVE(0.246,2.3402)
MOVE(0.0289,0.246)
WAIT IDLE
WA(pause)
MOVE(-0.2378,0.0361)
WAIT IDLE
WA(pause)
MOVE(-0.0407,-0.2683)
MOVE(-0.4951,-2.3293)
MOVE(-2.2909,-2.3461)
MOVE(-2.1154,-2.2507)
MOVE(-1.0916,-1.2691)
MOVE(-0.4775,-0.5552)

MOVE(-0.33,-0.5939)
MOVE(-0.6557,-0.9054)
MOVE(-0.6557,-1.0655)
MOVE(-0.0714,-0.1159)
MOVE(-0.6809,-1.2231)
MOVE(-0.5467,-1.6216)
MOVE(-0.1678,-0.6451)
WAIT IDLE
WA(pause)
MOVE(-0.4302,1.1189)
WAIT IDLE
WA(pause)
MOVE(0.2197,0.5953)
MOVE(0.2105,0.6244)
MOVE(1.0948,2.1893)
MOVE(0.0266,0.0431)
MOVE(0.2218,0.3604)
MOVE(0.5375,0.6774)
MOVE(1.4084,2.5345)
MOVE(2.7366,2.1985)
MOVE(2.4614,2.2796)
MOVE(0.842,2.3135)
MOVE(0.0464,0.3107)
WAIT IDLE
WA(pause)
MOVE(-0.1727,0.0263)
WAIT IDLE
WA(pause)
MOVE(-0.1233,-0.3232)
MOVE(-1.3227,-2.291)
MOVE(-2.5161,-2.2174)
MOVE(-2.8888,-2.1306)
MOVE(-1.5463,-2.7827)
MOVE(-0.0649,-0.2188)
MOVE(-1.2475,-2.7565)
MOVE(-0.2096,-0.349)
WAIT IDLE
WA(pause)
MOVE(-0.1519,0.4294)
WAIT IDLE
WA(pause)
MOVE(0.1519,0.5119)
MOVE(0.0321,0.1625)
MOVE(0.4232,2.1412)
MOVE(0.1392,0.4691)
MOVE(0.5356,0.9638)
MOVE(0.8968,1.6139)
MOVE(3.0013,2.0623)
MOVE(2.4808,2.199)
MOVE(1.9894,2.2094)
WAIT IDLE
WA(pause)
MOVE(0,1.7293)
WAIT IDLE
WA(pause)
MOVE(0,5.189)
WAIT IDLE
WA(pause)
MOVE(-16.5294,0)
WAIT IDLE
WA(pause)
'family 1
MOVE(0,-23.3772)
WAIT IDLE
WA(pause)
MOVE(4.2485,0)
MOVE(4.3543,0.1396)
WAIT IDLE
WA(pause)
MOVE(0.2989,0.6309)
WAIT IDLE
WA(pause)
MOVE(-0.2845,0.2573)
MOVE(-0.4542,0.4107)
MOVE(-0.8665,0.7716)
WAIT IDLE
WA(pause)
MOVE(0,0.7377)
WAIT IDLE
WA(pause)
MOVE(0.5158,-0.518)
MOVE(1.7004,-1.5375)
MOVE(-0.5138,-1.0845)
MOVE(-0.3094,-0.5002)
WAIT IDLE
WA(pause)
MOVE(0.5322,-0.2652)
WAIT IDLE
WA(pause)
MOVE(0.2192,0.5304)
MOVE(0.6828,1.4413)
WAIT IDLE
WA(pause)
MOVE(-2.6621,2.4071)
MOVE(-1.0695,0.7361)
WAIT IDLE
WA(pause)
MOVE(-0.1377,0.7459)
WAIT IDLE
WA(pause)
MOVE(0.8567,-0.4911)
MOVE(0.8353,-0.4042)
MOVE(1.7861,-1.5779)
MOVE(1.1931,-1.5343)
WAIT IDLE
WA(pause)
MOVE(-0.4874,-1.8531)
MOVE(-0.1139,-0.4247)
WAIT IDLE
WA(pause)
MOVE(0.7026,-0.51)
WAIT IDLE
WA(pause)
MOVE(0.1056,0.5994)
MOVE(0.3856,2.1884)
WAIT IDLE
WA(pause)
MOVE(-1.9592,2.6516)

MOVE(-0.584,0.528)
MOVE(-0.0907,0.082)
MOVE(-2.0954,1.1577)
MOVE(-1.1566,0.5597)
WAIT IDLE
WA(pause)
MOVE(-0.1749,1.0685)
WAIT IDLE
WA(pause)
MOVE(0.9349,-0.4993)
MOVE(2.1345,-1.1288)
MOVE(1.7077,-1.2397)
MOVE(2.1195,-2.7979)
MOVE(0.368,-3.1346)
MOVE(0,-0.4229)
WAIT IDLE
WA(pause)
MOVE(0.7411,-0.2149)
WAIT IDLE
WA(pause)
MOVE(-0.0551,0.4299)
MOVE(-0.2967,2.5333)
MOVE(-0.6223,1.5725)
MOVE(-0.0556,0.1406)
MOVE(-0.0215,0.0292)
MOVE(-1.0394,1.4067)
MOVE(-0.6911,0.9353)
MOVE(-1.7948,1.3175)
MOVE(-2.1217,1.1722)
MOVE(-0.8235,0.6762)
MOVE(-1.0412,0.8487)
WAIT IDLE
WA(pause)
MOVE(-0.3406,1.3945)
WAIT IDLE
WA(pause)
MOVE(0.8977,-0.8753)
MOVE(2.7936,-2.2938)
MOVE(0.4388,-0.2424)
MOVE(0.4668,-0.2579)
MOVE(2.3929,-1.7565)
MOVE(0.1039,-0.1233)
MOVE(0.8197,-0.9724)
MOVE(1.1272,-2.8484)
MOVE(0.0184,-0.1574)
MOVE(0.3051,-2.6048)
MOVE(0.0854,-0.5288)
WAIT IDLE
WA(pause)
MOVE(0.5312,0)
WAIT IDLE
WA(pause)
MOVE(-0.1008,0.4231)
MOVE(-0.3134,2.6762)
MOVE(-0.0369,0.3148)
MOVE(-1.0851,2.742)
MOVE(-0.0962,0.2432)
MOVE(-1.0146,1.2036)
MOVE(-1.6918,1.2418)
MOVE(-0.6506,0.5421)
MOVE(-1.1873,0.9893)
MOVE(-2.9844,2.4865)
MOVE(-0.3788,0.3982)
MOVE(-0.7515,0.702)
WAIT IDLE
WA(pause)
MOVE(0,1.092)
WAIT IDLE
WA(pause)
MOVE(0.7515,-0.7995)
MOVE(0.9875,-1.065)
MOVE(5.9963,-4.752)
MOVE(1.7108,-2.0389)
MOVE(1.1114,-2.862)
MOVE(0.3518,-3.2614)
MOVE(0,-0.5452)
WAIT IDLE
WA(pause)
MOVE(0.6183,0)
WAIT IDLE
WA(pause)
MOVE(0,0.474)
MOVE(-0.0718,1.433)
MOVE(-0.34,1.3859)
MOVE(-0.2065,1.5813)
MOVE(-0.036,0.2756)
MOVE(-0.0769,0.1944)
MOVE(-0.4556,1.1513)
MOVE(-0.0298,0.0754)
MOVE(-2.3902,2.8355)
MOVE(-0.6071,0.5058)
MOVE(-3.1783,2.6481)
MOVE(-0.7577,0.6313)
MOVE(-0.6554,0.5382)
MOVE(-0.4124,0.3386)
MOVE(-1.5583,1.6381)
MOVE(-0.6828,0.5722)
WAIT IDLE
WA(pause)
MOVE(0,0.7042)
WAIT IDLE
WA(pause)
MOVE(0.6828,-0.5243)
MOVE(0.7505,-0.6235)
MOVE(2.6333,-2.4599)
MOVE(1.7398,-1.3415)
MOVE(1.7711,-1.6033)
MOVE(0.9485,-0.7635)
MOVE(2.1567,-2.6225)
MOVE(0.122,-0.3758)
MOVE(0.6667,-1.9922)
MOVE(0.1902,-1.4321)
MOVE(0.2384,-0.9373)
MOVE(0.0489,-1.861)
MOVE(0,-0.5831)
WAIT IDLE
WA(pause)
MOVE(0.7151,0)

WAIT IDLE
WA(pause)
MOVE(0,0.5421)
MOVE(-0.1117,2.2272)
MOVE(-0.1399,0.6316)
MOVE(-0.2103,1.6106)
MOVE(-0.6042,2.0059)
MOVE(-0.1265,0.56)
MOVE(-0.0046,0.0054)
MOVE(-0.978,1.1601)
MOVE(-0.5891,0.6988)
MOVE(-0.7541,0.8946)
MOVE(-2.3114,2.0022)
MOVE(-1.4191,0.893)
MOVE(-0.9744,0.8118)
MOVE(-1.1378,1.2223)
MOVE(-1.094,1.15)
MOVE(-0.1341,0.141)
MOVE(-1.3919,1.0638)
MOVE(-0.6828,0.4362)
WAIT IDLE
WA(pause)

MOVE(0,0.6619)
WAIT IDLE
WA(pause)
MOVE(0.6828,-0.4688)
MOVE(1.6734,-1.2789)
MOVE(0.5432,-0.4694)
MOVE(0.6126,-0.5294)
MOVE(1.7258,-1.8539)
MOVE(1.4427,-0.9608)
MOVE(0.5106,-0.4665)
MOVE(2.0175,-1.7476)
MOVE(1.1526,-1.2235)
MOVE(0.3215,-0.3412)
MOVE(1.1361,-1.206)
MOVE(0.1961,-0.8679)
MOVE(0.6234,-2.1578)
MOVE(0.1893,-1.7548)
MOVE(0.1215,-0.5486)
MOVE(0.1165,-2.3244)
MOVE(0.019,-0.4303)
WAIT IDLE
WA(pause)
MOVE(0.3826,0)
WAIT IDLE
WA(pause)
MOVE(0,0.4073)
MOVE(-0.1447,2.8853)
MOVE(-0.238,1.8223)
MOVE(-0.6179,2.2337)
MOVE(-0.2308,1.0215)
MOVE(-0.0163,0.0173)
MOVE(-0.8358,0.8873)
MOVE(-1.0228,1.0857)
MOVE(-0.8059,0.8555)
MOVE(-1.4661,1.27)
MOVE(-0.197,0.1531)
MOVE(-1.1292,1.0318)
MOVE(-1.5522,1.1217)
MOVE(-1.0014,1.0758)
MOVE(-0.3497,0.3757)
MOVE(-0.7146,0.6175)
MOVE(-0.4731,0.4088)
MOVE(-1.9889,1.5201)
MOVE(-0.7515,0.4339)
WAIT IDLE
WA(pause)
MOVE(0,0.2735)
WAIT IDLE
WA(pause)
MOVE(0.7515,-0.3157)
MOVE(0.8174,-0.3871)
MOVE(0.5745,-0.2646)
MOVE(1.0331,-0.7739)
MOVE(1.1921,-0.9908)
MOVE(0.7353,-0.8221)
MOVE(0.6073,-0.6789)
MOVE(1.2361,-0.8147)
MOVE(1.7118,-1.5843)
MOVE(1.4052,-1.1679)
MOVE(2.8319,-2.9419)
MOVE(0.8553,-3.3633)
WAIT IDLE
WA(pause)
MOVE(0.8553,3.3633)
MOVE(2.8319,2.9419)
MOVE(1.4052,1.1679)
MOVE(1.7118,1.5843)
MOVE(1.2361,0.8147)
MOVE(0.6073,0.6789)
MOVE(0.7353,0.8221)
MOVE(1.1921,0.9908)
MOVE(1.0331,0.7739)
MOVE(0.5745,0.2646)
MOVE(0.8174,0.3871)
MOVE(0.5488,0.2599)
WAIT IDLE
WA(pause)
MOVE(-0.0733,0.5382)
WAIT IDLE
WA(pause)
MOVE(-0.4756,-0.2448)
MOVE(-1.0791,-0.511)
MOVE(-1.385,-0.6559)
MOVE(-1.7574,-1.1758)
MOVE(-1.1025,-1.1195)
MOVE(-1.0963,-0.7334)
MOVE(-2.5886,-2.471)
MOVE(-1.2381,-0.9404)
MOVE(-2.4593,-2.4973)
MOVE(-0.2938,-1.1174)
WAIT IDLE
WA(pause)
MOVE(-0.2938,1.1174)
MOVE(-2.4593,2.4973)
MOVE(-1.2381,0.9404)

MOVE(-2.5886,2.471)
MOVE(-1.0963,0.7334)
MOVE(-1.1025,1.1195)
MOVE(-1.7574,1.1758)
MOVE(-1.385,0.6559)
MOVE(-1.0791,0.511)
MOVE(-0.7515,0.3543)
WAIT IDLE
WA(pause)
MOVE(0,0.5556)
WAIT IDLE
WA(pause)
MOVE(0.7515,-0.3567)
MOVE(2.177,-1.0309)
MOVE(0.2314,-0.1191)
MOVE(1.1812,-0.6081)
MOVE(1.0924,-0.5624)
MOVE(4.4069,-3.8937)
MOVE(1.5529,-0.9315)
MOVE(0.4941,-0.7516)
MOVE(1.8641,-1.823)
WAIT IDLE
WA(pause)
MOVE(1.8641,1.823)
MOVE(0.4941,0.7516)
MOVE(1.5529,0.9315)
MOVE(4.4069,3.8937)
MOVE(1.0924,0.5624)
MOVE(1.1812,0.6081)
MOVE(0.2314,0.1191)
MOVE(2.177,1.0309)
MOVE(0.6033,0.29)
WAIT IDLE
WA(pause)
MOVE(0,0.5662)
WAIT IDLE
WA(pause)
MOVE(-0.6033,-0.303)
MOVE(-2.3985,-1.1358)
MOVE(-0.1962,-0.101)
MOVE(-1.2768,-0.6573)
MOVE(-1.8782,-0.9669)
MOVE(-0.5447,-0.4825)
MOVE(-2.4002,-2.1257)
MOVE(-0.7261,-0.6905)
MOVE(-0.1193,-0.109)
MOVE(-2.0282,-1.3414)
MOVE(-0.7141,-1.0417)
MOVE(-0.7177,-0.7619)
WAIT IDLE
WA(pause)
MOVE(-0.7177,0.7619)
MOVE(-0.7141,1.0417)
MOVE(-2.0282,1.3414)
MOVE(-0.1193,0.109)
MOVE(-0.7261,0.6905)
MOVE(-2.4002,2.1257)
MOVE(-0.5447,0.4825)
MOVE(-1.8782,0.9669)
MOVE(-1.2768,0.6573)
MOVE(-0.1962,0.101)
MOVE(-2.3985,1.1358)
WAIT IDLE
WA(pause)

MOVE(0,1.2128)
WAIT IDLE
WA(pause)
MOVE(0.6319,0)
WAIT IDLE
WA(pause)
MOVE(0,-0.6595)
WAIT IDLE
WA(pause)
MOVE(2.2096,-1.0831)
MOVE(2.9082,-1.546)
MOVE(1.4595,-1.1074)
MOVE(1.3165,-1.1905)
MOVE(1.3474,-1.3109)
MOVE(3.1269,-2.0142)
WAIT IDLE
WA(pause)
MOVE(3.1269,2.0142)
MOVE(1.3474,1.3109)
MOVE(1.3165,1.1905)
MOVE(1.4595,1.1074)
MOVE(2.9082,1.546)
MOVE(2.2096,1.0831)
MOVE(0.6319,0.3097)
WAIT IDLE
WA(pause)
MOVE(-1.9889,-0.1148)
WAIT IDLE
WA(pause)
MOVE(-1.1209,-0.5631)
MOVE(-2.9702,-1.5291)
MOVE(-2.136,-1.6119)
MOVE(-0.5961,-0.6136)
MOVE(-0.9514,-1.1398)
MOVE(-0.2419,-0.1887)
MOVE(-1.6576,-1.0963)
MOVE(-1.337,-0.8843)
WAIT IDLE
WA(pause)
MOVE(-1.337,0.8843)
MOVE(-1.6576,1.0963)
MOVE(-0.2419,0.1887)
MOVE(-0.9514,1.1398)
MOVE(-0.5961,0.6136)
MOVE(-2.136,1.6119)
MOVE(-2.9702,1.5291)
MOVE(-0.999,0.5631)
WAIT IDLE
WA(pause)
MOVE(3.3271,-0.6657)
WAIT IDLE
WA(pause)
MOVE(1.1242,-0.8346)

MOVE(2.8586,-2.2038)
MOVE(0.4524,-0.8985)
MOVE(0.4605,-0.2216)
MOVE(2.6664,-2.0803)
WAIT IDLE
WA(pause)
MOVE(2.6664,2.0803)
MOVE(0.4605,0.2216)
MOVE(0.4524,0.8985)
MOVE(2.8586,2.2038)
MOVE(0.4821,0.3996)
WAIT IDLE
WA(pause)
MOVE(-1.3927,-0.1773)
WAIT IDLE
WA(pause)
MOVE(-0.6657,-0.4884)
MOVE(-1.4016,-1.0577)
MOVE(-0.4781,-0.3608)
MOVE(-0.671,-1.2452)
MOVE(-0.1527,-0.2833)
MOVE(-2.1582,-1.6837)
WAIT IDLE
WA(pause)
MOVE(-2.1582,1.6837)
MOVE(-0.1527,0.2833)
MOVE(-0.671,1.2452)
MOVE(-0.4781,0.3608)
MOVE(-1.4016,1.0577)
MOVE(-0.4776,0.3589)
WAIT IDLE
WA(pause)
MOVE(1.0337,-0.1336)
MOVE(0.513,-0.4058)
MOVE(0.3324,-0.2508)
MOVE(0.8665,-0.6539)
MOVE(0.8663,-1.6075)
MOVE(0.0774,-0.1435)
MOVE(0.0263,-0.0205)
MOVE(1.6236,-1.2666)
WAIT IDLE
WA(pause)
MOVE(1.6236,1.2666)
MOVE(0.0263,0.0205)
MOVE(0.0774,0.1435)
MOVE(0.8663,1.6075)
MOVE(0.8665,0.6539)
MOVE(0.3324,0.2508)
MOVE(0.3956,0.2985)
WAIT IDLE
WA(pause)

MOVE(-1.5215,-0.0004)
WAIT IDLE
WA(pause)
MOVE(-0.2137,-0.4101)
MOVE(-1.2916,-2.3967)
MOVE(-0.4032,-0.3356)
MOVE(-0.758,-0.5913)
WAIT IDLE
WA(pause)
MOVE(-0.758,0.5913)
MOVE(-0.4032,0.3356)
MOVE(-1.2916,2.3967)
MOVE(-0.2581,0.5178)
WAIT IDLE
WA(pause)
MOVE(0.6895,-0.1077)
WAIT IDLE
WA(pause)
MOVE(0.1541,-0.4426)
MOVE(1.2339,-2.2897)
MOVE(0.2278,-0.1777)
MOVE(0.4056,-0.3164)
WAIT IDLE
WA(pause)
MOVE(0.4056,0.3164)
MOVE(0.2278,0.1777)
MOVE(1.2339,2.2897)
MOVE(0.2909,0.5503)
WAIT IDLE
WA(pause)
MOVE(-0.5837,0)
WAIT IDLE
WA(pause)
MOVE(-0.2927,-0.5828)
MOVE(-1.1854,-2.1996)
MOVE(-0.0964,-0.1789)
WAIT IDLE
WA(pause)
MOVE(-0.0964,0.1789)
MOVE(-1.1854,2.1996)
MOVE(-0.1501,0.3574)
WAIT IDLE
WA(pause)
MOVE(0.5766,-0.0883)
WAIT IDLE
WA(pause)
MOVE(0.159,-0.3017)
MOVE(0.6963,-1.292)
WAIT IDLE
WA(pause)
MOVE(0.6963,1.292)
WAIT IDLE
WA(pause)

MOVE(0,2.6209)
WAIT IDLE
WA(pause)
MOVE(13.5899,0)
WAIT IDLE
WA(pause)
MOVE(0,-3.2641)
WAIT IDLE
WA(pause)
MOVE(-1.2862,0)
WAIT IDLE
WA(pause)

MOVE(-1.9889,-1.5201)
MOVE(-0.4731,-0.4088)
MOVE(-0.7146,-0.6175)
MOVE(-0.3497,-0.3757)
MOVE(-1.0014,-1.0758)
MOVE(-1.5522,-1.1217)
MOVE(-1.1292,-1.0318)
MOVE(-0.197,-0.1531)
MOVE(-1.4661,-1.27)
MOVE(-0.8059,-0.8555)
MOVE(-1.0228,-1.0857)
MOVE(-0.8358,-0.8873)
MOVE(-0.0163,-0.0173)
MOVE(-0.2308,-1.0215)
MOVE(-0.6179,-2.2337)
MOVE(-0.238,-1.8223)
MOVE(-0.1447,-2.8853)
MOVE(0,-0.4073)
WAIT IDLE
WA(pause)
MOVE(0.4017,0)
WAIT IDLE
WA(pause)
MOVE(0,0.4303)
MOVE(0.1165,2.3244)
MOVE(0.1215,0.5486)
MOVE(0.1893,1.7548)
MOVE(0.6234,2.1578)
MOVE(0.1961,0.8679)
MOVE(1.1361,1.206)
MOVE(0.3215,0.3412)
MOVE(1.1526,1.2235)
MOVE(2.0175,1.7476)
MOVE(0.5106,0.4665)
MOVE(1.4427,0.9608)
MOVE(1.7258,1.8539)
MOVE(0.6126,0.5294)
MOVE(0.5432,0.4694)
MOVE(1.6734,1.2789)
MOVE(0.4756,0.3635)
WAIT IDLE
WA(pause)
MOVE(0,-0.6387)
WAIT IDLE
WA(pause)
MOVE(-0.4756,-0.3541)
MOVE(-1.3919,-1.0638)
MOVE(-0.1341,-0.141)
MOVE(-1.094,-1.15)
MOVE(-1.1378,-1.2223)
MOVE(-0.9744,-0.8118)
MOVE(-1.4191,-0.893)
MOVE(-2.3114,-2.0022)
MOVE(-0.7541,-0.8946)
MOVE(-0.5891,-0.6988)
MOVE(-0.978,-1.1601)
MOVE(-0.0046,-0.0054)
MOVE(-0.1265,-0.56)
MOVE(-0.6042,-2.0059)
MOVE(-0.2103,-1.6106)
MOVE(-0.1399,-0.6316)
MOVE(-0.1117,-2.2272)
MOVE(0,-0.4533)
WAIT IDLE
WA(pause)
MOVE(0.7151,0)
WAIT IDLE
WA(pause)
MOVE(0,0.4943)
MOVE(0.0489,1.861)
MOVE(0.2384,0.9373)
MOVE(0.1902,1.4321)
MOVE(0.6667,1.9922)
MOVE(0.122,0.3758)
MOVE(2.1567,2.6225)
MOVE(0.9485,0.7635)
MOVE(1.7711,1.6033)
MOVE(1.7398,1.3415)
MOVE(2.6333,2.4599)
MOVE(0.7505,0.6235)
MOVE(0.5488,0.4232)
WAIT IDLE
WA(pause)
MOVE(0,-0.6264)
WAIT IDLE
WA(pause)
MOVE(-0.5488,-0.5488)
MOVE(-1.5583,-1.6381)
MOVE(-0.4124,-0.3386)
MOVE(-0.6554,-0.5382)
MOVE(-0.7577,-0.6313)
MOVE(-3.1783,-2.6481)
MOVE(-0.6071,-0.5058)
MOVE(-2.3902,-2.8355)
MOVE(-0.0298,-0.0754)
MOVE(-0.4556,-1.1513)
MOVE(-0.0769,-0.1944)
MOVE(-0.036,-0.2756)
MOVE(-0.2065,-1.5813)
MOVE(-0.34,-1.3859)
MOVE(-0.0718,-1.433)
MOVE(0,-0.5224)
WAIT IDLE
WA(pause)
MOVE(0.6183,0)
WAIT IDLE
WA(pause)
MOVE(0,0.5936)
MOVE(0.3518,3.2614)
MOVE(1.1114,2.862)
MOVE(1.7108,2.0389)
MOVE(5.9963,4.752)
MOVE(0.9875,1.065)
MOVE(0.5488,0.5488)
WAIT IDLE
WA(pause)
MOVE(0.0838,-0.8637)
WAIT IDLE

WA(pause)
MOVE(-0.6326,-0.6796)
MOVE(-0.3788,-0.3982)
MOVE(-2.9844,-2.4865)
MOVE(-1.1873,-0.9893)
MOVE(-0.6506,-0.5421)
MOVE(-1.6918,-1.2418)
MOVE(-1.0146,-1.2036)
MOVE(-0.0962,-0.2432)
MOVE(-1.0851,-2.742)
MOVE(-0.0369,-0.3148)
MOVE(-0.3134,-2.6762)
MOVE(-0.1202,-0.6038)
WAIT IDLE
WA(pause)
MOVE(0.579,0.1807)
WAIT IDLE
WA(pause)
MOVE(0.057,0.5288)
MOVE(0.3051,2.6048)
MOVE(0.0184,0.1574)
MOVE(1.1272,2.8484)
MOVE(0.8197,0.9724)
MOVE(0.1039,0.1233)
MOVE(2.3929,1.7565)
MOVE(0.4668,0.2579)
MOVE(0.4388,0.2424)
MOVE(2.7936,2.2938)
MOVE(0.8221,0.6035)
WAIT IDLE
WA(pause)
MOVE(-0.2859,-1.1227)
WAIT IDLE
WA(pause)
MOVE(-1.0202,-0.8487)
MOVE(-0.8235,-0.6762)
MOVE(-2.1217,-1.1722)
MOVE(-1.7948,-1.3175)
MOVE(-0.6911,-0.9353)
MOVE(-1.0394,-1.4067)
MOVE(-0.0215,-0.0292)
MOVE(-0.0556,-0.1406)
MOVE(-0.6223,-1.5725)
MOVE(-0.2967,-2.5333)
MOVE(-0.0743,-0.6345)
WAIT IDLE
WA(pause)
MOVE(0.6388,0)
WAIT IDLE
WA(pause)
MOVE(0.1215,0.8425)
MOVE(0.368,3.1346)
MOVE(2.1195,2.7979)
MOVE(1.7077,1.2397)
MOVE(2.1345,1.1288)
MOVE(1.325,0.5981)
WAIT IDLE
WA(pause)
MOVE(-0.0877,-0.7501)
WAIT IDLE
WA(pause)
MOVE(-1.6339,-0.9769)
MOVE(-2.0954,-1.1577)
MOVE(-0.0907,-0.082)
MOVE(-0.584,-0.528)
MOVE(-1.9592,-2.6516)
MOVE(0.3856,-2.1884)
MOVE(0.1869,-1.0608)
WAIT IDLE
WA(pause)
MOVE(0.8217,0.4268)
WAIT IDLE
WA(pause)
MOVE(-0.3144,0.9693)
MOVE(-0.4874,1.8531)
MOVE(1.1931,1.5343)
MOVE(1.7861,1.5779)
MOVE(0.8353,0.4042)
MOVE(0.9915,0.4798)
WAIT IDLE
WA(pause)
MOVE(-0.1689,-0.6045)
WAIT IDLE
WA(pause)
MOVE(-1.1731,-0.8661)
MOVE(-2.6621,-2.4071)
WAIT IDLE
WA(pause)
MOVE(0.6828,-1.4413)
MOVE(0.3816,-0.6966)
WAIT IDLE
WA(pause)
MOVE(0.4563,0.2309)
WAIT IDLE
WA(pause)
MOVE(-0.396,0.7007)
MOVE(-0.5138,1.0845)
WAIT IDLE
WA(pause)
MOVE(1.7004,1.5375)
MOVE(1.0237,0.7536)
WAIT IDLE
WA(pause)
MOVE(-0.3223,-0.8084)
WAIT IDLE
WA(pause)
MOVE(-1.0521,-0.9364)
MOVE(-0.4542,-0.4107)
MOVE(-0.2845,-0.2573)
WAIT IDLE
WA(pause)
MOVE(0.2989,-0.6309)
WAIT IDLE
WA(pause)
MOVE(7.6894,0)
WAIT IDLE
WA(pause)
MOVE(0,23.2376)

WAIT IDLE
WA(pause)
MOVE(-35.0866,0)
WAIT IDLE
WA(pause)

'reinforcement strip
MOVE(5.75,0)
WAIT IDLE
WA(pause)
MOVE(0,-4.1464)
MOVE(0,-8.7248)
MOVE(3.5397,-10.0036)
WAIT IDLE
WA(pause)

MOVE(1.9535,-1.039)
MOVE(2.1285,-0.756)
MOVE(2.1255,-0.4356)
MOVE(2.4777,-0.142)
MOVE(2.4784,0.128)
MOVE(2.1279,0.4236)
MOVE(2.1327,0.744)
MOVE(1.9593,1.028)
WAIT IDLE
WA(pause)
MOVE(3.596,9.9835)
WAIT IDLE
WA(pause)
MOVE(0.0471,8.3711)
WAIT IDLE
WA(pause)
MOVE(0.25,-0.0014)
WAIT IDLE
WA(pause)
MOVE(-0.0474,-8.414)
WAIT IDLE
WA(pause)
MOVE(-3.6435,-10.1154)
WAIT IDLE
WA(pause)
MOVE(-2.0618,-1.0817)
MOVE(-2.1666,-0.7558)
MOVE(-2.1628,-0.4305)
MOVE(-2.5101,-0.1297)
MOVE(-2.5094,0.1438)
MOVE(-2.1603,0.4427)
MOVE(-2.1623,0.768)
MOVE(-2.0557,1.0933)
WAIT IDLE
WA(pause)
MOVE(-3.5865,10.1357)
WAIT IDLE
WA(pause)
MOVE(0,8.5177)
WAIT IDLE
WA(pause)
MOVE(-0.25,0)
WAIT IDLE
WA(pause)
MOVE(0,-8.5606)
WAIT IDLE
WA(pause)
MOVE(3.6332,-10.2679)
WAIT IDLE
WA(pause)
MOVE(2.1578,-1.1477)
MOVE(2.1962,-0.78)
MOVE(2.1952,-0.4499)
MOVE(2.5411,-0.1456)
MOVE(2.5419,0.1313)
MOVE(2.1977,0.4375)
MOVE(2.2005,0.7676)
MOVE(2.1643,1.1355)
WAIT IDLE
WA(pause)
MOVE(3.691,10.2472)
WAIT IDLE
WA(pause)
MOVE(0.0476,8.4569)
WAIT IDLE
WA(pause)
MOVE(0.25,-0.0014)
WAIT IDLE
WA(pause)
MOVE(-0.0479,-8.4999)
WAIT IDLE
WA(pause)
MOVE(-3.7385,-10.3791)
WAIT IDLE
WA(pause)
MOVE(-2.2667,-1.1893)
MOVE(-2.2344,-0.7794)
MOVE(-2.2325,-0.4444)
MOVE(-2.5736,-0.133)
MOVE(-2.6,0.149)
MOVE(-2.23,0.457)
MOVE(-2.23,0.792)
MOVE(-2.26,1.202)
WAIT IDLE
WA(pause)
MOVE(-3.68,10.4)
WAIT IDLE
WA(pause)
MOVE(0,8.6036)
WAIT IDLE
WA(pause)
MOVE(-0.25,0)
WAIT IDLE
WA(pause)
MOVE(0,-8.6465)
WAIT IDLE
WA(pause)
MOVE(3.7268,-10.5321)
WAIT IDLE
WA(pause)
MOVE(2.3622,-1.2563)
MOVE(2.2638,-0.804)

MOVE(2.2648,-0.4641)
MOVE(2.6045,-0.1493)
MOVE(2.6053,0.1346)
MOVE(2.2674,0.4514)
MOVE(2.2683,0.7913)
MOVE(2.3692,1.243)
WAIT IDLE
WA(pause)
MOVE(3.786,10.511)
WAIT IDLE
WA(pause)
MOVE(0.0481,8.5428)
WAIT IDLE
WA(pause)
MOVE(0.25,-0.0014)
WAIT IDLE
WA(pause)
MOVE(-0.0484,-8.5857)
WAIT IDLE
WA(pause)
MOVE(-3.8335,-10.6429)
WAIT IDLE
WA(pause)
MOVE(-2.4717,-1.2968)
MOVE(-2.3022,-0.8031)
MOVE(-2.3023,-0.4583)
MOVE(-2.637,-0.1362)
MOVE(-2.6362,0.1511)
MOVE(-2.2997,0.4713)
MOVE(-2.2977,0.816)
MOVE(-2.4643,1.3107)
WAIT IDLE
WA(pause)
MOVE(-3.7734,10.6643)
WAIT IDLE
WA(pause)
MOVE(0,8.5859)
WAIT IDLE
WA(pause)
MOVE(-4.5,4.5)
WAIT IDLE
WA(pause)

'mesh horizontal
MOVE(-0.036,-4.5)
WAIT IDLE
WA(pause)
MOVE(6.536,0)
WAIT IDLE
WA(pause)
MOVE(0,-4.2929)
WAIT IDLE
WA(pause)
MOVE(-6.5,-0.0538)
WAIT IDLE
WA(pause)

MOVE(0,-4.2391)
WAIT IDLE
WA(pause)
MOVE(6.5,0)
WAIT IDLE
WA(pause)
MOVE(0.642,-1.8143)
WAIT IDLE
WA(pause)
MOVE(-7.142,0)
WAIT IDLE
WA(pause)
MOVE(0,-4.7526)
WAIT IDLE
WA(pause)
MOVE(8.8236,0)
WAIT IDLE
WA(pause)
MOVE(1.3041,-3.6855)
WAIT IDLE
WA(pause)
MOVE(-10.1277,0)
WAIT IDLE
WA(pause)
MOVE(0,-3.161)
WAIT IDLE
WA(pause)
MOVE(19.9714,0)
MOVE(20.0286,-0.0001)
WAIT IDLE
WA(pause)
MOVE(0,5.4335)
WAIT IDLE
WA(pause)
MOVE(-9.3278,0)
WAIT IDLE
WA(pause)
MOVE(1.3945,3.8726)
WAIT IDLE
WA(pause)
MOVE(7.9333,0)
WAIT IDLE
WA(pause)
MOVE(0,4.0324)
WAIT IDLE
WA(pause)
MOVE(-6.4813,0)
WAIT IDLE
WA(pause)
MOVE(0.0282,5.0936)
WAIT IDLE
WA(pause)
MOVE(6.4531,0)
WAIT IDLE
WA(pause)
MOVE(0,3.4922)
WAIT IDLE
WA(pause)
MOVE(-6.4337,0)
MOVE(-27.0663,0.075)
WAIT IDLE

WA(pause)
MOVE(0,8)
WAIT IDLE
WA(pause)
MOVE(-4.5,0)
WAIT IDLE
WA(pause)
MOVE(0,-3.5)
WAIT IDLE
WA(pause)
MOVE(-2,0)
WAIT IDLE
WA(pause)

'mesh vertical

MOVE(0,3.5)
WAIT IDLE
WA(pause)
MOVE(5.2568,0)
WAIT IDLE
WA(pause)
MOVE(-0.0103,-8)
WAIT IDLE
WA(pause)
MOVE(3.027,-0.395)
WAIT IDLE
WA(pause)
MOVE(0,8.395)
WAIT IDLE
WA(pause)
MOVE(3.3336,0)
WAIT IDLE
WA(pause)
MOVE(0,-9.3059)
WAIT IDLE
WA(pause)
MOVE(2.6012,-0.4391)
WAIT IDLE
WA(pause)
MOVE(0,9.7449)
WAIT IDLE
WA(pause)
MOVE(3.0664,0)
WAIT IDLE
WA(pause)

MOVE(0,-9.959)
WAIT IDLE
WA(pause)
MOVE(2.8338,0.0619)
WAIT IDLE
WA(pause)
MOVE(0,9.8971)
WAIT IDLE
WA(pause)
MOVE(3.2293,0)
WAIT IDLE
WA(pause)
MOVE(0,-9.5237)
WAIT IDLE
WA(pause)
MOVE(2.9246,0.6427)
WAIT IDLE
WA(pause)
MOVE(0,8.881)
WAIT IDLE
WA(pause)
MOVE(2.6772,0)
WAIT IDLE
WA(pause)
MOVE(0,-8.304)
WAIT IDLE
WA(pause)
MOVE(1.8804,0.232)
WAIT IDLE
WA(pause)
MOVE(0,8.072)
WAIT IDLE
WA(pause)
MOVE(2.7052,0)
WAIT IDLE
WA(pause)
MOVE(0,-40)
WAIT IDLE
WA(pause)
MOVE(-2.7052,0)
WAIT IDLE
WA(pause)
MOVE(-0.5042,20)
WAIT IDLE
WA(pause)
MOVE(-2.0075,-5.5733)
WAIT IDLE
WA(pause)
MOVE(0,-14.4267)
WAIT IDLE
WA(pause)
MOVE(-3.0953,0)
WAIT IDLE
WA(pause)
MOVE(0,11.3984)
WAIT IDLE
WA(pause)
MOVE(-3.4534,-1.0322)
WAIT IDLE
WA(pause)
MOVE(0,-10.3662)
WAIT IDLE
WA(pause)
MOVE(-4.4848,0)
WAIT IDLE
WA(pause)
MOVE(0,10.0407)
WAIT IDLE
WA(pause)
MOVE(-3.0894,0.3468)
WAIT IDLE

```
            WA(pause)
            MOVE(0,-10.3875)                    UNTIL layer_number=layer
            WAIT IDLE
            WA(pause)
            MOVE(-3.4475,0)
            WAIT IDLE
            WA(pause)
            MOVE(0,11.4392)
            WAIT IDLE
            WA(pause)
            MOVE(-2.4643,1.3107)
            WAIT IDLE
            WA(pause)
            MOVE(0,-12.7499)
            WAIT IDLE
            WA(pause)
            MOVE(-3.027,0)
            WAIT IDLE
            WA(pause)
            MOVE(0,21.3045)
            WAIT IDLE
            WA(pause)
            MOVE(-0.7465,2.1097)
            WAIT IDLE
            WA(pause)
            MOVE(0,-23.4141)
            WAIT IDLE
            WA(pause)
            MOVE(-6.5,0)
            WAIT IDLE
            WA(pause)
            MOVE(0,36.5)
            WAIT IDLE
            WA(pause)
            MOVE(2,0)
            WAIT IDLE
            WA(pause)

'border
        MOVE(-1.5312,0)
        WAIT IDLE
        WA(pause)
        MOVE(0,-35.5753)
        WAIT IDLE
        WA(pause)
        MOVE(38.6202,0)
        WAIT IDLE
        WA(pause)
        MOVE(0,38.5663)
        WAIT IDLE
        WA(pause)
        MOVE(-37.089,0)
        WAIT IDLE
        WA(pause)
        MOVE(0,-2.991)
        WAIT IDLE
        WA(pause)

       layer=layer+1
```